GLOBAL DYNAMICS OF A DUMP COMBUSTOR USING MOMENTUM-DRIVEN COUNTERCURRENT SHEAR CONTROL

A DOCTORAL THESIS
SUBMITTED TO THE FACULTY OF THE GRADUATE SCHOOL
OF THE UNIVERSITY OF MINNESOTA
BY

Matthew J. Anderson

IN PARTIAL FULFILLMENT OF THE REQUIREMENTS
FOR THE DEGREE OF
DOCTOR OF PHILOSOPHY
IN MECHANICAL ENGINEERING

Paul J. Strykowski, Advisor

August 2011

Acknowledgements

I am tremendously thankful to Dr. Paul Strykowski for providing me with the opportunity and confidence to explore my research interests and the necessary guidance to avoid getting sidetracked along the way. His never ending energy, humor and companionship were invaluable in allowing me to reach this goal. I have learned tremendous amounts from him that extend much beyond the classroom and laboratory.

My colleagues in the laboratory played a vital role in my research. We celebrated in the successes and lamented in the failures (aka. learning experiences), I could not have asked for better people to go through this journey alongside. Many thanks go to Scott Beard, Alison (Behrens) Hoxie, Mike Hallberg, Tom Shepard and Pat Tracy for their imperative contributions. I would like to specifically recognize Pat for the data collection and processing that was essential in the culmination of this experimental work.

Professors Sean Garrick, Ellen Longmire, Krishnan Mahesh and Terry Simon have all made many contributions to both my education and thesis work and I would like to thank you all. Many University staff members have been very helpful and supportive throughout my education and research, thanks to John Gardner, Dale Lindbeck, Bob Nelson, Robin Russell, and Peter Zimmermann.

Thanks to all of my family, who taught me the importance of hard work and the value of education. Your support helped me through both the highs and lows of this academic career that started a very long time ago.

Finally, I would like to express my deepest gratitude to my wife, Michele. None of this could have happened without her constant love and support. She allowed me to concentrate on completing this dissertation and supported me on so many levels throughout this process. I am so grateful for her infinite support throughout the years of this process, especially in the final stages.

Thank you all.

Dedication

This thesis is dedicated to,

Mrs. K.L. Carter.

Look Grandmére, I finished!

Abstract

Countercurrent shear flow control has been shown as an effective method of increasing volumetric heat release within a dump combustor due to an increase in turbulence, specifically the large turbulent structures present in the flow field. Limitations in a previous suction-derived control mechanism motivated developing this fluidic control scheme using a secondary momentum-driven source.

Multiple momentum-driven facilities were developed and explored; two facilities that showed promise are presented and the results of the isothermal studies show increases in turbulence and three-dimensionality. Momentum-driven countercurrent shear acts to increase the shear within the flow while simultaneously decreasing the convective velocity, thus resulting in elevated peak turbulence levels and increases in both the scale of the turbulent structures and the cross-stream averaged turbulence levels. The effects of this enhanced countercurrent shear leads to a globally unstable flow field that is quite advantageous in combustion control.

Linear stability theory was used to provide guidance into the global flow fields created within these facilities, all of which contain multiple unstable profiles, each having their own stability parameters. Dissecting the flow created into a series of unstable profiles and using knowledge of the stability of these parallel flow profiles provides insight into the global stability of the flows created and how these flows can be used for fluidic control within a dump combustor.

Future studies will investigate the confinement of this flow field and will explore the use of momentum-driven countercurrent shear within a dump combustor

under premixed combustion. It is anticipated that the results of the momentum-driven control mechanism will mirror the effects of the suction based mechanism in reacting environments, specifically creating an enhanced combustor that has increased heat release rates and is less prone to combustion-related instabilities.

Table of Contents

List of Figures

List of Tables

Nomenclature

g ..... gap height below trailing edge, [mm]
h ..... channel height of secondary jet facility, [mm]
H ..... channel height of combustor entrance, [mm]
l_0 ..... integral length scale [m]
L ..... streamwise distance from trailing edge to secondary jet [mm]
M_c ..... convective Mach number
$\dot{m}$ ..... mass flow rate [kg/s]
$\dot{m}_1$ ..... primary mass flow rate [kg/s]
$\dot{m}_2$ ..... secondary mass flow rate [kg/s]
r ..... ratio of freestream velocities ($=U_2/U_1$)
$R_{1,1}$ ..... Spatial correlation function with respect to u' u' correlation
Re_x ..... Reynolds number based on streamwise distance
$Re_{\delta\omega}$ ..... Reynolds number based on vorticity thickness
Re_θ ..... Reynolds number based on momentum thickness
s ..... ratio of freestream densities ($=\rho_2/\rho_1$)
St ..... Strouhal number, dimensionless frequency
u ..... streamwise velocity component, [m/s]
U_1 ..... primary stream velocity, [m/s]
U_2 ..... secondary stream velocity, [m/s]
U_c ..... convection velocity, [m/s] ($=(U_1+U_2)/2$)
U_{jet} ..... core velocity of secondary jet, [m/s]
U^*_2 ..... relevant secondary stream velocity, [m/s]
u' ..... instantaneous streamwise velocity fluctuation from the local mean, [m/s]
u'_{rms} ..... time-averaged fluctuating streamwise velocity component, [m/s]
$\overline{u}$ ..... time-averaged streamwise velocity component, [m/s]
$\overline{u'v'}$ ..... time-averaged Reynolds stress, [m^2/s^2]
v ..... transverse velocity component, [m/s]
v' ..... instantaneous vertical velocity fluctuation from the local mean, [m/s]
v'_{rms} ..... time-averaged fluctuating vertical velocity component, [m/s]
$\overline{v}$ ..... time-averaged vertical velocity component, [m/s]
w ..... spanwise velocity component, [m/s]
w' ..... instantaneous spanwise velocity fluctuation from the local mean , [m/s]
w'_{rms} ..... time-averaged fluctuating spanwise velocity component, [m/s]
$\overline{w}$ ..... time-averaged spanwise velocity component, [m/s]
x ..... streamwise distance from splitter plate, [mm]
x_0 ..... shear layer streamwise virtual origin, [mm]
y ..... transverse distance from splitter plate, [mm]
y_0 ..... shear layer transverse virtual origin, [mm]
y_{05} ..... location of secondary-side shear layer edge, [mm]
y_{50} ..... location of shear layer center, [mm]
y_{95} ..... location of primary-side shear layer edge, [mm]
z ..... spanwise distance in facility, [cm]

ΔU ..... velocity difference between freestreams, [m/s] ($=U_1-U_2$)
δ ..... transverse distance from trailing edge to secondary jet, [mm]
δ_{exp} ..... experimental shear layer thickness, [cm]
δ^* ..... boundary layer displacement thickness, [cm]
δ_{99} ..... boundary layer thickness, [cm]
λ ..... normalized velocity ratio parameter ($=(U_1-U_2)/(U_1+U_2)$)
μ ..... dynamic viscosity [Pa s]
θ ..... shear layer momentum thickness, [cm]
θ_0 ..... boundary layer thickness of primary stream, [cm]
ρ ..... density, [kg/m^3]
ρ_1 ..... primary stream density, [kg/m^3]
ρ_2 ..... secondary stream density, [kg/m^3]
$\rho_{1,1}$ ..... two-dimensional spatial correlation coefficient
ω ..... vorticity, [sec^{-1}]

1 Introduction/Motivation

The focus of the present research is to explore the development of a turbulent flow field within a rearward-facing dump combustor geometry using momentum-driven countercurrent shear as fluidic control. An isothermal planar facility was used to investigate this complex flow field using two novel combustor facilities that employ a momentum-driven, counterflowing, secondary stream. The overall goal was to determine if a momentum-driven counter-current shear flow could be created and to test the viability of using this fluidic control in a combusting environment.

Ramjet engines conventionally employ dump combustors as a means of anchoring a continuous combustion process. The backward-facing step geometry creates flow separation conducive to turbulence production that enhances burning rates and creates a recirculation zone that stabilizes the flame via relight. In these high-speed air-breathing engines, the drag penalty associated with this geometry must be minimized without compromising flame stability. The turbulent combustion process found in dump combustors is very complex in nature as it involves both the fluid mechanics of a turbulent flow field and the complex chemical reaction that affects the physical properties of the fluid. Understanding the shear layer physics that essentially drives the turbulent fluid mechanics in this combustion process is vital for the design of a combustor that can control the reaction process. Minimizing the instabilities of the combustion process and creating a more compact and efficient combustor are the goals of using the various control strategies.

The majority of research conducted on countercurrent shear layers has used a vacuum source to create the driving mechanism for the secondary flow (Niccum 1990, Forliti 2001, Tang 2002). These techniques were used to address issues that were found in previously-designed, momentum-derived facilities, most prominently the global stagnation and flow reversal found by Humphrey and Li (1981). Creating the secondary flow by applying suction below the trailing edge was used to minimize the possibility of the global stagnation.

Creating this fluidic sink allows the flow to be drawn from a path of least resistance, which alleviates the likelihood of stagnation, but becomes problematic under combusting applications. For the unstable turbulent shear layer found in a dump combustor, the sink can be drawing products, reactants or some combination of both depending on the location of the flame and shear layer. The flow drawn by the sink will depend on the instantaneous pressure and velocity fields; this means that instantaneously the secondary countercurrent stream may not always be near the single-sided shear layer created by the primary flow. If the countercurrent shear layer is not created, or not consistently created over a long enough streamwise length, the benefits of mixing and turbulence production, for an elevated countercurrent velocity ratio, will not be achieved.

Other complications arise due to the fact that the flow rate and, therefore, velocity is set by the pressure difference between the sink vacuum pressure and the pressure in the shear flow. In closed and reacting applications the pressure in the combustor can oscillate and, therefore, the secondary velocity will not be constant. Even if the

secondary flow is choked, the upstream pressure oscillations directly affect the mass flow rate.

Using a momentum-derived device can eliminate the two above explained concerns. The secondary flow can be directed using a momentum-derived source such that the countercurrent shear layer is created at a known location and over a fixed spanwise distance. As well, the fuel/air mixture can be prescribed per the operating conditions such that proper equivalence ratio can be maintained. As for the oscillating pressure issue in combustion applications, choking the secondary flow for the momentum derived facility would fix the flow rate as the upstream pressure in this case is not oscillating.

Countercurrent shear, driven by a momentum source, can be used as fluidic control with the overall goal of creating a combustor that is compact, has low drag, high volumetric heat release that is not plagued by thermo-acoustic instabilities and an increased range of operating conditions.

2 Background

2.1 Dump Combustors

Dump combustor geometries have been studied extensively under both isothermal and reacting conditions. Dump combustors consist of a backward facing step and schematics of the basic designs are shown in Figure 1. Pitz and Daily (1983) and Gabruk and Roe (1994) have compared the differences in the velocity fields for isothermal and reacting conditions in planar and axisymmetric combustors, respectively. Both studies concluded that the reattachment length decreases under reacting conditions and the high turbulence levels are displaced from the center of the shear layer into the low-velocity, low-density recirculation zone. These studies have shown that isothermal flows are similar to reacting flows in the same geometry. While the flows are qualitatively similar, the additional heat release of the reacting flow affects the flow. The heat release due to the combustion process tends to straighten the flame interface; which, in turn, reduces the wrinkling of the flame. The turbulence seen in isothermal studies is reduced in the reacting studies.

The flow structure just downstream of the backward facing step consists of strongly two-dimensional vortices (Neto et al., 1993; Le et al., 1997; Lee and Sung, 2001; Schadow and Gutmark 1992). These structures, created by flow separation over the backward-facing step, are then convected downstream and transition to three-dimensional structures near the reattachment point (Le et al., 1997 and Neto et al., 1993). Transition to a more three-dimensional flow field increases mixing and

turbulence levels, creating higher heat release levels near reattachment. In reacting flows, the highly-coherent, two-dimensional structures are subject to thermo-acoustic instabilities under certain operating conditions, which must be mitigated for successful combustion (Poinsot et al. 1987). As flow separation within a dump combustor creates a shear layer, understanding of the development of shear flows is necessary for proper combustor design and implementation.

While the research presented is of a non-reacting flow, a brief background of some important combustion related topics is necessary for a complete discussion of the flow field and its possible application with reaction.

2.1.1 Flame anchoring

The backward-facing step geometry found in the asymmetric dump combustor creates flow separation conducive to turbulence production, enhancing burning rates, and a recirculation zone that stabilizes the flame via relight. The protection provided by the backward-facing step creates a low-velocity zone that contains products at elevated temperatures, which serves to ignite reactants passing over the step (called relight). Figure 2 shows the low speed recirculation zone necessary for flame anchoring found in multiple air breathing combustor geometries. The flame brush shows the location where the flame resides, in this turbulent combustion process the flame is not stationary and instantaneously may reside anywhere within this domain. The recirculation zone located behind the bluff bodies continuously supplies enough activation energy to initiate burning of the incoming reactants. The continuous nature of this re-ignition

process, in which there is large enough activation energy transfer from the products to the incoming reactants for stable combustion that is not reliant on an external activation source.

Further background into general flame anchoring theory can be found in Williams (1947), and Kundu et al. (1980) and Zukoskiand Marble (1956) for bluff body anchoring. Berhrens (2007) discussed in great detail the physical mechanisms within the shear flow found in a countercurrent dump combustor that provides a flame anchor.

2.1.2 Thermo-acoustic Instabilities

While the study presented here was confined to isothermal experiments, the results of this research regarding the flow field will be applied to reacting environments. Therefore, a background of combustion instabilities, specifically thermo-acoustic instabilities will be presented.

The confined flow found in a dump combustor is susceptible to this instability as the separated flow created by the sudden expansion acts as a shear flow that has coherent structures. The structures created by the shear flow, which are initially two-dimensional, have been found to be periodic and to be affected by the combustion process (Smith and Zukoski, 1985). A thermo-acoustic instability is the result of a coupling between the unsteady heat release due to these flow structures with the acoustic field creating by the combustor geometry. The flow entering the combustor consists of premixed reactants, these reactants can be contained within the flow structures and only allow for combustion at the interface while the flow is being

convected downstream. If the flow structure grows large enough and impinges on the combustor wall, rapid breakdown of the structure will occur ultimately leading to three-dimensional mixing and burning and creating a spike in pressure. This pressure spike travels back upstream to the separation point and manipulates the boundary condition of the flow. Ultimately, a stronger two-dimensional structure is created which results in less mixing within the shear layer until the structures impinge on the surface of the combustor walls. The creation of this positive feedback loop amplifies the initial separating flow structures and, therefore, creates more periodic heat release and pressure fields. This instability can result in large pressure oscillations within the combustor and the consequences of this can lead to loss of flame stability (blow out), mechanical fatigue to the combustor and decreased combustor efficiency as unburned hydrocarbons can exit the combustor.

2.2 Shear Layers

A shear layer develops when a primary stream of fluid interacts with a secondary stream of fluid at a different velocity. The two streams may also be differing in density, temperature, viscosity, Mach number, and chemical composition, among others. The mixing between the two streams is contained in the region of the shear layer. There are three basic types of shear layers; Figure 3 shows the velocity profiles of these types schematically shown with step discontinuities in the velocity profiles.

Shear flows are described by two primary parameters the velocity ratio and the normalized velocity ratio. The velocity ratio (r) is defined as:

$$r = \frac{U_2}{U_1} \qquad \textbf{2.1}$$

and the normalized velocity ratio parameter (λ) is defined as:

$$\lambda = \frac{U_1 - U_2}{U_1 + U_2} \qquad \textbf{2.2}$$

The normalized velocity ratio is frequently used as it shows the ratio of the velocity difference of the two streams, normalized relative to the convective velocity of the flow. Figure 3a, a free shear layer, is a fundamental flow of a primary stream exhausting into a quiescent fluid. A coflowing shear layer can be seen in Figure 3b, this exists when two quasi-parallel streams of fluid are flowing in the same direction, but with different velocity magnitudes. Coflowing shear layers are found in mixing processes and aviation applications e.g. a jet engine exhaust while in flight. Figure 3c shows a counterflowing shear layer, where the secondary stream velocity is opposite that of the primary stream. Counterflowing shear layer are found naturally occurring in separating flow, but also have been created for flow control (Forliti, 2001).

As the two steams of fluid interact, momentum is diffused though viscosity and turbulent transport; the resulting mean profiles are shown in Figure 4. Shear layers are commonly defined by the velocity profile, but are also substantially impacted by the additional parameters shown in the figure. A complete description of a shear layer requires profiles of all the parameters shown in Figure 4 (U(y), ρ(y), T(y), μ(y) and M(y)). The thickness of the shear layer and the growth rate have been quantities of interest within the research community (Birch and Eggers, 1972) since the initial work of Liepmann and Laufer (1947). Multiple definitions have been used to quantify the shear layer thickness; a commonly used definition is the vorticity thickness, δ_ω

$$\delta_{\omega} = \frac{U_1 - U_2}{\left(\frac{\partial u}{\partial y}\right)_{\max}} \qquad \textbf{2.3}$$

where the numerator is the difference in the freestream velocities and the denominator, $(du/dy)_{max}$, is the maximum cross-stream mean velocity gradient, the maximum gradient is located near the middle of the shear layer. Other measurements of shear layer thicknesses are used; one is the velocity thickness δ_{vel}, defined as:

$$\delta_{vel} = y_{95} - y_5 \qquad \textbf{2.4}$$

where y_{95} is the location where the velocity is $u = U_2+0.95(U_1-U_2)$ and y_5 is where $u = U_2+0.05(U_1-U_2)$, u is a function of location in x and y and is the local mean velocity component in the streamwise direction.

2.2.1 Spatial Shear Layer Development

Shear layer development occurs in both space and time, though one usually dominates. So called "temporally developing shear layers" take a flow at a uniform initial condition and the shear layer develops in time due to a shear applied to the flow. A tilting tank that contains two stratified fluids that are initially in equilibrium and then tipped creates a countercurrent shear layer that is growing in time (Thorpe, 1971). This flow is not commonly found in engineering flows but has been used for physical insight of the shear flow and confirmation of computational experiments.

While temporally developing shear layers are useful for fundamental studies and computational models, spatially developing shear layers are the focus of this study. Figure 5 shows the spatially developing shear layer.

The development can be broken down into two regions in space; the developing region and the fully developed region. The developing region can further be broken down into a two-dimensional region and a three-dimensional region. All of these regions have distinct flow features

As the two streams flow past the splitter plate, the difference in momentum is allowed to diffuse. The shear created between the two steams will lead to the formation of vortices. These highly-organized vortical structures are found to be strongly correlated in the spanwise direction. The interaction and eventual breakdown of these spanwise structures leads to three-dimensional turbulence and transition into the three-dimensional portion of the developing region.

Upon the collapse of mean and fluctuating velocity statistics across the shear layer onto a single curve, the shear layer has entered the fully developed region. When using the proper local variables to normalize these profiles, the flow is shown to be independent of any upstream disturbances. The mean velocity profiles collapse before the higher order turbulent statistics, such as the Reynolds stresses, collapse. This has been shown to be the case for turbulent boundary layers as well (Hussain and Zedan, 1978).

The turbulent transport of momentum throughout the entire shear layer results in a growth of the shear layer. The rate of growth of the shear layer has been shown to be linear in the streamwise direction in the fully-developed region, both experimentally (Hussain and Zedan, 1978) and analytically (Ho and Huang, 1982). The growth and location of the shear layer in the fully developed region can be used to obtain the so-called virtual origin of the shear layer.

The growth rate of the shear layer in the developing region is dependent on the parameters of the two streams. The velocity ratio, r, density ratio, s, and convective Mach number, M_c, have been shown to be the important factors in the growth rate of the shear layer, as has the boundary layer thickness and boundary layer states (turbulent, laminar, or transitional) at the location of separation from the plate (Forliti 2001). The exact relationship between the growth rate and these parameters has yet to be concluded, but several approximations exist (Miles and Shih, 1968; Birch and Eggers, 1972; and Brown and Roshko, 1974).

2.2.2 Shear Layer Initial Conditions

Shear layers can be thought of as linear and nonlinear amplifiers of the disturbances within the initial flows that enter into the shear layer. The mean velocity profile and its associated boundary layer, defined by θ_0, δ^* and/or δ_{99}, and the unsteady velocity profiles have large effects on the developing region of the flow. Figure 6 shows the mean and fluctuating velocity profiles for turbulent and laminar boundary layers in a flow with minimal freestream turbulence levels.

The development region of a shear layer is dominated initially by nonlinear amplifications of the initial disturbances of the flow, therefore a turbulent boundary layer has a direct impact on the development of the shear layer. Bradshaw (1966) showed the effect the boundary layer status has on the development of the Reynolds stresses. The growth rate of the shear layer is affected by the status of the boundary layer, the growth rate is larger for the laminar boundary layer (Ho and Huerre, 1984;

Browand and Latigo, 1979). The large spanwise structures that Lasharas et al. (1986 & 1988) showed required laminar boundary layers as well as large spanwise aspect ratios to mitigate end wall effects.

2.3 Countercurrent Shear Layer

Countercurrent shear layers are created with a negative secondary velocity; therefore, the velocity ratio is $r < 0$. With the two streams moving in opposite directions, the convective velocity, relative to a reference frame defined by a fixed point in space, normally the splitter plate, is much less than the convective velocity in a coflowing shear layer with a similar velocity difference. This allows the flow to develop more rapidly in space than in the coflowing shear layer. A critical velocity ratio of 13% counterflow, or $\lambda = 1.3$, was predicted by Huerre and Monkewitz (1984), as required for transition from convective to absolute instability for a hyperbolic tangent velocity profile. This profile closely represents a planar laminar shear layer velocity profile. Numerous experimental studies have shown a bifurcation in the flow field as the counterflow velocity ratio exceeds 13% of the primary stream (Niccum 1990, Forliti 2001, and Tang 2002). Changes in the turbulence kinetic energy, spectral content of the turbulence energy and structure of the flow are some of the effects of this transition. Tang (2002) also reported a deviation of the collapse of turbulence quantities for counterflow velocities that were greater than the critical ratio.

As previously explained, the countercurrent shear layer is commonly found in separating flows, where a recirculation zone drives the opposing velocity stream. The

countercurrent shear layers created by flow blockages and sudden expansions are not typically able to reach the critical velocity ratio required for absolutely unstable flow. This does not mean that this flow is not possible, careful design can create a countercurrent shear layer with a velocity ratio that supports the absolutely unstable criterion, hydrodynamic stability background to follow in a subsequent section.

Countercurrent shear layers have received little attention relative to the coflowing shear layers. Abramovich (1963) first studied a jet issuing into a counterflowing channel and a separating flow due to a step in a channel. The findings of this work are that the countercurrent shear layer growth rate is independent of velocity ratio. Keep in mind that this study was done over a very small range of velocity ratios. The next studies on countercurrent shear layers were performed by Thorpe (1968 & 1971), using a tilting tank to study a temporally developing flow with a negative velocity ratio of r = -1. The experiments showed the vortex rollup process between the two streams but, due to the convective velocity of zero, the flow became unstable.

2.3.1 Momentum Derived Counterflow

The first attempt to study a spatially-developing, countercurrent shear layer was made by Humphrey and Li (1981). Two momentum-driven streams were combined as shown in Figure 7. The streams were separated by splitter plates and constrained by horizontal walls at the top and bottom.

The facility was designed to set up a countercurrent shear layer to study the mixing of the two streams; instead, a global stagnation point was created, shown in

Figure 7. The stagnation of the streams forced the flow to turn 180° and return from the side of its origin.

Alvi et al. (1996) created a momentum-driven countercurrent shear layer using two Mach 2 jets oriented in opposite directions. The jets were aligned such that the single-sided shear layer of one just came into contact with the single-sided shear layer of the opposite jet. Because they were aligned with no dead zone between the two jets, a countercurrent shear layer was established with zero convection velocity. The facility is shown in Figure 8. This study reported enhanced mixing, which supported the idea of a global instability, and not convective instabilities. No detailed measurements were made to support the claim of a global instability.

2.3.2 Suction Derived Counterflow

As momentum-driven countercurrent shear layers were proving to be experimentally difficult to create, Strykowski and Niccum (1992) developed an axisymmetric facility to investigate the critical velocity ratio proposed by Huerre and Monkewitz (1985) and the density ratio effects by Pavithran and Redekopp (1989). The axisymmetric jet was used to study the spatial development of a jet with suction applied through an annulus around the jet, Figure 9 shows the facility.

The critical velocity ratio measured in this axisymmetric shear layer study agreed well with the critical velocity ratio found using linear stability theory. Upon reaching a velocity ratio of $\lambda = 1.3$, the shear layer showed a dramatic transition by suppressing the typical vortex pairing, affecting the overall mixing. Axisymmetric jets

can be used to study planar shear layers so long as the radius of the jet is much greater than the shear layer thickness. This can be accomplished near the shear layer origin but as the shear layer is convected downstream, the shear layer grows to where this assumption is not valid. The solution to this problem is to investigate planar shear layers developing from planar jets.

The first planar counterflowing facility was developed by Khemakhem (1997), again using suction to drive the secondary flow. The countercurrent shear layer was created but difficulties in measurement techniques created uncertainties and required continued research. Tang (2002) was the first to provide detailed measurements within a turbulent countercurrent shear layer. A planar facility that employed suction at the trailing edge of a primary flow to create opposed secondary flow was used to analyze the fully developed region of a countercurrent shear layer with velocity ratios over the range $1.0 < \lambda < 1.85$. Figure 10 shows the facility used by Tang (2002). The curved bottom wall and downward sloping upper wall is to facilitate a flow having a zero streamwise pressure gradient. As the shear layer is displaced downward due to the elevated growth rate of the countercurrent shear layer, the curved bottom wall allows free entrainment without the shear layer impinging on the lower wall.

Spanwise PIV data were taken over multiple domains and hot wire anemometry was used to measure the quantities of interest within the fully-developed region. The location of the fully developed region was proposed by Tang (2002) for countercurrent shear flows. A similarity Reynolds number, Equation 2.5, based on the velocity difference of the two streams and the streamwise distance from the virtual origin was used.

$$\mathrm{Re}_{x,sp} = \frac{(U_1 - U_2)(x_{u',sp} - x_0)}{\nu} \qquad \textbf{2.5}$$

The location of similarity in the streamwise velocity fluctuations was found to be approximately $\mathrm{Re}_{x,sp}$ = 600,000. Tang (2002) found that farther downstream than this streamwise location, time-averaged flow statistics, specifically u', v' and u'v', were self-preserving when normalized properly by local coordinates.

The shear layer streamwise, transverse and Reynolds stresses' (u', v', u'v') shape functions for velocity ratios λ<1.3 were shown to collapse to a single profile (Tang 2002). With increasing velocity ratios, the velocity profiles appear to asymptote to a different self-similar profile.

2.4 Linear Stability Theory

The hydrodynamic instability of a fluid is its inability to sustain the flow field against small perturbations that are common in most physical flows. In other words if a flow field is subjected to a small perturbation and the reaction of the flow amplifies the perturbation, that flow is said to be unstable and if the flow dissipates the perturbation, the flow is said to be stable. Coupling this definition with the equations governing the flow physics, the Navier-Stokes equations, allows a spatial and temporal analysis of the flow field and the response to a perturbation. A complete analysis of the three-dimensional, non-linear, governing equations must be solved in order to determine the response of the flow field. This would require a direct numerical simulation (DNS) which is very computationally expensive. Using a one-dimensional, parallel-flow profile as the initial condition to the flow field, and using linearized governing

equations allows for much less expensive computations. The response of the flow field is allowed to evolve in space and time, this analysis is known as linear stability analysis. Even with the simplified analysis, linear stability theory has been shown to accurately predict the response of a system (Ho and Huerre, 1984).

Within the unstable flow regime there are two types of instabilities; convective and absolute instability. Figure 11 conceptually shows the two regimes on a time-space coordinate system. The plots show how a disturbance that is initiated at the origin (t = 0 and x = 0) grows. Figure 11a shows the disturbance growing in time and being convected downstream. While the disturbance grows, which, by definition, means that the flow is unstable, the disturbance is being convected downstream such that the effects are not seen at x = 0 at times greater than t = 0. Absolutely unstable flow, shown in Figure 11b, differs, as the perturbation is seen at x = 0 for all times greater than t = 0. Linear stability theory is commonly used to help guide and understand a variety of flow fields where one would find a transition between convectively and absolutely unstable flows. The required parameters of importance when determining unstable regimes have been shown to be ratios of velocity, density, viscosity and Mach numbers. Schematics of some basic shear flows are shown in Figure 12, all of which have different velocity or density ratios where the transition has been predicted by linear theory. The planar counter current shear layer and the wall bounded recirculation bubble profiles shown in Figure 12 b & d are found in the flow fields of the present study. The critical velocity ratios required for transition, as predicted by linear stability theory, are

$\left.\bar{U}_2 \middle/ \bar{U}_1\right|_{critical} = -0.13$ for parallel shear flows (Huerre and Monkewitz, 1985) using tanh

mean velocity profiles and $\bar{U}_2 / \bar{U}_1 \big|_{critical} = -0.30$ for wall bounded recirculation bubbles (Hammond and Redekopp, 1998) using Falkner-Skan boundary layer profiles.

2.5 Coanda Jet

The manipulation of the secondary jet was used in this study to investigate momentum-driven countercurrent shear. A free jet issuing from a nozzle entrains fluid on both sides due to the shear layers created. Figure 13 shows a two-dimensional free jet and its entrainment between the high momentum core and the quiescent fluid in which the jet issues. When a curved surface is added tangentially to the edge of the nozzle exit, the jet bends towards the curved surface; Squire (1950) and Wilson (1970) have explained this phenomenon. Figure 14 depicts a two-dimensional jet being curved downwards due to the addition of a curved surface of radius R.

The entrainment of fluid on the lower shear layer is constrained by the curved surface. This fluid that is entrained through the lower shear layer must be replaced by ambient fluid that must flow along the curved surface and must draw fluid from further downstream. A lower pressure within this constricted region between the jet and the curved surface is necessary to draw the fluid from the surrounding downstream fluid. The pressure differential between the surroundings and the lower wall draws the jet towards the lower surface; this is known as the "Coanda" effect.

This effect was described originally by Young (1800) and was named after a French engineer who patented the effect in 1932. The Coanda effect is the deflection of a jet towards a surface due to a pressure differential. If the pressure differential is large

enough, due to sufficiently large entrainment rates, the jet can become attached to the curved surface. This attachment is commonly thought of as the Coanda effect but attachment is not necessary, it is only a consequence of a strong Coanda effect.

The attached jet remains insensitive to perturbations in the flow under steady conditions, which results in the jet re-establishing itself to the conditions prior to the perturbation. This stable configuration will keep the jet attached to the curved surface and the low pressure near the surface will be held based on the equations of motion. The equations of motion for a steady, laminar, inviscid and incompressible flow in cylindrical coordinates, neglecting body forces, are:

$$u_r \frac{\partial u_r}{\partial r} + \frac{u_r}{r}\frac{\partial u_r}{\partial \theta} - \frac{u_\theta^{\,2}}{r} = -\frac{1}{\rho}\frac{\partial P}{\partial r} \qquad \textbf{2.6}$$

$$u_r \frac{\partial u_\theta}{\partial r} + \frac{u_\theta}{r}\frac{\partial u_\theta}{\partial \theta} - \frac{u_r u_\theta}{r} = -\frac{1}{\rho r}\frac{\partial P}{\partial \theta} \qquad \textbf{2.7}$$

If parallel flow is assumed, $u_\theta = u_\theta(r)$ and $u_r = 0$ then the equations of motion reduce to:

$$\frac{\partial P}{\partial r} = \frac{\rho u_\theta^{\,2}}{r} \qquad \textbf{2.8}$$

This results in a pressure gradient that increases with the square of the velocity and decreases with radius. The pressure increases from a minimum value at the curved surface to atmospheric pressure at the outer boundary of the jet. It is this pressure gradient that creates the stable flow configuration and keeps the jet attached to the curved surface.

2.6 Conclusions

Momentum-driven countercurrent shear is explored in this present work where multiple geometric facilities develop flow fields that are used to investigate counterflowing planar jets. The confines of this work lie within a larger research program that has explored the benefits of using countercurrent shear layers for control within a dump combustor. The work of Forliti (2001) and Behrens (2007) have shown the effect of suction-derived countercurrent shear within a dump combustor. Countercurrent shear has shown great promise in increasing heat release rates in rearward-facing step dump combustors, but the limitations of suction based facilities motivated the current study.

Partially confined momentum based facilities will be used to explore the option of using this control strategy within a dump combustor. The present work is the initial concept validation of momentum-based control and expands on the work of Alvi et al. (1996) and Humphrey and Li (1981). This study will employ two facilities, one having an arrangement similar to that of Alvi et al. and the second using the Coanda effect to create momentum-driven countercurrent shear to avoid the global stagnation observed by Humphrey and Li. This initial study, while using an open facility, will provide insight as to the viability of implementing this control strategy into a dump combustor application.

3 Facility and Experimental Methods

Experiments were performed in the Combustion Control Laboratory at the University of Minnesota; this chapter will describe the experimental facility and diagnostics techniques used to perform these experiments. The facility consisted of an air delivery system with multiple modular facilities that created momentum-driven countercurrent shear. Isothermal flows were studied in these experiments, which allowed for multiple measurement techniques. Hot wire anemometry and particle image velocimetry were the primary velocity measurement techniques used.

3.1 Momentum-driven facilities

The momentum-driven facilities that were used in the present work are modifications of the asymmetric rectangular dump combustor used by Forliti (2001) and Behrens (2007). Counterflow for these previous studies was generated by suction based means, whereas the counterflow developed for the present study is driven by a momentum derived source.

3.1.1 Primary air delivery system

The flow provided to the experimental facility is shown schematically in Figure 15, the primary flow was supplied via a Roots blower and the secondary flow was driven from the building's compressed air system. Control of the primary air flow rate

was accomplished by a variable-frequency drive on the blower. A percentage of the mass flow rate from the blower was bleed off into the laboratory in order to minimize the back pressure on the blower and the remaining air flow was ducted to the facility. The flow rate entering the facility was metered and recorded via a venturi meter.

In order to facilitate PIV experiments, the flow must be seeded with tracer particles that follow the flow, olive oil droplets were used as the particles in this facility. The droplets were created in a Laskin nozzle where compressed air enters the Laskin nozzle, creates the olive oil droplets and carries these tracer particles to the main flow. This auxiliary, seeded flow was introduced to the primary flow of the facility, such that the tracer particles were well mixed with the main flow, before entering the cavity combustor. The seed density was controlled by varying the air flow through the Laskin nozzle. The auxiliary air flow was measured and recorded to account for the additional mass flow entering the facility.

The primary air, seeded for PIV studies and non-seeded for hotwire studies was then ducted and conditioned before entering the test facility. A diffuser smoothly takes the flow from a 50.8 mm circular tube to a 160 x 120 mm rectangular channel into a plenum that used two perforated plates for flow conditioning. The plates were followed by a two-dimensional nozzle with a 6:1 area reduction, the conditioning and acceleration of the flow resulted in a stable and thin boundary layer providing a nominally top-hat velocity profile to a rectangular inlet duct having a vertical dimension of 20mm, the velocity and turbulence profiles are shown in Figure 16 with the corresponding spectra shown in Figure 17. The peaks in the spectral data are results from the blower blades. Experiments were conducted for a single primary flow velocity

inlet velocity of 10.1 ± 0.4 m/s, corresponding to an inlet Reynolds number of 14,000 based on the inlet channel height H.

Secondary flow for these experiments was provided by the buildings compressed air system. The air pressure was regulated and flow was controlled and recorded by a rotometer. For PIV experiments this flow needs to contain tracer particles, similar to the primary flow an auxiliary airflow was supplied to a second Laskin nozzle and then introduced to the secondary stream before the jet hardware. The flow was conditioned again in a similar manner as the primary flow; consisting of a section of honeycomb, two screens and an area contraction.

Multiple modular momentum-driven facilities were attached to these air deliver systems. The primary airflow entered the test section through a 20mm x 160mm rectangular slot and the secondary flow through a 2mm x 158mm rectangular slot. Two modular facilities using these inlet conditions will be explained below and the results of the flow fields created will be discussed in a subsequent chapter.

3.1.2 Geometry I: Closed facility

The first modular test section will be known as Geometry I, the closed test section which is shown in Figure 18 andFigure 19 with the sidewalls removed in Figure 19 to show the flow conditioning. Downstream of the secondary jet, an upper wall encloses the facility to the exhaust duct, creating a "closed facility." Below the trailing edge of the primary stream is an opening to the room which allows all for the gas of the secondary jet to escape. This allows for a fundamental study of the flow field. In

application, these gases could be captured and returned to the primary flow further downstream.

Many length scales exist within this facility and are important in the development of the flow field. The height, H, is of the inlet primary channel flow, fixed at 20mm for all experiments. The streamwise distance, L, the secondary jet is located downstream of the splitter plate. This was fixed at 20mm, equal to the primary channel height. The final expansion of the closed facility was fixed at 2H (40mm), and the secondary slot jet thickness, h, was fixed at H/10 (2mm). The spanwise dimension of the test facility is Z = 8H. The facility consisted of 9.5mm stainless steel upper and back walls. A fused quartz window positioned in the upper wall for laser sheet optical access and the side wall was made of 9.5mm polycarbonate for optical access.

The vertical location of the secondary jet played a vital role in the development of the flow field of the present study. As the primary flow expands over the trailing edge, which has a thickness of T = 0.05H (1mm), a shear layer is created. If this shear layer were free to develop without the secondary jet or secondary jet hardware, the entrainment of the stagnant air below the trailing edge would act to diffuse momentum and the shear layer would grow as it is convected downstream. Careful placement of the secondary jet was required such that the jets can interact. But it should not be too far into the primary stream, or it will block the main flow. The location that was used for the present study was $\delta = 0.15H$.

3.1.3 Geometry II: Coanda facility

The Coanda test section is shown schematically in Figure 20 and images of the facility are shown in Figure 21. In this facility the secondary jet is located out of the primary stream, by locating the secondary jet at a cross-stream location of y/H = -1 the hardware does not affect the streamwise development of the primary shear layer. The flow from the secondary jet is directed towards the trailing edge by rotating the jet and attaching a curved surface to the lower wall of the planar jet, displayed in Figure 20. This curved surface utilizes the Coanda effect to keep the jet attached to the surface, directing it up towards the trailing edge and turning the flow to create nominally parallel countercurrent flow that is in the vicinity of the trailing edge.

Again, many length scales are present in this facility that are important in the development of the flow field. The primary flow channel inlet height is defined as H and set to 20mm, the secondary jet height (h) was H/10, consistent with the closed facility study. The spanwise dimension of the facility was kept constant at Z = 8H, and the facility consisted of the same side and top walls that allow for optical access. Differing from the Geometry I, this study was performed with the lower wall (downstream of the secondary jet) removed and the facility was open to the ambient room conditions downstream of the secondary jet. The open facility allowed for free entrainment by the secondary jet.

The radius of curvature for the curved surface (r) was constant and set to be 89mm for all experiments. The gap height (g) was a very critical parameter for this study. The effect of gap height was studied in this facility, with an optimal gap height to be experimentally determined. The streamwise distance from the trailing edge to

where the secondary jet was located, varied slightly with gap height but was nominally fixed to be 35mm.

3.1.4 Forcing facility

Inlet conditions play a significant role on the development of the structures within a shear layer (Dziomba and Fiedler, 1983). In order to study the effects of forcing on the development of the flow field periodic flow excitation was introduced via a loudspeaker. A cavity housing a loudspeaker that was driven by an amplified sign wave was attached to the plenum downstream of the flow conditioning section and upstream of the two-dimensional contraction. Both the amplitude of the forcing and the frequency were controlled independently. Figure 22 shows a schematic of the forcing facility, this facility was removed for non-forced studies.

A second forcing facility arrangement was necessary when stronger, more two-dimensional, perturbations to the primary inlet flow were required in the Geometry II study to be discussed. Motivation for this stronger forcing will be discussed in the results and discussion section regarding the Geometry II flow field. When this stronger forcing was required the same loudspeaker and signal generator were used, however the acoustic waves were ducted downstream of the two-dimensional contraction, as shown in Figure 23. This location allowed for greater excitation at the primary flow exit that penetrated the shear layer.

3.2 Experimental Methods

3.2.1 Data Acquisition

The data was acquired via a National Instruments compact DAQ system; this consists of a compact DAQ chassis (P/N cDAQ-9172) and multiple plug in modules and a PC to control the system via a Labview experiment program. The chassis can sample at 5MS/s through at 24 bits, this chassis is connected to a PC to store the data through a Hi-Speed USB port. The host computer is a Dell Optiplex 755 running MS Windows XP operating system, multiple Labview programs were used to record the data. The Labview programs were used to record the run conditions for all experiments, control two Newport linear traverses and to record measurement signals.

Two types of modules were used in conjunction with the chassis to record both thermocouples and voltage measurements. NI9211 modules were used to sample 4 thermocouples, each at 24 bits and 14 Samples/sec. NI9239 modules were used to sample voltage signals, each can sample 4 channels of +/-10V simultaneous at 24 bits up to 50ksample/sec/channel. Temporally-resolved data were sampled at 2 kHz.

3.2.2 Hotwire

Single-point velocity measurements are acquired using constant-temperature hot-wire anemometry. This technique captures time-varying velocity measurements by correlating the convective heat transfer from the sensor to the velocity of the fluid. A Dantec 55P05 boundary layer probe was used to take the measurements, this probe has

gold plated prongs with a platinum-plated tungsten wire. The sampling wire of this probe is of a 5μm diameter and 1.25mm length. This probe was chosen not for it's boundary layer measurement possibilities but the constrained domain this probe allowed access to the more locations. It was inserted from the downstream section of the test facility therefore minimizing the effect on the overall flow field. The probe was kept at a constant temperature, approx 250˚C by a Dantec 55M10 CTA standard bridge; this is an overheat ratio of approximately 1.75.

This hotwire was calibrated using Pitot probe measurements, both probes mounted closely in the primary flow. The Pitot probe had an outer diameter of 2.1 mm and an inner diameter of 1.6 mm. The differential pressure between the total pressure of the probe and the static pressure in the facility was measured by a MKS 10-torr pressure head. These calibration measurements were taken at a location of x/H = -0.5 and y/H = -0.5. The calibration used was a form of King' Law (Goldstein, 1996), shown as

$$E_m^{\ 2} = A + BU^{0.5} \qquad \textbf{3.1}$$

where E_m is the mean voltage measured across the hotwire bridge, U is the velocity determined by the Pitot probe measurement, A and B are constants determined by Matlab program written to determine the calibration constants.

The hot-wire anemometer was used to quantify the baseline configurations of both the facility and the second jet, and to record time accurate velocity traces to be used for frequency analysis. The individual flows can be analyzed using hot-wire anemometry, but this measurement technique was not used in the mixing experiments due to its errors in low speed flow and directional ambiguity.

3.2.3 Schlieren

Flow visualization was used for multiple qualitative studies within these facilities. The primary flow, after being pumped through the roots blower and plumbing system, was approximately 10°C warmer than the ambient air. Schlieren imaging captures gradients in density and, since the primary air was warmer than the ambient air and the secondary air, this technique was used to observe the interaction between the two fluid streams. The Schlieren system consisted of two first-surface f5 15cm primary mirrors, an automotive headlamp used as the light source and Nikon D-70 camera set up in a Z-type configuration. Images were captured using a Nikkor 105mm micro lens, at an F-stop of f/8 and a shutter speed of 1/8000s which essentially froze the density field. Post processing of the images in Matlab rotated, cropped and converted the images to grayscale, but no additional image post-processing was performed.

3.2.4 PIV

A non-invasive imaging technique was used to capture the 2-D flow field; the technique that was used is called particle image velocimetry (PIV). PIV measures instantaneous 2-D velocity fields by seeding the flow with submicron particles that follow the flow, capturing two images and correlating those images. Multiple 2-D image pairs are used to extract multiple flow statistics.

Tracer particles were delivered into the flow field as described in the facilities section of this chapter. As the camera records the scattered light from the tracer

particles and the velocity vectors are created based on the displacement of these tracer particles it is imperative that the particles follow the flow. Olive oil droplets were used for this present study, the droplets were created via Laskin nozzles that were designed to create submicron sized particles (Gerbig and Keady, 1985). According to Melling (1997) the 0.98μm diameter olive oil droplets cutoff frequency is 10kHz, this is the highest frequency that the particles can track the fluid. The energy associated at this frequency is orders of magnitude less than the peak energy frequencies, as shown in Figure 17, therefore the particles should track the flow for all relevant scales.

Two Continuum Surelight I-10 Nd:YAG lasers were used to illuminate the seed droplets. Each laser produces a beam at 532 nm and power output was variable up to 230 mJ/pulse. PIV techniques require a planer light sheet, the output beam is transformed though two lenses; first through a spherical lens to focus the beam such that the sheet is narrow enough in the field of view and secondly though a cylindrical lens to create the sheet. The beam waist from the spherical lens was located just before the test section such that the thickness of the light sheet is sufficient that any spanwise movement will not lose particles between laser pulses. The lasers operated at 5 Hz with a pulse duration of 5ns, which would essentially freeze the seed droplets. These two lasers were triggered independently and had a variable pulse separation of 20 microseconds, on average, but was varied according to the flow conditions.

A TSI Powerview Plus 4mP digital camera was positioned orthogonal to the laser sheet in the combustor. This camera contained two 2048 x 2048 pixel CCD arrays, this allowed for the camera to take a second image in very quick succession while the first image was dumped to the second CCD. The camera was fitted with a

60mm Nikon AF Micro-Nikkor lens and a narrow band filter to minimize ambient light. The camera was controlled using a TSI 64 bit frame grabber.

All of this hardware was controlled and synchronized using a TSI model 610035 LaserPulse synchronizer and TSI Insight 3g software on a Dell Precision T5500 workstation operating on MS Windows operating system. The overall PIV setup in this facility is shown in Figure 24.

3.2.5 PIV Image Processing and Vector Validation

For the present work, the image processing was done using TSI Insight 3G software. A Gaussian curve-fit algorithm was chosen with interrogation regions of 32 x 32 pixels and 50% overlapping of neighboring interrogation regions. These interrogation regions were approximately 0.5 mm x 0.5 mm for the side view domain, and, for the spanwise PIV domain, the interrogation regions were 1.0mm x 1.0 mm.

Multiple filtering techniques were applied to the vector fields to remove any invalid velocity vectors. Particles moving into or out of the light sheet, large velocity gradients, high displacement within an interrogation zone, reflected laser light from boundaries, and buildup of seeding on optically clear access windows to the flow all are causes of erroneous correlations. These inaccurate correlation peaks can lead to lowered signal-to-noise ratios in the correlation domain, and, if large enough, can lead to velocity vectors that do not accurately model the true fluid velocity. Filtering of the vector fields must be done to remove the invalid vectors before any further processing of the data can commence.

Filtering of the initial vectors is done in multiple steps within the TSI Insight software. Within the processor, the software must have a minimum intensity and a minimum peak-to-noise threshold to even calculate an initial velocity vector. The minimum intensity is set to make sure that there are enough particles within the domain to track. If too few particles are present there can be no vector. Secondly, the peak-to-noise threshold is set to confirm that the peak correlation is well above the noise of the other correlation peaks. If either of these criteria is not met the vector is not reported.

After the initial vectors are calculated, every vector is filtered according to global displacement ranges and neighboring values. As the velocities entering the flow field are well established and an overall understanding of the flow field is known, global bounds of the velocity field are used to set a range of velocities in both the vertical and streamwise components. All vectors were evaluated according to this range and if they were found not to be contained in the range they were removed. Neighboring vectors were then used to evaluate the validity of the remaining vectors. This filter used a 3 x 3 region surrounding the vector and if either the vertical or streamwise velocity components of the vector were not within a stipulated range of the region's mean value, the vector was removed.

Upon the removal of these invalid velocity vectors, the secondary peak from the initial correlation was used to fill in the missing data and then was re-filtered to confirm the validity of the new data. If the secondary peak is not acceptable then a final filling is used, the mean of the surrounding velocity vectors is used to fill in the missing data.

3.2.6 PIV Post-Processing

Each PIV experiment consisted of approximately 450-500 image pairs. With the instantaneous velocity fields calculated per the processing previously described, post processing was completed by a combination of Tecplot and Matlab codes. The velocity vector values were ensemble averaged to determine local mean and standard deviations of the velocity. Reynolds stresses were calculated based on instantaneous velocity deviations from the mean. Statistical quantities were calculated via the following equations:

$$\overline{U}(x,y) = \frac{\sum_{i=1}^{N} u_i}{N} \quad \textbf{3.2}$$

$$\overline{V}(x,y) = \frac{\sum_{i=1}^{N} v_i}{N} \quad \textbf{3.3}$$

$$u'_{rms}(x,y) = \sqrt{\frac{\sum_{i=1}^{N-1}\left(u_i(x,y) - \overline{U}(x,y)\right)^2}{N-1}} \quad \textbf{3.4}$$

$$v'_{rms}(x,y) = \sqrt{\frac{\sum_{i=1}^{N-1}\left(v_i(x,y) - \overline{V}(x,y)\right)^2}{N-1}} \quad \textbf{3.5}$$

$$\overline{u'v'}(x,y) = \frac{\sum_{i=1}^{N}\left(u_i(x,y) - \overline{U}(x,y)\right)\left(v_i(x,y) - \overline{V}(x,y)\right)}{N} \quad \textbf{3.6}$$

$$\omega(x,y) = \frac{\sum_{i=1}^{N}\left(\left.\frac{\partial v}{\partial x}\right|_{x,y} - \left.\frac{\partial u}{\partial y}\right|_{x,y}\right)}{N} \quad \textbf{3.7}$$

Spatial gradients in velocity were computed using 2nd order central differencing of the discrete data, applying 2nd order single directional differencing at the boundaries. These spatial gradients are used for the instantaneous strain rates and the vorticity calculations.

In order to confirm statistical convergence, velocity statistics at a single location are plotted verses the number of samples acquired. In Figure 25 a-d, it can be seen that the flow statistics, even the higher order statistics, are converged well below the 450 independent samples.

3.2.7 Spatial Correlation Functions and Integral Length Scales

PIV data can be used to calculate spatial information in addition to local velocity statistics. As PIV data consist of many instantaneous spatial velocity fields, ensemble averaging of the instantaneous fields can provide insight into the length scales present in the flow. The streamwise velocity fluctuation from the local mean velocity (u') is used as the correlation quantity. The normalized spatial correlation function is defined as:

$$R_{11}(x_0, y_0; \Delta x, \Delta y) = \frac{\overline{u'(x_0, y_0) * u'(x_0 + \Delta x, y_0 + \Delta y)}}{\overline{[u'(x_0, y_0)]^2}} \qquad \textbf{3.8}$$

where R_{11} is the correlation function, x_0 and y_0 are the coordinates of the reference point and Δx and Δy are the displacements from the reference point.

Measuring the large turbulent scales present in the flow was accomplished by using the spatial correlation function, and the definition of the integral length scale. The

integral length scale commonly used in shear layer development within dump combustors (Behrens,2007 and Forliti 2001) is defined as:

$$l_0(x) = \int_{y=-\infty}^{y=+\infty} R_{11}(x_0, y_0; \Delta x = 0, \Delta y = y)dy \qquad \textbf{3.9}$$

which correlates the cross-stream dimension of the turbulence structures around a reference point (x_0,y_0). At each spanwise location, x_0, the reference y location, y_0, was defined as the location of maximum turbulence energy.

Two dimensional spatial correlation coefficients were calculated using spanwise PIV data to quantify spanwise coherence. The correlation coefficient was calculated as:

$$\rho_{1,1}(x_0, y_0; \Delta x, \Delta z) = \frac{\overline{u'(x_0, y_0) * u'(x_0 + \Delta x, y_0 + \Delta y)}}{u'_{rms}(x_0, y_0) * u'_{rms}(x_0 + \Delta x, y_0 + \Delta y)} \qquad \textbf{3.10}$$

which is similar to the correlation function other than the normalization by both the reference location Rms velocity fluctuation and the local Rms velocity fluctuation. The reference location for this correlation was chosen to be $x/H \approx 0.5$ and $z/H \approx 0$, located on the correlation plots by an "+".

4 Results and Discussion

In this chapter the results are presented in two main sections. First, the closed moment-driven facility, Geometry I, was investigated and the flow field documented. Secondly, the Coanda facility, known as Geometry II, was used to explore momentum-driven countercurrent shear. Nine secondary flow rates were used to control the turbulent flow field for both facilities, secondary mass flow rates were varied from the baseline ($\dot{m}_2 = 0$) up to 35% of the primary flow. Prior to creating these countercurrent flow fields the secondary jet was documented.

4.1 Secondary Jet

A general quantification of the secondary jet that was used in both facilities was documented. The height of the secondary jet (h), shown in Figure 18 & Figure 20was 2mm and the spanwise component of the facility was 160mm which results in an aspect ratio of 80. Spanwise uniformity of streamwise velocity was measured to by less than 5% of the mean, as shown in Figure 26. With this minimal variability in the spanwise direction and the large aspect ratio, a two-dimensional planar jet was created as the control variable for the flow field. The test conditions vary from 0% to 36% of the primary mass flow rate and are summarize in Table 1. The Reynolds numbers, based on jet height, of these flow rates are within a transitional range for planar jets. The development of the flow in this range has been shown by Suresh et al. (2008) to have dependence on the Reynolds number.

Table 1: Secondary jet flow conditions

$\dot{m}_2/\dot{m}_1$	U_{max}	Re_h
0%	0	0
5%	8.5	1200
9%	12.8	1800
14%	18.6	2500
18%	24.7	3400
23%	29.9	4100
27%	37.2	5100
32%	42.2	5800
36%	48.8	6700

Hotwire measurements were taken in the x-y plane and used to show the development of the mean and fluctuating streamwise, U, velocity components, shown in Figure 27. Flow is shown in this figure, flowing from right to left as this is the counterflowing momentum stream and the flow will be flowing in this direction for this study.

Due to physical hardware constraints, the jet facility does not include a two-dimensional contraction near the jet exit. The flow is conditioned with screens and honeycombs and a contraction, but then experiences a 90° turn followed by a 10h straight length that allows for boundary layer development. The long developing region creates a more developed profile rather than a top-hat profile, this results in thicker boundary layers and an exit profile that is not a fundamental flow. The development of this planar jet was not of interest in this study and therefore careful documentation of the jet exit conditions were taken. The mean streamwise velocity contours show basic symmetry, Figure 27, while the streamwise velocity fluctuations exhibit some

asymmetry. A profile taken at x/h = 2 again shows the basic streamwise velocity component for all flow rates, Figure 28.

4.2 Geometry I Results: Closed momentum-driven facility

The flow field created by using the secondary jet, previously described and shown in Figure 18 in a closed countercurrent arrangement, was explored and the basic effects of this field were quantified. Initial studies selected a vertical location of the secondary jet ($\delta = 0.15H$), this key parameter was held constant as slight variations greatly affected the flow field.

4.2.1 Mean flow fields

The overall flow fields for this geometry were obtained for this geometry using 3 overlapping PIV domains. Figure 29 shows the streamlines based on the mean velocity fields for all secondary jet flow rates. The baseline case, zero secondary flow, is shown in Figure 29a. This field basically consists of a single sided shear layer, $\lambda = 1$, located at the origin of the coordinate system followed by a sudden expansion located at x/H = 3 and y/H = -0.15. Flow is entrained from below the trailing edge into the primary flow due to the shear layer. The large recirculation zone located downstream of the sudden expansion and the secondary, smaller, recirculation zone located near the secondary jet hardware and the lower surface have been reported by many other rearward facing step flows (So and Ahmed, 1988, Le et al. and Forliti 2001). While reattachment of the stagnation streamline on the lower wall was not captured in this

facility it appears that it would behave similar to that seen in the work shown by Forliti (2001).

The development of the mean streamlines can be seen in Figure 29a-i, starting with the baseline and increasing the secondary mass flow rate up to 36% of the primary flow. Initially, a recirculation bubble is apparent above the secondary jet upon even the smallest amount of secondary flow. This bubble is allowed to develop due to what appears to be a time-averaged stagnation point between the primary and secondary flows. This stagnation point moves further upstream with increasing counterflow, due to the increased momentum of the secondary jet. This creates a larger recirculation zone above the secondary jet hardware with increasing secondary flow.

The secondary flow rate has an effect of shorting the streamwise length of the recirculation zone downstream of the secondary jet hardware. The reattachment point moves from out of the domain ($x/H > 8$) for the zero control case (baseline) to x/H less than six, which is a recirculation zone of less than 3. This result is at a minimum, a 40% reduction in streamwise extent of the recirculation zone.

There are multiple recirculation zones present in this closed facility. Figure 30 schematically shows four different zones and their appropriate nomenclature used for this discussion. The primary recirculation zone is created due to the secondary jet penetrating into the primary stream, this causes a stagnation location and forces the primary flow up. The entrainment characteristic of the secondary jet creates reverse flow along the top of the jet hardware that is then turned around and mixed with the primary stream. The accelerated and separated flow then reattaches to the jet hardware downstream creating a recirculation bubble. The secondary recirculation zone is a

product of the entrainment of the secondary jet on the bottom side of the jet and the stagnation point that is created between the primary flow and the secondary jet. The downstream recirculation zone is created due to the closed facility, this is a result of a backwards facing step geometry. The downstream secondary zone is also created by the backward facing step.

The mean streamlines show a general trend of shortening the downstream recirculation zone and increasing the primary recirculation zone with increased secondary flow. The overall mean streamlines within this flow field remain similar with increasing secondary flow, that is, there is no abrupt change to the streamlines when increasing counterflow.

Contours of the mean streamwise velocity, $\overline{U}$, are shown in Figure 31, a-i corresponding to varying secondary flow rates. Mean velocities are normalized by the maximum $\overline{U}$ of the primary flow entering the facility under the baseline run conditions, $\overline{U}_0$. Streamlines are overlaid to illustrate the effects of the recirculation bubbles on the streamwise velocities.

Mean streamwise velocity values are used to provide insight as to the instability transition between convective and absolute according to stability theory. Huerre and Monkewitz (1985) reported transition from convective to absolute instability at 13% counterflow for free shear layers, where Hammond and Redekopp (1998) showed that larger reverse flows, approximately 30%, are necessary for the transition within wall-bounded separation bubbles. Both countercurrent shear layers and wall-bounded recirculation bubbles, which behave similarly to separation bubbles, are found in this flow field and affect the development of the turbulent nature of this field.

The baseline flow field, shown in Figure 31a, shows reverse flow in the recirculation zone downstream of the secondary jet hardware, as expected due to the facility confinement, and shows entrained flow in the vicinity of the trailing edge. Streamwise mean velocity contours, Figure 31b-i, show the effects of increasing the secondary flow rate. The effects of secondary flow are evident in the mean streamwise velocity in multiple locations. First, within the primary recirculation bubble, the primary velocity is accelerated due to the increase in size of this bubble. As the bubble increases in the cross-stream dimension, it acts as a blockage and the primary flow must accelerate up and through the constricted cross-sectional area and, therefore, has a larger positive velocity magnitude. The additional momentum of the secondary jet, in the x negative direction, entrains more flow along the jet hardware and with increasing secondary flow creates a larger negative velocity magnitude. Profiles through the streamwise center of the primary recirculation zone shown in Figure 32, show this effect. The values are summarized in Table 2. It is also noted that the streamwise center of the recirculation bubble is moved upstream with increasing secondary flow.

Table 2: Primary recirculation zone statistics

$\dot{m}_2/\dot{m}_1$	Streamwise center of recirculation bubble	Bubble height/H	$-U_2/U_1$
0%	N/A	N/A	0
5%	x/H = 1.35	.32	0.22
9%	x/H = 1.3	.35	0.26
14%	x/H = 1.15	.42	0.30
18%	x/H = 1.1	.51	0.37
23%	x/H = 1.0	.52	0.33
27%	x/H = 0.95	.56	0.30
32%	x/H = 0.90	.59	0.33
36%	x/H = 0.85	.61	0.38

Next, the effects of the secondary flow can be seen in the recirculation region that is present downstream of the secondary jet hardware. Increases in secondary mass flow rate showed a decrease in the streamwise extent of the downstream recirculation zone. The magnitude of the reverse flow within this recirculation zone does increase slightly with increased secondary flow, as is shown in Figure 33. The overall velocity ratio is affected, but not greatly, by the secondary flow and the streamwise extent over which this is velocity ratio is present is decreased with increasing secondary flow, Table 3 tabulates the effects of secondary on the downstream recirculation zone.

Table 3: Downstream recirculation zone statistics

$\dot{m}_2/\dot{m}_1$	Streamwise center of recirculation bubble	$-U_2/U_1$
0%	x/H = 5.1	0.18
5%	x/H = 4.5	0.14
9%	x/H = 4.3	0.16
14%	x/H = 4.1	0.19
18%	x/H = 4.0	0.19
23%	x/H = 3.8	0.21
27%	x/H = 3.8	0.23
32%	x/H = 3.8	0.26
36%	x/H = 3.8	0.27

It can also be noted that the potential core velocity of the main flow is decreased with increased secondary flow. The primary peak velocity is shown to slowly decrease from the baseline through 18% secondary flow, above which the potential core appears to remain constant, refer to Figure 31a-i. The creation of the recirculation bubble above the secondary jet acts as a flow blockage in the primary stream and accelerates the primary flow upwards of 50% of the inlet velocity. With increased secondary flow two competing factors affect the potential core length; the acceleration of the primary flow

due to the "blockage" and the increasing countercurrent shear due to the increased reverse velocity with the bubble. The result are a potential core length that is unaffected by the acceleration caused at higher secondary flow rates.

Trailing edge mean velocity profiles were examined to determine velocity ratio at each secondary flow level. Figure 34 shows the mean streamwise velocity profiles for all secondary flow levels. As can be seen by the profiles and the corresponding U2/U1 ratios reported in Table 4, 23% secondary flow is required to achieve negative velocity at the trailing edge. At secondary flow rates of 27% and larger the velocity ratio critical for absolute instabilities (-13%) has been reached and exceeded, if the profiles are of a free shear layer, but only the 32% secondary flow case reaches the critical velocity ratio if the profiles are of a wall bounded type.

Table 4: Trailing edge velocity ratio, Geometry I

$\dot{m}_2/\dot{m}_1$	U_2/U_1
0	0.02
5%	0.01
9%	0.02
14%	0.04
18%	0.07
23%	-0.07
27%	-0.24
32%	-0.32
36%	-0.22

The mean velocity flow fields provided insight into how the momentum-driven secondary flow effects the development within this geometry. Mean streamlines showed trends of both increases in the size of the primary recirculation zone and a decrease in streamwise extent of the downstream recirculation zone with increasing

secondary mass flow rate. Velocity ratios created in the primary recirculation zone exceeded the requirements of absolute instabilities for wall bounded flows for secondary mass flow greater than 14% of the primary mass flow rate.

4.2.2 Turbulent Statistics

While mean flow characteristics are helpful in determining how control mechanisms may influence the overall flow field (i.e. thru the mean flow stability) the turbulence quantities quantify how the control mechanism may impact the performance of a combustor. Fluctuating velocities were measured in the streamwise and cross-stream directions, u'_{rms} and v'_{rms}, respectively, where the turbulence reported is the rms of the deviation from the mean velocity. Normalized total turbulence,

$$\frac{\sqrt{(u'_{rms})^2 + (v'_{rms})^2}}{\overline{U}_O} \qquad \textbf{4.1}$$

is calculated from the individual velocity fluctuations in the streamwise and cross-stream directions. All turbulence values reported have been normalized by $\overline{U}_0$.

The streamwise turbulence values are reported in Figure 35, starting with the baseline (Figure 35a); note the streamwise turbulence values of approximately 20% originating at the trailing edge and then again a second shear layer developing from the secondary jet hardware. Increasing the secondary flow rate causes an increase in streamwise turbulence, initially the turbulence appears to originate within the primary recirculation bubble and then convect downstream. Upon higher counterflow levels, streamwise turbulence appears to grow along a line from the training edge to the

secondary jet. Peak values of streamwise turbulence increase to slightly greater than 100% of the value of the inlet velocity. Not only are the peak values of streamwise turbulence large but the overall location over which they encompass increase with increasing secondary flow. As results will show later, this apparent turbulence is due to a flopping of the secondary jet.

The normalized cross-stream rms turbulence values, $v'_{rms}/\overline{U}_0$, are also shown to increase with increasing secondary flow, as seen in Figure 36a-i. In a combustion application this vertical fluctuation leads to flame wrinkling and can lead to increased volumetric heat release. As can be seen, the cross-stream turbulence values are slightly lower than the streamwise turbulence values. Peak cross-stream turbulence values approach 90% of the inlet velocity and appear near the trailing edge.

The secondary flow appears to similarly affect both the cross-stream and streamwise turbulence levels throughout the flow field. This allows the normalized total turbulence to provide a qualitative measure of the mixing within the facility, Figure 37 shows the streamwise, cross-stream and total turbulence for 14% secondary flow condition showing a similar trend for these statistical measurements. Figure 38a-i show the evolution of the total turbulence contours with increasing secondary flow and Figure 39 show the cross-stream averaged total turbulence distributions for all secondary flow rates. The discontinuities that are located at x/H = 1 & 3 are a result of the change in cross-stream PIV interrogation domain (i.e. the channel widens at x/H = 3.0). This quantification of turbulence shows a trend of increasing turbulence throughout the entire streamwise location with increasing secondary flow with the largest magnitude of turbulence located near the secondary jet.

Total turbulence and mean streamwise velocity profiles presented in Figure 40 show the inlet conditions for a backward-facing step flow beginning at the downstream edge of the secondary jet hardware, x/H = 3. Looking at this sudden expansion as itself a backward facing step and the secondary jet upstream of this location is just a mechanism to create turbulence applied to the inlet of this step flow helps to explain the change in downstream recirculation zone. The mean streamwise velocity profiles at this location begin as a top-hat profile in the baseline case and become asymmetric with increasing counterflow. As the primary recirculation bubble grows with increasing counterflow this blockage acts to create a larger boundary layer at the inlet of this backward-facing step. The boundary layer gradually increases for the first two secondary flow rates (5% & 9%) and then appears to converge for all other secondary flow rates (14% and greater) at a much larger boundary layer thickness and the profile appears to be inflectional. With these mean profiles it is noted that the mass flow though this section of the facility decreases with secondary flow, a reduction of 20% in mass relative to the baseline case was seen for the highest secondary flow case. This supports the entrainment by the secondary jet and could also account for the decreased size of the recirculation zone.

It has been shown (So and Ahmed, 1988) that increases in inlet turbulence shorten the recirculation zone downstream of a sudden expansion. Figure 40b show the turbulence profiles at x/H = 3, the inlet profiles for this backward facing step. The turbulence levels increase as a function of secondary flow rate and this change in the inlet conditions to this flow field causes the change in the downstream recirculation zone.

4.2.3 Instantaneous Velocity Fields

One of the advantages of PIV is that hundreds of instantaneous two-dimensional velocity vector fields are captured and used to obtain mean flow statistics. Analyzing these instantaneous velocity vector fields provides valuable insight into the flow behavior. Figure 41 &Figure 42 are representative samples of the instantaneous velocity vector fields for the 9% and 32% cases, respectively. The first PIV domain is shown in these images, as a fundamental understanding of the mixing characteristics of this region is of interest.

For a low secondary flow case (9%) shown in Figure 41, it can be seen that the secondary jet appears to get turned around into the primary stream for all instances in time. The jet's position does slightly fluctuate but remains within a small general range. Downstream of the turned secondary jet there are instances where a recirculation bubble appears to form above the secondary jet hardware and other instances where the bubble doesn't exist in the instantaneous snapshots. In general flow structures appear to be somewhat small (i.e. on the scale of the secondary jet) and they do not penetrate very far into the primary flow.

Figure 42 by comparison shows instantaneous velocity fields for a large secondary flow rate (32%). The flow structures appear to be much larger than those observed in Figure 41, and the structures work their way substantially into the primary stream, both in the vertical direction and also further upstream than the previous case, the range of scales present in this case is also much larger. The recirculation zone for the 23% secondary flow case can be seen in some instantaneous images and not in others. Since recirculation, or local reverse flow, is not observed in the instantaneous

images, the time-averaged recirculation is not indicative of local flow conditions. This phenomenon raises concern whether this recirculation bubble can be used as a reliable flame anchor, if the recirculation zone does not exist at an instance in time then there is a strong possibility of flame blow out at that instance.

Schlieren images qualitatively captured the instantaneous density fields, over a similar domain to the previous instantaneous velocity vector fields. Figure 43, Figure 44, & Figure 45 are representative instantaneous Schlieren images that correspond to the baseline, 9% and 14% secondary flow rate cases. The images of the baseline flow, Figure 43, show the development of the fundamental structures of the two-dimensional portion of a shear layer. The secondary jet hardware can be seen to be located such that the development of these structures is not inhibited (in fact it may be enhanced).

At the smallest level of secondary flow studied the two-dimensional structures seen in the baseline images have been broken down. The 9% secondary flow case, Figure 44, shows the remnants of the primary shear layer and shows a slight flopping of the secondary jet. The stagnation of the secondary jet is apparent in the 14% secondary flow case Figure 45, the vertical flopping of the secondary jet becomes more apparent in this higher flow rate case as well.

Consequently it is believed that the large scale flopping motion of the secondary jet as shown in the PIV and Schlieren images is responsible for the large apparent turbulence levels found within this flow field. While the large turbulence values would be beneficial in the mixing characteristics of this flow field, the large scale flopping and the primary recirculation zone that appears to not consistently exist would be quite detrimental for combustion applications.

While the unsteady nature of this flow seen in the instantaneous imagining techniques was deemed to be a not acceptable for use as a control mechanism in reacting flow, further investigation into the flow within this geometry was still explored. The underlying stability characteristics of this flow field was of interest and frequency analysis can be used to investigate the dynamics of this flow.

4.2.4 Spectra and Effects of Forcing

Streamwise velocity time traces were captured via hot wire anemometry (HWA) at a probe location of x/H = 1.5 and y/H = 0.5 and spectral data was extracted via a Fast Fourier Transforms (FFT) to determine the effect of secondary flow on the velocity spectra. This location was selected as it is outside of the primary recirculation bubble for all secondary flow rates, as HWA cannot distinguish between positive and negative velocities and this location has minimal, if any, negative flow. The data presented are from the un-calibrated hotwire voltage signals; calibration was not necessary as this data was used for FFT analysis. Qualitative trends can be observed as a function of frequency and relative amplitudes can be compared but the overall magnitude is that of the hotwire voltage not fluid velocity.

Figure 46 shows the spectral distributions for all secondary flow rates; the scales of interest were found to be relatively low frequencies. Figure 47a-i show the spectral development of the flow field for all secondary flow rates for the frequencies of interest, nominally less than 250 Hz. Figure 47 a & b, corresponding to the baseline and 5% secondary flow case show two peaks, at 166Hz and 225Hz (only approximate within 1

Hz or less), that correspond to the blower's natural frequencies. These peaks are inherent within the facility. The 9% secondary flow case, Figure 47 c, shows amplification over a band of frequencies from approx 100-240Hz. A transition in frequency content can be seen for all cases with a secondary flow greater than ~ 14%, Figure 47 d-i. Lower frequencies become amplified starting with the 14% secondary flow case as shown in Figure 47d. The dominate frequency shifts from the facility noise (167 Hz) to a much lower frequency, centered around ~ 68 Hz. Figure 47 e-i, show the evolution of the field with increasing secondary flow the low frequencies are shown to increase and the dominate frequency increases with increasing secondary flow, quantified in Table 5.

As the dominate frequency is thought to be a result of the recirculation bubble and the unstable flow field created, a scaling of the frequency is proposed based on the physics of the bubble. A Strouhal number defined as:

$$St = \frac{f \cdot h_{bubble}}{\overline{U}_1 - \overline{U}_2} \qquad \textbf{Equation 4.2}$$

is used to non-dimensionalize the frequency. Where $\overline{U}_1$ & $\overline{U}_2$ correspond to the maximum and minimum mean streamwise velocities of the cross-stream velocity profile taken though the center of the primary recirculation bubble and h_{bubble} is the height of the dividing streamline at the streamwise center of the recirculation bubble. The mean velocity profile through the center of the bubble, shown in Figure 32, is of a similar shape to that of the wall bounded Falkner-Skan profile. The scales chosen to normalize frequency are based on the physics of this profile (i.e. the velocities seen within the profile and the size of the bubble).

Table 5: Locally dominate frequency for all secondary flow rates found in geometry I

$\dot{m}_2/\dot{m}_1$	Dominate frequency [Hz]	St #
0%	222	0
5%	167	0.064
9%	167	0.068
14%	68	0.031
18%	72	0.035
23%	77	0.036
27%	87	0.042
32%	99	0.049
36%	111	0.058

This scaling has not been proven to be universal, as only this facility has been examined. Further analysis and scaling studies are necessary to determine if these are the correct parameters.

Looking into the development of this field and the transition seen at a secondary flow rate of 14% a transition was thought to exist; further analysis including forcing of the primary stream was investigated. Figure 48 shows the response of the flow field for three forcing frequencies (200 Hz, 100Hz and 50Hz) for all secondary flow cases, these frequencies were chosen as they were close to the frequencies of interest within this facility. For all forcing frequencies the response of the flow field produced a dominate frequency that depended on the forcing frequency for secondary flow rates 9% and less. For secondary flow rates of 14% and greater the dominate frequency was unaffected by the inlet forcing.

The second forcing study varying the inlet forcing amplitude at a single frequency, 100 Hz was chosen, and the response of the flow at that same frequency is

quantified and shown in Figure 49 for all secondary flow rates. The solid symbols in Figure 49 correspond to secondary flow rates greater than 14%, the amplitude of the measured frequency for these cases remain constant for the different forcing amplitude. The amplitude of the 100Hz component within the flow field is shown to be dependent on the forcing level for secondary flow rates of less than 14%. The inlet forcing studies show that a transition is seen at the 14% secondary flow case which agrees with the initial conclusion based on the change in spectra in the baseline (un-forced) studies. Both forcing studies provide strong evidence of a global transition within this geometry at 14% secondary mass flow rate.

4.2.5 Bubble profiles

Further investigation into the primary recirculation bubble and the velocity statistics within the bubble were explored. For this analysis the 14% secondary mass flow case was chosen as this is at the threshold where a transition has been potentially observed. Hammond and Redekopp (1998) reported that a Falkner-Skan profile with reverse flow velocity of 30% of the free stream value becomes absolutely unstable. As previously reported this 14% secondary flow rate case was the first to report a velocity ratio at the bubble centerline above 30%, hence the reason for the further analysis of this flow field.

Mean streamwise velocity profiles are displayed for multiple x/H locations within the primary recirculation zone. Figure 50 overlays these profiles upon the mean streamlines that highlight the recirculation bubble. While the reflection of the laser

light sheet near the secondary jet hardware prevented velocity vectors near the surface, overall the profiles closely replicate the profiles used by Hammond and Redekopp (1998), namely are of the Falkner-Scan type.

Velocity statistics within the bubble domain are shown in Figure 51. The family of velocity profiles developed at different streamwise locations within the bubble are analyzed for velocity ratio, $\overline{U}_2/\overline{U}_1$ maximum rms streamwise velocity fluctuation and maximum total turbulence. The velocity ratio begins positive and with increase streamwise location (x/H) the ratio becomes negative, locating the beginning of the recirculation bubble and becomes a maximum magnitude near the center of the recirculation zone. The magnitude of the reverse flow is greater than the critical velocity ratio proposed by Hammond and Redekopp (1998) for transition from convective to absolute unstable flow of -30%. This velocity ratio exists over a finite spanwise length of about x/H ~ 0.25 before the velocity ratio magnitude decreases and ultimately the ratio approaches zero with increasing x/H location.

In general it is thought that the first absolutely unstable profile is the location where turbulence measures begin to increase drastically, as at this location the disturbances in the flow are amplified. Upstream of that profile the flow is nominally less disturbed as amplifications of disturbances are convected downstream, this is not the case in this flow field as shown in Figure 51. The streamwise location of the largest peak turbulence levels is shown to be well upstream of the profile that meets the criteria for absolute instability. It is conjectured that this upstream turbulence is a result of the flopping of the secondary jet creating an oscillatory flow field. This forcing of the secondary jet may result of the global unstable mode developed within the recirculation

bubble but the large turbulence levels seen both in the rms streamwise fluctuating velocity and in the total turbulence profiles displayed in Figure 51.

4.2.6 Geometry I Conclusions

The primary effect of the secondary flow rate on the overall development of the flow field was shown to be large increases in turbulence though out the flow field. Broadband turbulence was created and permeated though out the entire flow field. The large turbulence levels reported were in fact not "turbulence" but a band (non-broadband) of flow disturbances believed to be due to the flopping motion of the secondary jet. While the unsteady flopping of the secondary jet is not a problem by itself, the absence of local instantaneous reverse flow was not conducive for the creation of a stable flame anchor.

Many different unstable profiles were created within this facility and the all profiles behaved in a manner of amplifying disturbances. The primary recirculation zone appears to dominate the spectral content but the complex nature of the entire field leads to a broad spectral profiles within the field. Transitions were seen at 14% secondary flow and this is where the primary recirculation bubble was found to have reverse flows that exceed the 30% of the primary, the requirement proposed by Hammond and Redekopp (1998).

4.3 Geometry II results: Coanda Facility

The second facility in the study creates a countercurrent shear layer using a momentum-driven source within a facility known as Geometry II. Motivated from the results of Geometry I, modifications were made to the previous facility hoping to create a momentum-driven control mechanism to be used in a reacting flow. The modifications included; adding a lower surface to the exit of the secondary jet to suppress the unsteadiness and moving the secondary jet hardware away to accommodate the shear layer spatial growth in the cross-stream direction. The idea behind moving the secondary jet hardware out the direct development of the shear layer this facility should allow for the fundamental development of the momentum-driven counter-current shear layer.

A curved surface was attached to the secondary jet to both direct the flow up to the trailing edge and to utilize the Coanda effect to keep the secondary jet attached to the surface due to the pressure gradient created. The benefits of the curved surface were twofold; creating the pressure gradient that acts to keep the secondary jet "attached" to the curved surface and to allow for the spatial growth of the shear layer.

4.3.1 Secondary Coanda Jet

Initial studies of the secondary jet that is attached to the curved surface were performed to confirm the Coanda effect in absence of the primary flow and hardware, and to document the secondary wall-bounded flow in this facility. The secondary jet

hardware from the previous facility was used and secondary flow rates from the closed facility were the used for all Geometry II (Coanda facility) experiments.

Determining the effect of the curved surface near the exit of an exhausting jet has been well researched (Wilson, 1975). For the current study, an extensive analysis of the Coanda effect on the secondary jet was deemed unnecessary; it is only the effect on the mean velocity that is vital in creating the desired countercurrent shear layer. Figure 52 a-i show development of the secondary jet and the Coanda effect on mean and turbulence velocity fields. The four radial profiles show that the jet is attached to the surface for all flow cases. Turbulence contours are normalized by the primary velocity, $\overline{U}_0$, not the centerline jet velocity; this is the reason for the elevated turbulence levels in the plots. As anticipated the curved surface acts to direct the secondary jet along the curved surface such that the flow is basically horizontal when it interacts with the primary stream. This was deemed ideal to create countercurrent shear and allow for the shear layer lateral growth.

4.3.2 Mean Flow fields

The results provided from the development of the secondary jet along the curved surface were used to down select three gap sizes g = 8, 6, and 4 mm, used in the Geometry II facility shown in Figure 20. PIV studies for all secondary flow rates were conducted for each of these facilities to determine the effect of the gap height.

The largest gap height g = 8mm placed the secondary stream farthest away from the primary flow. Cross-stream profiles of the mean streamwise velocity taken at the

trailing edge (x/H = 0) are shown in Figure 53a for all secondary flow rates. All the velocity profiles show a near-zero velocity zone between y/H = 0 and y/H = -0.1, ie. a "dead zone." This zero velocity zone is a region of stagnant flow or a "dead zone" where the two fluid streams are not interacting. There is a shear layer created by the primary steam and a second shear layer created from the secondary jet. The ability of these two layer to communicate depends on the scald of the dead zone, relative to the respective shear layer thickness.

The 6mm gap height essentially moves the secondary jet and its development vertically upwards in the cross-stream direction. With this facility (g = 6mm) the shear layer created by the primary stream just contacts the shear layer created by the secondary jet, creating a continuous velocity gradient.. The cross-stream mean streamwise velocity profiles at the trailing edge shown in Figure 53b do not display the dead zone that was apparent in the 8mm gap facility. The velocity gradient between the primary stream and the secondary is smooth and a counter-current profile has been created.

The smallest gap height, g = 4mm, again moves the secondary jet further vertically into the primary stream. Figure 53c shows the resulting cross-stream mean streamwise velocity profiles for all secondary flow rates. With the smallest gap the momentum of the secondary jet is forced further into the primary stream creating a global stagnation point, similar to that seen my Humphrey and Li (1981), has been setup in this flow field and therefore has turned both streams 180°. The small reverse flow that is seen in Figure 53c is actually flow from the primary stream that is turn around

and forced out of the slot below the trailing edge due to the high pressure created at the stagnation point between the primary impingement with the secondary.

From these results it has been seen that the 6mm gap height, g/H = 0.3 is the facility that best creates a momentum-driven countercurrent shear layer, with a smooth shear layer profile. The dead zone between the two single-sided shear layers with the larger gap does not create a countercurrent shear layer and the smaller gap creates a global stagnation point and reverses the two flows and again does not create the counter-current shear layer that is of interest in this study. The facility with g/H = 0.3 will be used for all future results and discussion regarding the Coanda facility.

Mean streamlines are shown in Figure 54a-i, starting with the baseline. Figure 54a-i shows the development of the mean flow field through all secondary flow rates up to 36% of the primary flow. The baseline case behaves similar to both a single sided shear layer ($\lambda = 1$) and a backward-facing step flow. As the gap below the trailing edge is open to the environment the primary flow is free to entrain the fluid below the splitter plate, this entrainment can be seen by the single streamline in Figure 54a that originates from the gap. The partial enclosure of the flow field by the secondary jet hardware and the curved surface act to create what appears to be the beginning of a recirculation zoned that would be present in a confined backward-facing step flow. As the shear layer develops spatially it continues to entrain fluid, the location of the secondary hardware forces entrainment from below the layer to originate from farther downstream. This facility is open further downstream therefore a complete and closed recirculation zone does not exist, but if the facility were to be closed a complete recirculation zone would exist.

The effect of the secondary jet on the mean flow field can be seen in Figure 54b-i. Upon the addition of secondary flow the velocity field does not drastically change until a secondary flow of 23% is achieved. For secondary flow rates above 23% a closed recirculation region is observed between the curved lower surface and the primary stream. By increasing the secondary flow above 23% the recirculation zones grow spatially and acts as a flow blockage forcing the primary flow to accelerate over the "bubble".

Mean streamwise velocity iso-contours are shown Figure 55a-i, superimposed on these contours is a single black line that corresponds to $\overline{U} = 0$. The baseline contour shown in Figure 55a shows the basic development of a single sided shear layer and the line corresponding to zero streamwise velocity helps to illustrate that there is entrained flow out of the gap as that is above the separating line.

As seen by the streamlines in Figure 54a-i the secondary flow acts to create a fluidic blockage and forces the primary flow to travel up and over the "blockage". As the secondary flow is increased so is the cross-stream dimension of the blockage; an acceleration of the primary flow over this blockage is shown in the mean contours. The magnitude of the primary flow and the secondary flow change with increasing secondary flow but the general shape of the velocity contours remains unchanged. Looking at the line that corresponds to the zero mean streamwise velocity there is very minimal movement between secondary flow cases.

The creation of a recirculation zone due to the secondary flow allows for increasing velocity ratios over a substantial streamwise extent of the facility. The stability of the velocity profile plays a critical role in the development of the flow field,

especially near the trailing edge. Figure 56 illustrates the effect of secondary flow on the streamwise development of the velocity ratio within the facility. The ratio upstream of the secondary jet exit (approx $x/H \approx 1.7$) is shown to be above 30% at the lowest control case and approaching 200% in the highest flow case. As expected the ratios increase with increasing secondary flow and with distance downstream of the trailing edge. A sharp decrease is seen downstream of the secondary jet exit, as the reverse velocity in that region is only due to the entrainment by the secondary jet at locations greater than $x/H = 1.7$.

4.3.3 Turbulent Statistics

The mean profiles in Figure 53Figure 54 indicate that a countercurrent shear layer can be successfully created using a momentum source. Evaluating the turbulence quantities will provide insight into the corresponding disturbance field and whether it holds promise for reacting flow control.

Figure 57 -Figure 61 show the development of the turbulent nature of this flow field with increasing secondary flow. The figures show the rms cross-stream, streamwise and total turbulence for multiple secondary flow rates. The trends observed in these cases were consistent with conditions not reported here. The streamwise velocity fluctuations are nominally greater than the cross-stream fluctuations, as shown in Figure 57 -Figure 61. With additional secondary flow it can be seen that the turbulence levels uniformly increase. The cross-stream averaged total turbulence

distributions, Figure 62, show the turbulent evolution of the flow field as a function of streamwise location.

Mean streamwise velocity profiles are overlaid on the total turbulence contours in Figure 63, demonstrating that the peak turbulence within the shear layer is located where the mean velocity gradient exists. The largest magnitude of the velocity gradient, $\partial\bar{U}/\partial x$, appears to be located at where the mean streamwise velocity is positive, not centered around the zero streamwise velocity line, as it should be near $(\bar{U}_1+\bar{U}_2)/2$. For all non-zero secondary flow cases, it is shown that counter-current shear profiles exist for the entire domain captured. Note that only the x-component of the velocity vector is used in this plot; the mean velocity vectors near the secondary curved surface do not cross the solid surface.

The cross-stream width of the large turbulence values shows the extent that this control mechanism affects the flow field, i.e. it's a very thick shear layer. Figure 64a-i show the turbulence profiles at discrete streamwise locations for all secondary flow rates. In a combusting application, the larger the cross-stream extent of high turbulence zone will provide more turbulence within the flame creating more surface area for the flame and ultimately higher heat release rates. The extent of the high turbulent zone can be readily seen in the turbulence profiles, Figure 64a-i, and the increase in secondary flow increases the overall extent of the large turbulence levels. Again, large turbulence values show up in the secondary flow, this is a result of the large secondary flow velocity and the normalization of the turbulent statistics with primary flow velocity values.

The Reynolds stress term, $\overline{u'v'}/\overline{U_0}^2$, normalized by inlet velocity is a measure of the cross-stream transport of mass and momentum due to the mixing created by the disturbed flowfield. Reynolds stress contours are shown in Figure 65, these show an increase in peak levels within the developing shear layer as well as a cross-stream broadening of the large magnitude stress values with increasing secondary flow rates. The increase in transport coupled the large turbulence levels and the velocity gradients show increased mixing within the shear layer due to the secondary flow.

4.3.4 Instantaneous Velocity Vector Fields

The instantaneous velocity fields provided from the PIV measurements offer some validation as to the flow behavior. Figure 66 &Figure 67 show typical instantaneous velocity fields for the 5% and 32% secondary flow cases. Multiple flow characteristics are to be pointed out, first the secondary jet is attached to the curved surface, due to the Coanda effect, for all instances in time for both secondary flow cases. Unlike geometry I, this facility restrains the secondary jet from flopping and creates the countercurrent shear layer in both an instantaneous sense as well as a time averaged flow field. By the secondary jet sticking to the curved surface it allows for the development of the shear layer and resultant recirculation zone, without secondary jet flopping.

The turbulent structures seen in the higher secondary flow case are much larger than the lower case, but both cases create structures over a range of length scales. The larger scales should help increase the overall surface area of the flame in a reacting

environment. Finally it can be seen that the penetration of the turbulent structures into the primary stream is seen in both cases, though to a much more substantial effect for the 32% case. The higher secondary flow case does have large structures that penetrate the primary flow further upstream and closer to the trailing edge. This is a result of the lower convective velocity of the countercurrent shear layer created, the larger secondary flow rate results in a slower the convective velocity and therefore the shear layer grows much more rapidly.

4.3.5 Length scales

The integral length scale is a measure of the fluid scales present in the flow field, previously described in Chapter 3. As previously explained in the experimental methods section it is the cross-stream dimension of the turbulent structures that is quantified. This cross-stream integration allows for a length scale measurement at each streamwise location such that the streamwise development of structure sizes can be analyzed.

The streamwise development of the integral length scale for the baseline, 5% and 36% secondary flow cases are shown in Figure 68. As shown by Forliti (2001) and Behrens (2007) an increase in counterflow creates larger integral length sclaes and elevated growth rates near the trailing edge. This same trend was observed in this Coanda facility when the counterflow was created by a momentum-driven source, opposed to the suction-based secondary flow used by Forliti and Behrens.

The growth of the shear layer was confined in the dump combustor used by Forliti (2001) and Behrens (2007) and the resultant length scales appear to have an abrupt change in growth rate represents where the confinement impedes the growth of the shear layer as apparent at $x/H \approx 0.75$ in Figure 68. As the Coanda facility is open to the ambient environment downstream of the secondary jet hardware, the integral length scale is allowed to continue to grow which accounts for the larger length scale measurements than were reported by Forliti (2001).

4.3.6 Spanwise PIV Measurements

PIV measurements were taken with the facility rotated 90° and the laser sheet positioned at $y/H = 0$, coincident with the trailing edge. This measurement plane allowed for analysis of the spanwise coherence of structures within the flow field and provided insight into the three-dimensional nature of the flow field. Spanwise velocity measurements were taken for all secondary flow rates and the domain captured extended from $-2.75 \leq z/H \leq 2.75$ (68% of facility overall span) and in the streamwise direction from the trailing edge to $x/H = 5$.

Comparing the baseline total turbulence profile in the span, Figure 69a, to the baseline x-y total turbulence, Figure 57c, it can be seen that the maximum turbulence levels begin around one step height downstream of the trailing edge and in both views the peak turbulence is around 30%. With increasing secondary flow the turbulence domain is shown to gradually increase in total turbulence reaching 80%, at 36% secondary flow. Peak turbulence levels were seen at a x/H location of approximately

one and uniform in the span for all secondary flow cases. Low turbulence levels were seen near the trailing edge, the values would increase rapidly to a peak around x/H = 1 and then would gradually decrease with downstream location.

The streamwise and spanwise turbulence components where analyzed individually to determine the effect of the secondary flow on the velocity field. Figure 70-Figure 78 show the evolution of both the rms spanwise and rms streamwise velocity fluctuations for all secondary flow rates. Both the streamwise and spanwise turbulence components are shown to increase with increasing secondary flow rate. The streamwise component does appear to have a peak around one step height downstream of the trailing edge (x/H =1.0), where this peak is not apparent in the spanwise turbulence contours. Both spanwise and streamwise turbulence levels appear to be spanwise uniform, the highest secondary flow rate cases do show some slight side wall effects but overall the contours show the same effects that the total turbulence plots showed. A uniform increase in turbulence is seen in both velocity components measured, the spanwise component has slightly less turbulent energy as expected within a planar shear layer but the overall trends show similar effects.

Spanwise uniformity of the rms turbulent statistics in the flow field allows for averaging over the spanwise extent of the domain captured by the PIV window. This averaging produced a distribution of streamwise, spanwise and total turbulence as a function of streamwise location, shown in Figure 79a-c. The profiles show that the secondary flow rate acts to shift the development of the turbulence upstream toward the trailing edge. The increases in spanwise turbulence show that there is an increase in three-dimensionality brought on by the secondary flow rate.

This increase in three-dimensional flow can readily be seen in instantaneous velocity fields in this spanwise plane. Figure 80 displays representative velocity fields of the baseline case (0% secondary flow), the field is very undisturbed for the first 0.5 – 1.0 step heights and then structures are seen to develop and grow in scale in the streamwise direction. This development can be confirmed with the spanwise turbulence distribution shown in Figure 79c. The baseline case has almost zero spanwise turbulence near the trailing edge (x/H = 0), but note the jump in turbulence at over the x/H = 0.5 to x/H = 1.5, this is exactly where the turbulent structures are seen in the instantaneous velocity fields. At a modest secondary flow rate of 9%, Figure 81 shows instantaneous velocity fields that show much more chaotic behavior than the baseline. Structures are seen at the trailing edge and the overall nature of the flow field consists of structures that are not apparent in the baseline case. Increasing the secondary flow rate even higher, Figure 82 shows instantaneous velocity fields of the 32% secondary flow rate case. The turbulent structures appear to be much larger and have a much more violent nature to the flow, this would be expected with the growth rate of this shear layer as shown in the side view analysis as well as the large turbulence values.

4.3.7 Spectral Content

Uncalibrated HWA streamwise velocity time traces were used to determine the frequency distribution in the flow field. The probe location was fixed to the same location as the closed facility, x/H = 1.5 and y/H = 0.5. The uncalibrated data is to be used for qualitative trends. Figure 83 shows the spectral distribution for all secondary

flow rates, again the frequencies of interest are found to be below 250 Hz. Analyzing each secondary flow case individually provides insight into development of the flow field, Figure 84a-i show this development.

The baseline case, Figure 84a, has three facility peaks (approx 55, 110 and 165 Hz) otherwise it is a very quiet flow. At 5% secondary flow, Figure 84b, the facility peaks appear to be decreased and frequencies below ~100Hz appear to have some low amplitude energy. The 9% secondary flow case, Figure 84c, continues this trend with increasing amplitude below 100Hz. A frequency hump around 45Hz appears to develop at this secondary flow rate (9%) and continues throughout all increasing secondary flow cases, shown in Figure 84b-i. Increasing the secondary flow rate appears to create disturbance growth at the lower frequencies, centered around 45Hz. The growth of these frequencies appears to be a direct result of the additional secondary flow, but opposed to the closed facilities spectral distributions are this flow field is more spectrally broad, dominate peaks are not apparent and a transition is not seen.

4.3.8 Effects of Forcing

Spanwise PIV measurements were used to capture the effects of forcing on spanwise coherence within the combustor and the effect the secondary flow has on these structures. Thermo-acoustic instabilities impose very strong two-dimensional structures on the flow field; preliminary studies were performed using an acoustic two-dimensional forcing to superimpose an inlet flow similar to the inlet flow of a facility experiencing a thermo-acoustic instability under reacting conditions.

A stronger, more two dimensional forcing was necessary for this study relative to the forcing study performed on geometry I. In order to accomplish strong two-dimensional forcing the acoustic speaker was ducted into a two-dimensional slot just downstream of the contraction, explained in the facility section and shown in Figure 23. The spanwise plane of interrogation was set to y/H = 0.05, this was to capture the high-speed side of the shear layer as the flow structures are more readily seen here and uncertainties in the measurements are decreased.

Forcing of the primary flow was accomplished by a function generator and an acoustic speaker, the frequency was set to 275 Hz, which was based on the dominate frequency found in the shear layer. The representative instantaneous images of the baseline case (zero secondary flow) are shown in Figure 85 without acoustic forcing and Figure 86 with the 275Hz forcing. Contours of the instantaneous deviation of the streamwise velocity from the local mean are used to determine the correlation of the flow fields. Spanwise averaged u' values are displayed at the bottom of each image as a function of streamwise location to help illustrate the streamwise coherence of the flow field for each instantaneous velocity vector field. In the baseline case, two-dimensional forcing strengthened the two-dimensionality of structures that were created within the shear layer.

For this forcing study an additional secondary flow case was studied, a 3% secondary flow, to determine the effects of an even lower flow rate. Instantaneous velocity fields of this 3% case are shown in Figure 87 when unforced and Figure 88 under the forced inlet conditions. As can be seen, the streamwise correlation of both the forced and unforced conditions are much less at the 3% case than at the baseline case.

The forced case does show some streamwise structure correlation, but nowhere near as strong as the baseline case. This shows that even at a very low secondary flow rate there is the effect of creating a more three-dimensional flow field. Figure 89 and Figure 90 again show instantaneous flow fields of force and unforced inlet conditions, but this time for the 5% secondary flow case. The spanwise structures are virtually non-existent at this level of counterflow; even for the forced inlet flow the average u' streamwise velocity distributions show no correlation, as do all flow fields with larger secondary flow rates.

To further show the effects of the secondary flow rate on the forced and unforced flow fields, correlation coefficients (defined in equation 3.10) are calculated for the entire domain, these coefficients use an ensemble average of the correlation functions to display an overall correlation plot. Figure 91a, shows a slight spanwise correlation in the unforced cases while Figure 91b shows the highly correlated structures present when the flow is acoustically forced. The bands of positive and negative regions clearly show the spanwise aligned structures that are created in this flow. When the secondary flow is set to the lowest flow rate, 3%, Figure 92 shows that a slight spanwise correlation can be seen in the forced case. The correlation seen in the forced case is less than the forced baseline case which shows the effect of the secondary flow beginning to break down the two-dimensional structures. While the 5% secondary flow completely removes any spanwise structures as evident in Figure 93, as the force and unforced case appear to have comparable correlation coefficient distributions.

It can be seen that by 5% secondary flow the imposed two-dimensional structures that were forced on the primary inlet flow were broken down into a three-

dimensional flow field. The 3% secondary flow case resulted in lower correlated structures, but there was still some resemblance of the initial spanwise structures. The velocity ratio of this 3% secondary flow rate case never exceeds the 30% criteria that has been proposed by Hammond and Redekopp (1998) for a transition from absolute to convective unstable flow profiles, as shown in Table 6.

Table 6: Trailing edge velocity ratio, Geometry II

$\dot{m}_2/\dot{m}_1$	U_2/U_1
0	0.05
3%	-0.09
5%	-0.31
9%	-0.50
14%	-0.62
18%	-0.78
23%	-0.93
27%	-1.11
32%	-1.28
36%	-1.49

Rapid breakdown of coherent spanwise structures to a fully three-dimensional flow can be indicative of a stability transition. As the two-dimensional structures were still somewhat apparent in the 3% secondary flow rates case and the stability criteria of a velocity ratio of greater than 30% was not reached, this could lend credence to the idea that this flow field experiences a global transition where the mean profiles predict and absolutely unstable wall bounded profiles. More discussion to follow in the subsequent chapter.

4.3.9 Geometry II Conclusions

The secondary flow rate within the Coanda facility showed a similar effect as the closed facility; increasing secondary flow resulted in an increase in turbulence within the facility. The difference is that the curved surface that created the Coanda effect fixed the secondary jet location and didn't allow for the flapping that was seen in the closed facility.

Within this flow field a momentum-driven countercurrent shear layer was established without the unsteadiness seen in Geometry I, therefore a more fundamental shear flow was created. A transition was seen to occur once above the 30% reverse flow velocity ratio in the forcing study. This suggests that the stability of this flow field created by the Coanda surface follows the theory of the Falkner-Skan type profiles of a wall bounded recirculation bubble rather than the tanh profiles of a planar countercurrent shear layer.

4.4 Conclusions

The primary goal of this research was to create a momentum-driven countercurrent shear flow and to determine if the criteria for absolute instability could be established, and if so, whether global instabilities – made possible by a finite spatial domain of absolute instability – could be used as a practical control mechanism for reacting flows. Supplying sufficient secondary mass flow rates in both geometries, I and II, created the conditions for absolute instability. When the secondary flow rates were sufficiently elevated, increased disturbance levels were seen in both geometries as

well as increased three-dimensionality of the disturbance field.. The spectral behavior of the streamwise velocity fluctuations differed slightly between the two geometries, but overall both flow fields displayed the growth of an unstable global mode over a band of disturbance frequencies. The frequency range of the most amplified disturbances was considerably lower than the frequencies of disturbances created by the secondary jet, provide strong evidence that the shear layer evolution was dominated by a global mode, and not the advection of turbulent kinetic energy from the secondary jet.

It is expected that the two geometries would vary in their performance as a control mechanism within a reacting flow. Geometry I created high disturbance levels and flow structures were of large scales, but the unsteady nature of the secondary flow would require a separate flame anchor. Similar elevated disturbance levels and flow structures were seen in Geometry II, additionally increases in three-dimensionality were shown and a more steady recirculation zone was present that could act as a flame anchor.

5 Discussion

Two facilities were used to explore the use of momentum-driven countercurrent shear as a fluidic control mechanism within a backward-facing dump combustor geometry. Isothermal studies were conducted to provide insight into the mean and fluctuating velocity fields as well as the possible use of momentum-driven countercurrent shear flow as a control mechanism for a reacting flows. The two facilities successfully created momentum-driven countercurrent shear – in contradistinction to the work of Humphrey & Li who were unsuccessful in creating this flow in 1981 - but the nuances of the flow development in the two facilities are different. In this section, we will explore the underlying stability characteristics of the two flows in an attempt to provide a more complete physical understanding of these unique shear flows.

5.1 Flow stability

In the absence of a general solution to the equations of motion, the fluid mechanics community – and our laboratory in particular – has relied extensively on the teachings of stability theory to advance our fundamental understanding of flow physics. Linear theory is particularly insightful when examined in the context of global instabilities, and while the precise nature of a nonlinear global mode is unknown a priori, the onset can be remarkably well predicted by the presence of a finite domain of absolute instability (Forliti et al., 2005 and Niccum and Strykowski, 1992).

Prototypical examples in the literature where absolutely unstable velocity fields (linear, parallel) have accurately predicted global mode onset include the Karman vortex street behind cylinders, the development of low-density jets, and the axisymmetric jets with external flow, as well as numerous examples of confined flows such as Rayleigh-Benard convection, Taylor-Couette flow, and temporal shear layers. Conditions necessary to establish absolute instability for reacting flows will depend at least on the mean velocity and density fields, the latter of which tends to be stabilizing owing to the presence of denser reactants making up the high-speed stream (Pavithran and Redekopp, 1989). The present work has focused on isothermal conditions, so future work will be required to fully assess the efficacy of countercurrent shear in a reacting environment.

In the step geometry that was studied using suction-based countercurrent shear (Forliti, 2001), a low-pressure region was introduced in the dump plane creating local reverse flow in the separating shear layer. This suction-based counterflow generates a near field velocity profile of Type-A as shown in Figure 94a. The aim of previous research had been to create conditions of local absolute instability in the separating shear layer with the expectation that such instabilities will effectively convolute the flame sheet and increase volumetric heat release rates. The level of reverse velocity needed to achieve absolute instability in a constant density field of Type-A is approximately 13%, but this may be increased to as much as 50% depending on the density ratio anticipated during reaction (Pavithran and Redekopp, 1989 and Niccum and Strykowski 1992).

Downstream of a step or obstruction typical in flame anchors, we expect a region of recirculating flow, having profiles qualitatively of Type-B as shown in Figure 94a. Spatio-temporal stability theory of a generic separated region – modeled using a family of Falkner scan profiles having the general shape of Type B (Hammond and Redekopp, 1998)– suggests that the wall-bounded nature of the reverse flow behind a step produces reverse velocities on the order of 20% of the forward primary stream velocity, which is insufficient to achieve local absolute instability. Previous research (Forliti, 2001) demonstrated that suction applied in the dump plane could enhance the strength of the recirculation region of Type-B – and was found to increase overall turbulence levels in the region below that step – however the approach had limited impact in elevating turbulence in the primary (reactant) stream, and was not particularly successful in eliminating thermo-acoustic instabilities (Behrens, 2007). This was due in part to the fact that the suction produced a flow field more akin to Type A than Type B.

The present research has examined the role that counter shear may play in active control of flame holding through detailed flow fields made possible using a momentum-driven secondary stream. The challenge at the outset is to understand the stability characteristics of Type-A and Type-B profiles (and other variants) and how these flow conditions can be achieved at higher overall vorticity levels than has been possible with suction. The schematic shown in Figure 94b provides an initial concept sketch used to explore possible configurations for the implementation of a secondary momentum stream. Several features of this configuration were seen as critical for active control using a momentum source. The momentum of the secondary jet must be kept a distance δ below the trailing edge, yet sufficiently close so that the entrainment into the

secondary jet effectively draws reverse flow along the lower wall of the combustor (defined here by the upper surface of the secondary jet). It was also critical that the conditions did not give rise to global stagnation flow as was seen by Humphrey & Li (1981).

The local stability characteristics of the velocity fields found within Geometery I & II created by the secondary momentum source were explored in an attempt to better understand the flow development observed in the laboratory. Geometry I (closed facility) attempted to create a flow field that was enclosed downstream of the control mechanism and thereby more readily implemented in a dump combustor. The flow field that was created was comprised of multiple unstable mean profiles, as shown by the sequence of cross-stream velocity profiles previously shown in Figure 50, for the 14% secondary mass flow rate case in Geometry I. The velocity profiles shown are over a streamwise distance from $0.5 \leq x/H \leq 2.0$, these profiles can be seen (see Figure 50) to be of Type B. The profiles not seen in this figure, both upstream and downstream are of Type A. For a secondary flow rate of 14%, as displayed, the velocity ratios meet the criteria of absolutely unstable profiles over the range of approximately $1.0 \leq x/H \leq 1.25$ and convectively unstable over the rest of the domain. Previous spectral results demonstrated a transition at 14% secondary flow rate and Figure 95 shows a jump in turbulence at this same secondary flow rate.

Geometry II created a countercurrent flow beginning at the trailing edge of Type B. The development of the velocity profiles, shown in Figure 96, transition from profiles of Type B into Type A profiles further downstream. In between the two distinctive types there appears to be a combined profile. Figure 97, show the

combination of Type A and Type B profiles, such as seen at x/H = 1.25 in Figure 96. As the high velocity near the curved surface is not likely to be pertinent to the stability of the shear layer, a new variable $\overline{U}^*_2$ has been defined as the relevant secondary velocity magnitude. When the high velocity secondary flow that creates a Type B velocity profile is not near the shear layer this velocity is not of physical importance to the velocity ratio experienced by the shear layer and therefore should not be used in stability analysis. Once the high velocity, near the curved surface, is removed from the shear layer stability the flow transitions effectively to a Type A profile, and the new relevant secondary velocity is used in stability analysis. Figure 97, shows an example velocity profile where the high velocity, wall bounded flow (from the secondary jet) is located so far removed from the shear layer that this velocity is not relevant to the development of the shear layer. All important velocity magnitudes are displayed in the figure.

Absolutely unstable flow conditions were not met until approximately one step height downstream for the lowest secondary flow rate (3%), as shown in Figure 98 by the shaded region displaying that the relevant curve is above the appropriate critical velocity ratio (Type A in this region). This is consistent with the two-dimensional forcing study that showed remnants of the two-dimensional structures until one step height downstream of the trailing edge. The 5% secondary flow case can be seen to be well above the requirements of absolute instability for all streamwise locations, as shown in Figure 99. The shaded region exists for entire streamwise domain captured, beginning with the Type B profile transitioning to a Type A profile displaying that the relevant curve is above the critical velocity ratio at all locations. The three-

dimensionality of the flow in the forcing study was seen over the entire domain for this secondary flow rate. As the flow field meets the velocity requirements for absolute instabilities over the entire streamwise domain and the flow is seen to be very three-dimensional, a global transition in the stability of the flow field is said to exist at 5% secondary flow and above.

The cross-stream averaged total turbulence is shown in Figure 100, for the baseline, 3% and 5% secondary flow rate. It can be seen that the turbulence level increases with secondary flow rate, upon the 5% case the overall turbulence has increased from the baseline case, while the 3% case shows only a slight increases in turbulence.

The differences in the overall development of the flow fields within these two geometries are summarized in Figure 101 & Figure 102. In Geometry I, the profiles beginning at the trailing edge are of an entraining free shear layer if the secondary jet does not penetrate past the trailing edge or a profile similar to that of a lip wake profile for larger secondary flow rates. Moving downstream the profile develops into a Type B profile due to the secondary jet driving the reverse flow in the region in front of and above the secondary jet hardware, upon large enough secondary flow rates (14%) the criteria for absolute instability is reached within this profile. Downstream of this recirculation zone the flow becomes more of a channel flow before it sees a secondary sudden expansion creates a Type A profile downstream of the backward facing step. Geometry II, in comparison begins with a Type B profile at the trailing edge before transitioning into a type A profile.

5.2 Combustion applications

The analysis of Geometry I was complicated because so many unstable profiles were created within the flow field: the counter-current shear layer created at the trailing edge of the facility and a wall bounded recirculation bubble developed above the secondary jet hardware, which was the focus of the previous discussion section. Add to that the backward facing step downstream of the secondary jet hardware and the flow becomes a collection of many profiles, each having their own stability criteria.

The flow field within Geometry I created by the secondary jet was shown to have very large total turbulence levels, values greater that 100% normalized turbulence values were reported. These large values are a result of flopping mode of the secondary jet as seen by the instantaneous PIV velocity vector fields. This unsteadiness of the two-dimensional secondary jet creates an unsteady primary recirculation zone above the secondary jet hardware. As this recirculation zone was only apparent in some instances in time and non-existent in other, this would not create a flame anchor.

Spectral experiments provided evidence for a global transition in this flow field for secondary flow rates of 14% and greater. This transition corresponds to the primary recirculation bubble reaching the convective to absolute criteria proposed by Hammond and Redekopp (1998). The overall stability of this flow is driven by the primary recirculation zone that then couples with the flopping mode of the secondary jet to create an unstable highly disturbed flow field.

This facility and control mechanism could be used in a combustion application, the flame anchor would reside behind the secondary jet hardware that acts as a bluff body and the secondary jet would be used to create a broadband disturbance upstream

of the reaction zone. The gases exhausting below the trailing edge would have to be capture and then re-ducted into the flow field further downstream.

To eliminate the possibility of the flopping mode of the secondary jet and to move the secondary jet hardware out of the development of the countercurrent-shear layer geometry II was developed. This facility utilized a curved surface to direct the secondary flow and create a momentum-driven countercurrent shear layer that was free to develop spatially.

This facility showed great promise as a fluidic control mechanism for a combustion application, the mean profiles supported the possibility of a flame anchor and the turbulence generated within the field was indicative of a combustor that could create high volumetric heat release rates. The results of the superimposed two-dimensional forcing study illustrated how the control mechanism would also break down coherent two-dimensional structures, similar to those that are created by thermo-acoustic instabilities, into highly three-dimensional flow very quickly and with a minimal (3%) amount of secondary flow. This demonstrated how the countercurrent flow created by the Coanda facility would make a combustor much less susceptible to this detrimental combustion instability.

For even the lowest secondary flow rate (3% used in the two-dimensional forcing study) velocity ratios were found to be greater that the critical ratio need for absolute instability of a countercurrent shear layer but not that of a recirculation bubble. The lower limit of the secondary flow rate in these experiments was due to separation of the secondary jet from the curved surface. Decreasing the secondary flow rate creates a lower limit where the entrainment of the shear layer becomes stronger than the force

due to the pressure gradient created by the Coanda effect. The secondary jet doesn't remain attached at this flow rate and therefore the jet separates and doesn't behave according to a countercurrent shear layer. The primary flow entrains fluid from below the trailing edge and the secondary jet is wrapped around, therefore the velocity profile of interest is not created. Geometry modifications could create a momentum-driven countercurrent shear layer that would remain attached at lower velocity ratios.

As this thesis was part of an ongoing research project, future studies should explore this flow; both continuing the isothermal work and expanding the research into reacting studies implementing the results presented. A fundamental study of the momentum-driven Coanda facility exploring geometric parameters to create velocity ratios approaching the critical counter current shear layer velocity ratio, $\lambda = 1.3$ should be explored. As the Coanda facility showed promise in a reacting atmosphere, a study of the effects of confinement and the subsequent behavior of this reacting flow would provide insight as to the differences between momentum-driven and suction derived countercurrent shear as a control mechanism within a dump combustor.

The present study has shown that momentum-driven countercurrent shear can be created in a confined geometry, and its effects on an isothermal flow field show promise as a fluidic control mechanism within a dump combustor. The increases in turbulence, large scale mixing and three-dimensionality, along with a flame anchor location seen in the isothermal fields suggest that this control mechanism will be advantageous regarding the overall goal of creating a compact, low-drag combustor while minimizing combustion instabilities.

6 References

Abramocich G.N., The Theory of Turbulent Jets, The MIT Press, Cambridge, MN, 1963.

Anderson M.J. and Strykowski P.J., "Exploiting global instabilities for efficient flame anchoring and compact combustion," Proc. 21st ONR Propulsion Conf, Monetery CA, 2009.

Alvi F.S., Krothapalli A., and Washington, D., "Experimental study of a compressible countercurrent turbulent shear layer," *AIAA Journal*, Vol. 34, n. 4, 1996, pp.728-735.

Behrens A.A., "Reacting flow studies in a dump combustor: Enhanced volumetric heat release rates and flame anchorability," PhD Thesis, University of Minnesota, Minneapolis, MN, 2007.

Behrens A.A., Anderson M.J., Forliti D.J. and Strykowski P.J, "The role of enhanced recirculation in controlling turbulent combustion and flame anchoring in a step combustor," Proc. 17th ONR Propulsion Conf., Boston, MA, 2004, pp48-53.

Behrens A.A., Anderson M.J., and Strykowski P.J., "PIV measurements in a premised JP10/air dump combustor: Role of counterflow on turbulence and heat release," Proc. 18th ONR Propulsion Conf., Moneterey CA, 2005, pp. 143-148.

Behrens A.A., Lutz, J.M. and Strykowski P.J., "Instantaneous flame anchor measurements behind a rearward-facing step," *AIAA Journal*, Vol. 47, n. 6, 2009, pp. 1350-1357.

Behrens A.A. and Strykowski P.J., "Controlling volumetric heat release retes in a dump combustor using countercurrent shear," *AIAA Journal*, Vol. 45, n. 6, 2007, pp. 1317-1323.

Birch S.F. and Eggers J.M., "A critical review of the experimental data for developed free turbulent shear layers," Free Turbulent Shear Flows Conference Hampton VA, July 1972 (NASA SP-321, V.1, 1973), pp. 11-40.

Bradshaw, P., "The effect of initial conditions on the development of a free shear layer," *Journal of Fluid Mechanics*, V. 26, n.2, 1966, pp. 225-236.

Bernal L.P. and Rosko A., "Streamwise vortex structure in plane mixing layers," *Journal of Fluid Mechanics*, Vol. 170, 1986, pp. 499-525.

Brown G.L. and Roshko, A., "On density effects and larger structure in turbulent missing layers," *Journal of Fluid Mechanics*, V64, n. 4, 1974, pp. 775-816.

Browand F.K. and Latigo B.O., "Growth of the two-dimensional mixing layer from a turbulent and nonturbulent boundary layer," *Physics of Fluids*, Vol. 22, n. 6, 1979, pp. 1011-1019

Dziomba B. and Fiedler H.E., "Effect of initial conditions on two-dimensional free shear layers," *Journal of Fluid Mechanics*, Vol. 152, 1985, pp. 410-442.

Forliti D.J.," Controlling dump combustor flows using countercurrent shear," PhD Thesis, University of Minnesota, Minneapolis MN, 2001.

Forliti D.J. and Strykowski, P.J., "Controlling turbulence in a rearward-facing step combustor using countercurrent shear," *Journal of Fluids Engineering*, Vol. 127, n. 3, 2005, pp. 438-448.

Forliti D.J., Tang B.A., and Strykowski, P.J., "An experimental investigation of planar countercurrent turbulent shear layers," *Journal of Fluid Mechanics*, Vol. 530, 2005, pp. 241-264.

Gabruk R.S. and Roe L.A., "Velocity characteristics of reacting and nonreacting flows in a dump combustor," *Journal of Propulsion and Power*, Vol. 10, n. 2, 1994, pp.148-154.

Gillgrist R.D., Forliti D.J. and Strykowski P.J., "On the mechanisms affecting fluidic vectoring using suction," *Journal of Fluids Engineering*, Vol. 129, 2007, pp. 91-99.

Goldstein R.J., "Fluid Mechanics Measurements," 2nd Edition, Taylor and Francis, Washington DC, 1996.

Hammond D.A. and Redekopp L.G. "Local and global instability properties of separation bubbles," European Journal of Mechanics, B/Fluids, Vol. 17, n. 2, 1998, pp. 145-164.

Ho C.M. and Huang L.S., "Subharmonics and vortex merging in mixing layers," *Journal of Fluid Mechanics*, Vol. 119, 1982, pp. 443-473.

Ho C.M. and Huerre P., "Preturbed free shear layers," Annual Review of Fluid Mechanics, Vol. 16, 1984, 356-424.

Huerre P. and Monkewitz P.A., "Absolute and convective instabilities in free shear layers," *Journal of Fluid Mechanics*, Vol. 159, 1985, pp. 151-168.

Humphrey J.A.C. and Li S., "Tilting, stretching, pairing and collapse of vortex structures in confined counter-current flow," *Journal of Fluids Engineering*, Vol. 103, 1981, pp. 466-470.

Husain Z.D. and Hussain A.K.M.F., "Axisymmetric mixing layer: influence of the initial and boundary conditions," *AIAA Journal,* V. 17, 1979, pp. 48-55.

Husain Z.D. and Hussain A.K.M.F., "Natural instability of free shear layers," *AIAA Journal,* V. 21, n. 11, 1983, pp. 1512-1517.

Hussain A.K.M.F. and Zedan M.F., "Effects of the initial condition on the axisymmetric free shear layer: effects of the initial momentum thickness," *Physics of Fluids,* V21, n.7, 1978, pp. 1100-1112.

Hussain A.K.M.F. and Zedan M.F., "Effects of the initial condition on the axisymmetric free shear layer: effects of the initial fluctuation level," *Physics of Fluids*, V21, n.9, 1978, pp. 1475-1481.

Kundu K.M., Banerjee D. and Bhaduri D., "On Flame Stabilization by Bluff-Bodies." *Journal of Engineering for Power, Transactions ASME*, V102, n.1, 1980, pp. 209-214.

Khemakhem A.S.D., "An experimental study of turbulent countercurrent shear layers," PhD Thesis, University of Minnesota, Minneapolis MN, 1997.

Lasheras J.C., Cho J.S. and Maxworthy T., "On the oration and evolution of streamwise vertical structures in a plane, free shear layer," *Journal of Fluid Mechanics*, Vol. 172, 1986, pp. 231-258.

Lasheras J.C., and Choi H., "Three-dimensional instability of a plane free shear layer: and experimental study of the formation and evolution of streamwise vortices," *Journal of Fluid Mechanics,* Vol. 189, 1988, pp. 53-86.

Le, H., Moin, P., and Kim, J., "Direct numerical simulation of turbulent flow over a backward-facing step," *Journal of Fluid Mechanics*, Vol. 330, 1997, pp 349-374.

Lee, I., and Sung, H.J., "Characteristics of wall pressure fluctuations in separated and reattaching flows over a backward-facing step: Part I Time-mean statistics and cross-spectral analyses," *Experiments in Fluids*, Vol. 30, 2001, pp. 262-272.

Liepmann H.W. and Laufer J., "Investigations of free turbulent mixing," NACA TN-1257, 1947, pp. 1-68.

McManus, K.R., "Effects of Controlling Vortex Formation on the Performance of a Dump Combustor," Standford University Press, Palo Alto, CA, Topical Report, T-262, June 1990.

McManus, K.R., Vandsburger, U., and Bowman, C.T., "Combustor performance enhancements through direct shear layer excitation," *Combustion and Flame*, Vol. 82, 1990, pp. 75-92.

Mehta R.D., "Effect of velocity ratio on plane mixing layer development: incluence of the splitter plate wake," *Experiments in Fluids*, Vol. 10, 1991, pp. 194-204.

Miles J.B. and Shih J.S., "Similarity parameter for two-stream turbulent jet-mixing region," *AIAA Journal*, V.6, n. 7, 1968, pp. 1429-1431.

Monkewitz P.A. and Huerre P., "Influence of the velocity ration on the spatial instability of mixing layers," *Physics of Fluids*, V. 25, n 7, 1982, pp. 1137-1143.

Neto, A.S., Grand, D., Metais, O., and Lesieur, M., "A numerical investigation of the coherent vortices in turbulence behind a backwad-facing step," *Journal of Fluid Mechanics*, Vol 256, 1993, pp. 1-25.

Niccum D.L., "The influence of velocity ratio on a counterflowing circular jet," MS Thesis, University of Minnesota, Minneapolis MN, 1990.

Niccum D.L. and Strykowski P.J., "The influence of velocity and density ratio on the dynamics of spatially developing mixing layers," *Physics of Fluids A*, Vol. 4, n. 4, 1992, pp. 770-781.

Paschereit, C.O., and Gutmark, E.J., "Control of High-Frequency Thermoacoustic Pulsations by Distributed Vortex Generators," *AIAA Journal*, Vol. 44, No. 3, 2006, pp. 550-557.

Pavithran S. and Redekopp L.G., " The absolute-convective transition in subsonic mixing layers'" *Physics of Fluids A*, Vol. 1, 1989, pp. 1736-1739.

Pitz R.W. and Daily J.W., "Combustion in a turbulent mixing layer formed at a rearward-facing step,"*AIAA Journal*, Vol. 21 n. 11, 1983, pp. 1565-1570.

Poinsot, T.J., Trouve, A.C., Veynante, D.P., Candel, S.M., Esposito, E., "Vortex Driven Acoustically Coupled Combustion Instability," *Journal of Fluid Mechanics*, Vol. 177, 1987, pp. 265-292.

Schadow, K.C., and Gutmark, E., "Combustion Instability Related to Vortex Shedding in Dump Combustors and Their Passive Control," *Progress in Energy and Combustion Science*, Vol. 18, 1992, pp. 117-132.

Smith, D.A., and E.E. Zukoski, "Combustion Instability Sustained by Unsteady Vortex Combustion," *AIAA/SAE/ASME/ASEE 21st Joint Propulsion Conference*. 1985 Monterey, CA: AIAA, New York, NY.

So, R.M.C. and Ahmed, S.A., "Characteristics of dump combustor flows," *International Journal of Heat and Fluid Flow,* Vol. 10, n. 1, 1989, pp. 66-74.

Squire, H.B., "Jet Flow and Its Effect on Aircraft," *Aircraft Engineering*, Vol. 22, March 1950, pp. 62-67.

Strykowski, P.J. and Niccum D.L., "The influence of velocity and density ratio on the dynamics of spatially developing mixing layers," *Physics of Fluids A*, Vol 4. 1992, pp. 770-781.

Suresh P.R., Srinivasan K., Sundarafajan, T., and Sarit K.D., "Reynolds number dependence of plane jet development in the transitional regime," Physics of Fluids, Vol 20. n. 4 2008.

Tang B.A., "An experimental investigation of planar countercurrent turbulent shear layers," MS Thesis, University of Minnesota, Minneapolis, MN, 2002.

Thorpe S.A., "A method of producing a shear flow in a stratified fluid," *Journal of Fluid Mechanics*, Vol. 32, 1968, pp. 693-704.

Thorpe S.A., "Experiments on the instability of stratified shear flows: miscible fluids," *Journal of Fluid Mechanics*, V. 46, 1971, pp. 299-319.

Van der Veer M.R. and Strykowski P.J., "Counterflow thrust vector control of subsonic jets: countinuous and bistable regimes," Journal *of Propulsion and Power*, Vol. 13, n. 3, 1997, pp. 412-420.

Williams G.C., "Basic studies on flame stabilization." *Journal of the Aeronautical Sciences*, Vol 16 n.12, 1949, pp. 714-722.

Wilson, D.J., "An Experimental Investigation of the Mean Velocity, Temperature and Turbulence Fields in Plane and Curved Two-Dimesnional Wall Jets: Coanda Effect," PhD Thesis, University of Minnesota, Minneapolis MN, 1970.

Winant C.D. and Browand F.K., "Vortex pairing: the mechanism of turbulent mixing-layer growth at moderate Reynolds number," *Journal of Fluid Mechanics*, Vol.63, n. 2, 1974, pp. 237-255.

Young, T., Outlines of Experiments and Inquiries Respecting Sound and Light," Lecture to the Royal Society, Jan. 1800; also Journal of the Royal Aeronautical Society, Vol. 61, 1957 pp.106-150

Zukoski, E.E. and Marble, F.E., "Experiments Concerning the Mechanism of Flame Blow-off from Bluff-Bodies. *Proceedings of the Gas-Dynamics Symposium on Thermochemistry*, 1956.

Appendix A: Figures

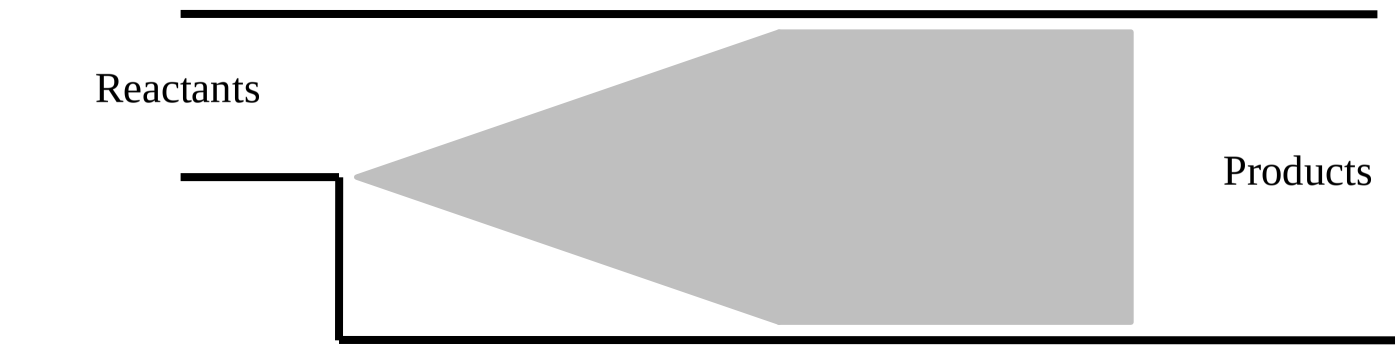

Planar asymmetric rearward facing step

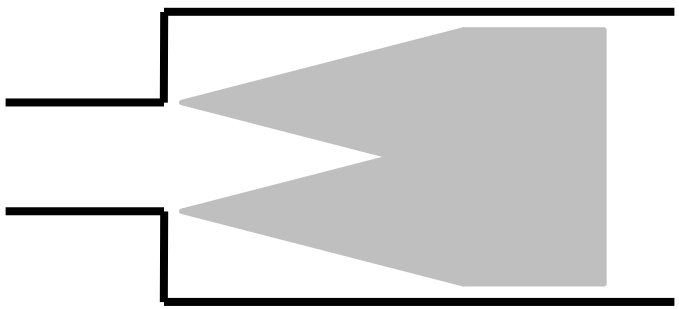

Planar symmetric rearward facing step

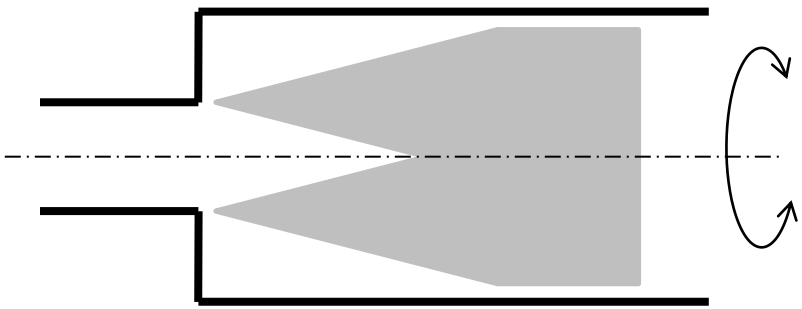

Axisymmetric rearward facing step

Figure 1: Dump Combustor Geometries

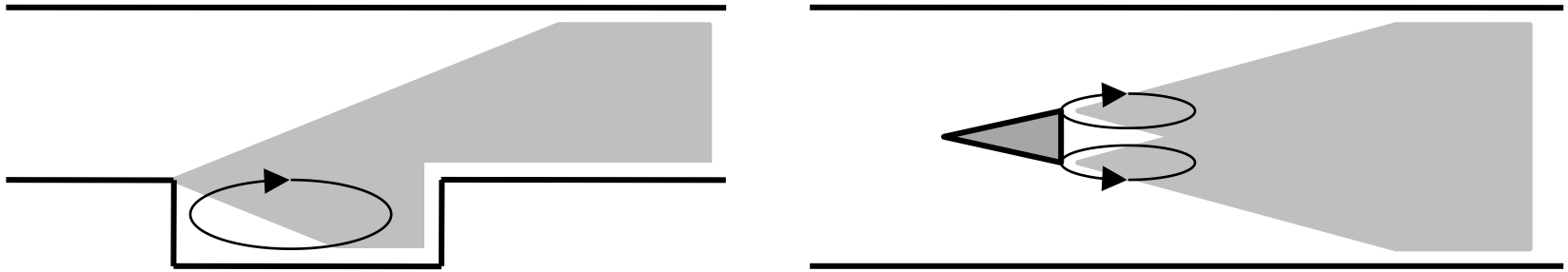

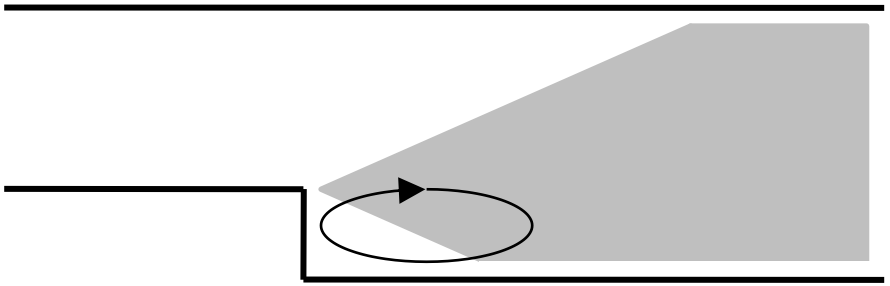

Figure 2: Combustor geometries with flame anchors and flame brush locations

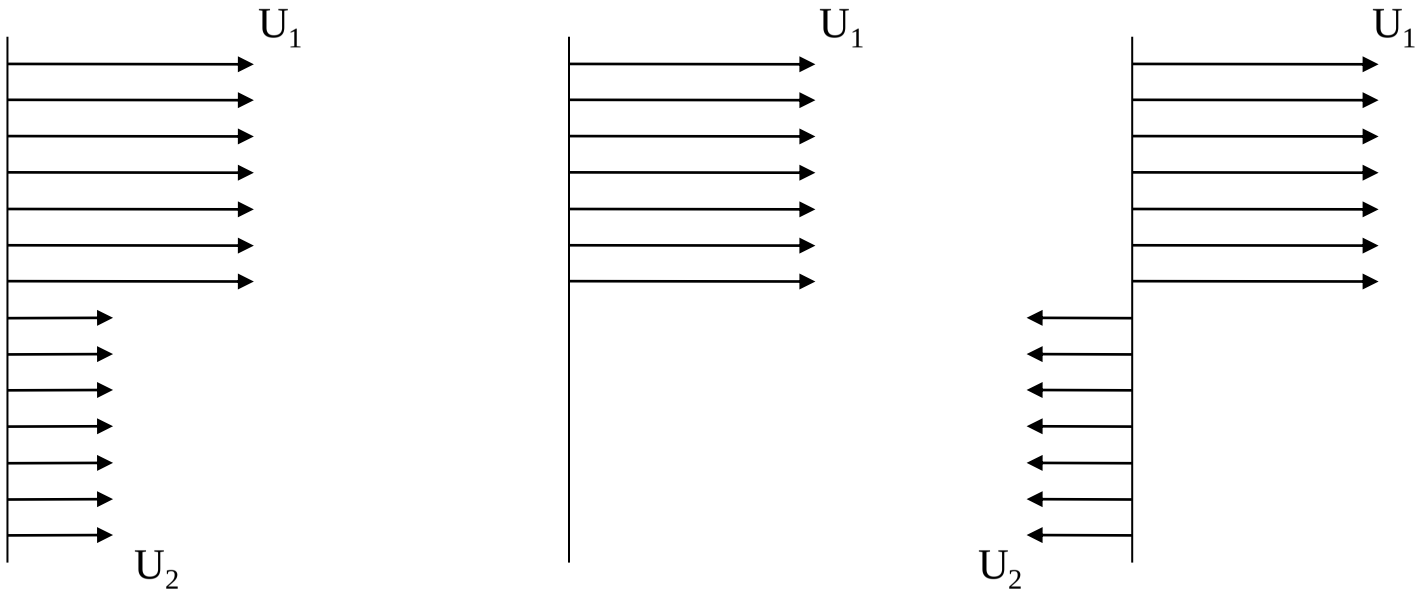

Coflowing Shear Layer
$0<\lambda<1$

Free Shear Layer
$\lambda=1$

Counterflowing Shear Layer
$\lambda>1$

Figure 3: General shear layers

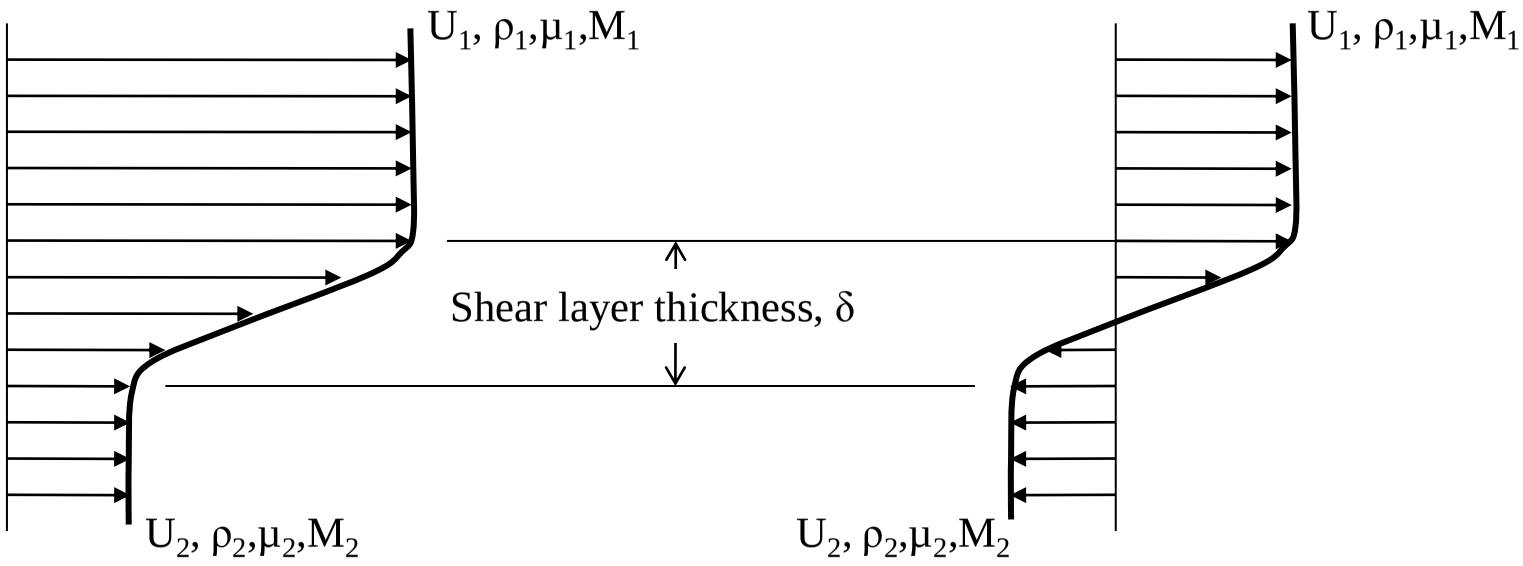

Coflowing Shear Layer
$0<\lambda<1$

Counterflowing Shear Layer
$\lambda>1$

Figure 4: Shear layer velocity profiles

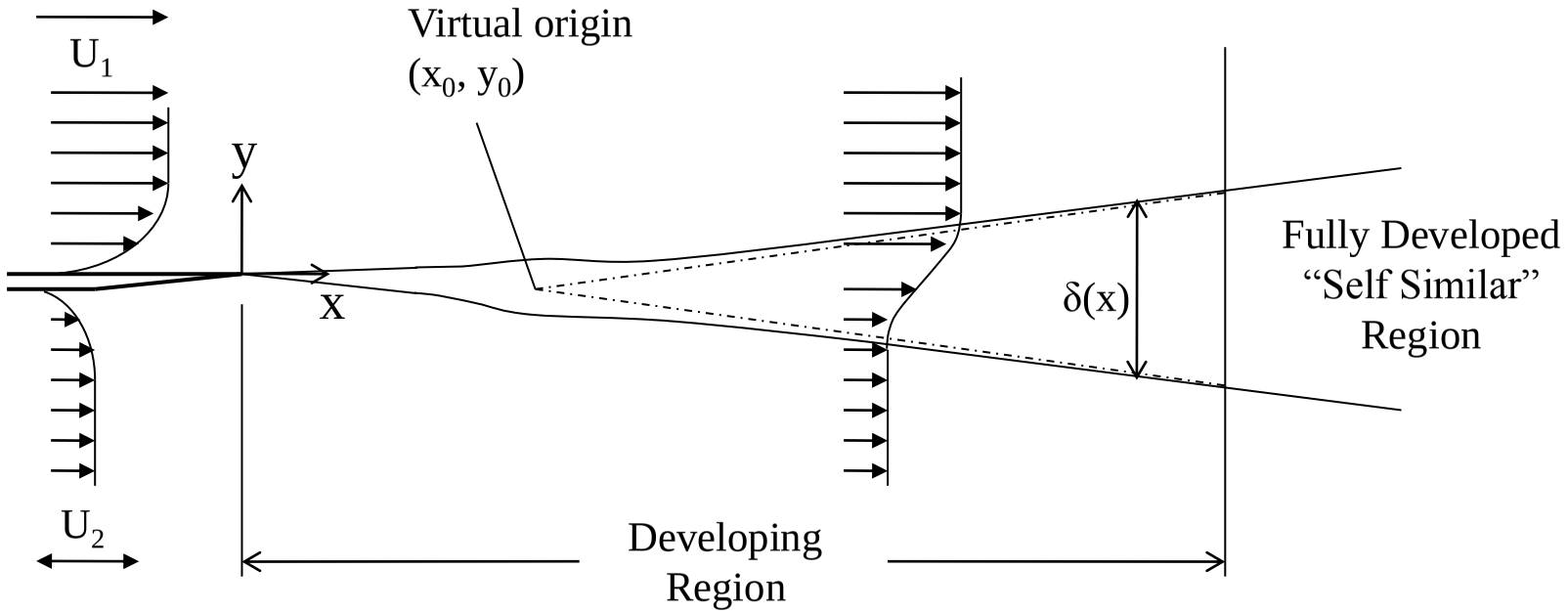

Figure 5: Shear layer development

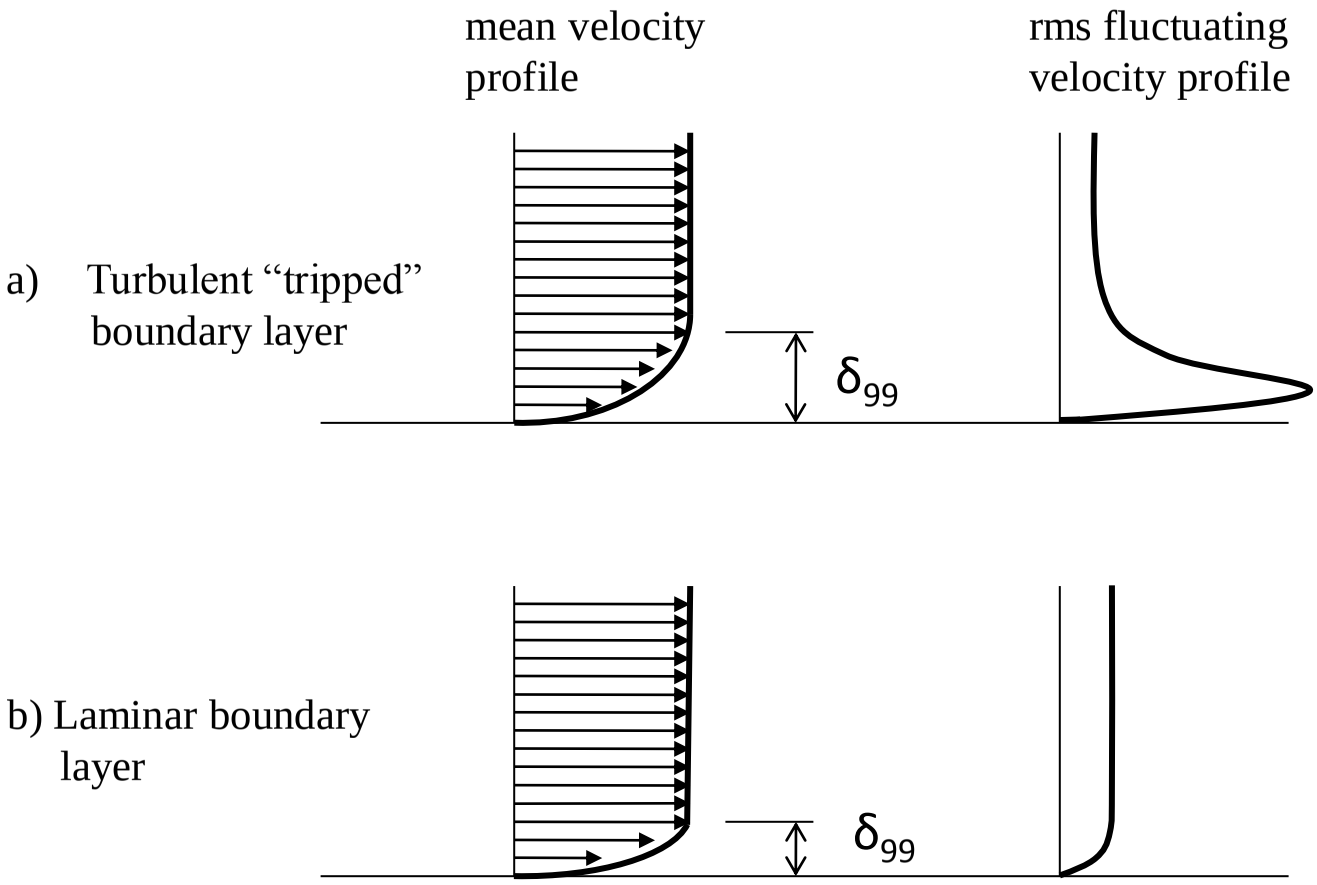

Figure 6: Boundary layer profiles

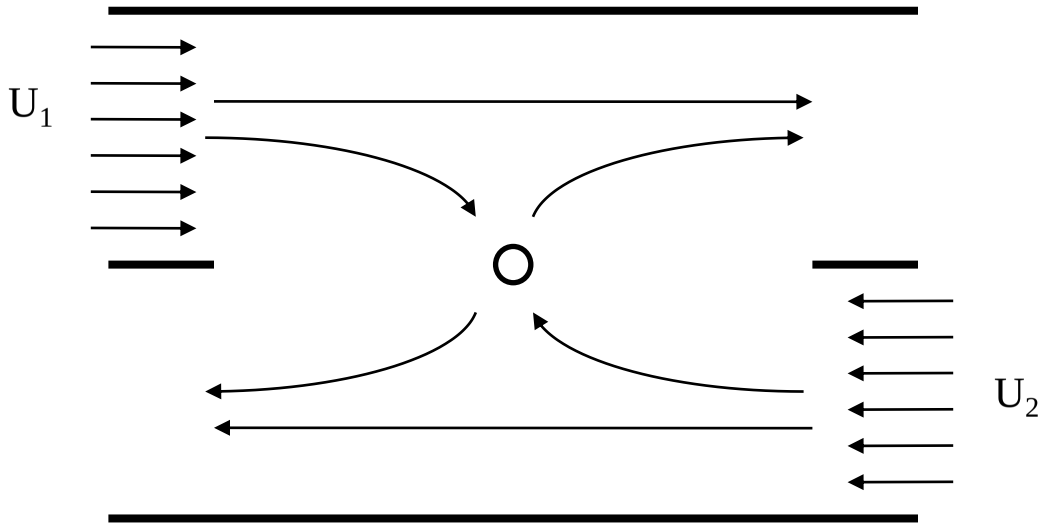

Figure 7: Planar facility with global stagnation (Humphrey and Li, 1981)

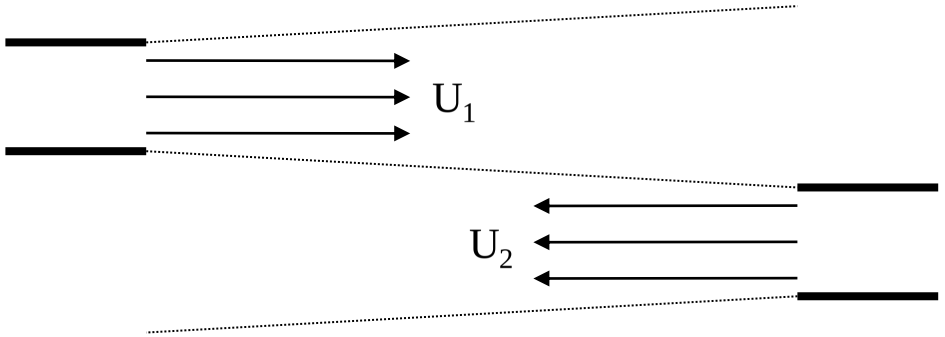

Figure 8: Planar momentum driven jets (Alvi, 1996)

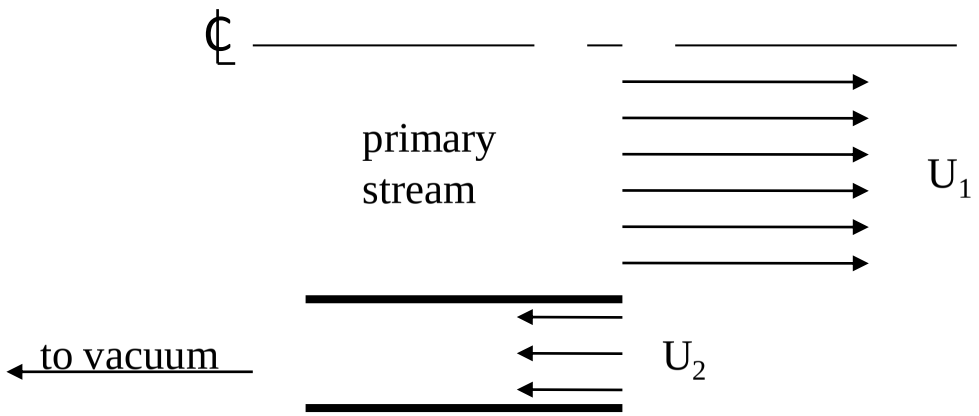

Figure 9: Axisymmetric countercurrent facility (Niccum, 1992)

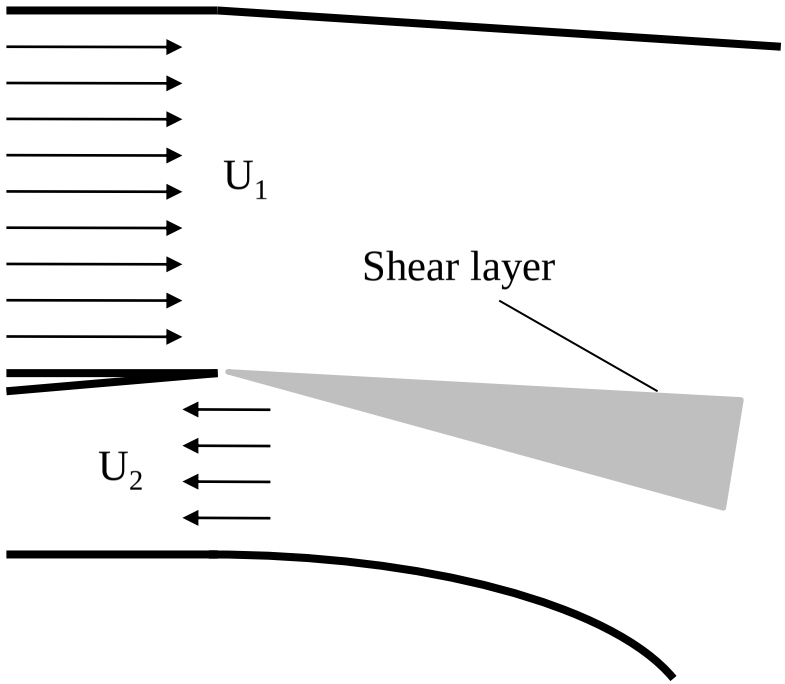

Figure 10: Planar countercurrent facility (Tang, 2002)

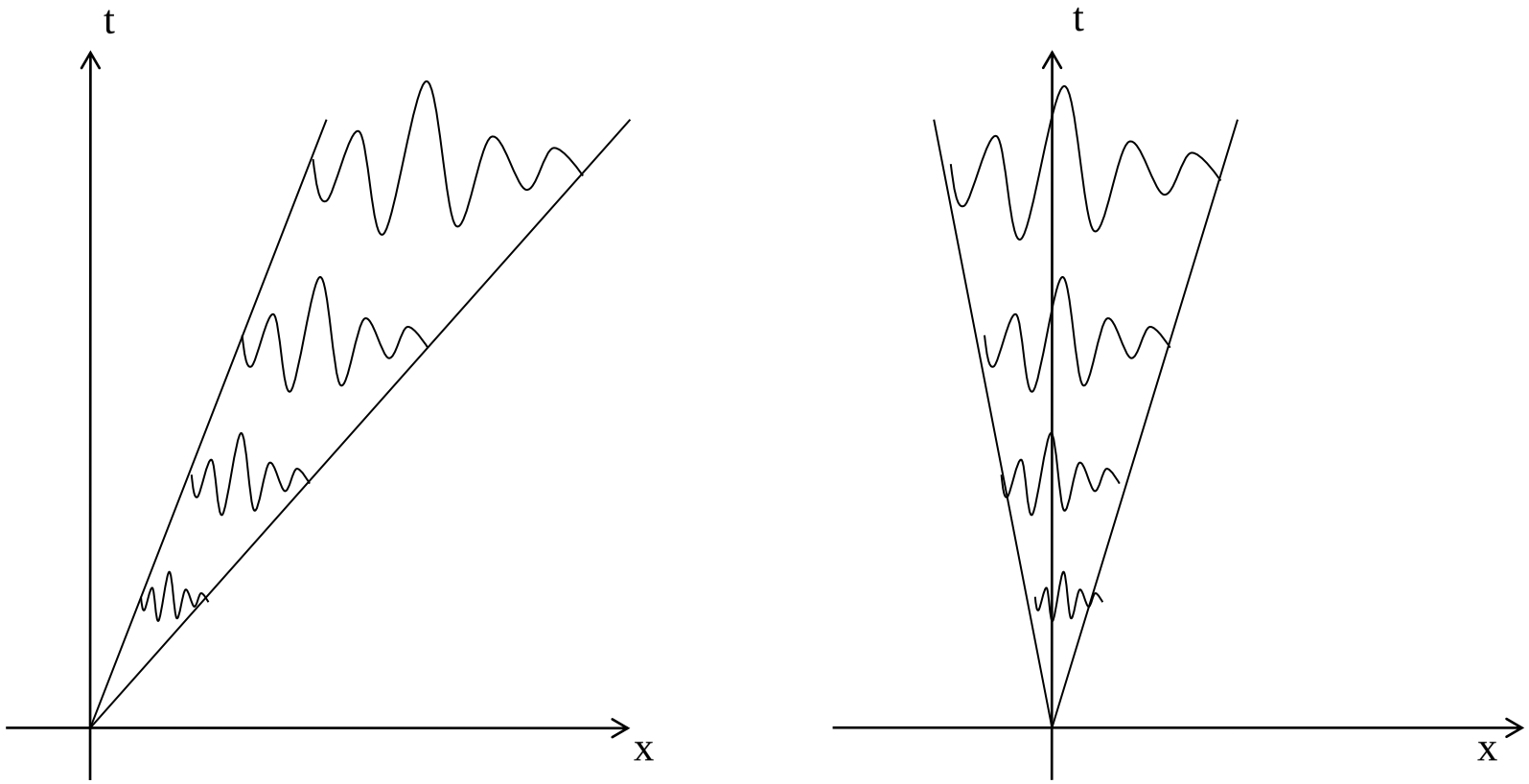

a.) Convectively unstable

b.) Absolutely unstable

Figure 11: Convective and absolute instabilities

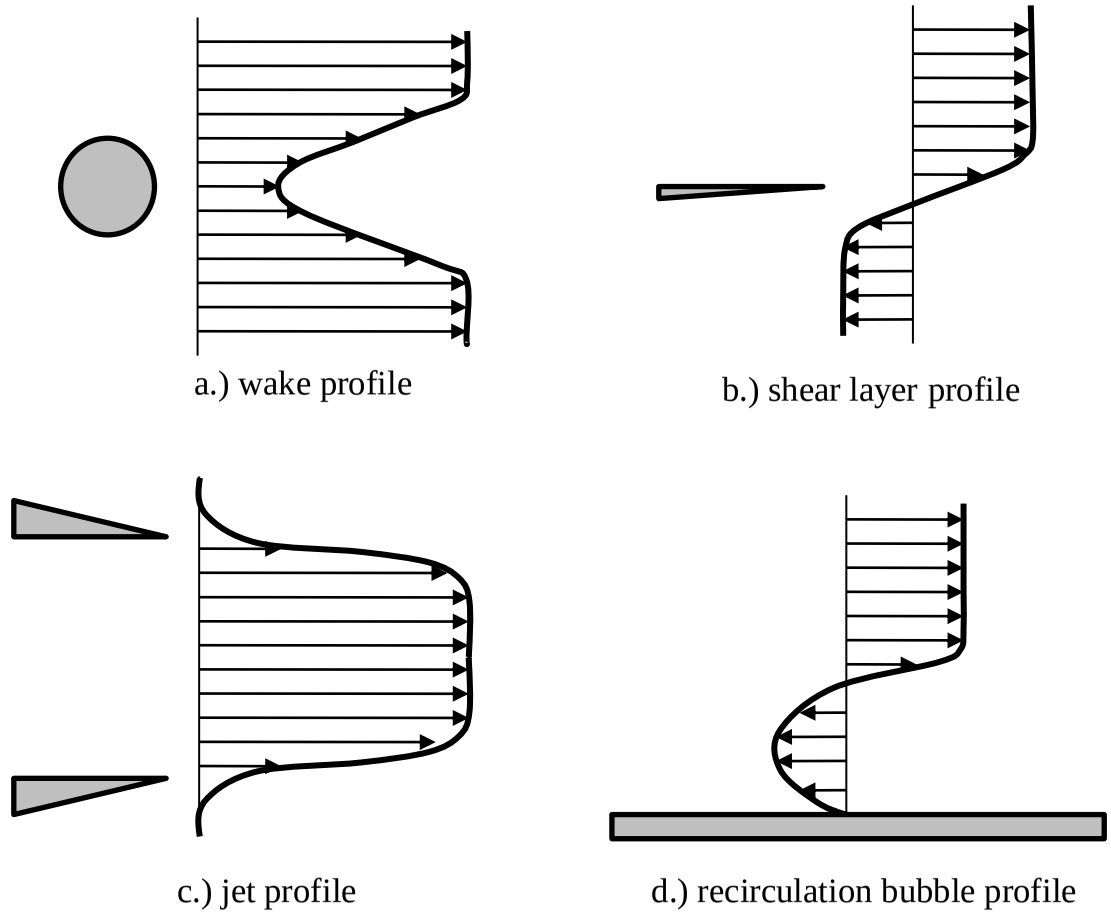

Figure 12: Mean velocity profiles used in stability analysis

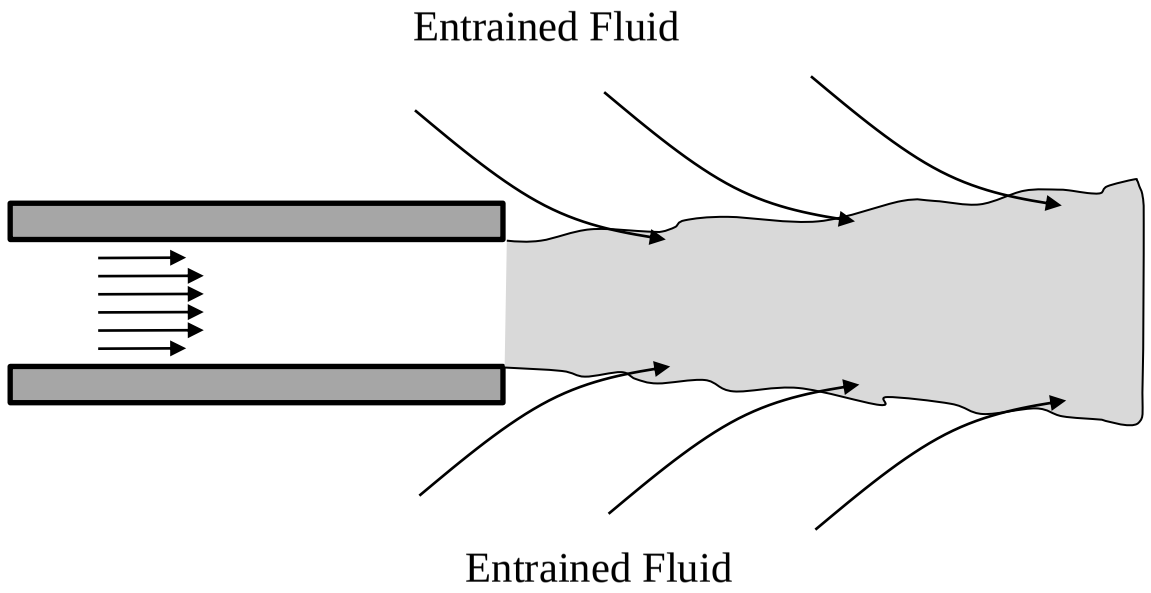

Figure 13: Free jet showing entrainment

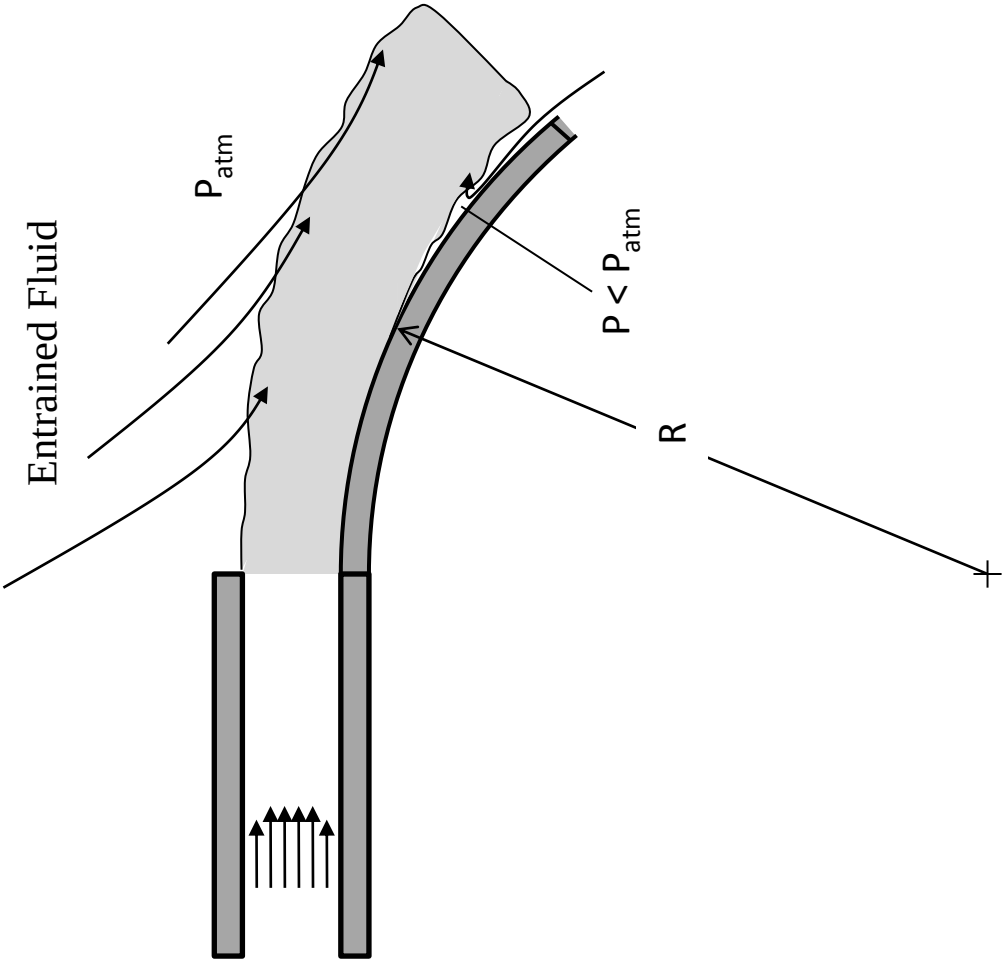

Figure 14: Coanda effect

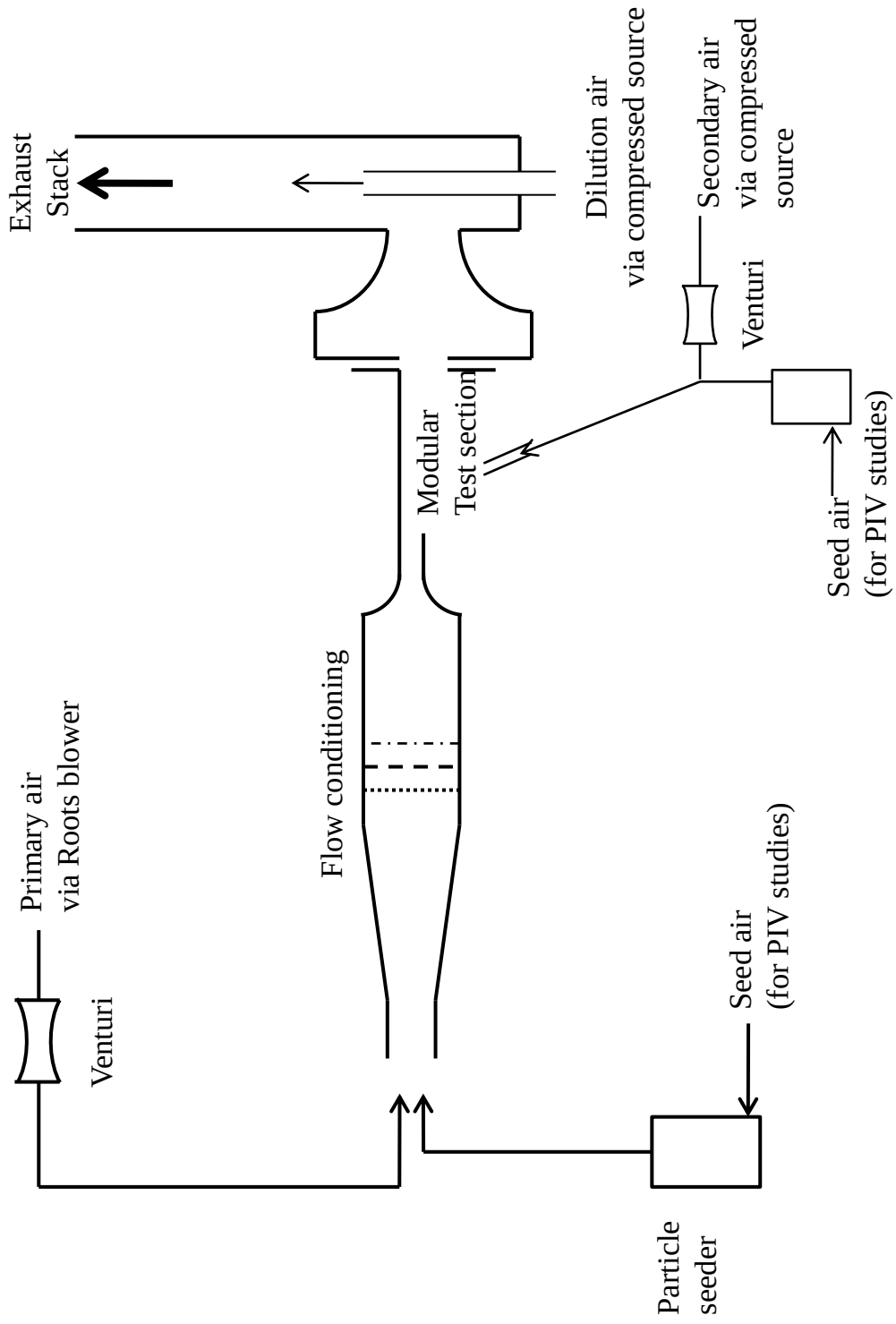

Figure 15: Facility flow schematic

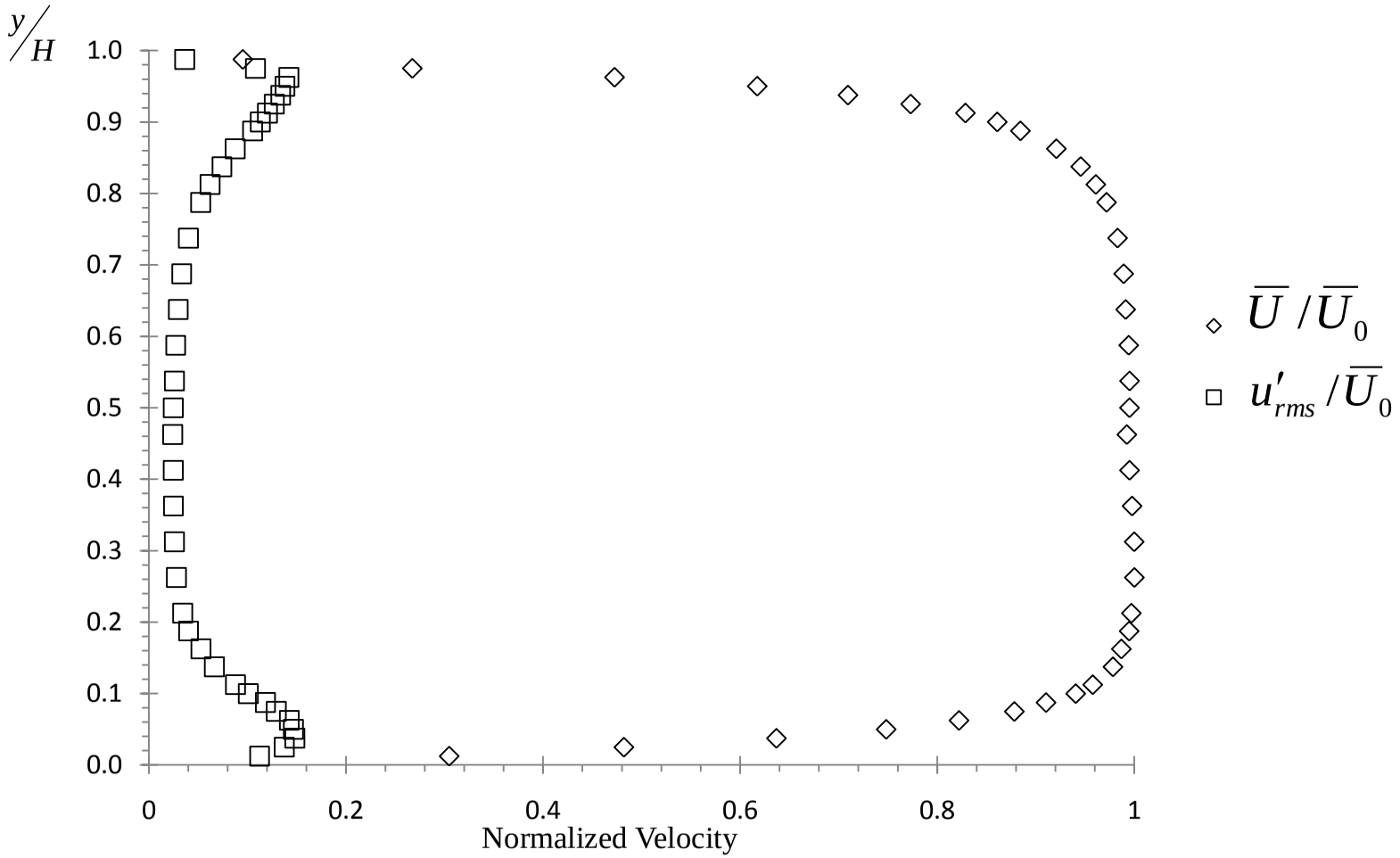

Figure 16: Test facility inlet conditions

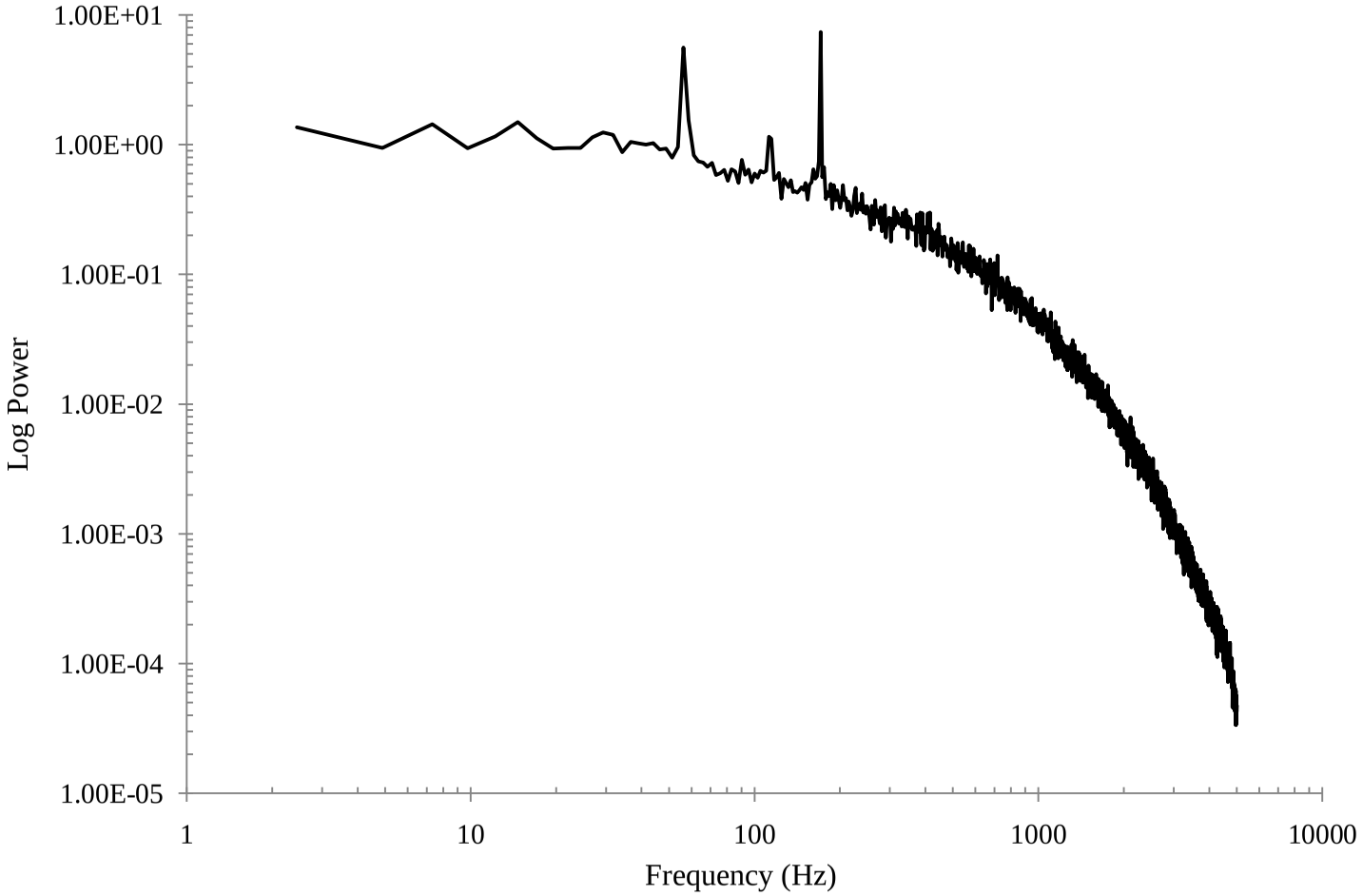

Figure 17: Test facility inlet spectra

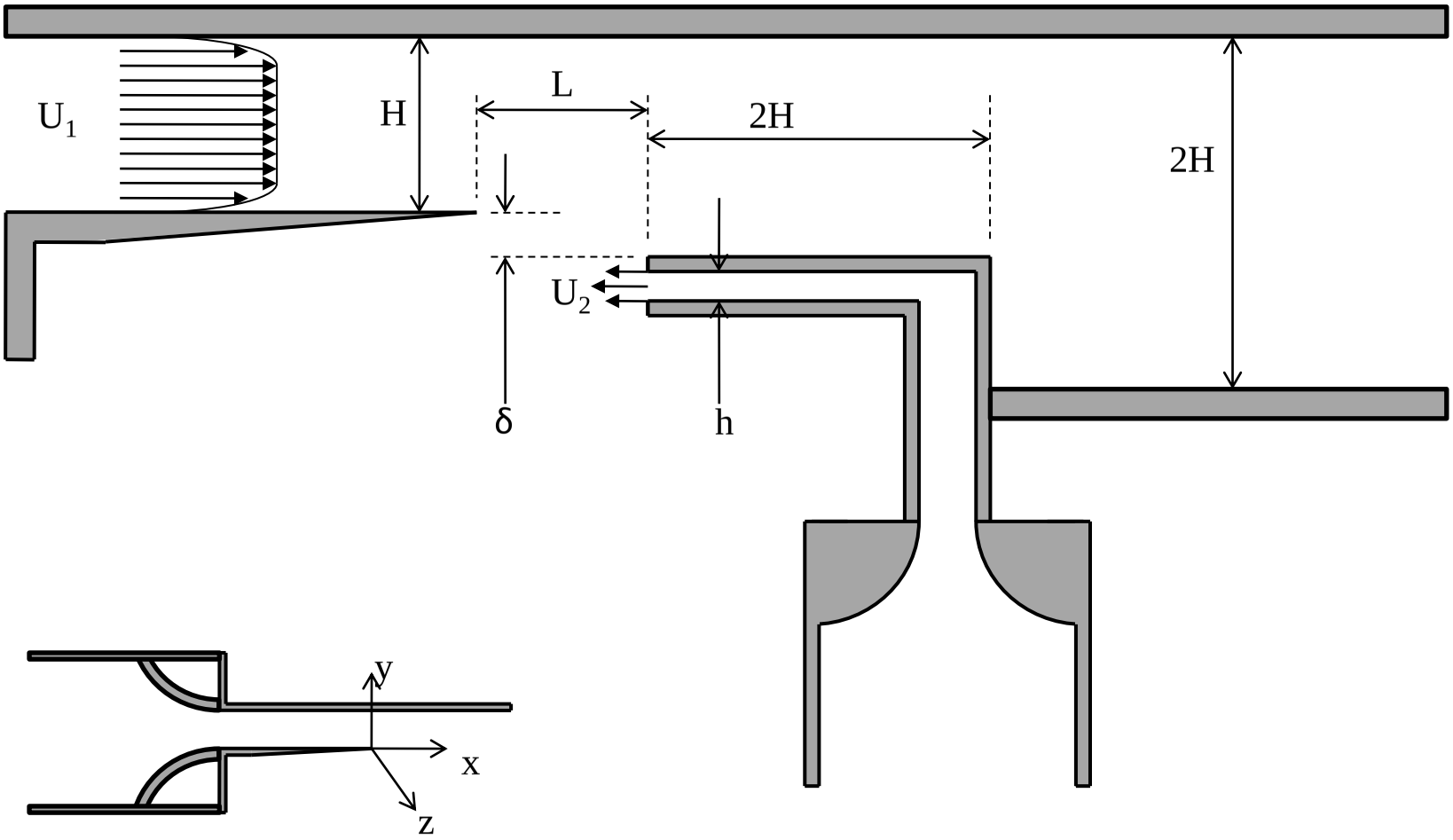

Figure 18: Geometry I-Closed facility

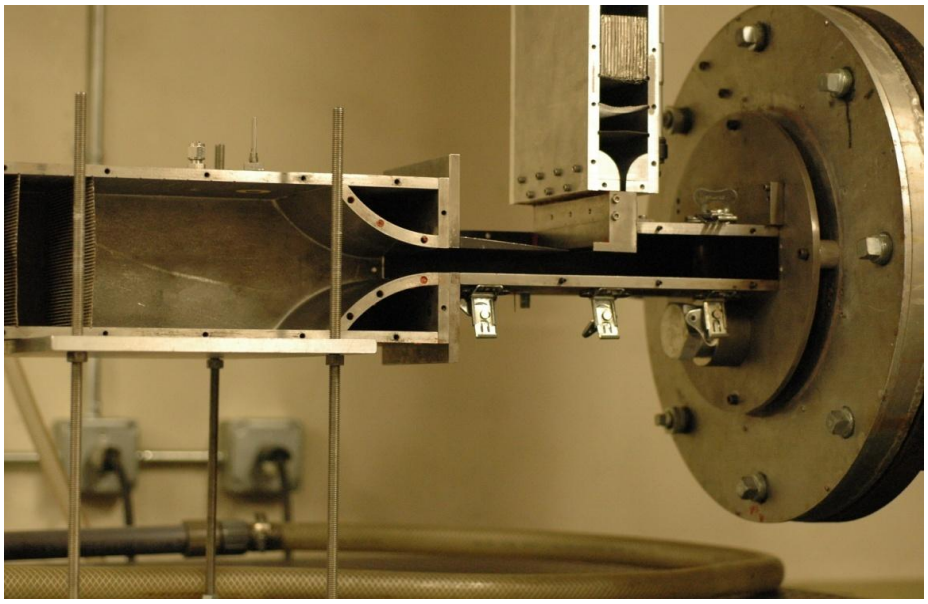

Figure 19: Geometry I - Images of closed facility

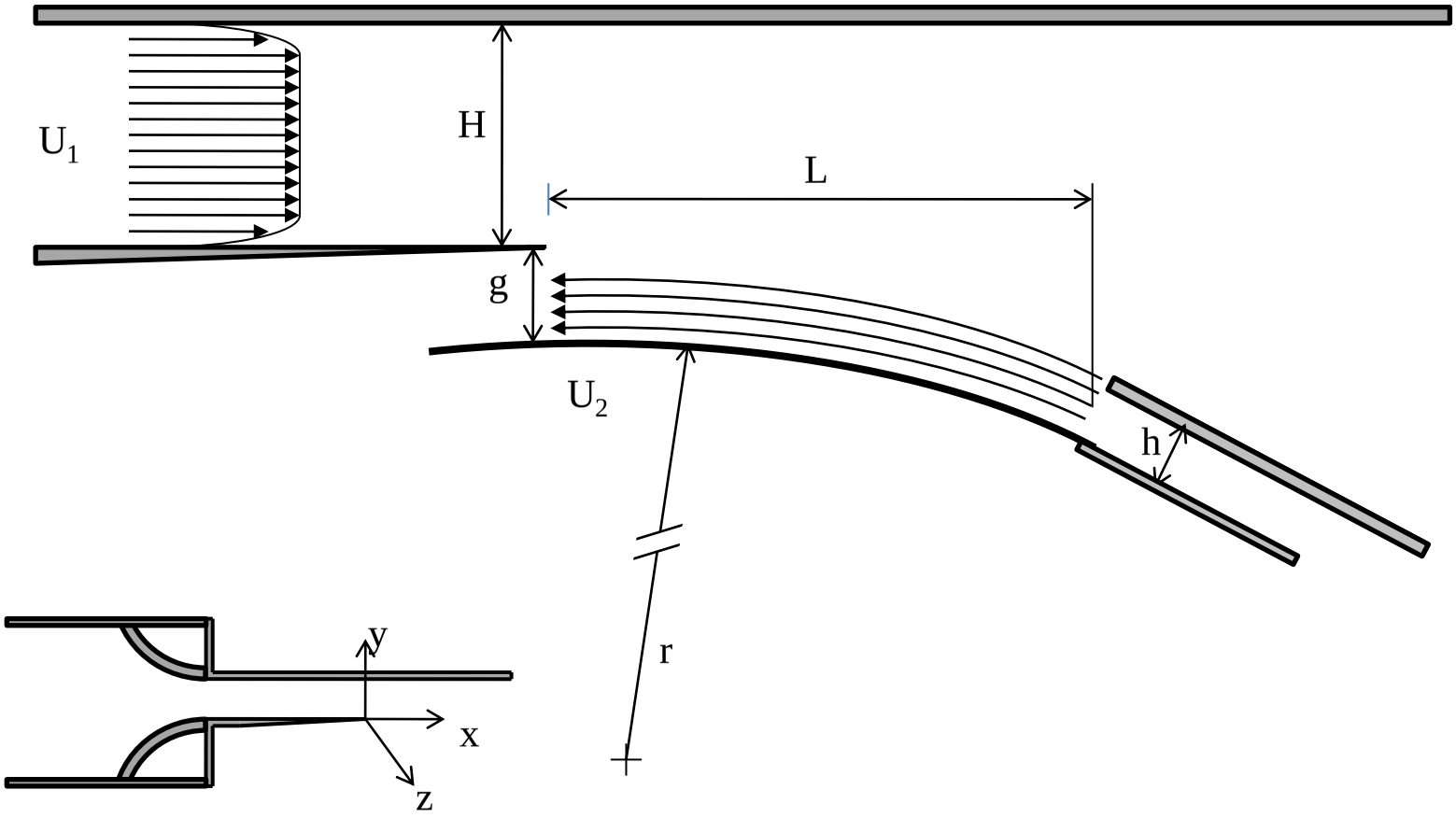

Figure 20: Geometry II - Coanda facility

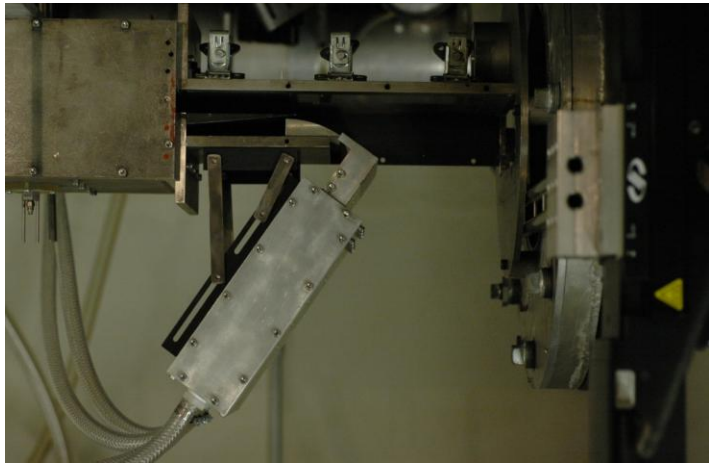

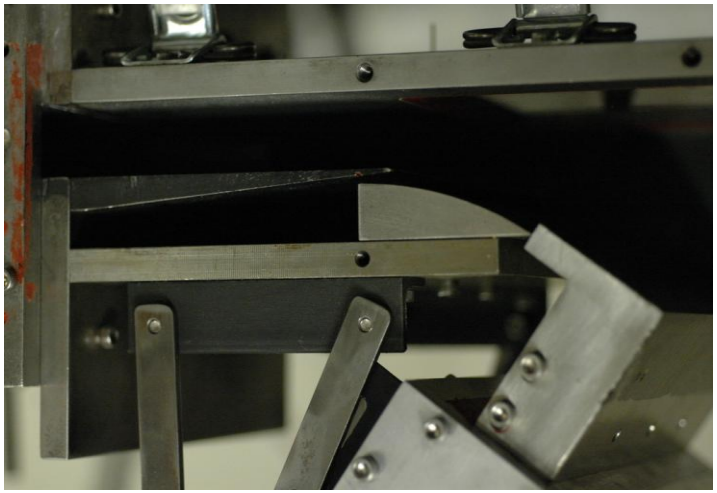

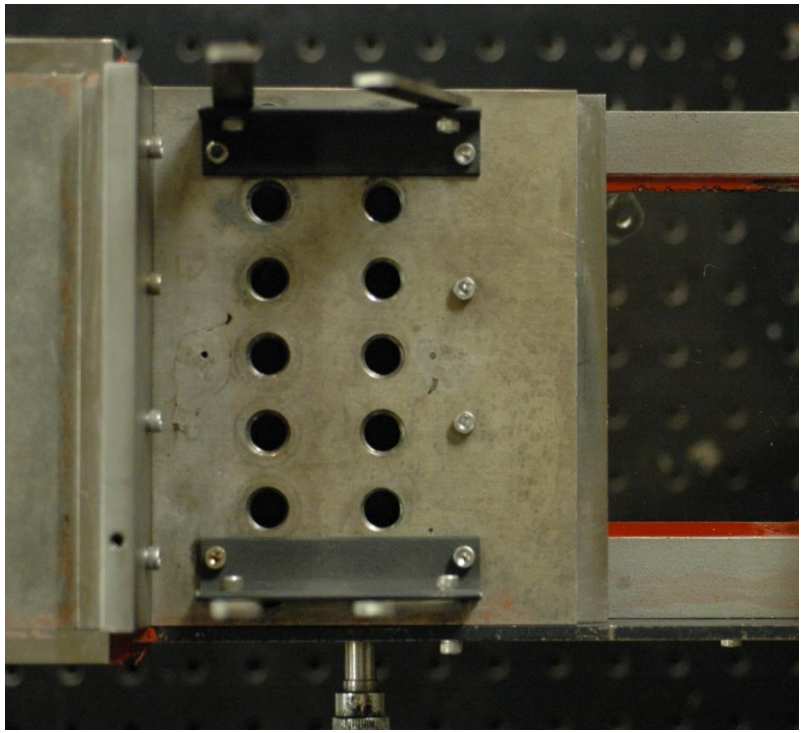

Figure 21: Geometry II - Coanda facility images

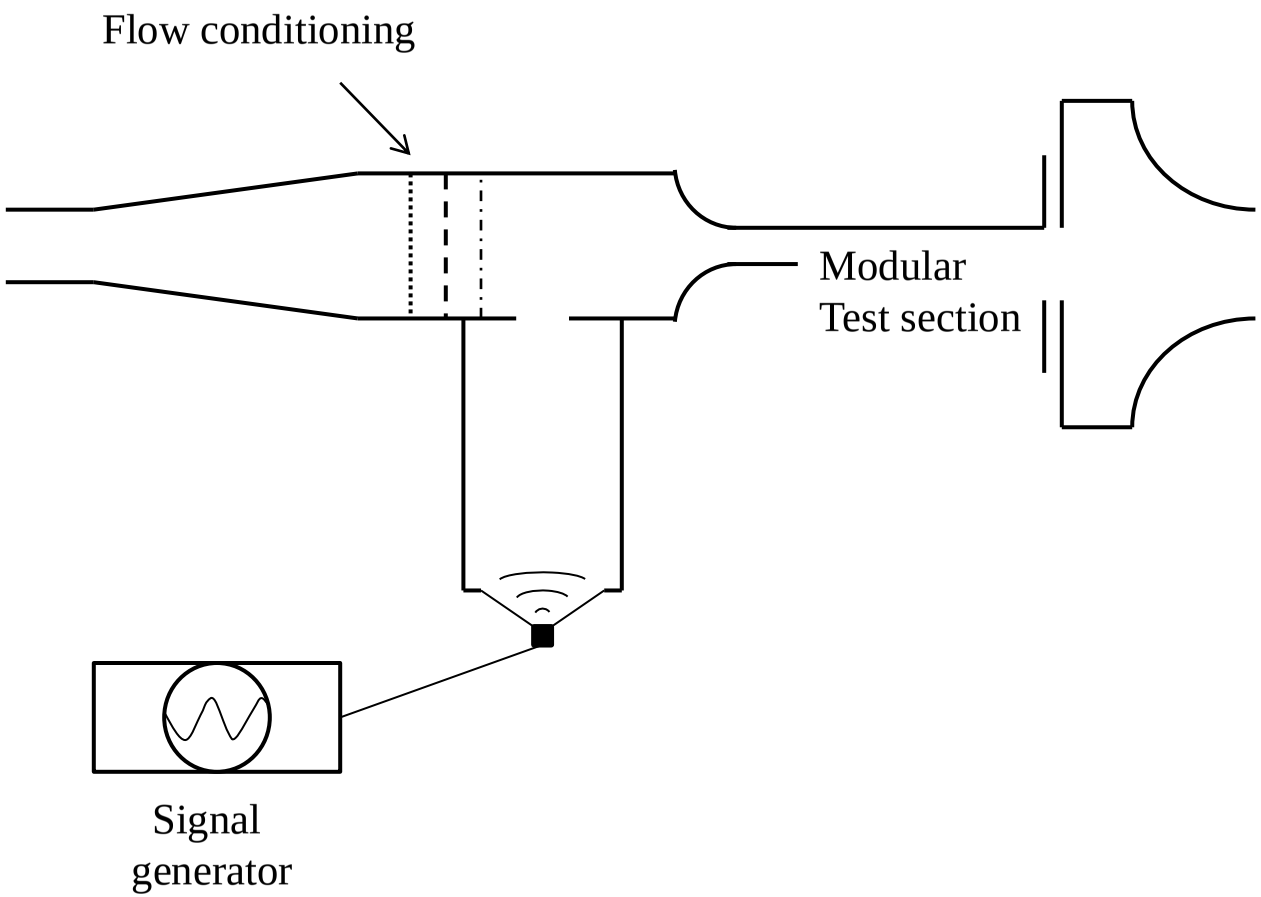

Figure 22: Schematic of acoustic inlet forcing of geometry I facility

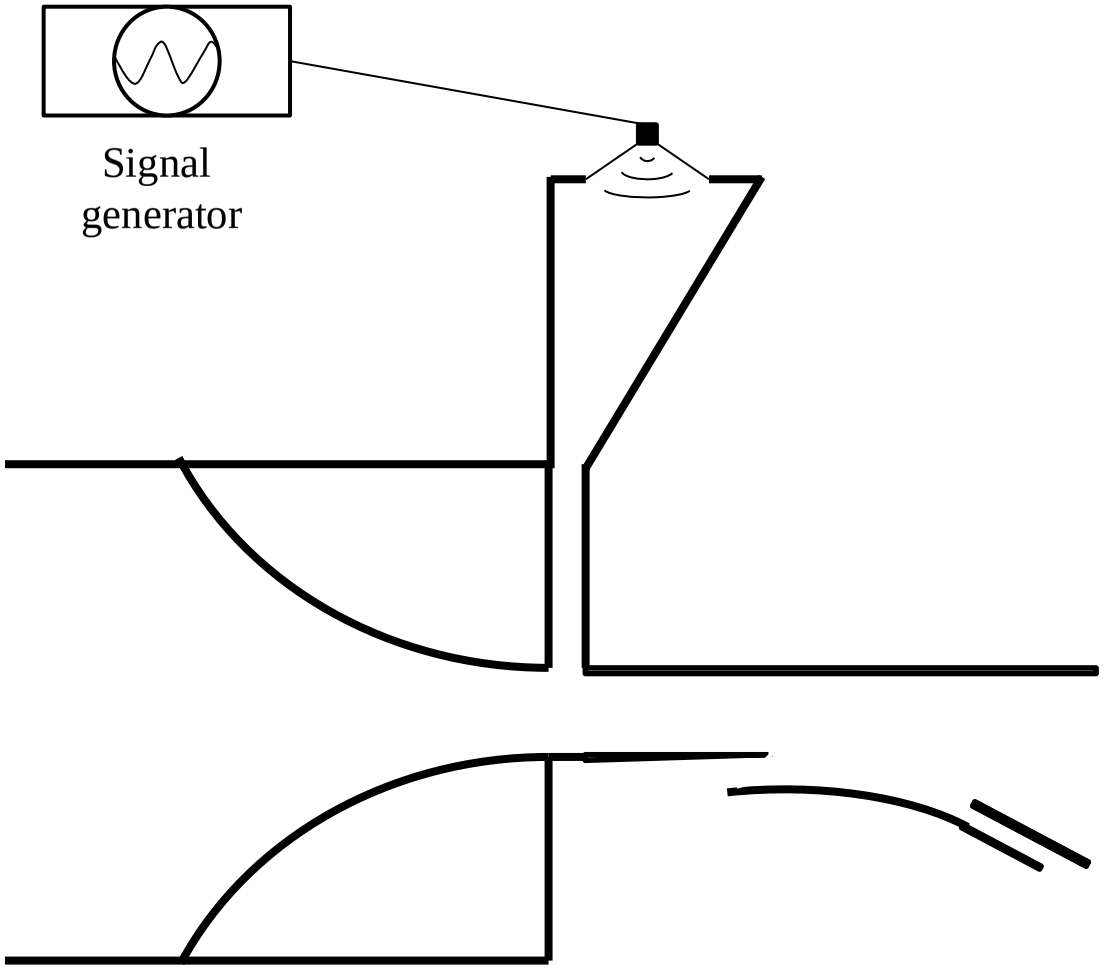

Figure 23: Schematic of two-dimensional acoustic forcing of geometry II facility

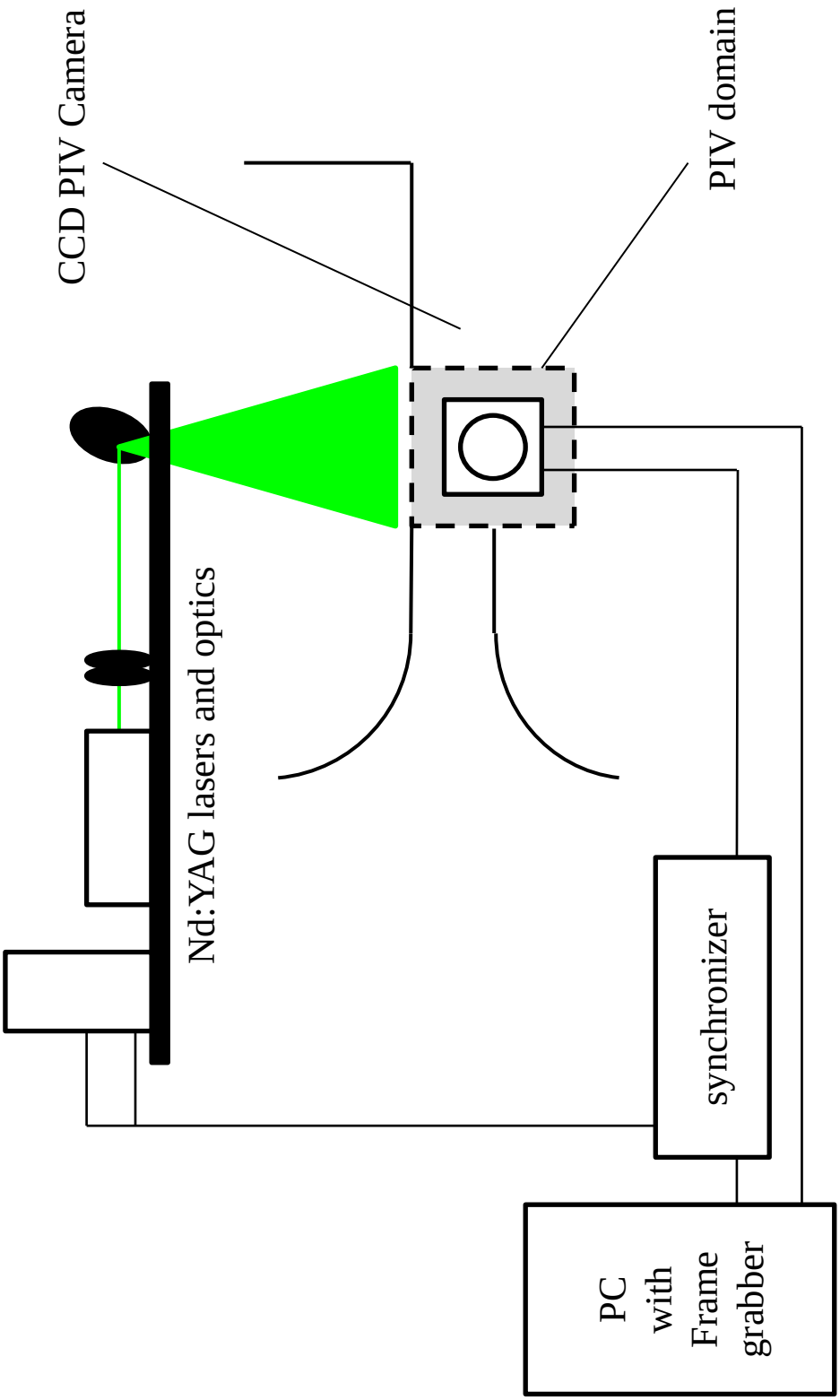

Figure 24: PIV experimental setup

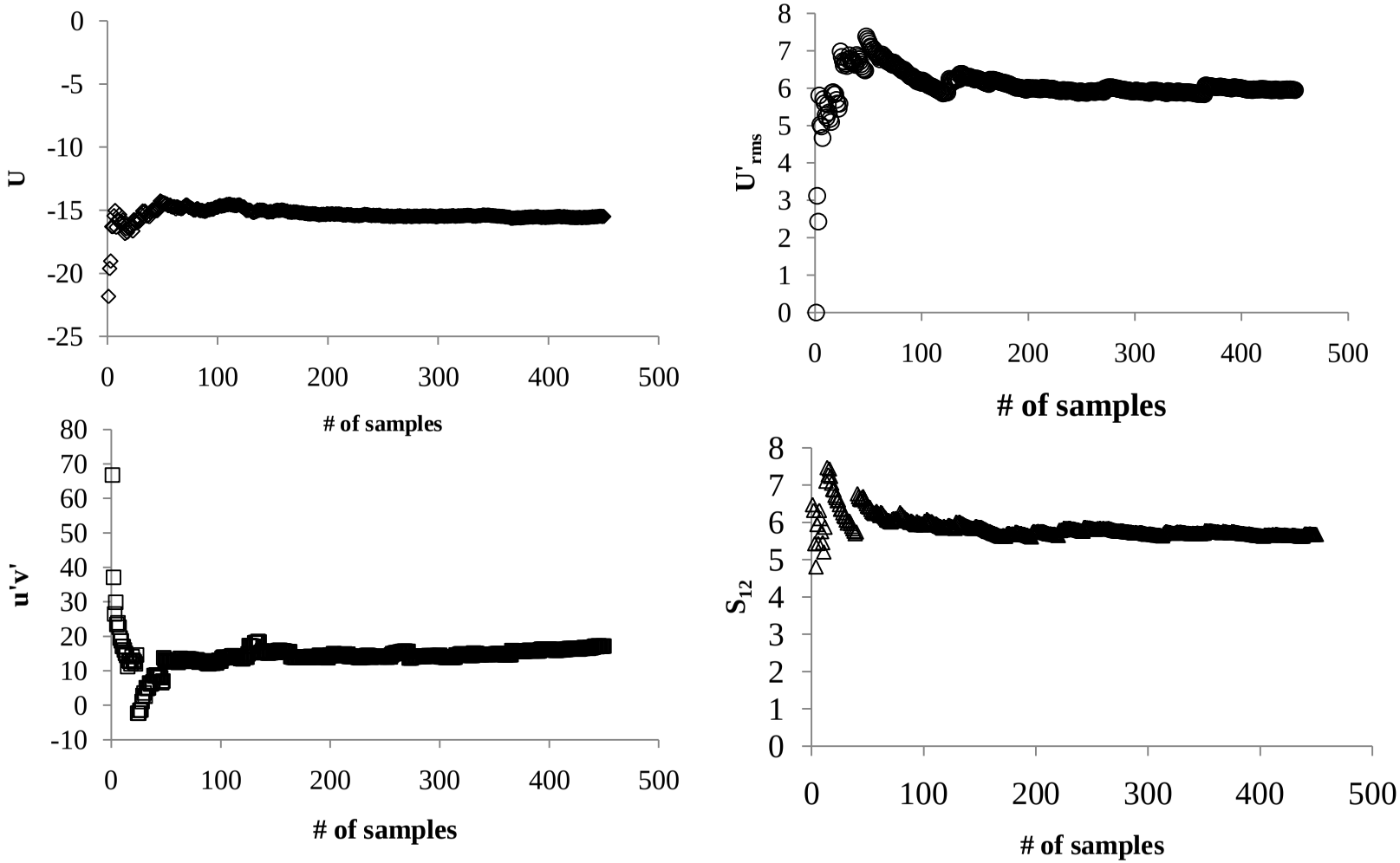

Figure 25: PIV statistics convergenece

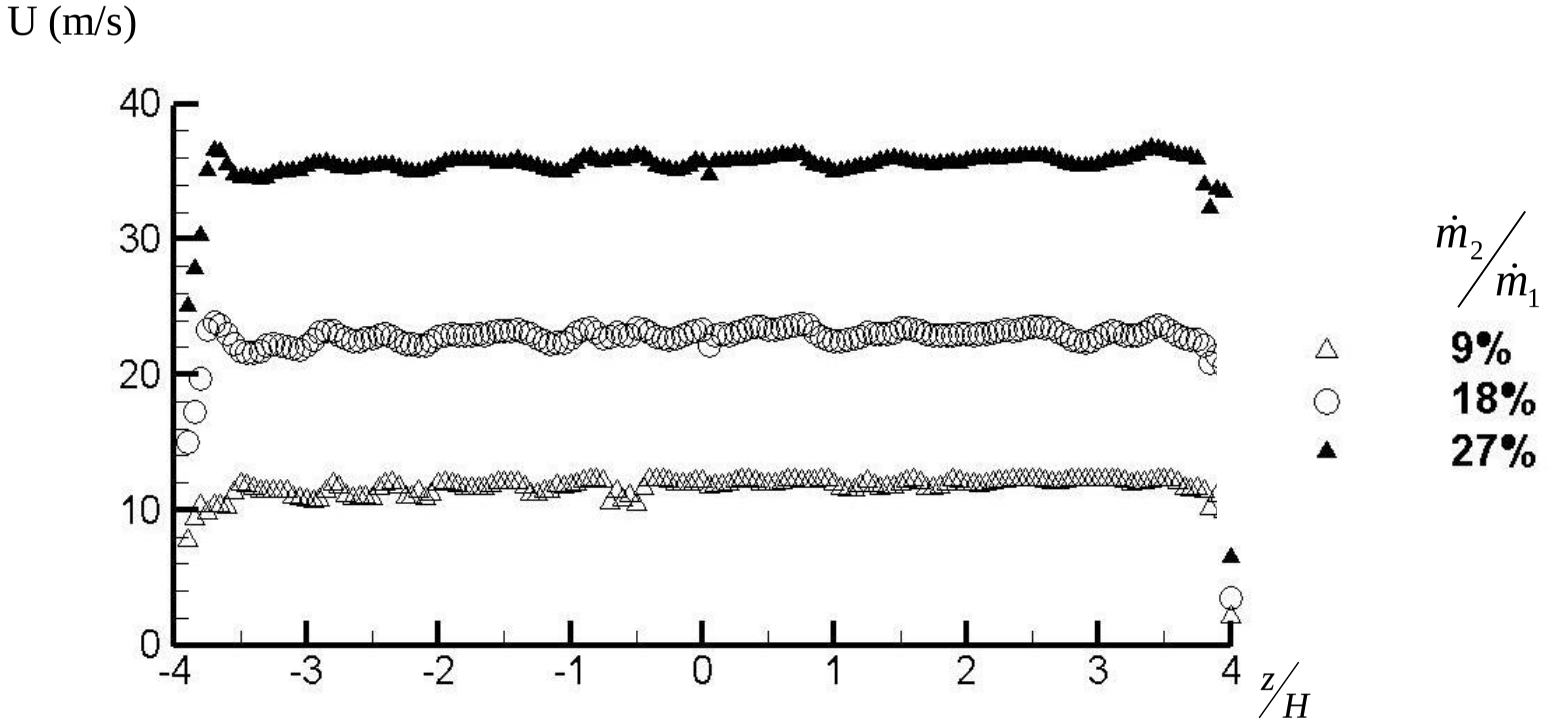

Figure 26: Spanwise mean streamwise velocity profiles of secondary jet

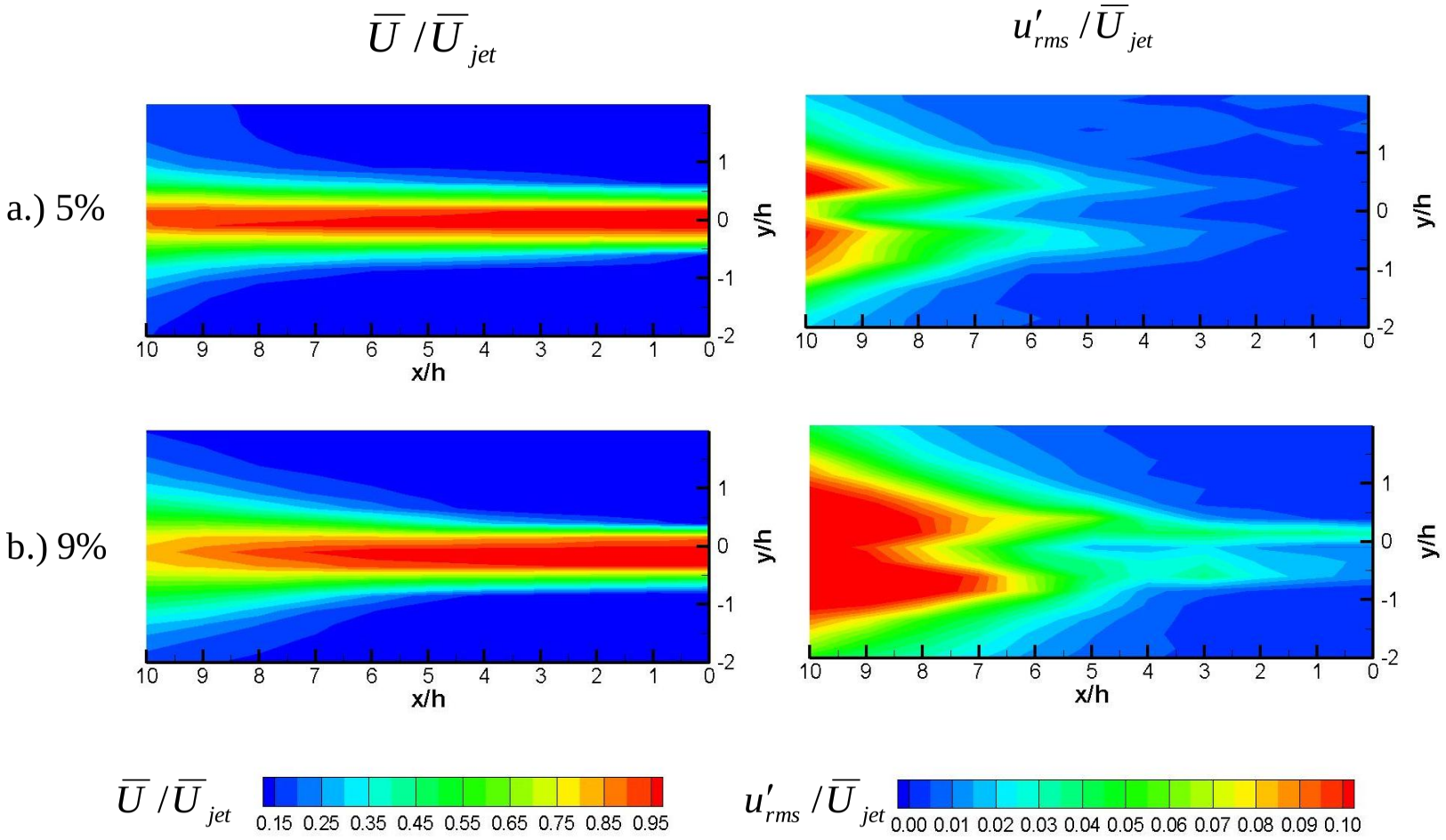

Figure 27 a & b: Streamwise mean and rms velocity contours for the secondary jet

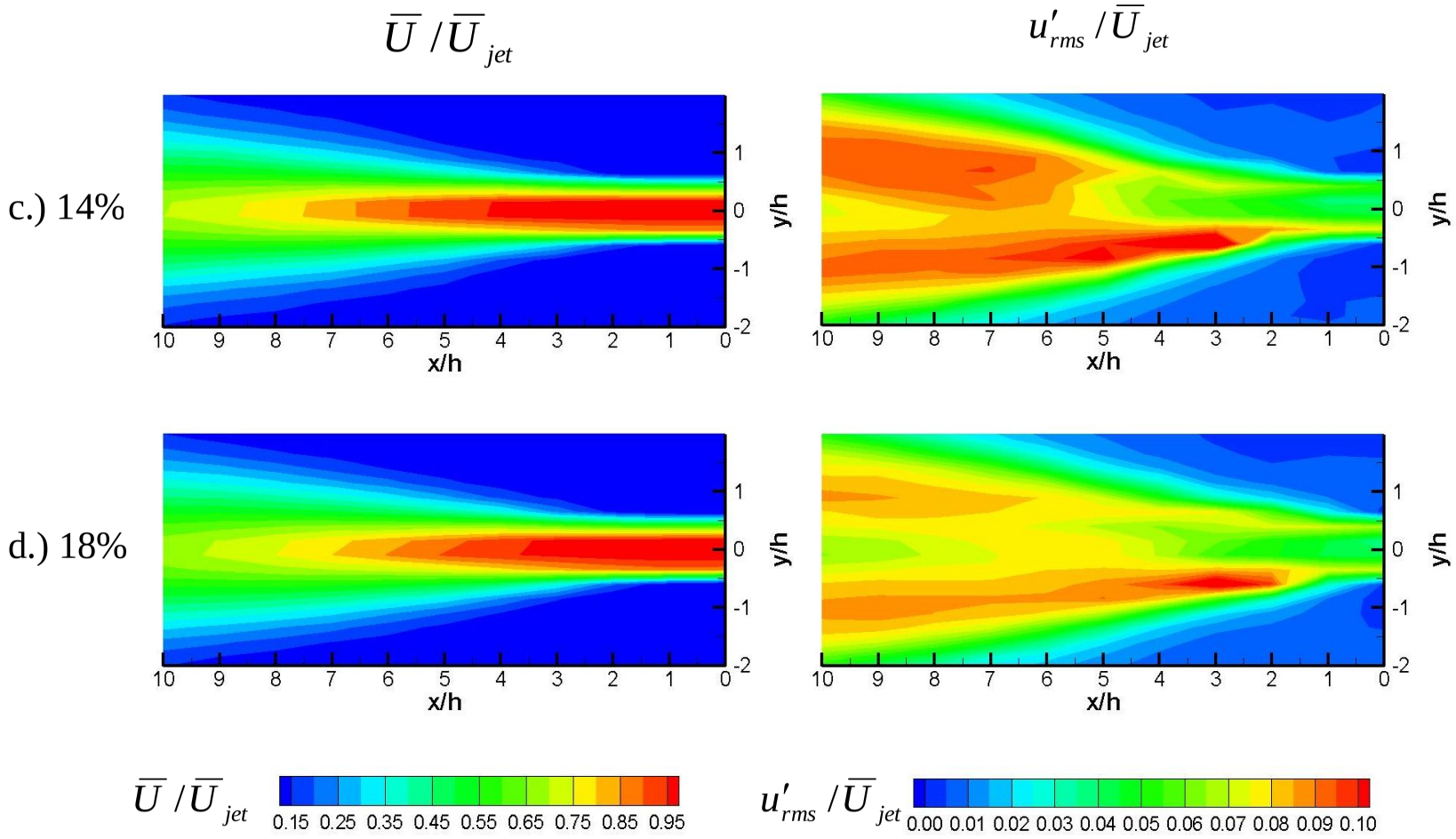

Figure 27 c & d: Streamwise mean and rms velocity contours for the secondary jet

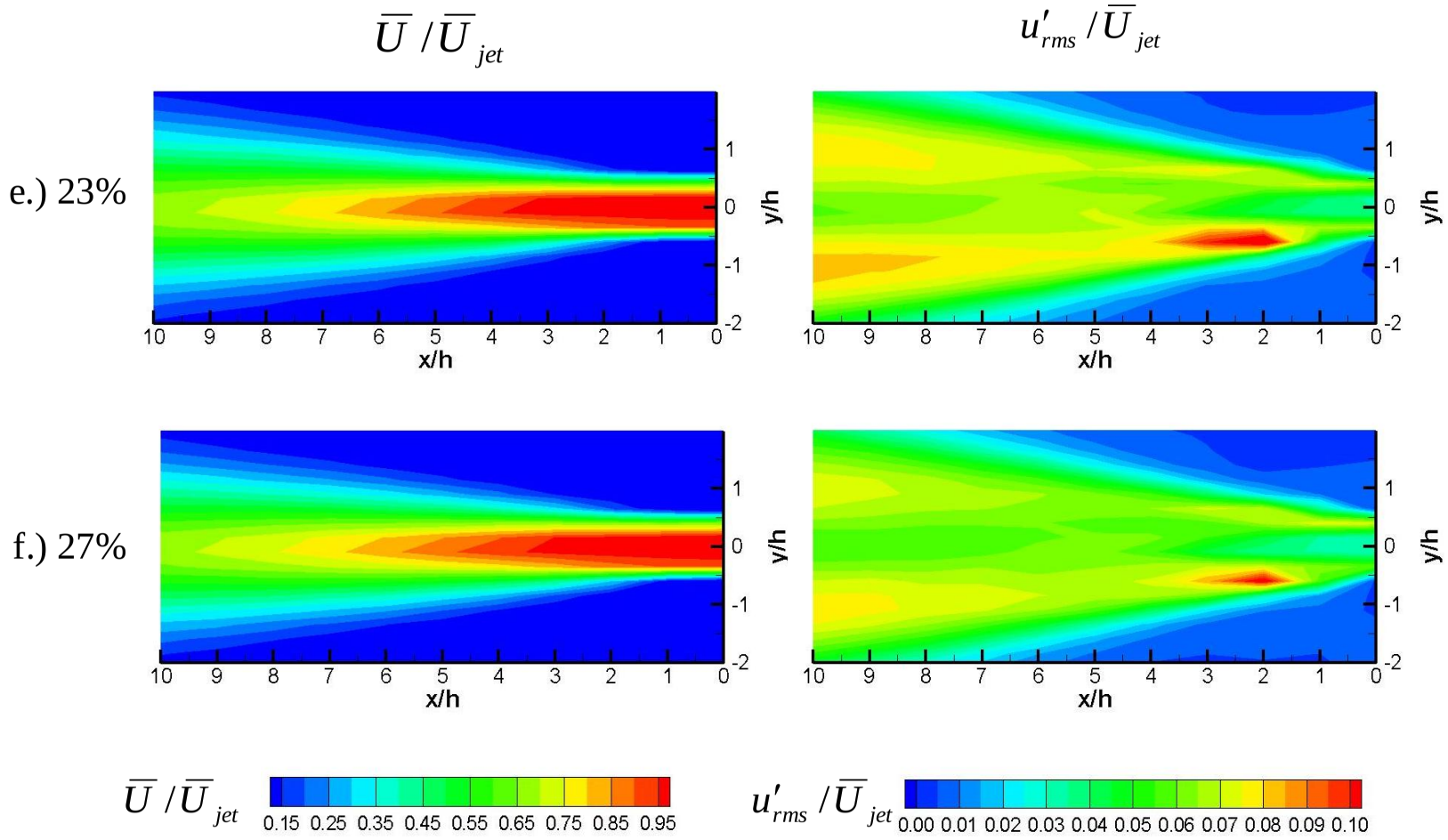

Figure 27 e & f: Streamwise mean and rms velocity contours for the secondary jet

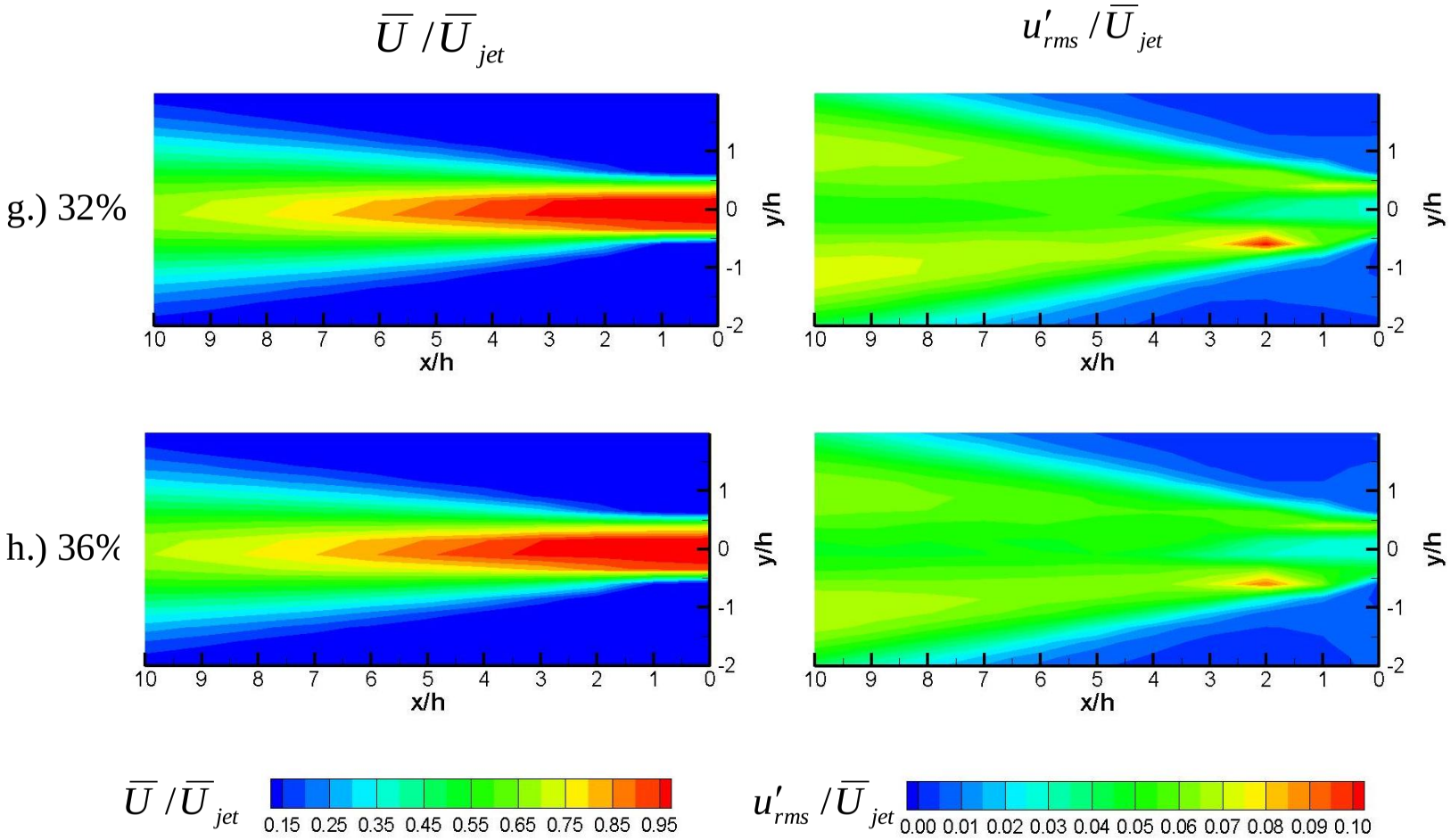

Figure 27g & h: Streamwise mean and rms velocity contours for the secondary jet

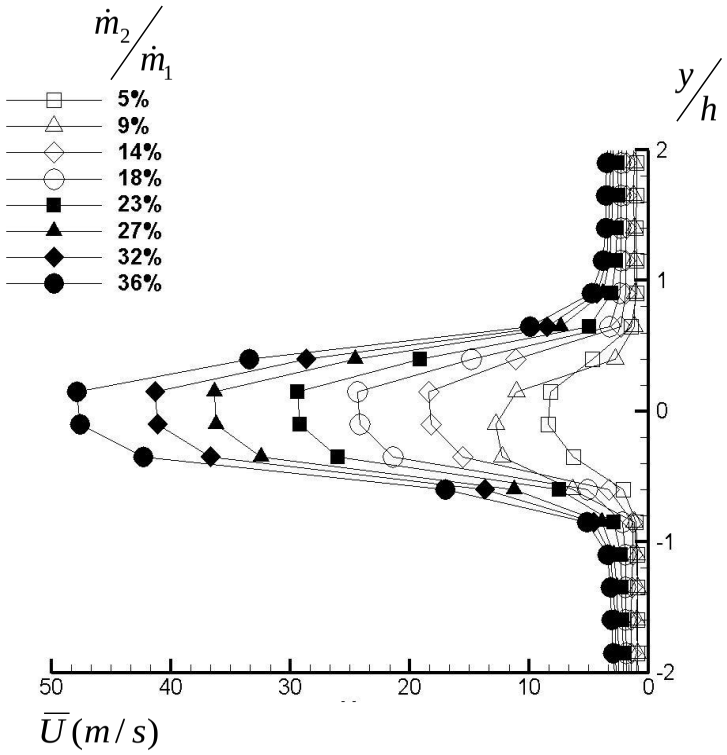

a.) Mean streamwise velocity profiles

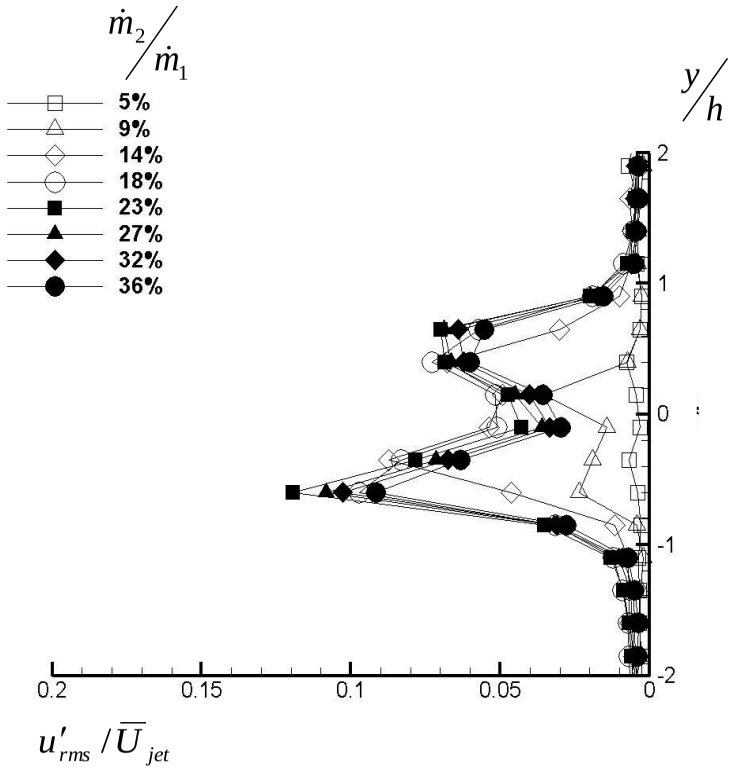

b.) Rms streamwise velocity fluctuation profiles

Figure 28: Mean and rms streamwise velocity profiles at x/h = 2

a.) 0%

b.) 5%

c.) 9%

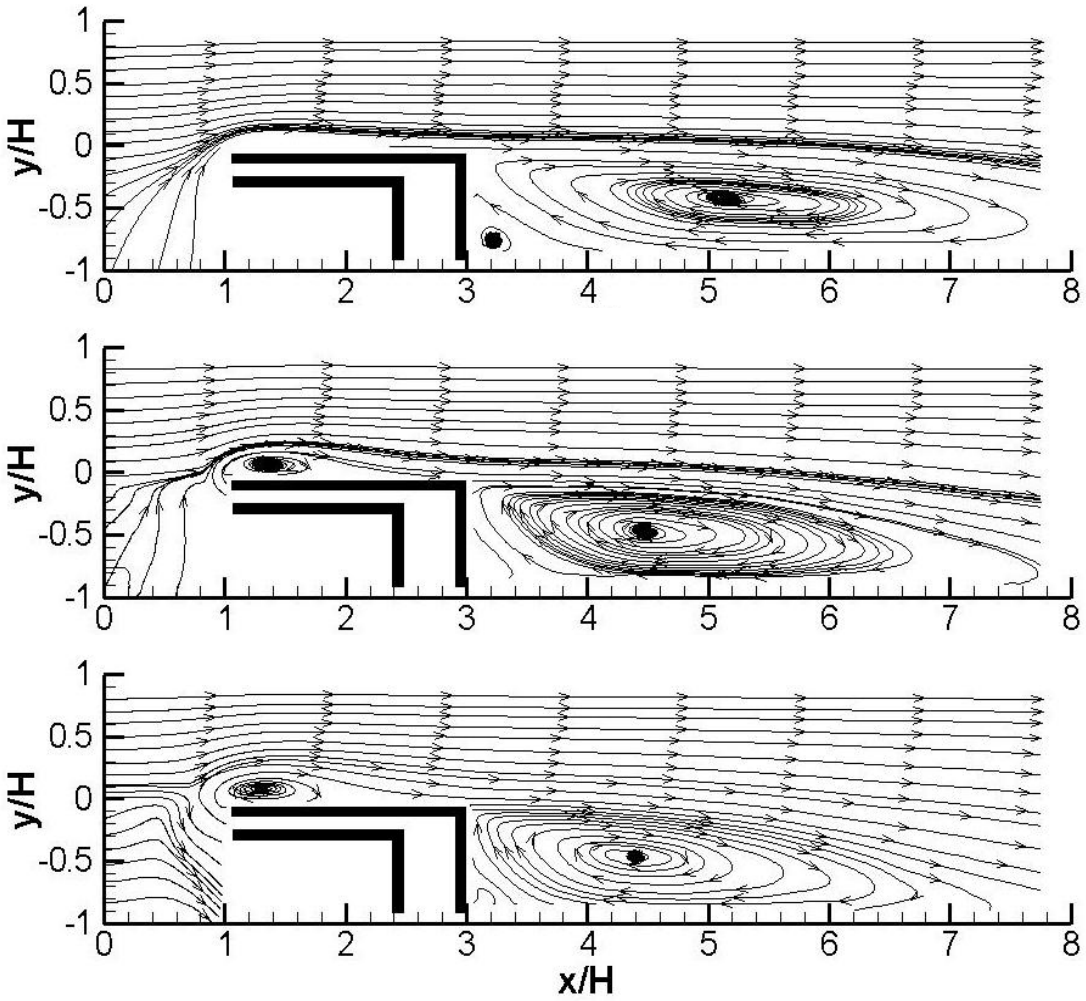

Figure 29 a - c: Streamlines of the mean velocity fields for geometry I at all secondary flow rates

d.) 14%

e.) 18%

f.) 23%

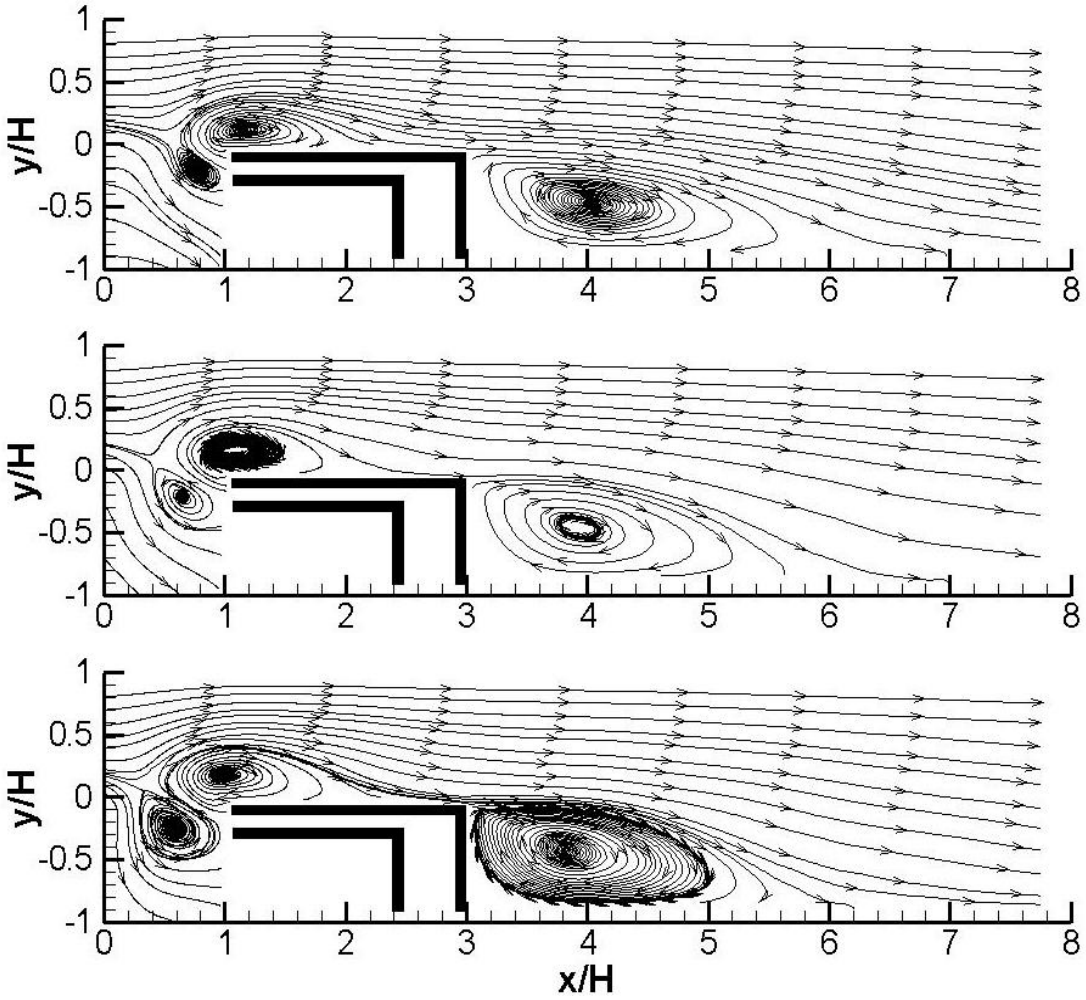

Figure 29 d - f: Streamlines of the mean velocity fields for geometry I at all secondary flow rates

g.) 27%

h.) 32%

i.) 36%

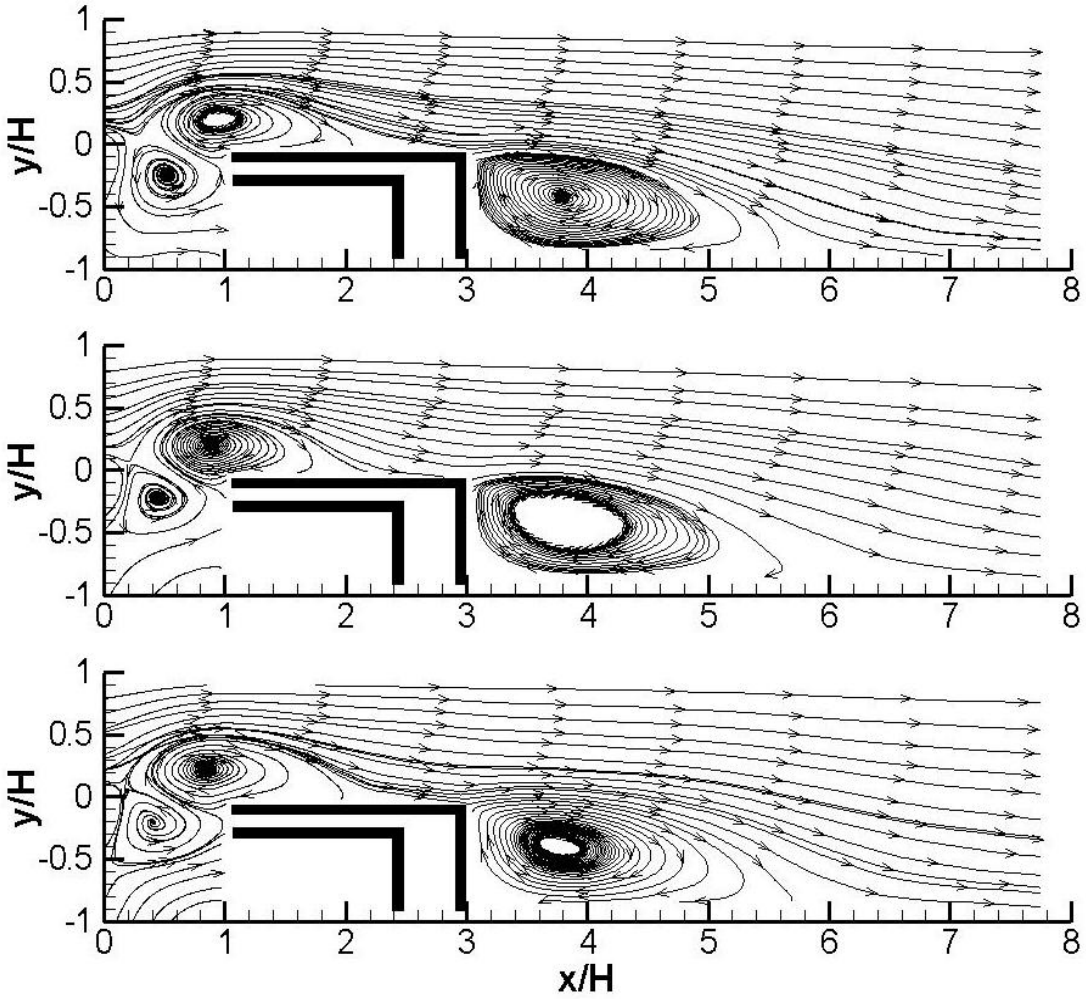

Figure 29 g - i: Streamlines of the mean velocity fields for geometry I at all secondary flow rates

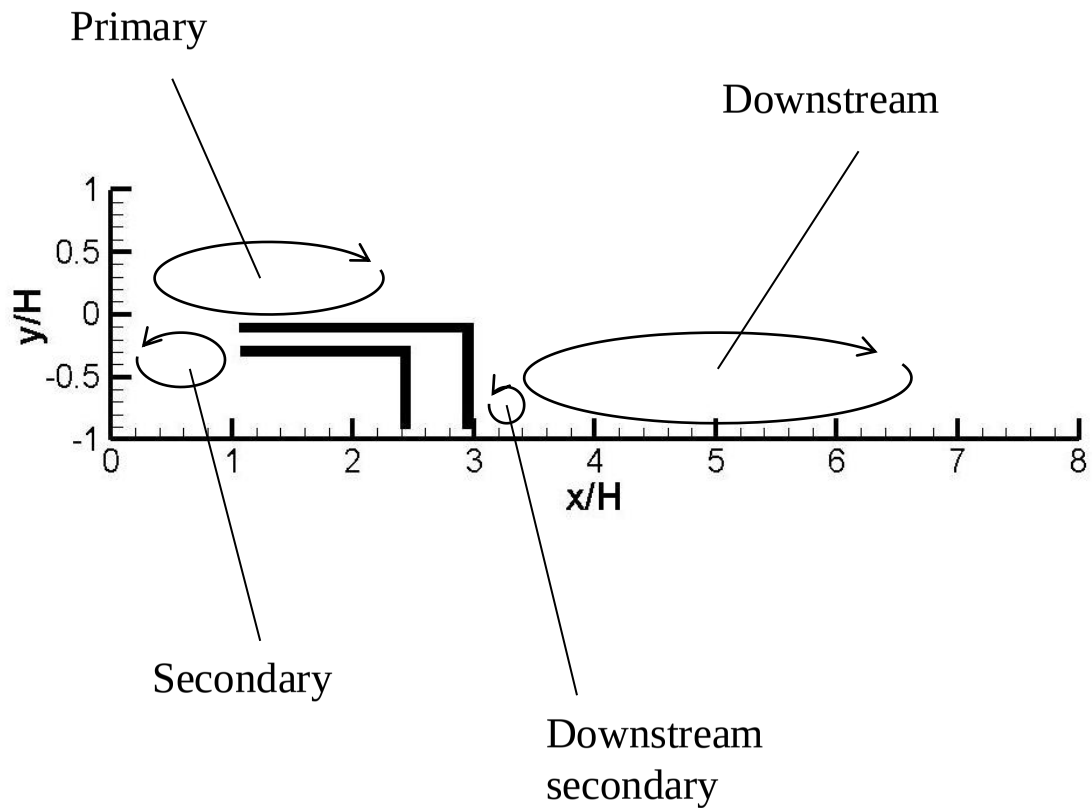

Figure 30: Recirculation zones schematic

a.) 0%

b.) 5%

c.) 9%

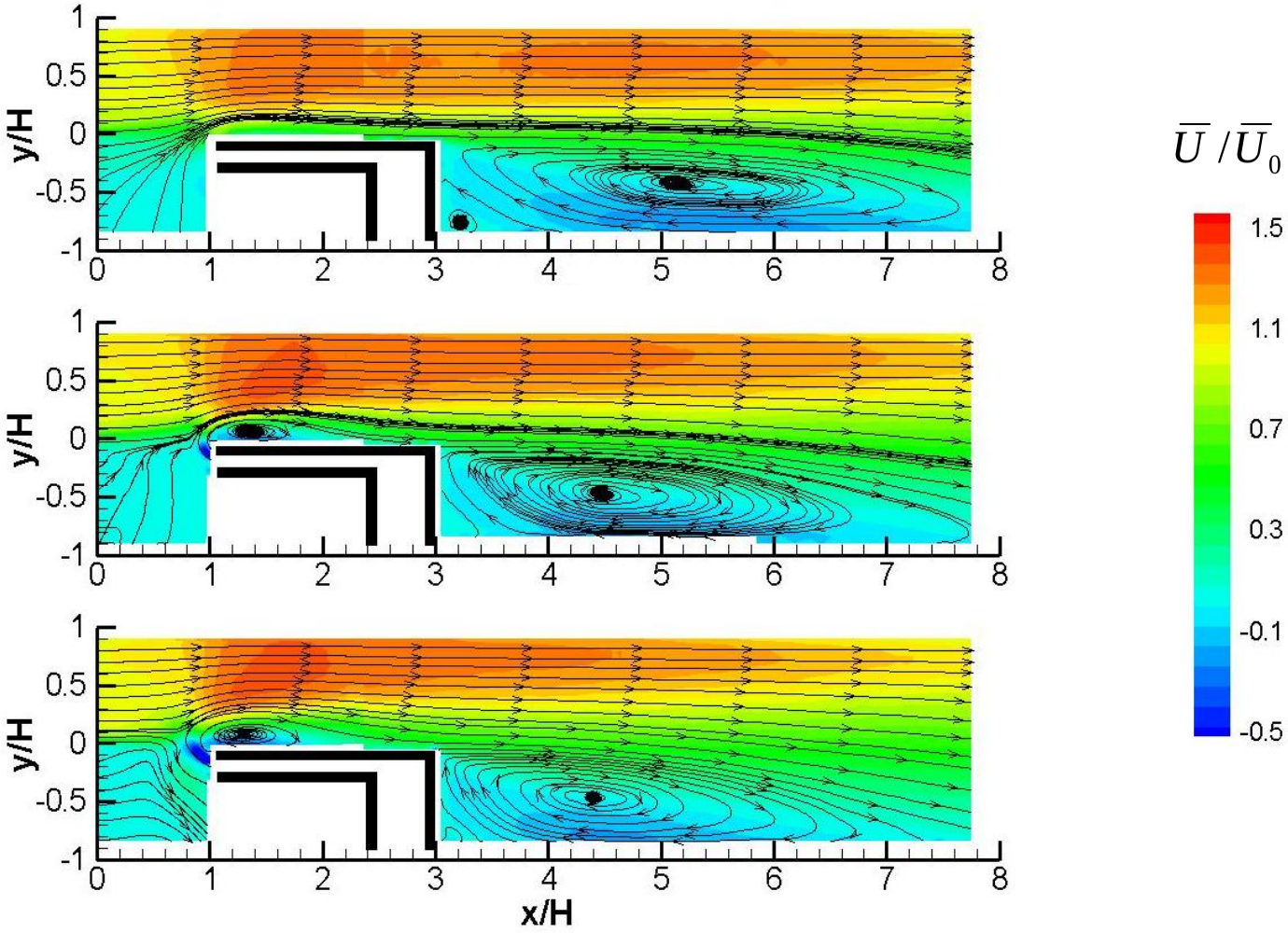

Figure 31 a - c: Mean streamwise velocity contours for geometry I at all secondary flow rates

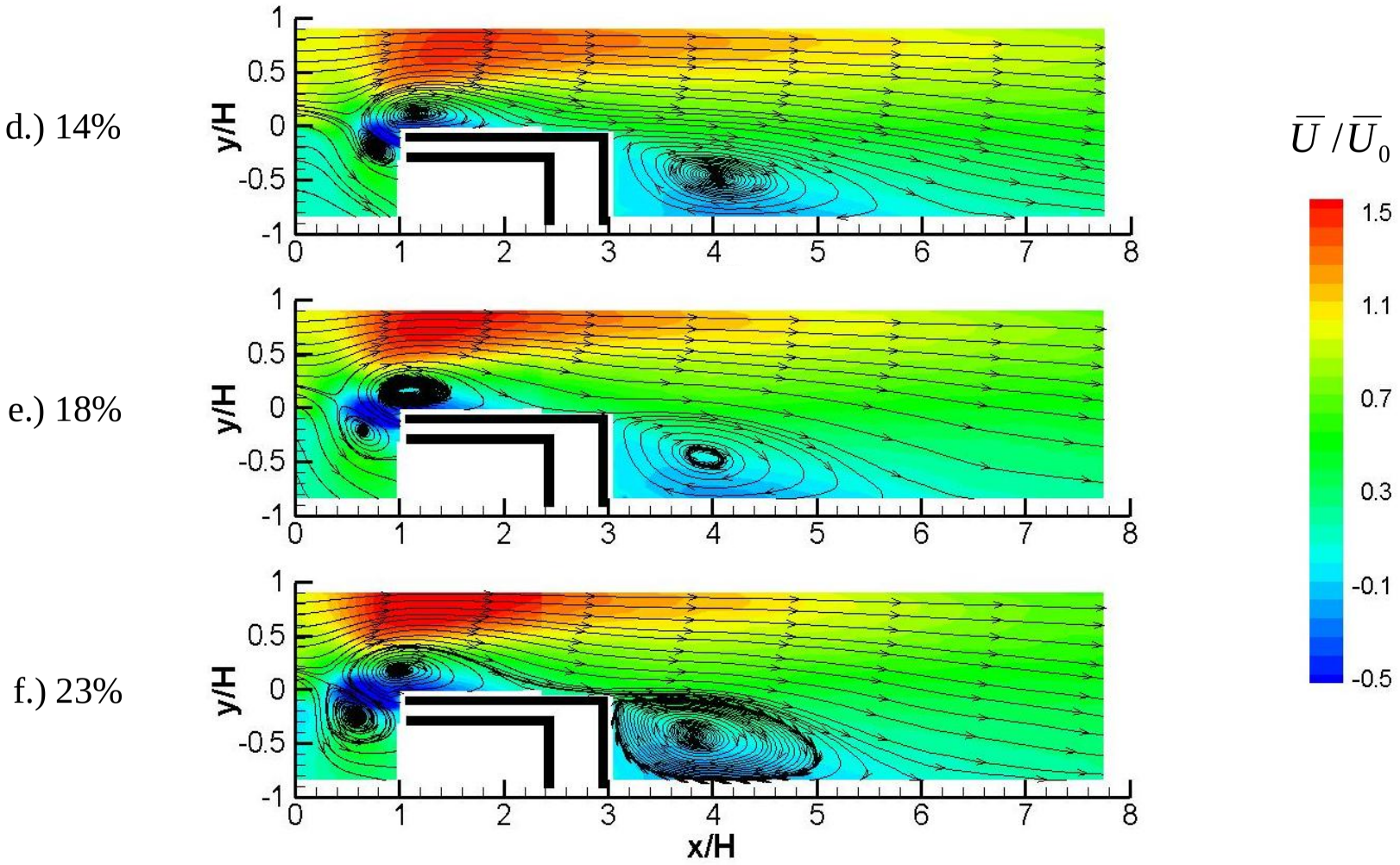

Figure 31 d - f: Mean streamwise velocity contours for geometry I at all secondary flow rates

g.) 27%

h.) 32%

i.) 36%

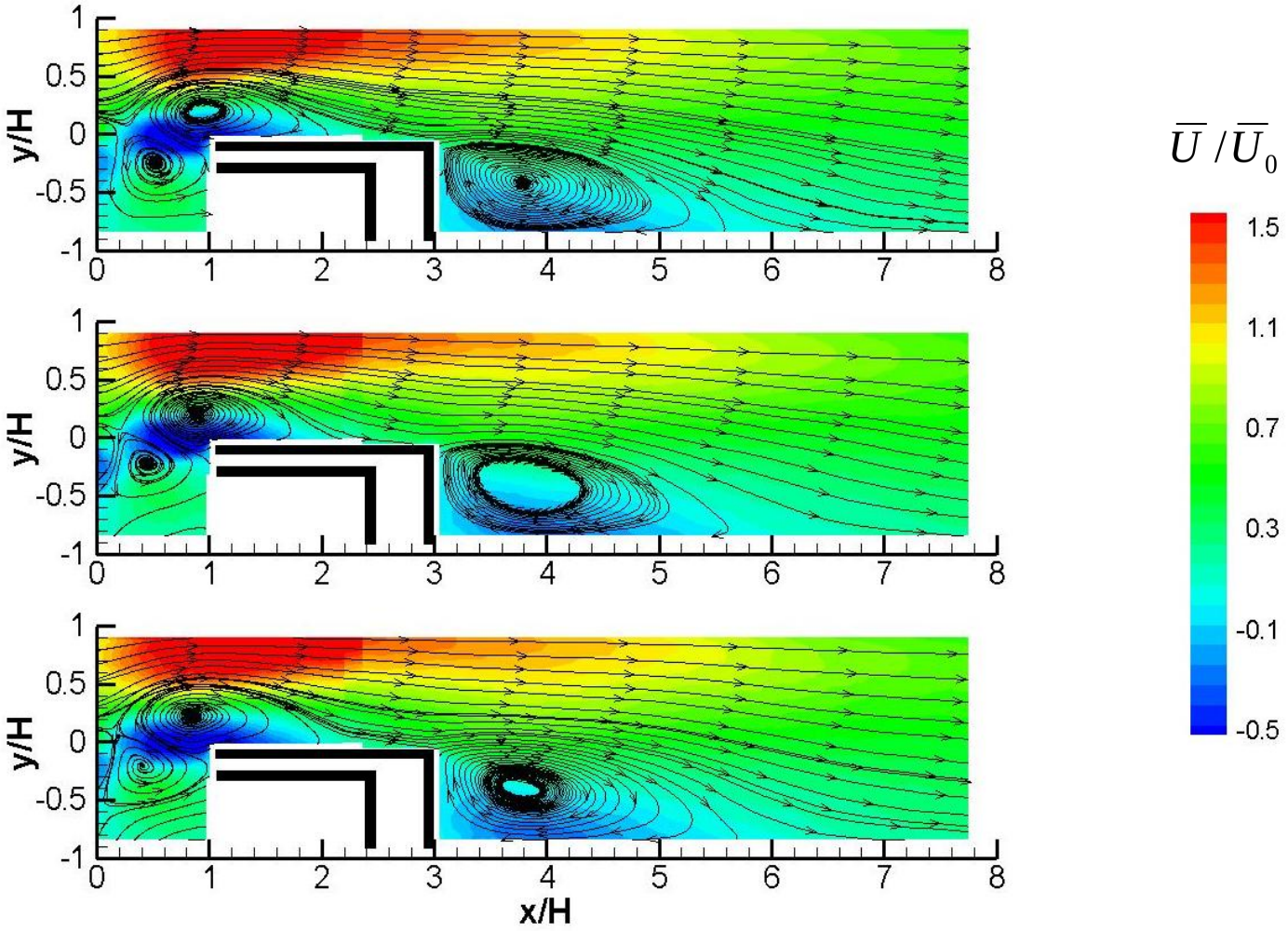

Figure 31 g - i: Mean streamwise velocity contours for geometry I at all secondary flow rates

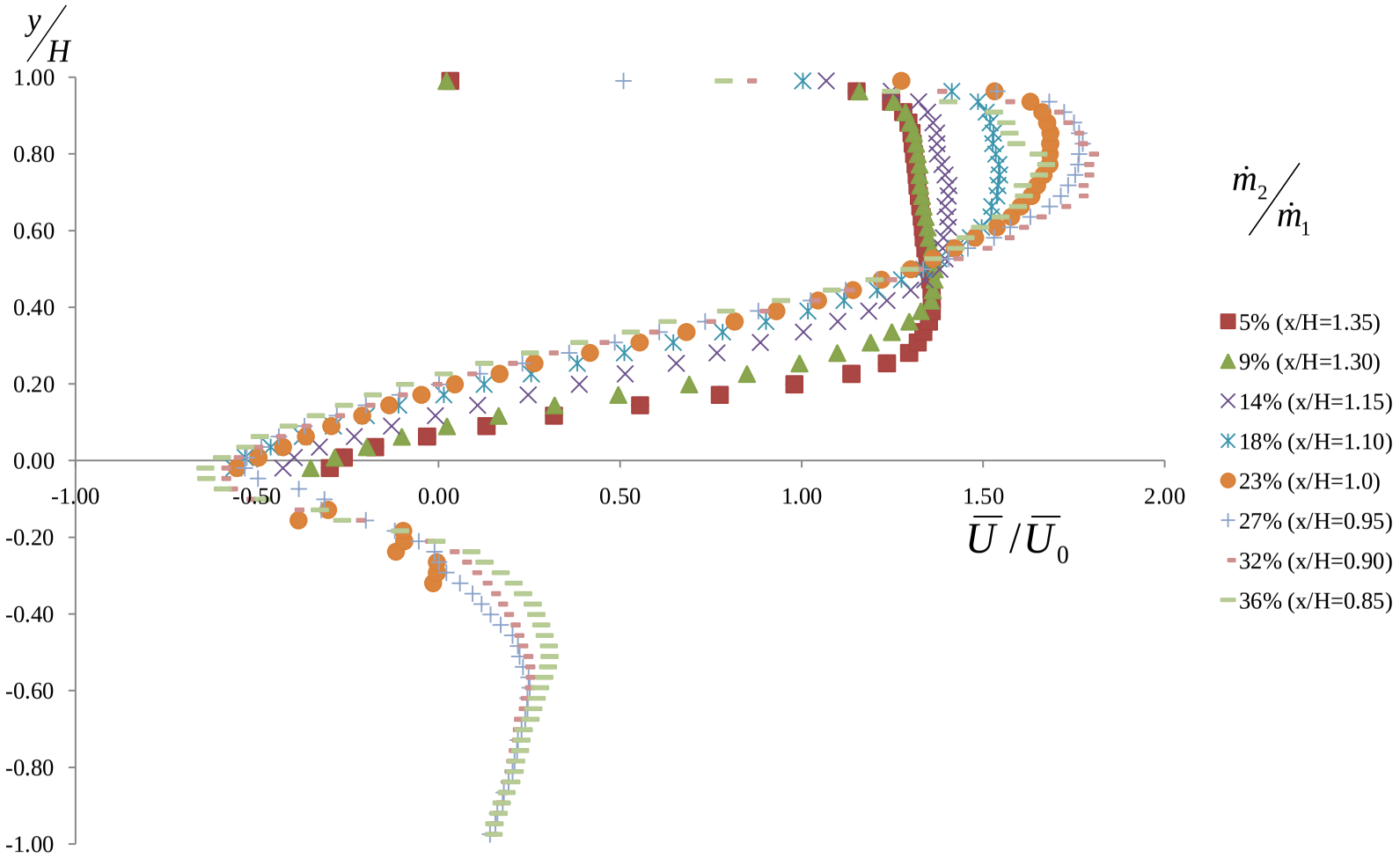

Figure 32: Mean streamwise velocity profiles through center of primary recirculation bubble

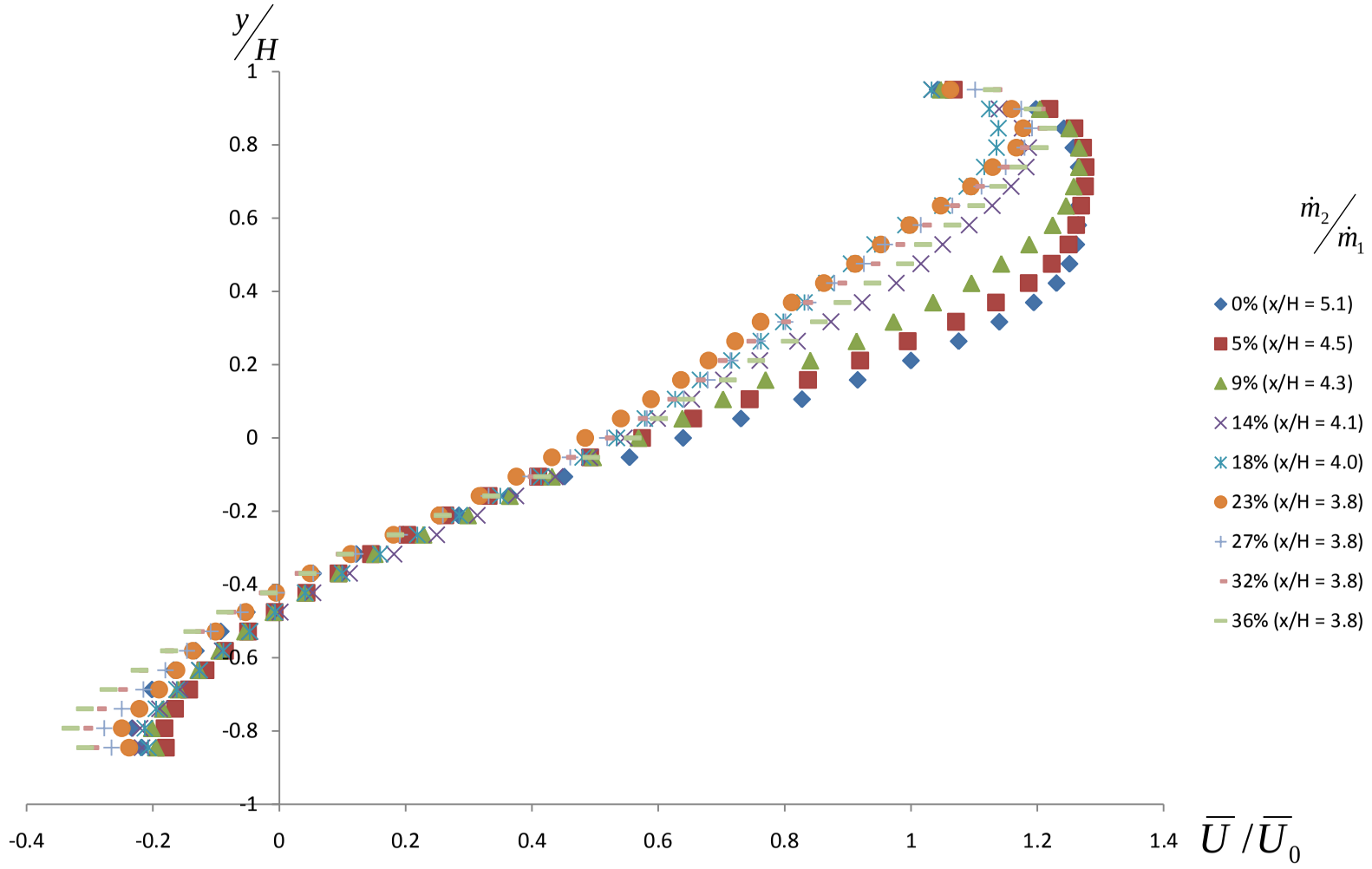

Figure 33: Mean streamwise velocity profiles through the center of the downstream recirculation bubble

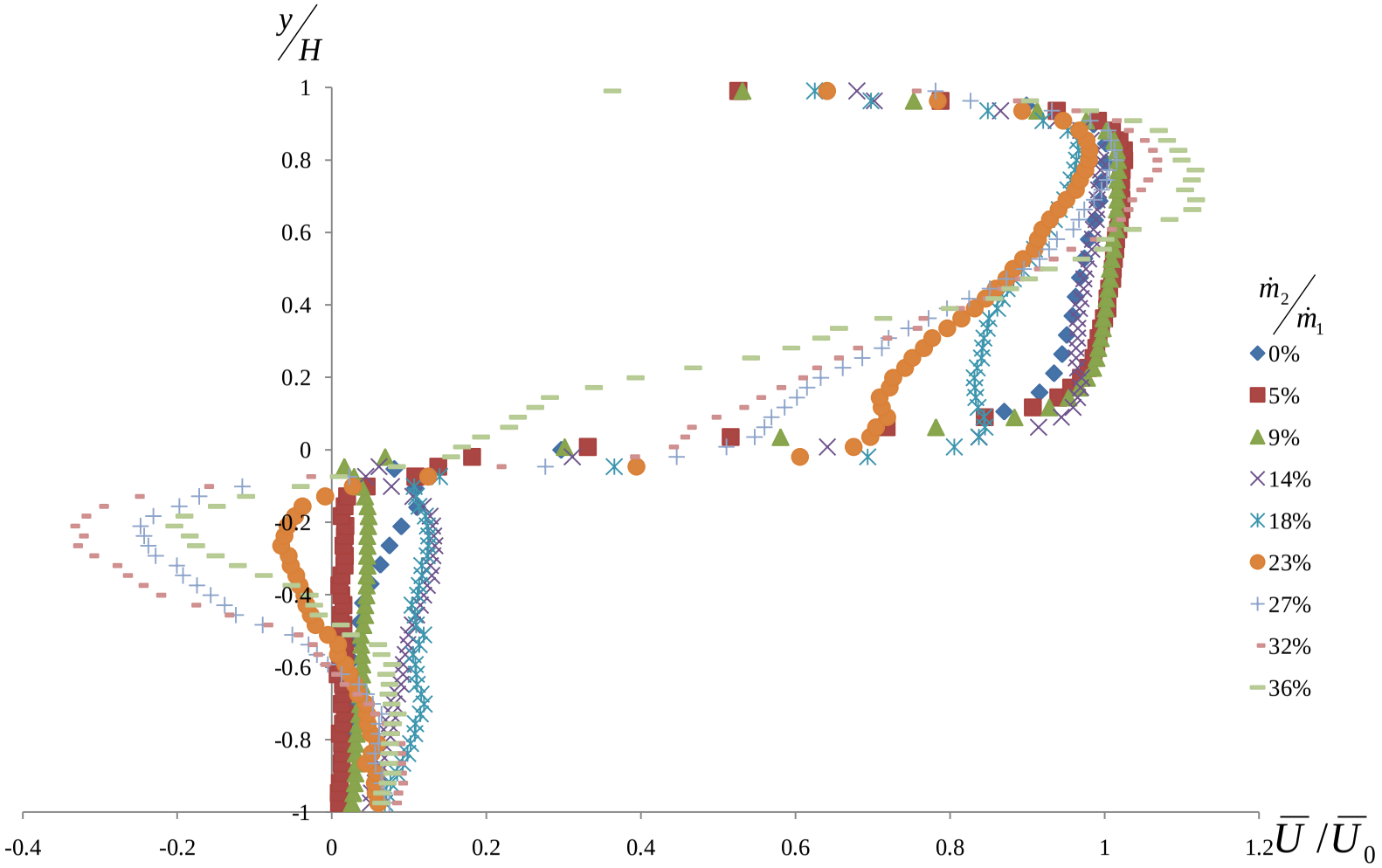

Figure 34: Trailing edge (x/H = 0) mean streamwise velocity profiles for all secondary flow rates

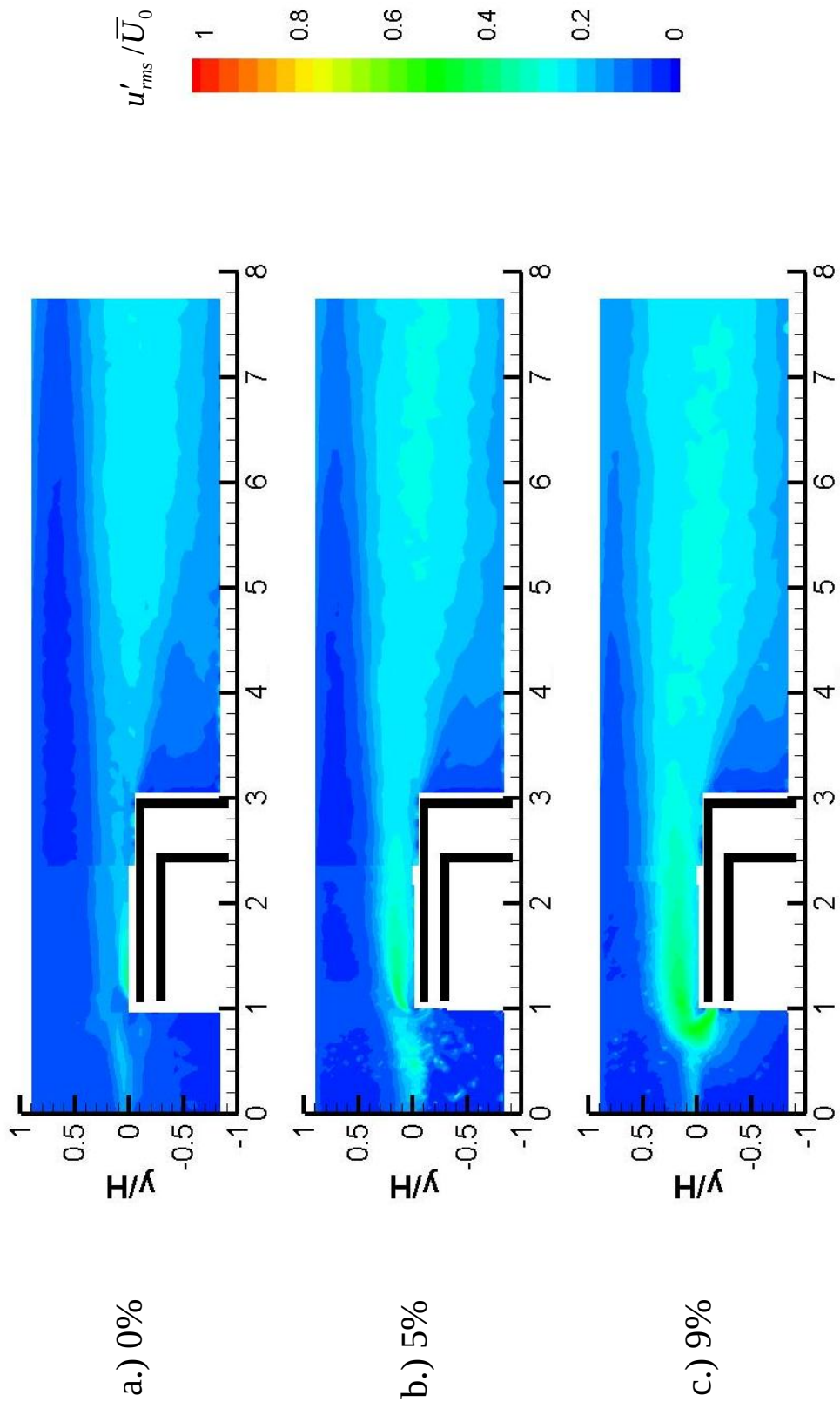

Figure 35 a - c: Rms streamwise velocity fluctuation contours for geometry I at all secondary flow rates

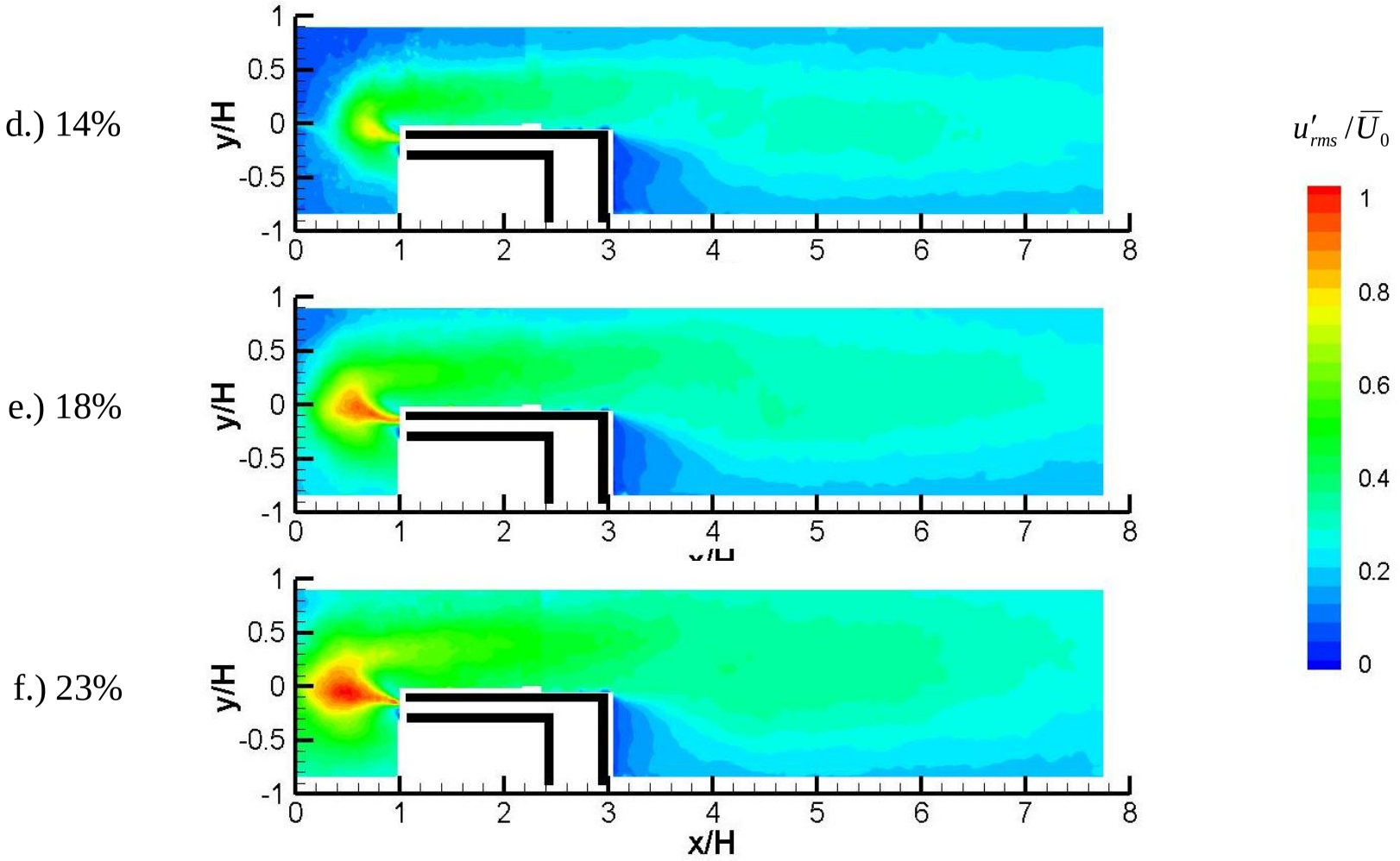

Figure 35 d - f: Rms streamwise velocity fluctuation contours for geometry I at all secondary flow rates

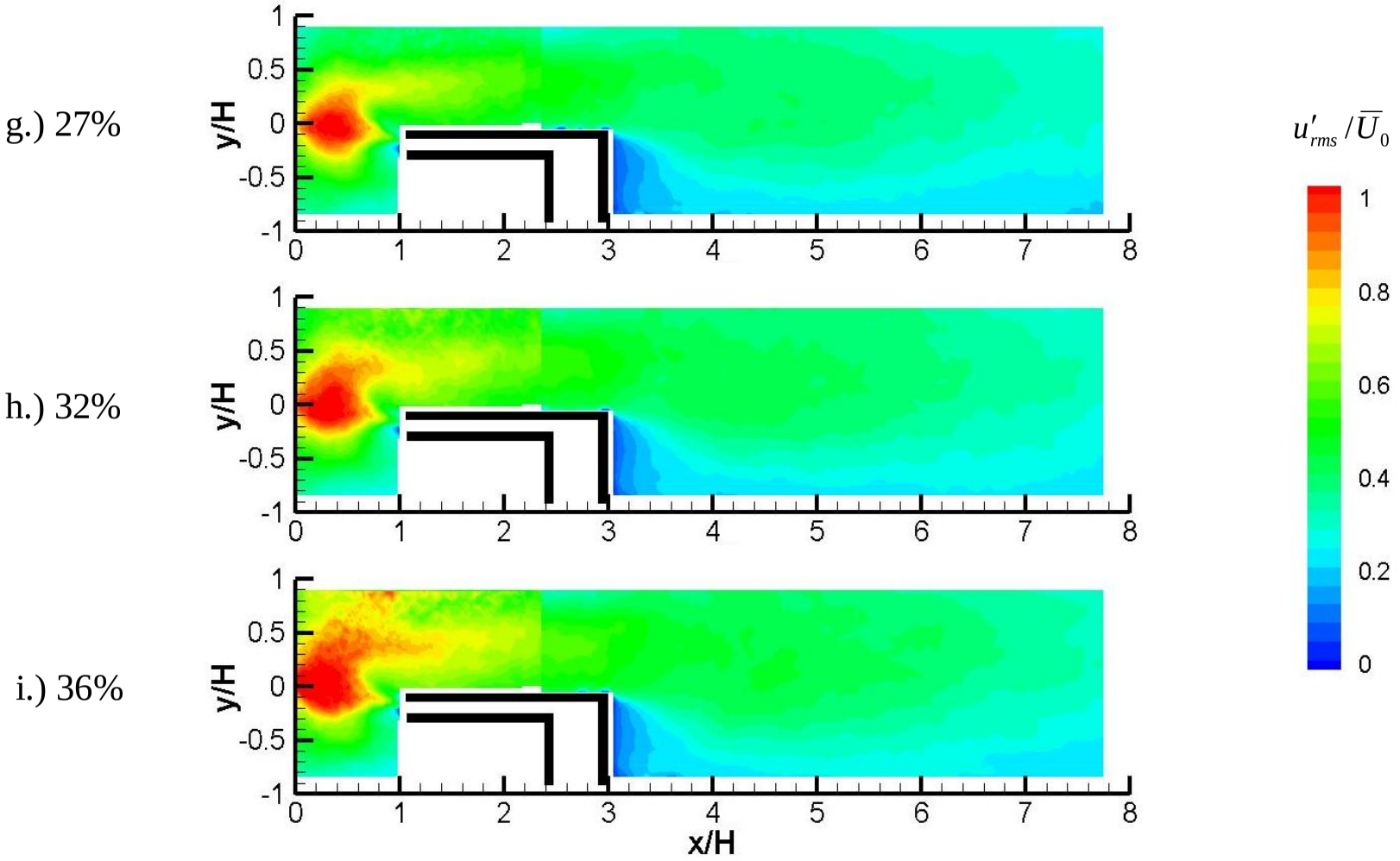

Figure 35 g - i: Rms streamwise velocity fluctuation contours for geometry I at all secondary flow rates

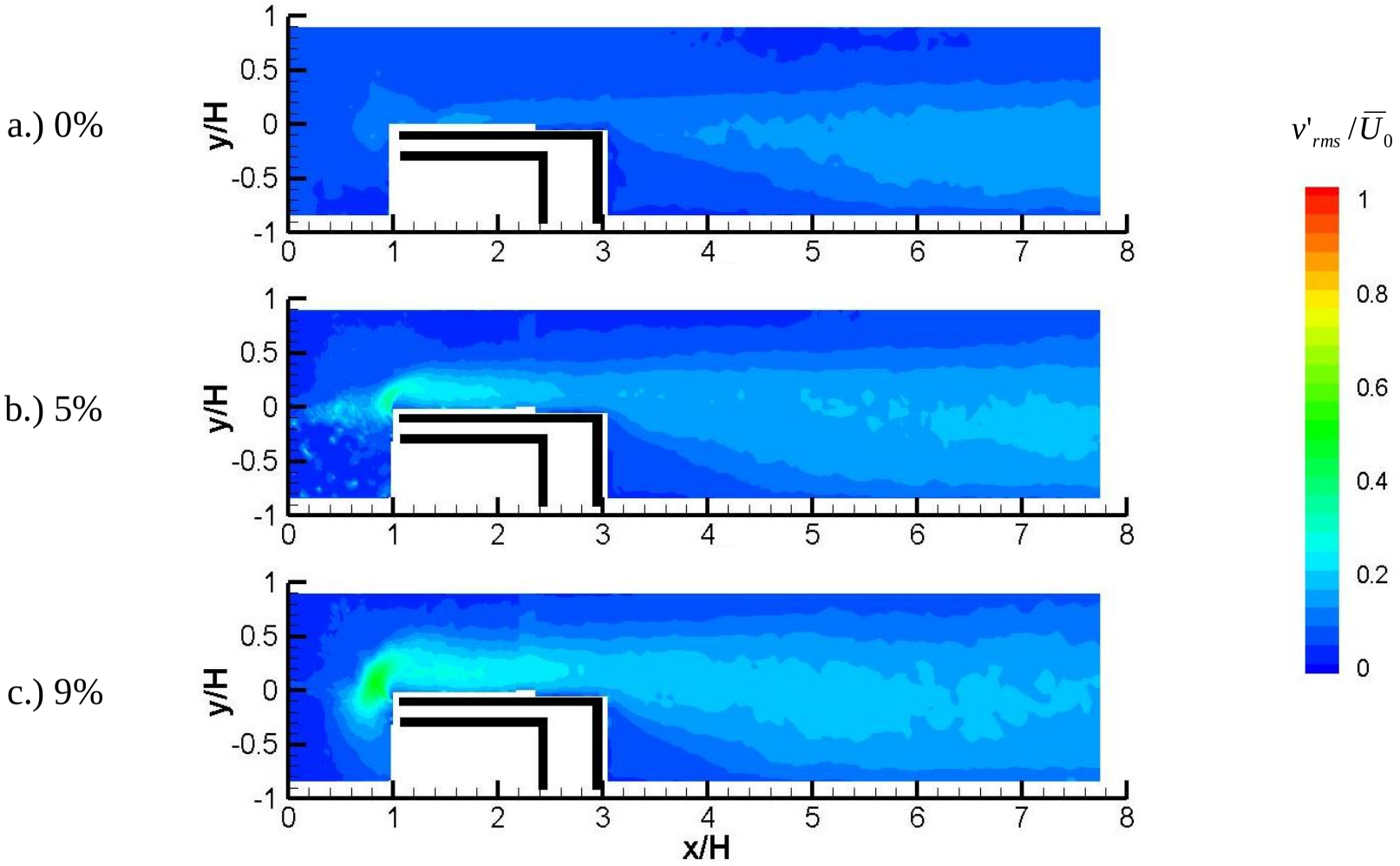

Figure 36 a - c: Rms cross-stream velocity fluctuation contours for geometry I at all secondary flow rates

d.) 14%

e.) 18%

f.) 23%

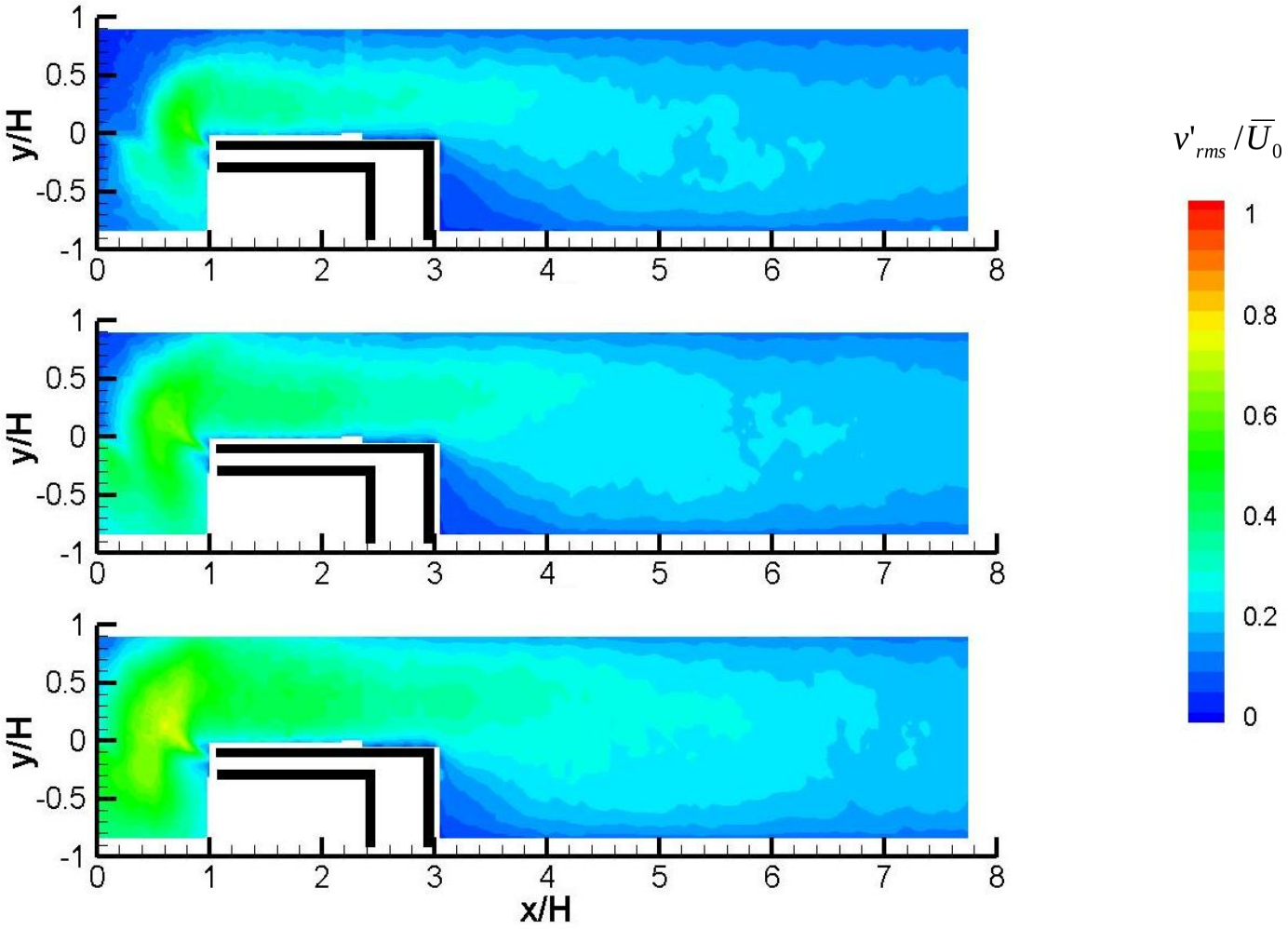

Figure 36 d - f: Rms cross-stream velocity fluctuation contours for geometry I at all secondary flow rates

g.) 27%

h.) 32%

i.) 36%

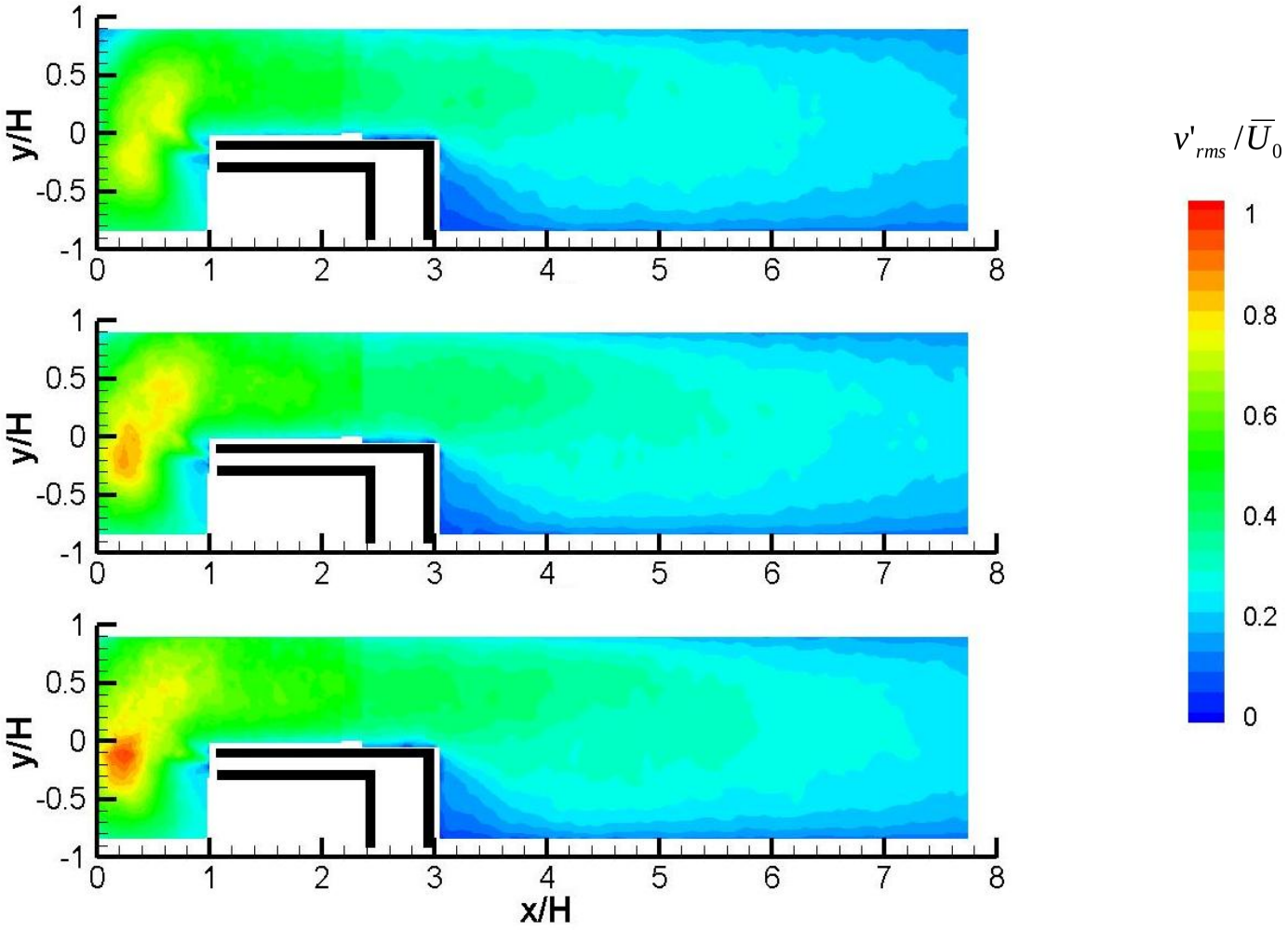

Figure 36 g - i: Rms cross-stream velocity fluctuation contours for geometry I at all secondary flow rates

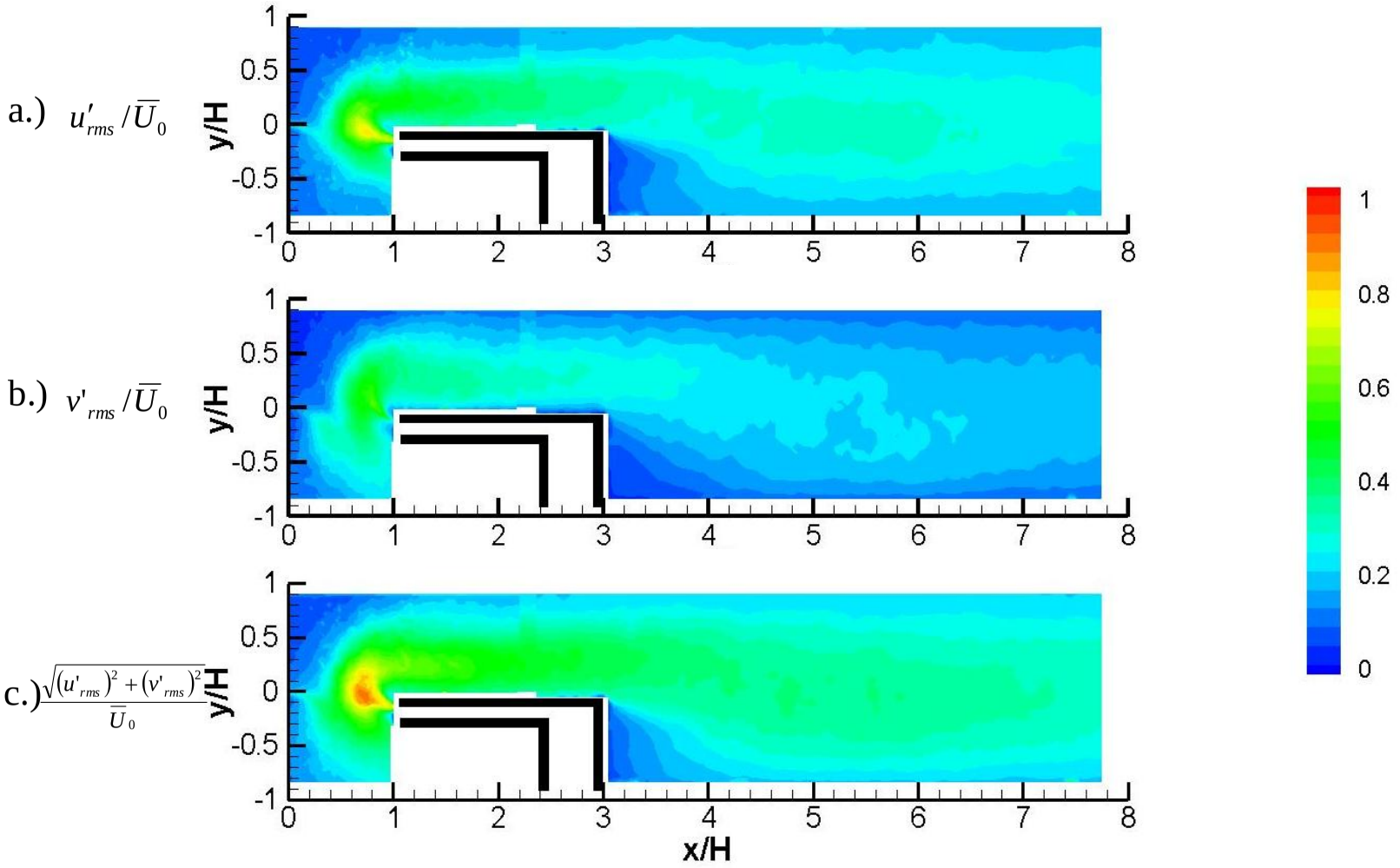

Figure 37: Streamwise, cross-stream and total turbulence for geometry I at 14% secondary flow rate

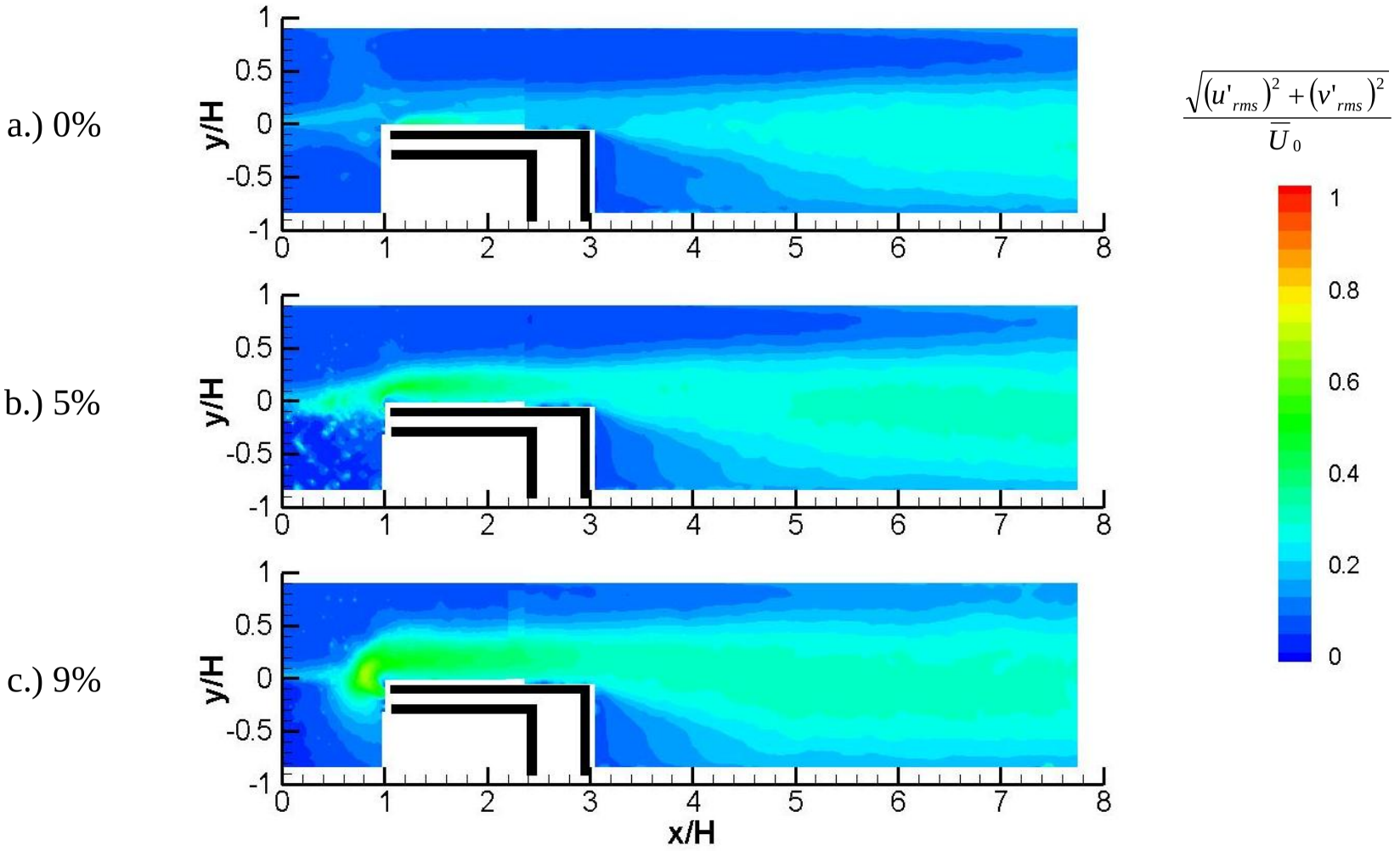

Figure 38 a - c: Total turbulence contours for geometry I at all secondary flow rates

d.) 14%

e.) 18%

f.) 23%

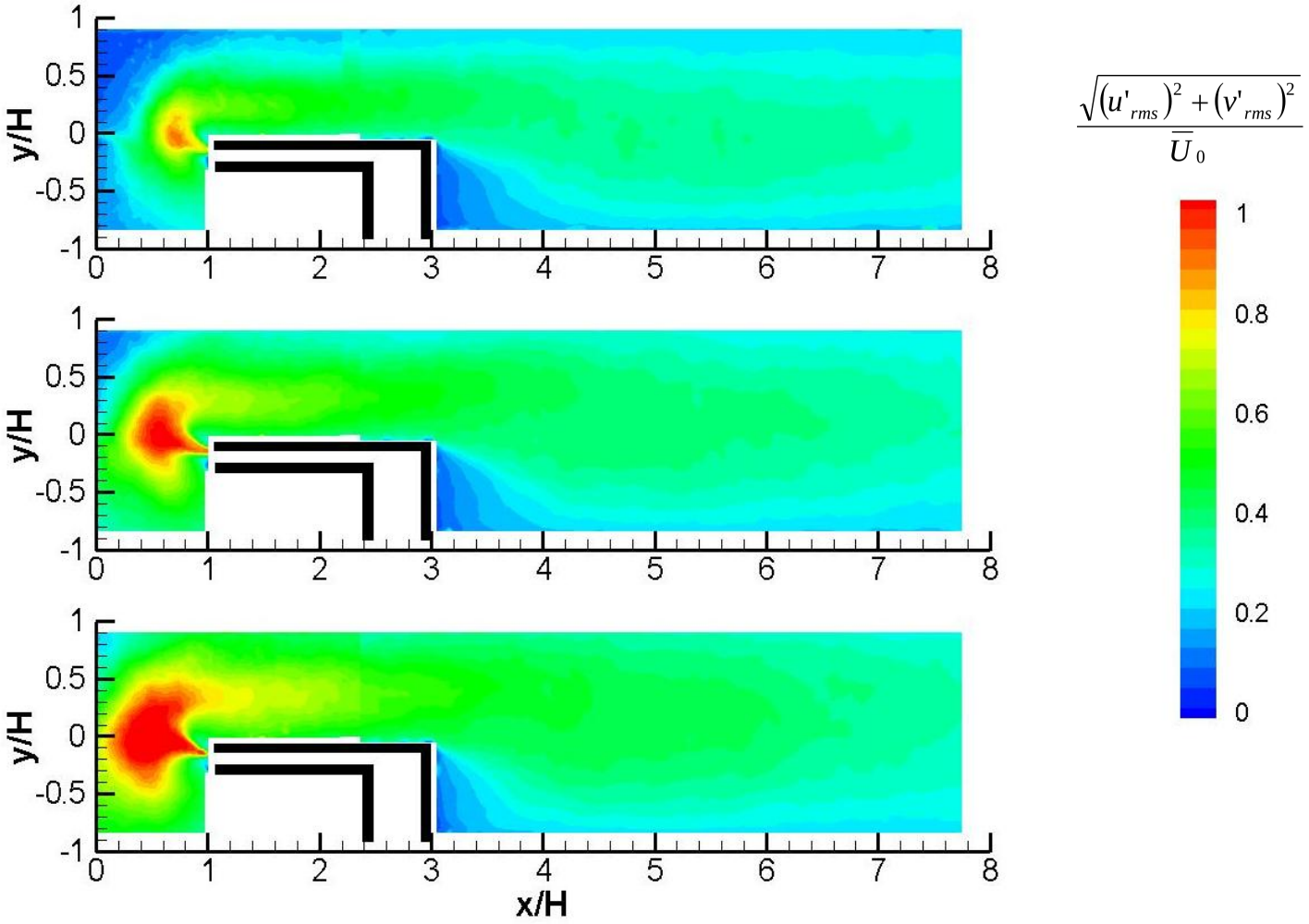

Figure 38 d - f: Total turbulence contours for geometry I at all secondary flow rates

g.) 27%

h.) 32%

i.) 36%

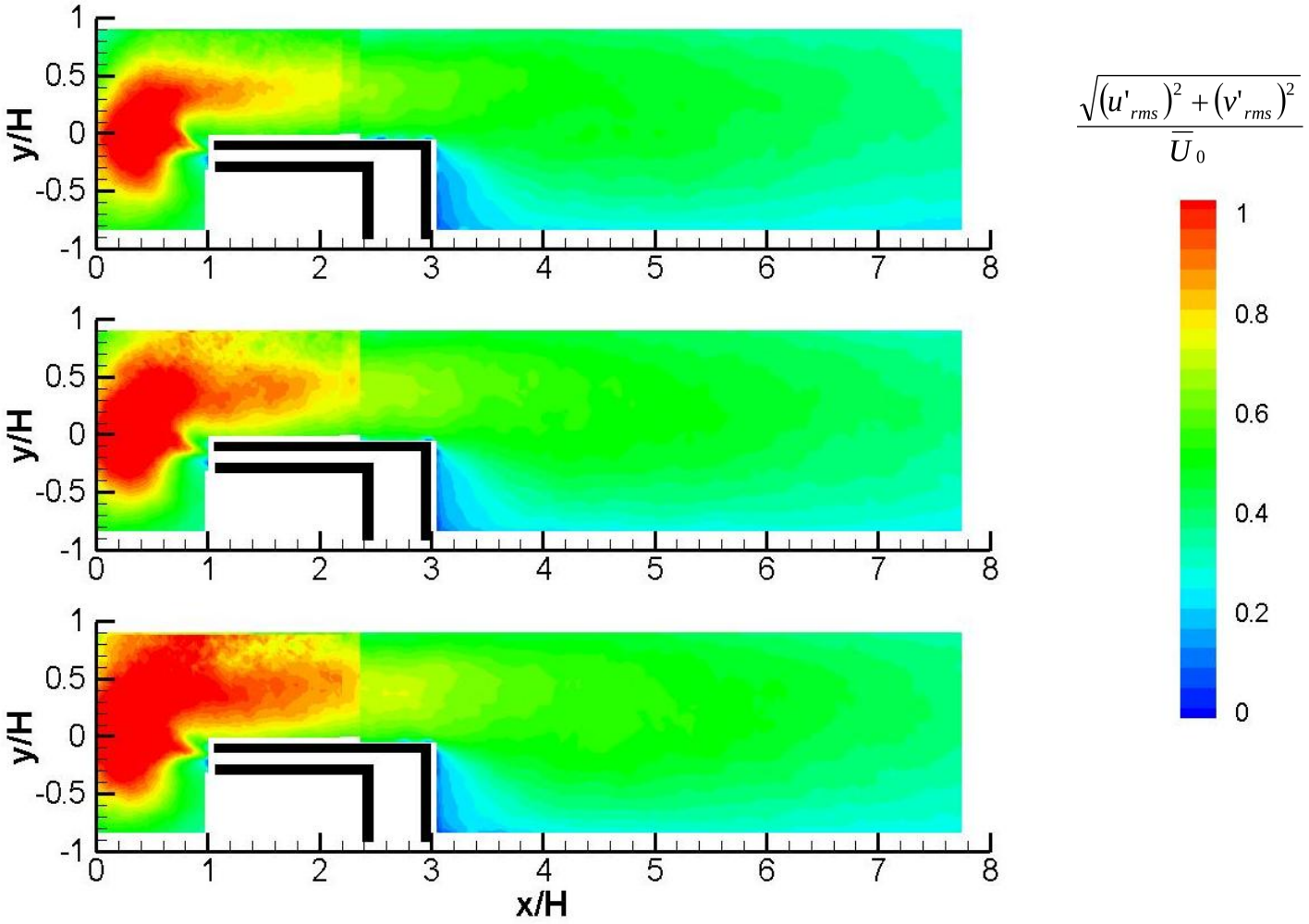

Figure 38 g - i: Total turbulence contours for the closed facility at all secondary flow rates

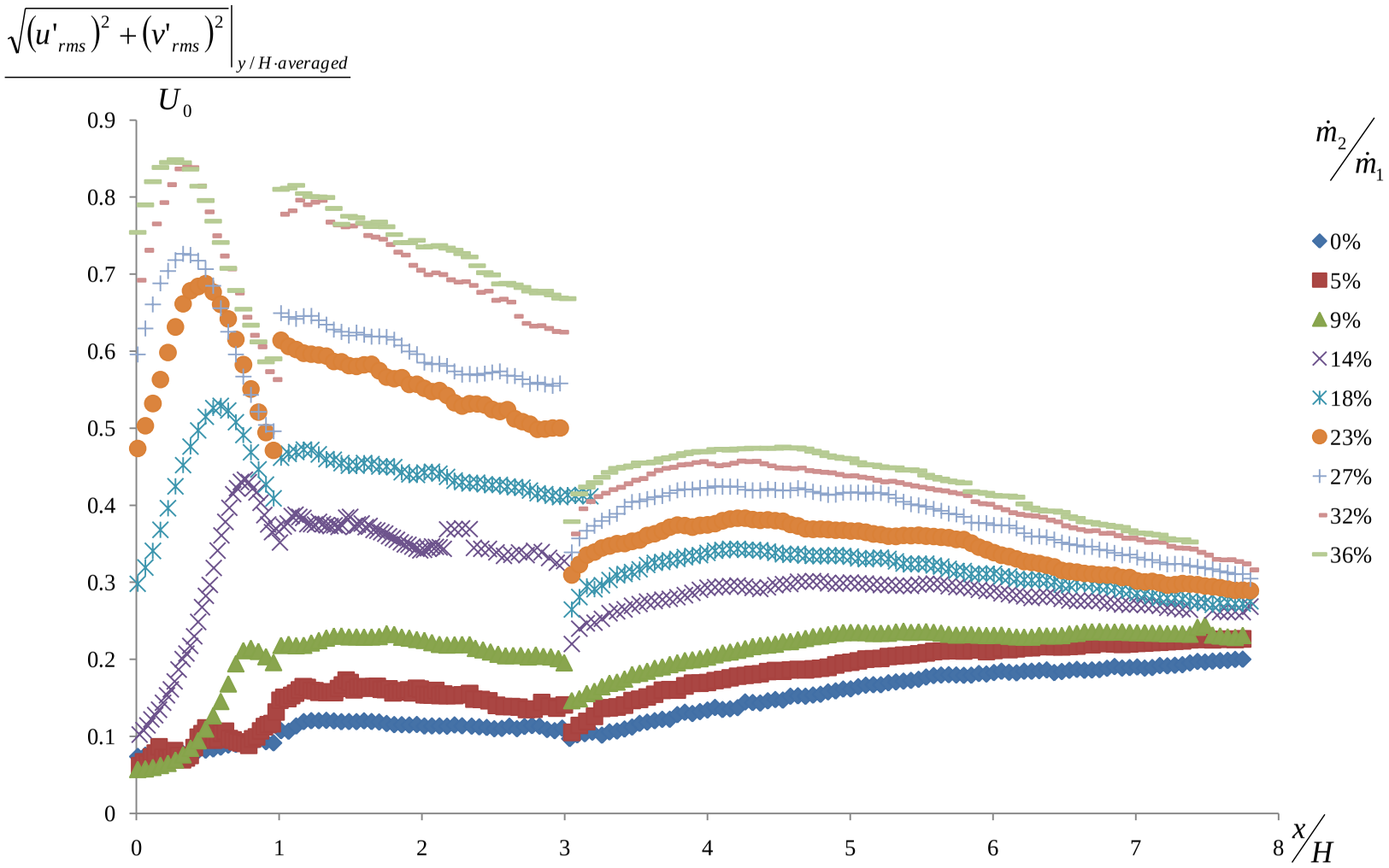

Figure 39: Cross-stream averaged total turbulence for geometry I

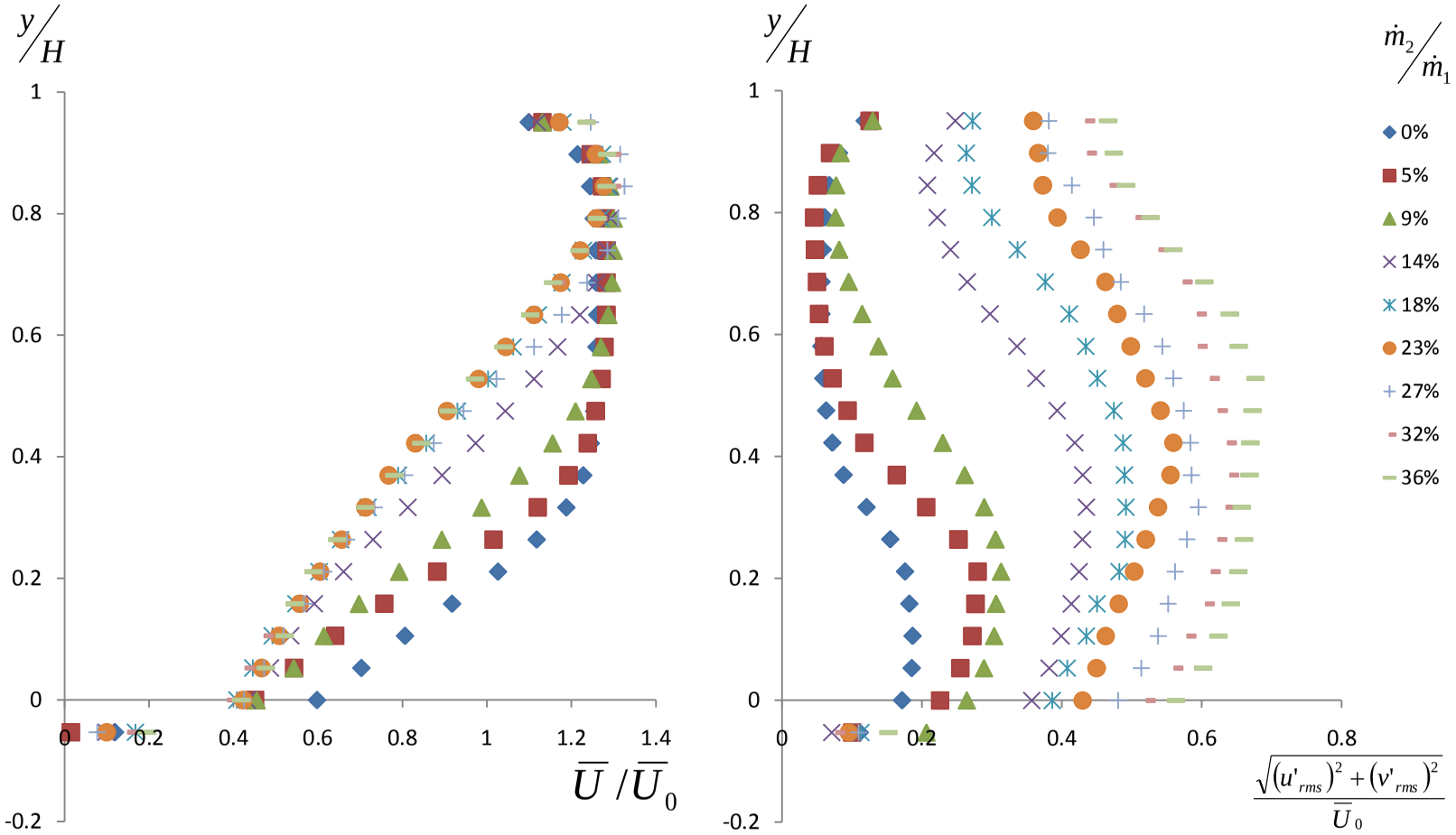

a.) Mean streamwise velocity profiles

b.) Total turbulence profiles

Figure 40: Velocity profiles at x/H = 3 for geometry I at all secondary flow rates

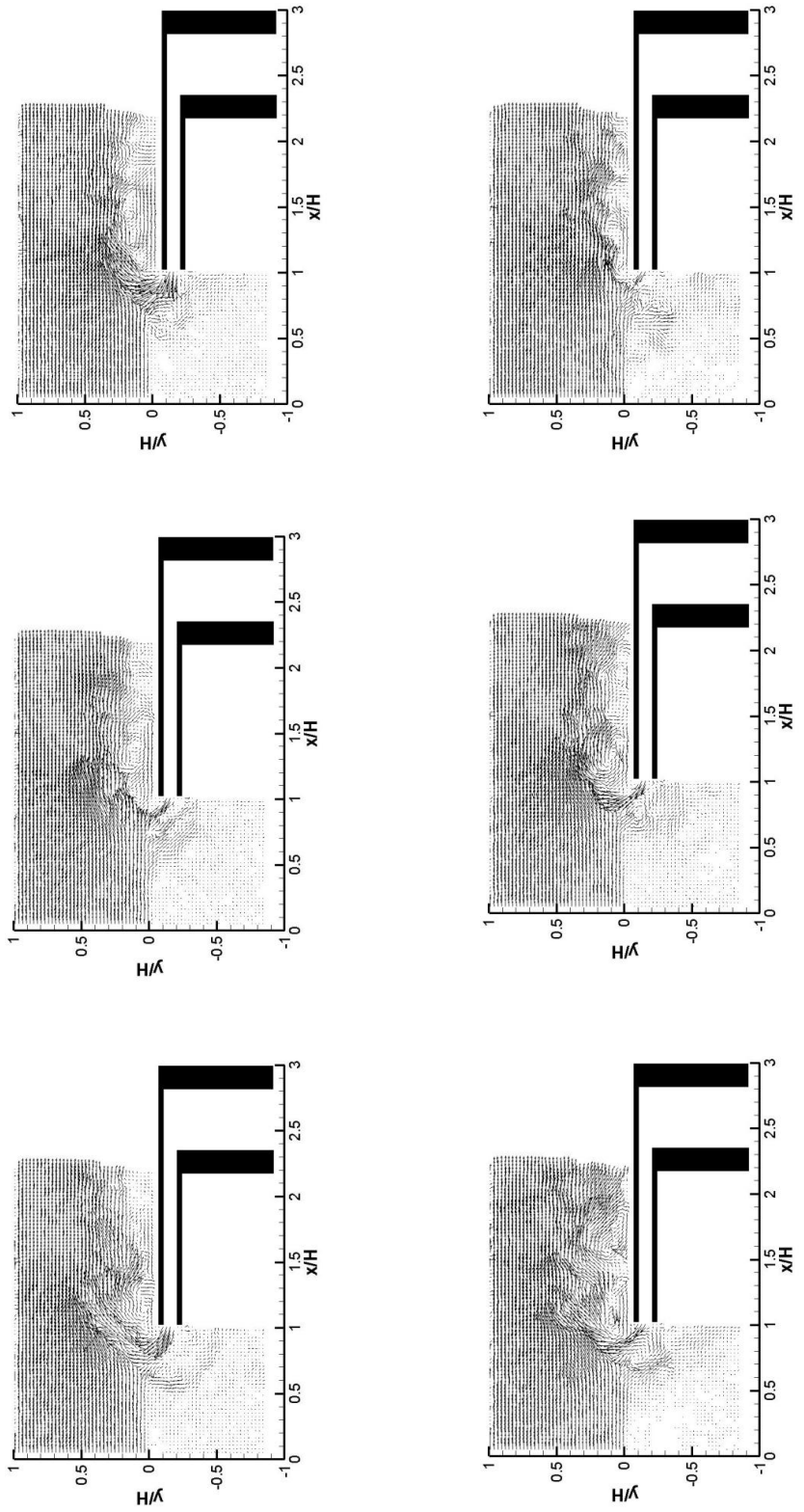

Figure 41: Instantaneous velocity vector fields for low (9%) secondary flow rate

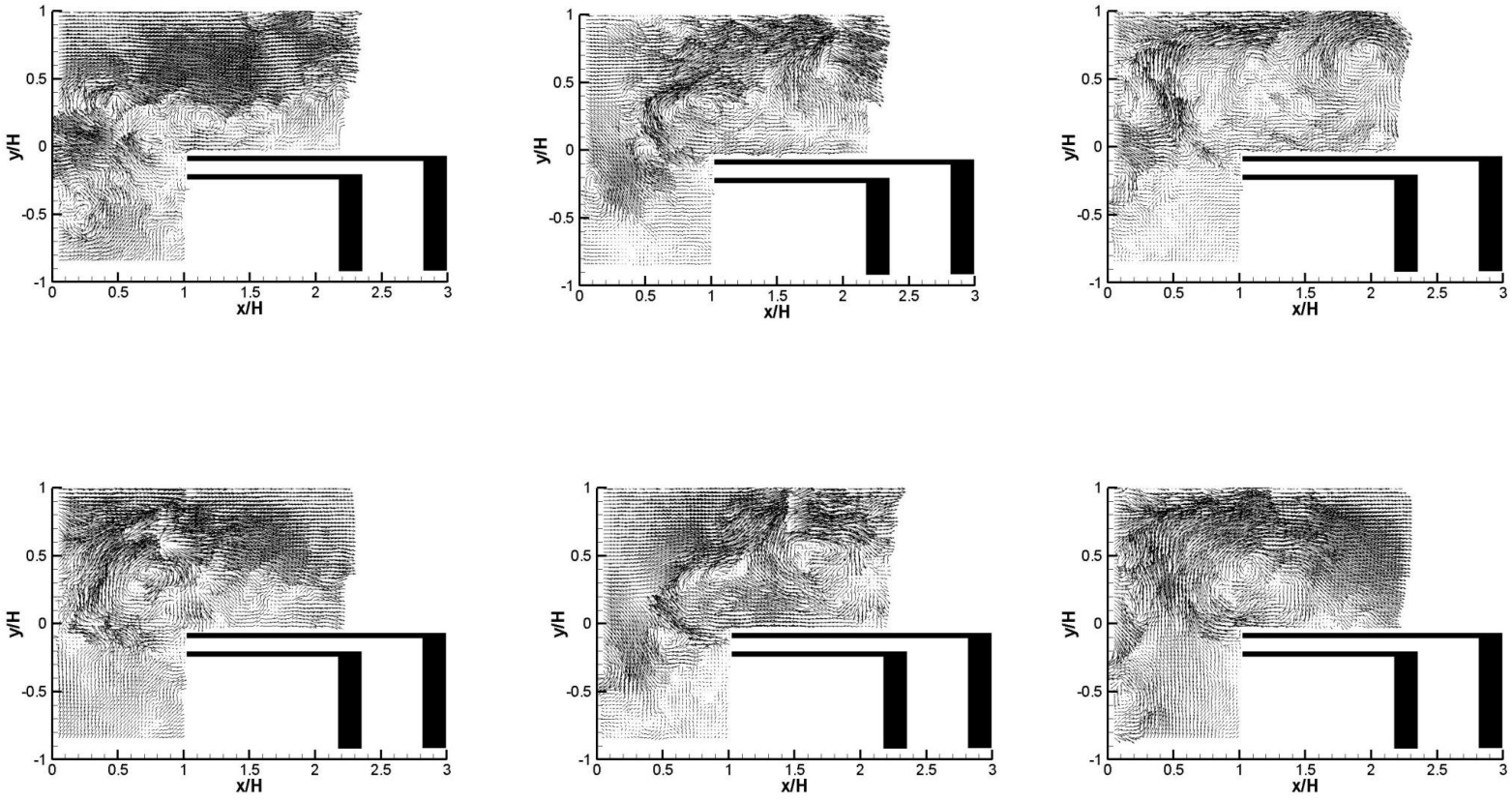

Figure 42: Instantaneous velocity vector fields for high (32%) secondary flow rate

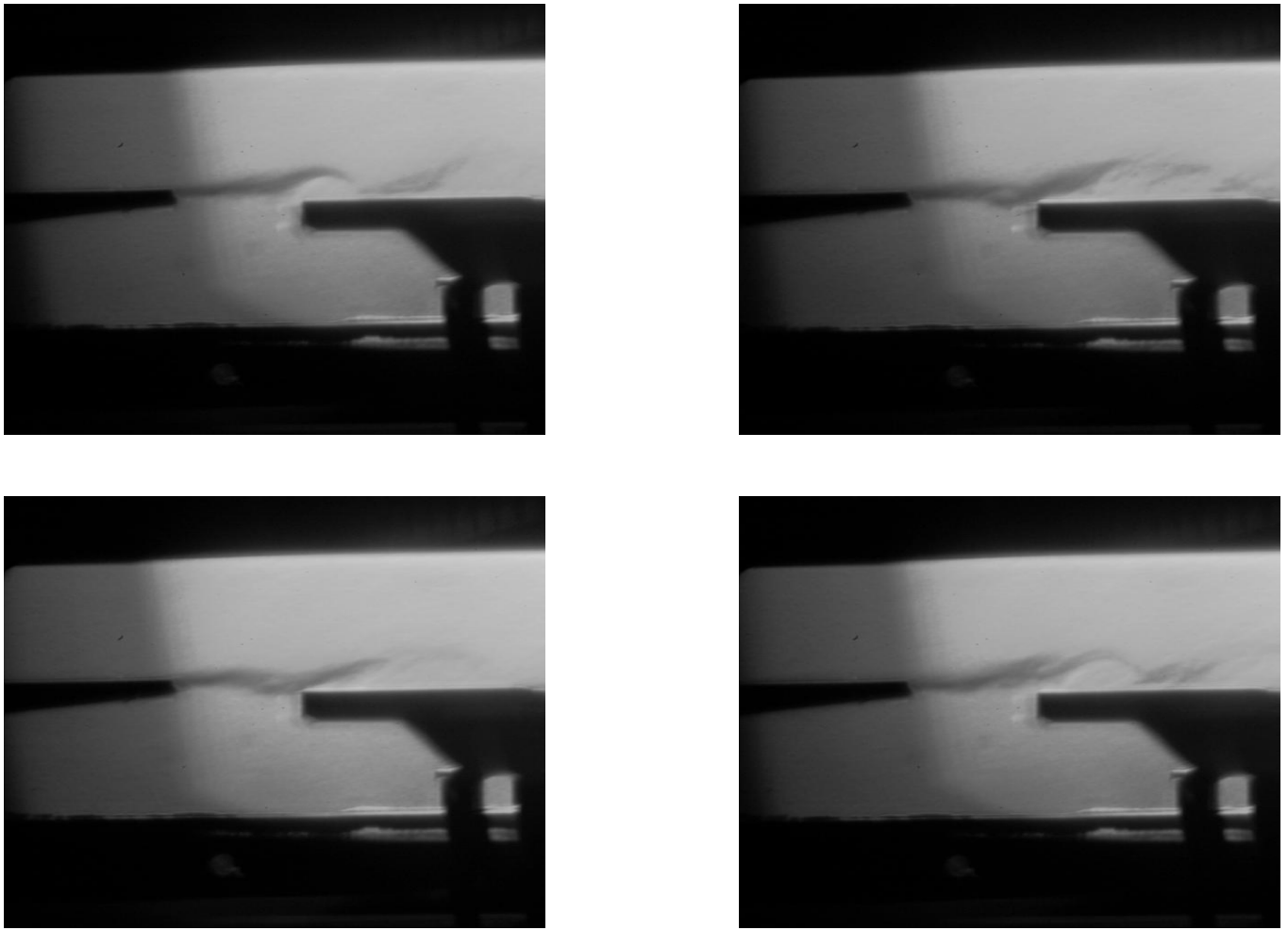

Figure 43: Instantaneous Schlieren images for baseline case (0%)

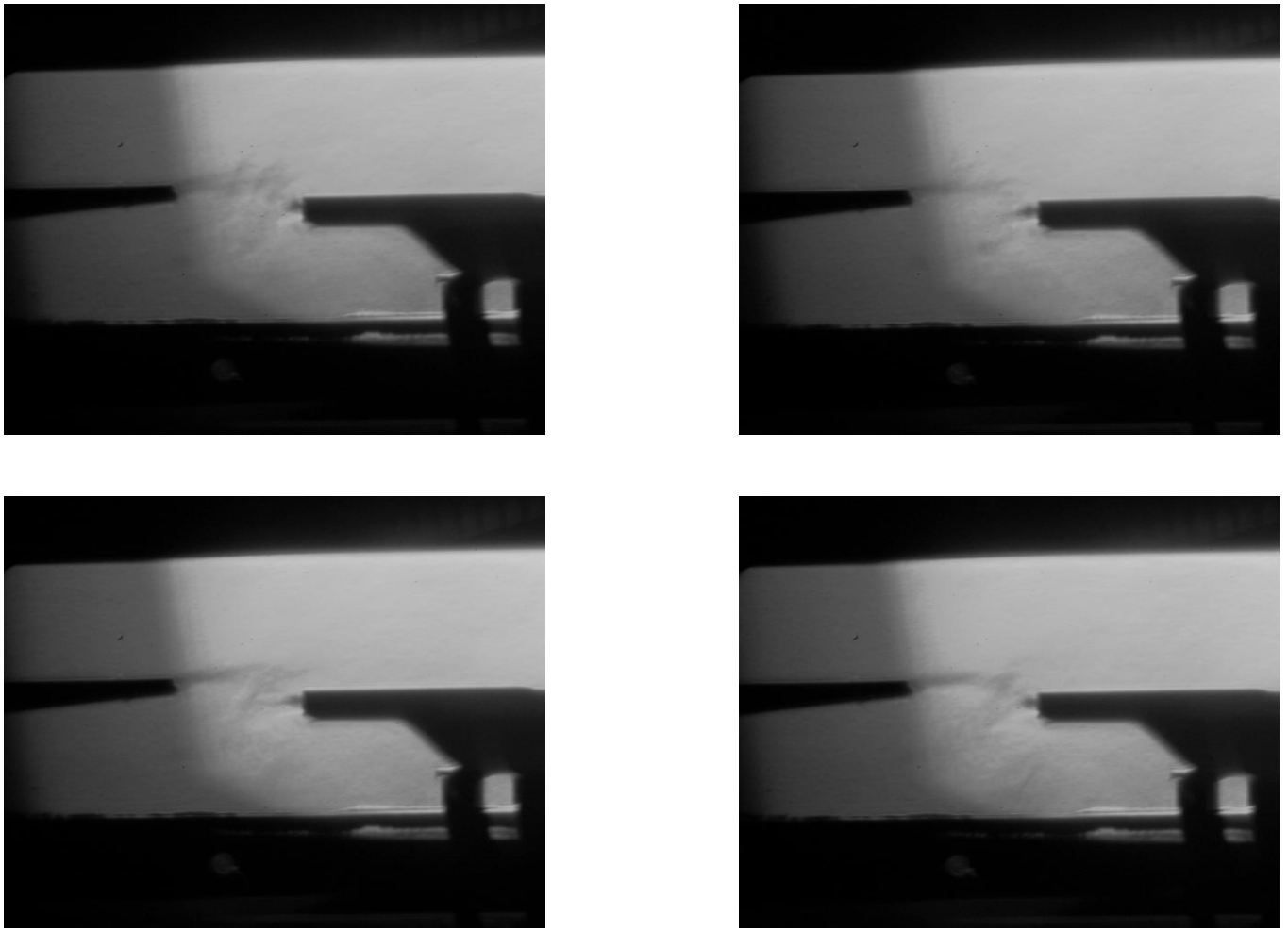

Figure 44: Instantaneous Schlieren images for 9% case

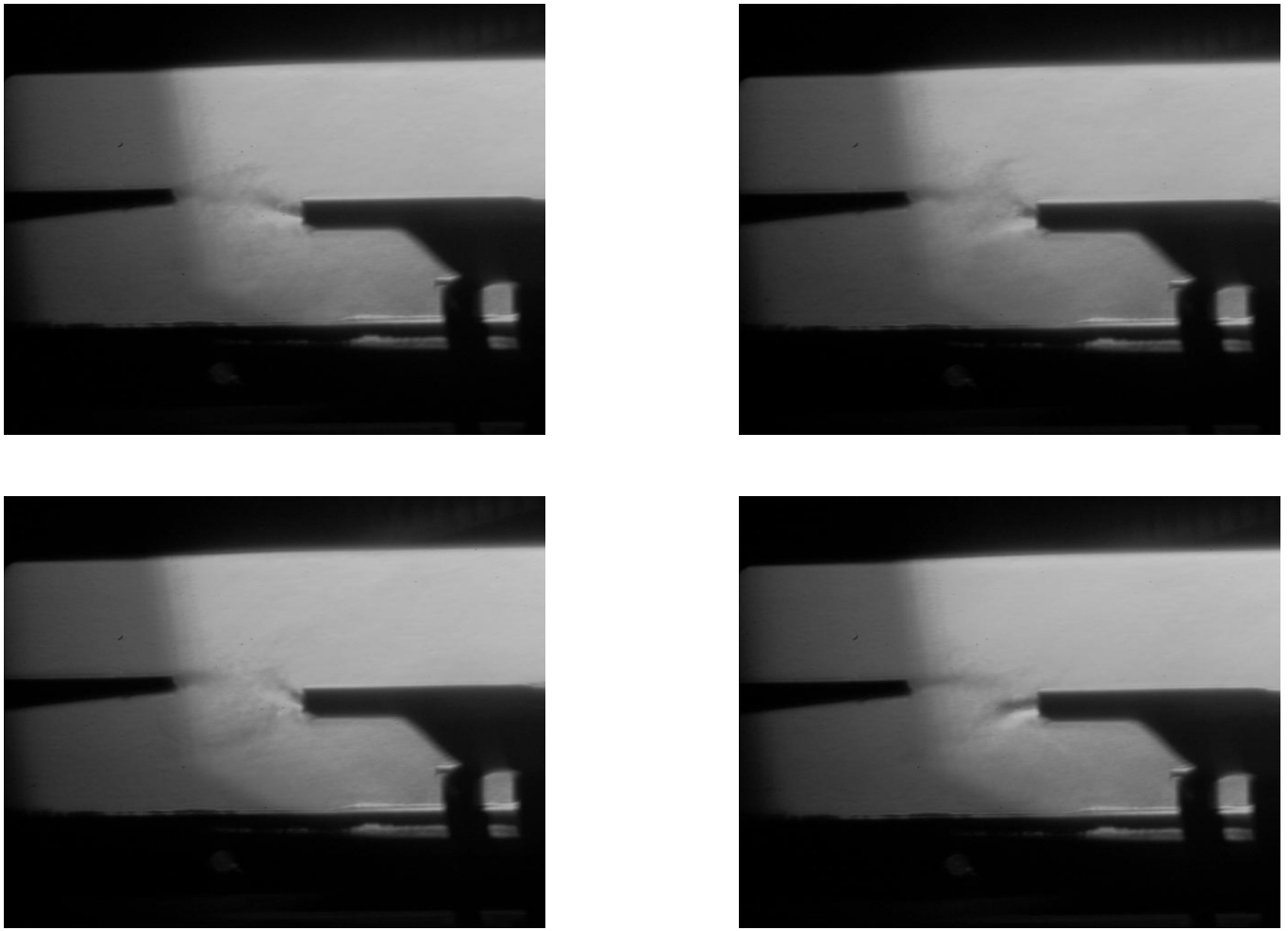

Figure 45: Instantaneous Schlieren images for 14% case

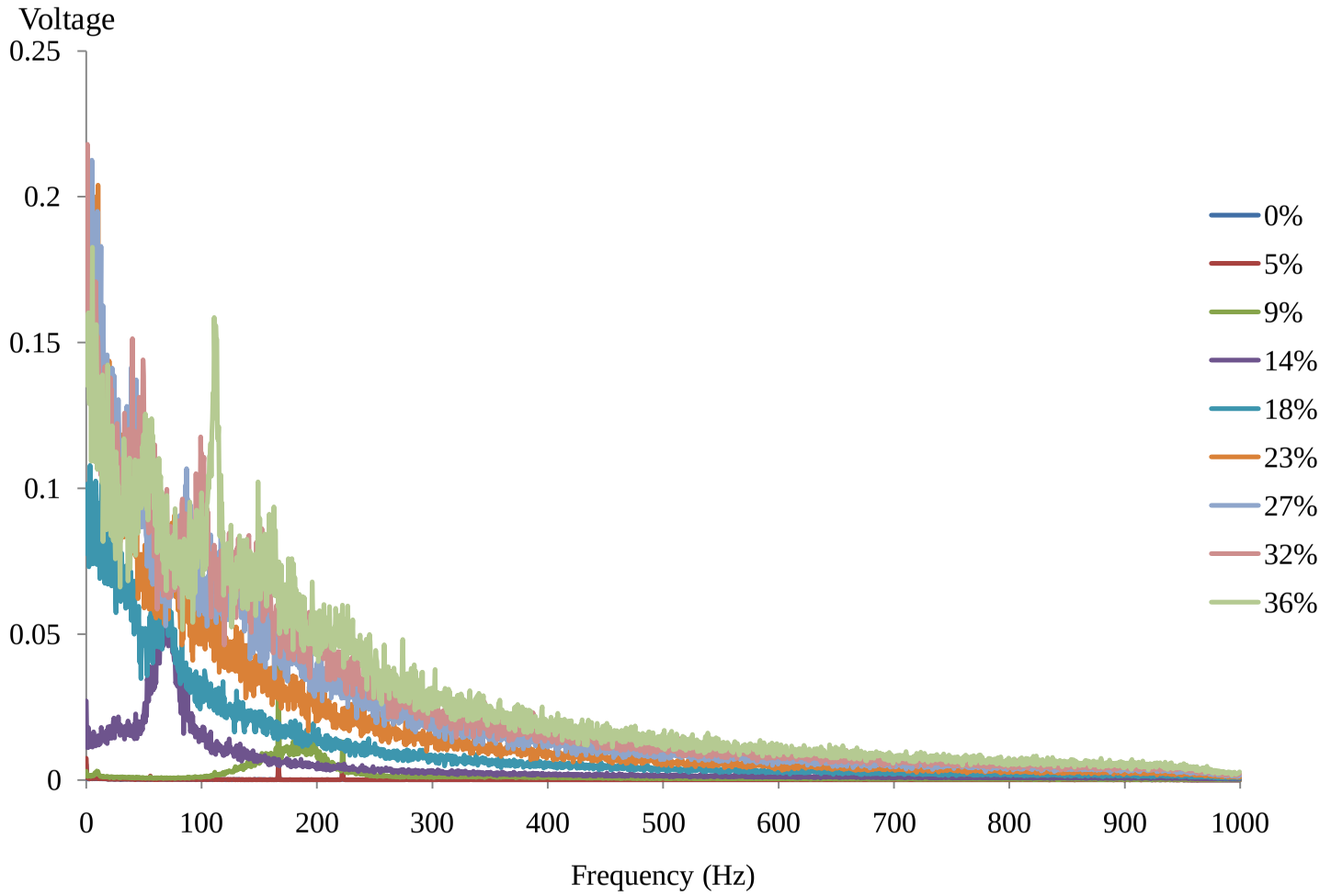

Figure 46: Spectral distribution in geometry I for all secondary flow rates

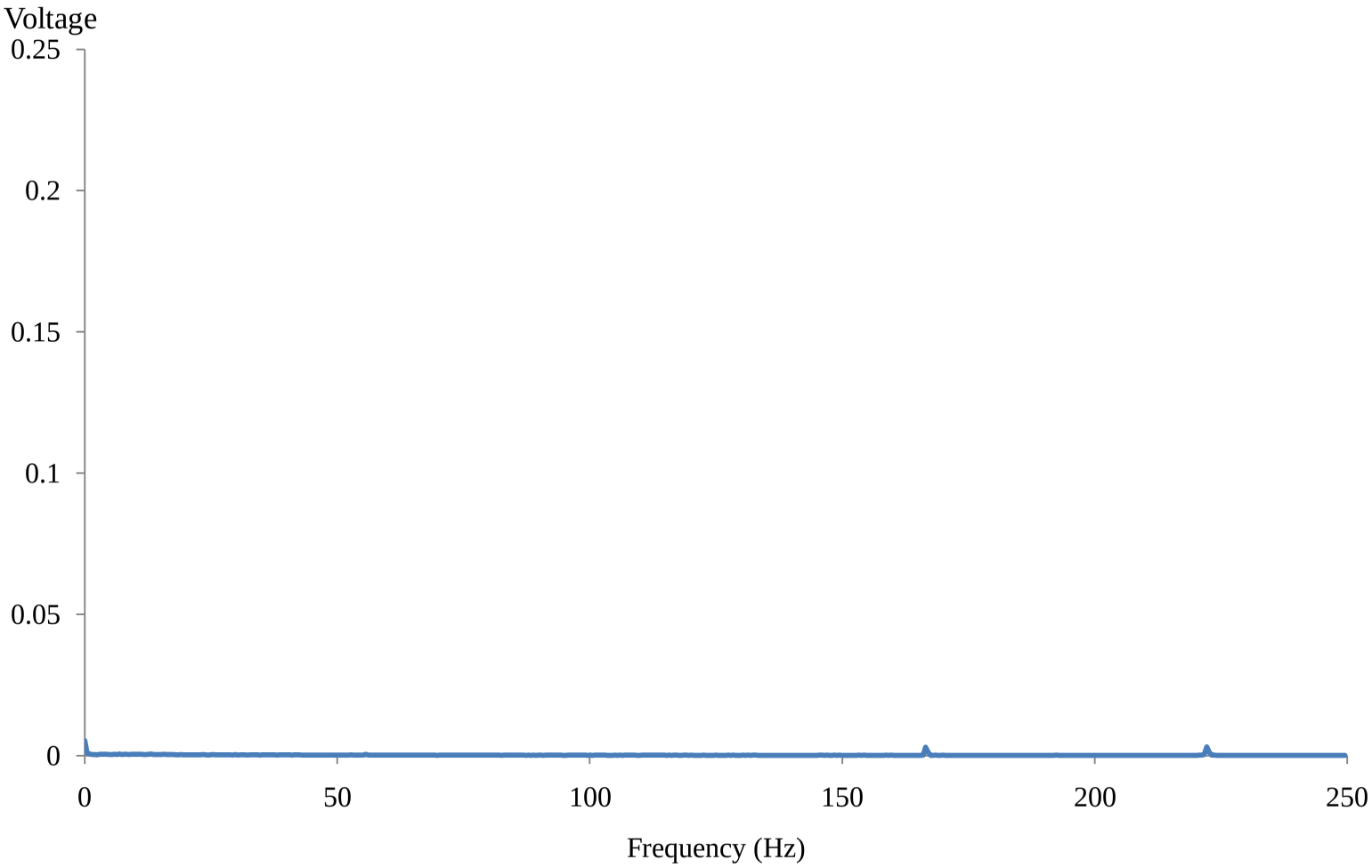

Figure 47: Spectral distributions in geometry I
a.) 0% secondary flow rate

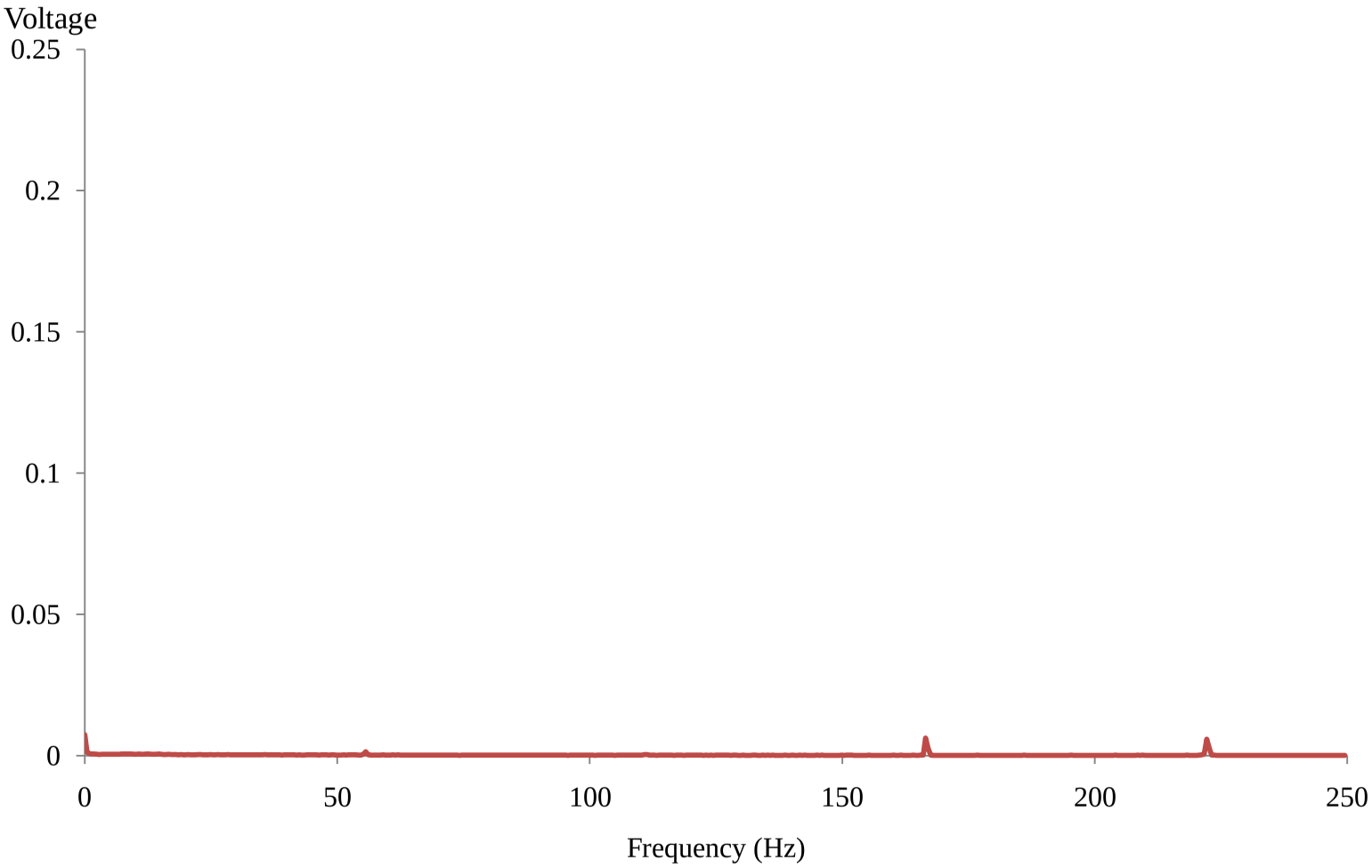

Figure 47: Spectral distributions in geometry I
b.) 5% secondary flow rate

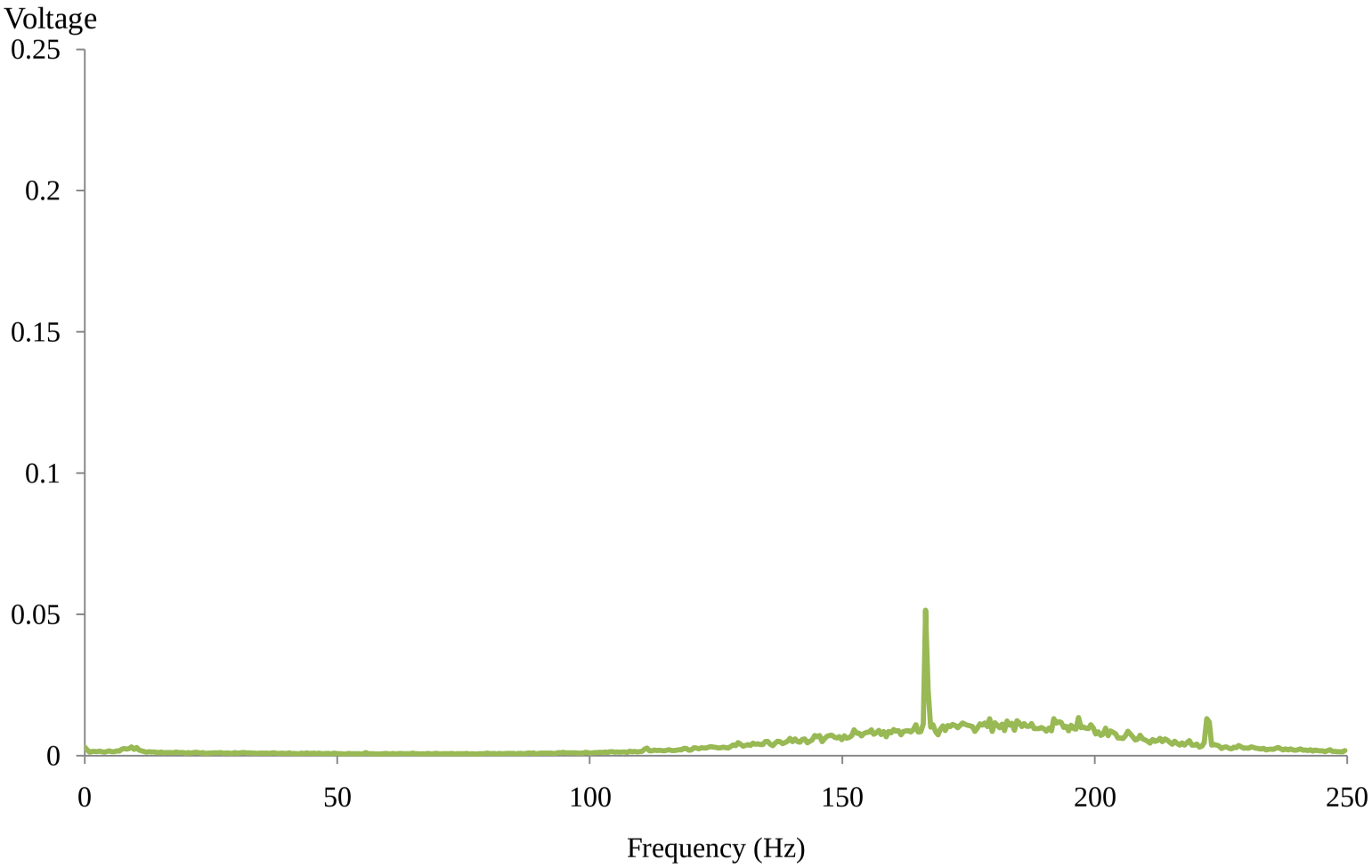

Figure 47 : Spectral distributions in geometry I
c.) 9% secondary flow rate

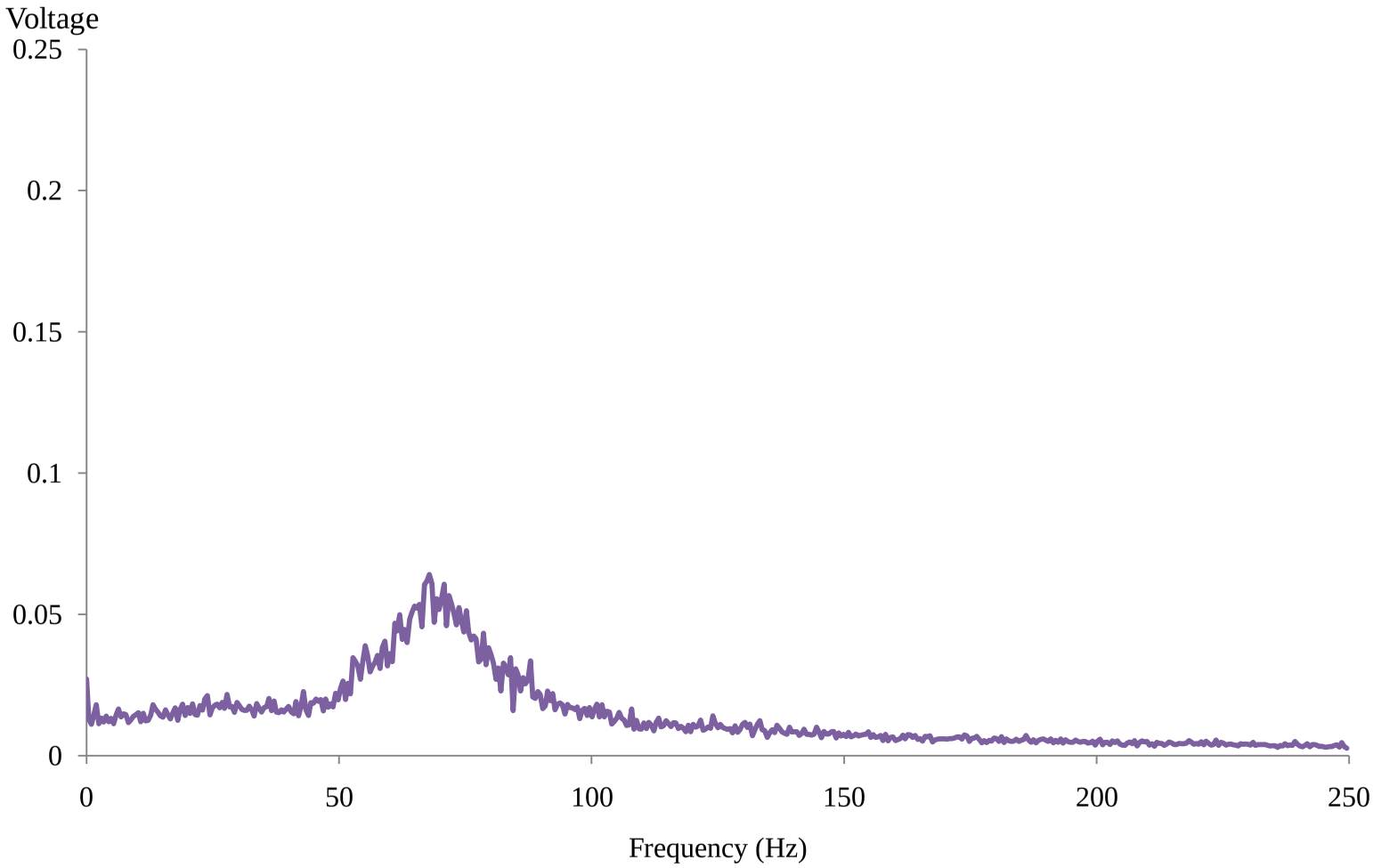

Figure 47 : Spectral distributions in geometry I
d.) 14% secondary flow rate

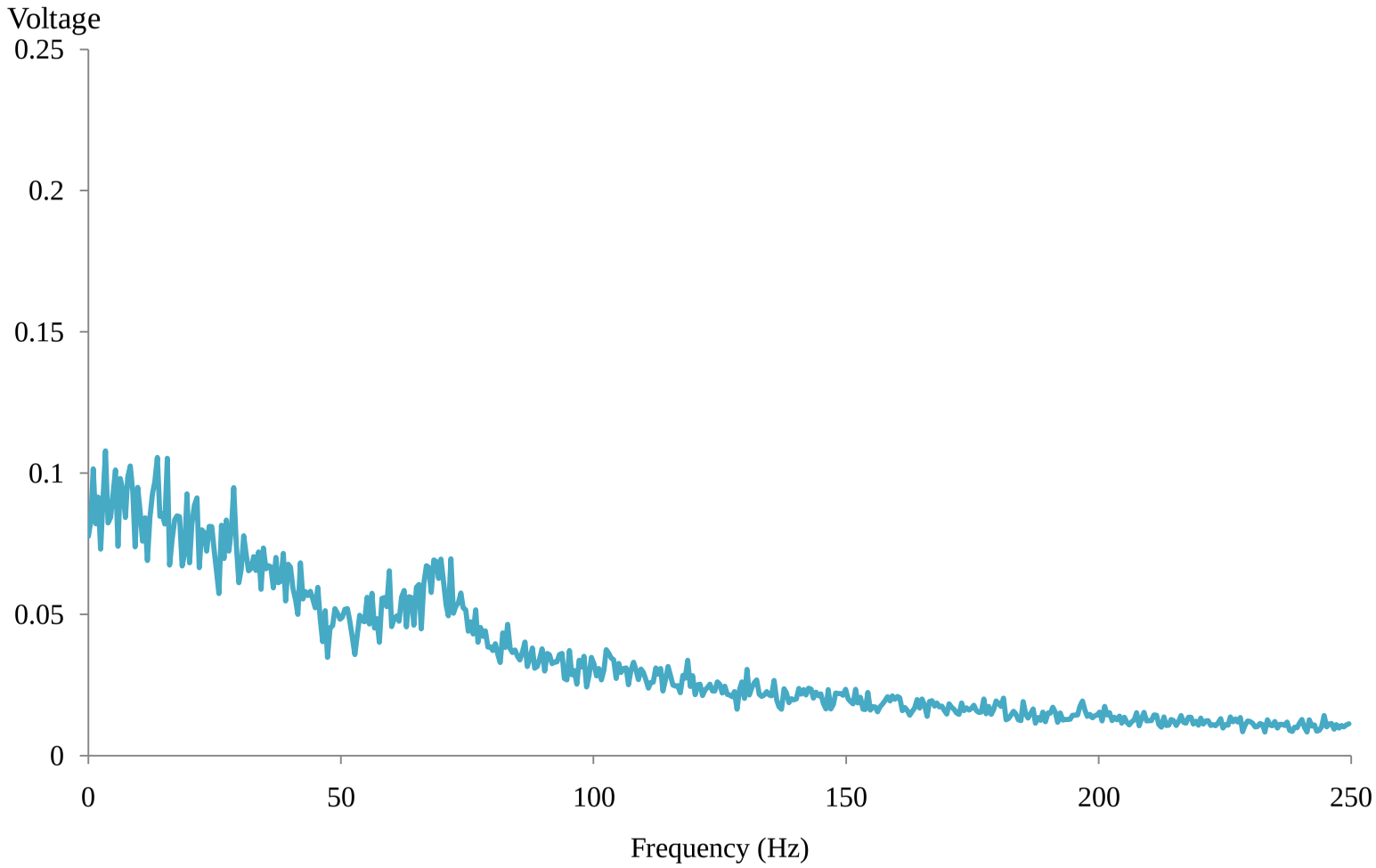

Figure 47 : Spectral distributions in geometry I
e.) 18% secondary flow rate

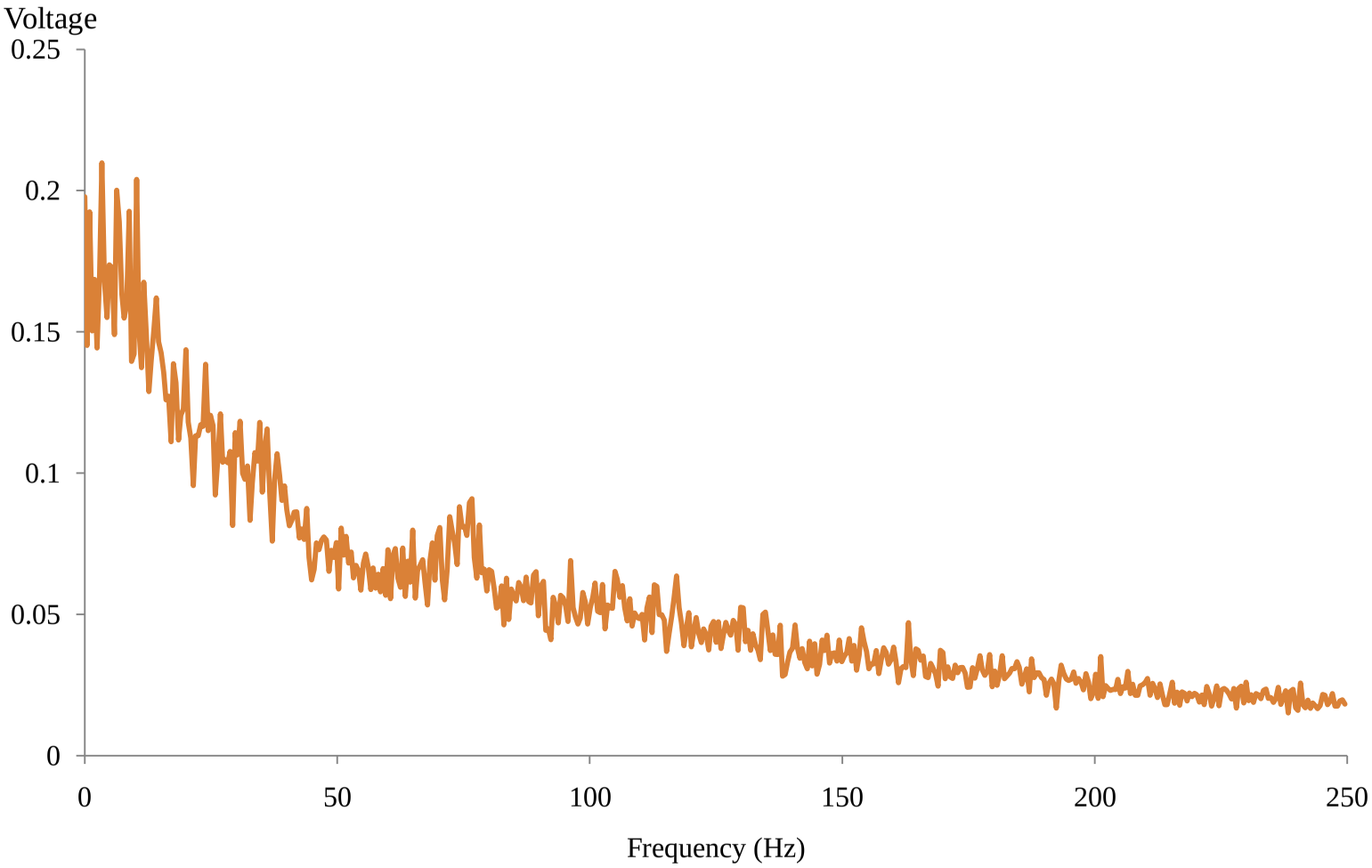

Figure 47 : Spectral distributions in geometry I
f.) 23% secondary flow rate

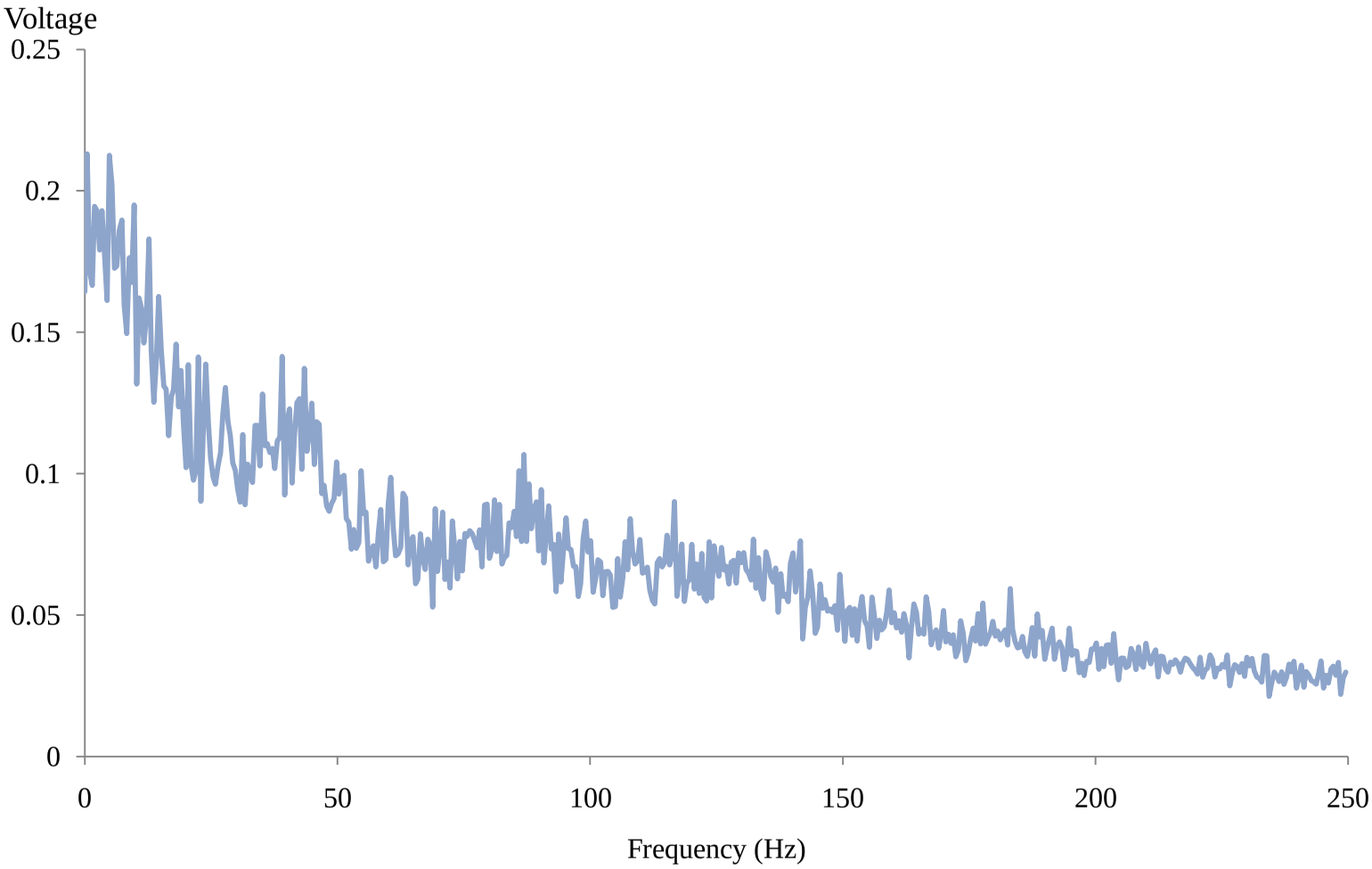

Figure 47 : Spectral distributions in geometry I
g.) 27% secondary flow rate

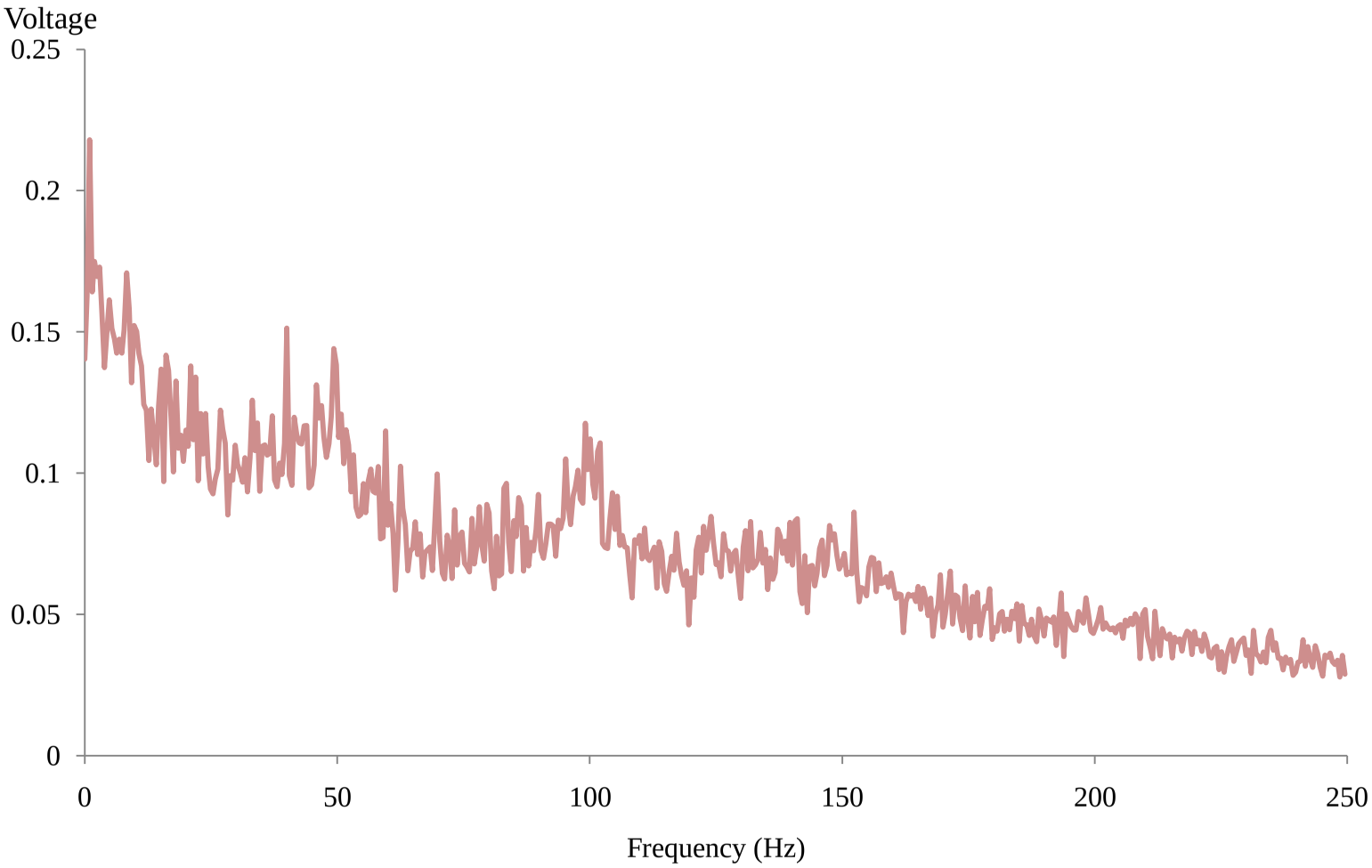

Figure 47 : Spectral distributions in geometry I
h.) 32% secondary flow rate

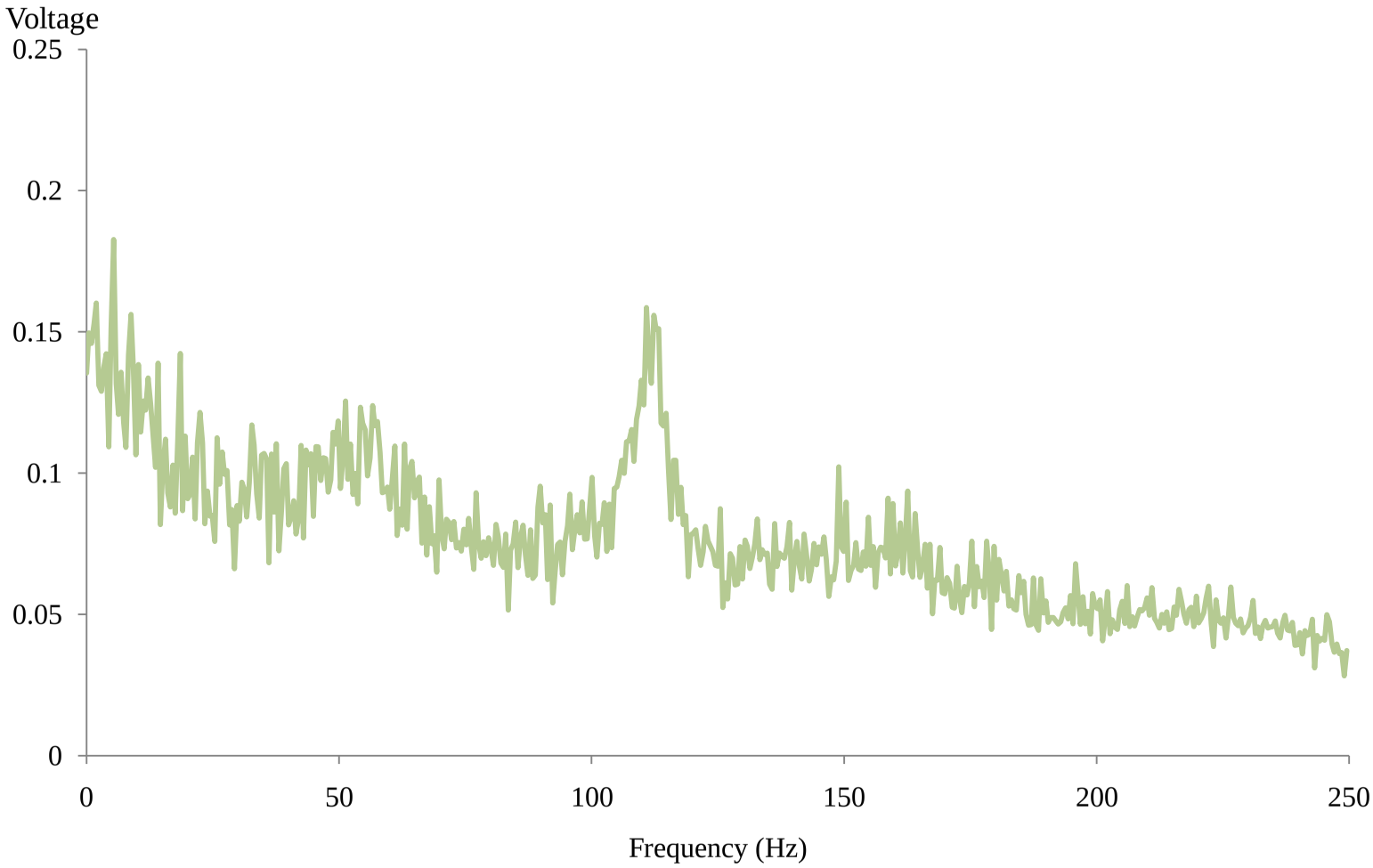

Figure 47 : Spectral distributions in geometry I
i.) 36% secondary flow rate

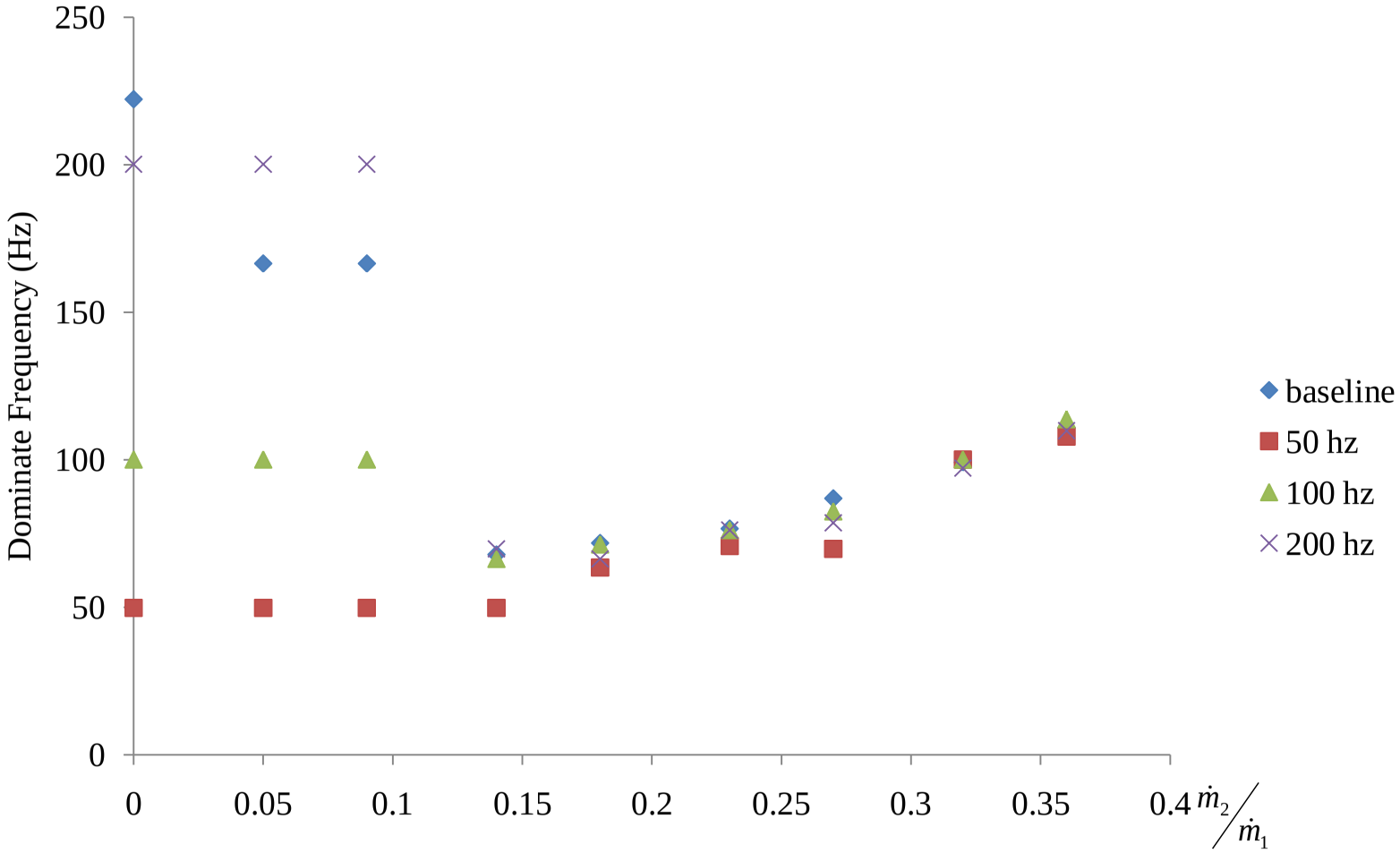

Figure 48: Dominate frequency flow response vs. secondary flow rate for varied inlet forcing

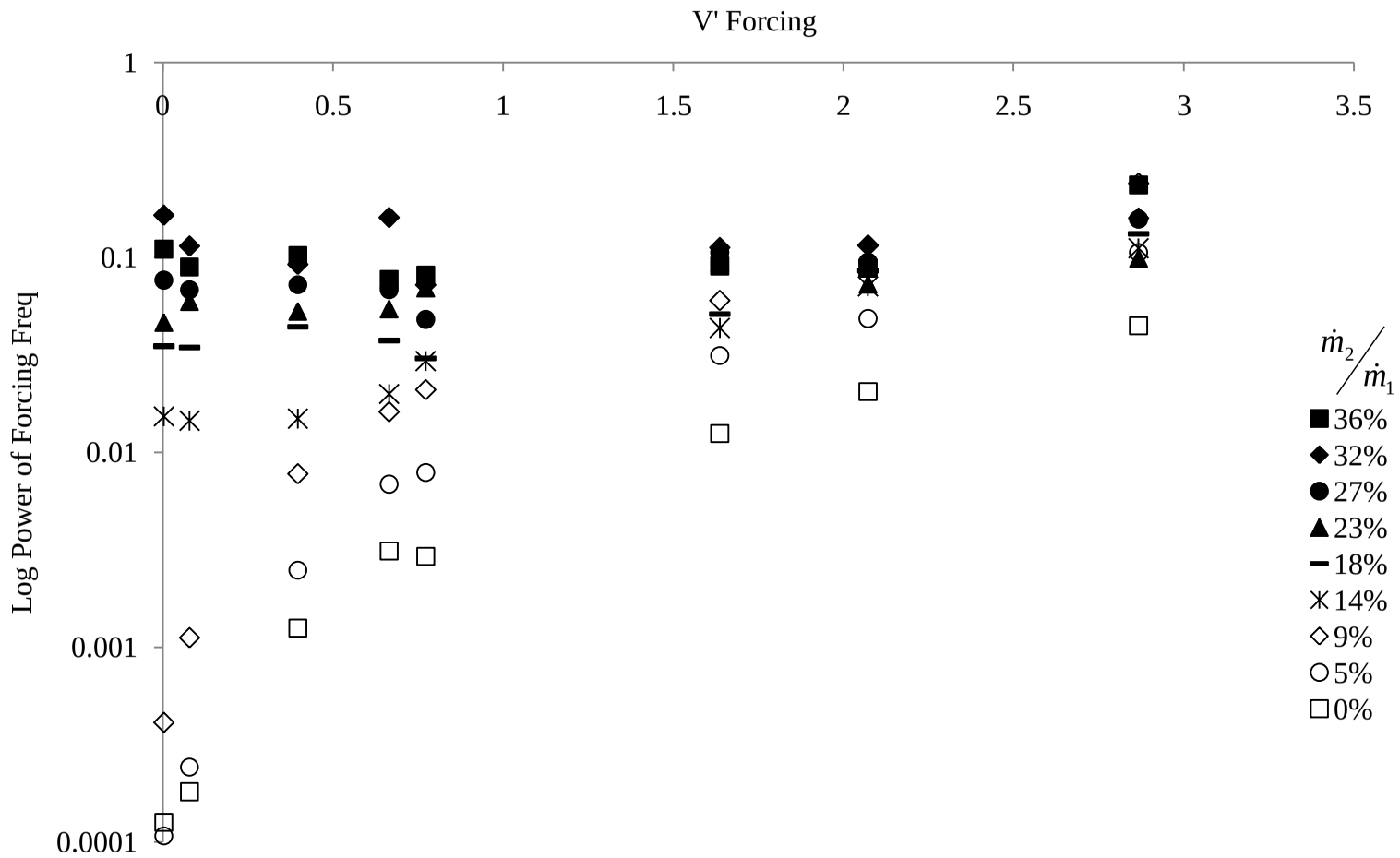

Figure 49: Frequency response vs forcing amplitude for all secondary flow rates

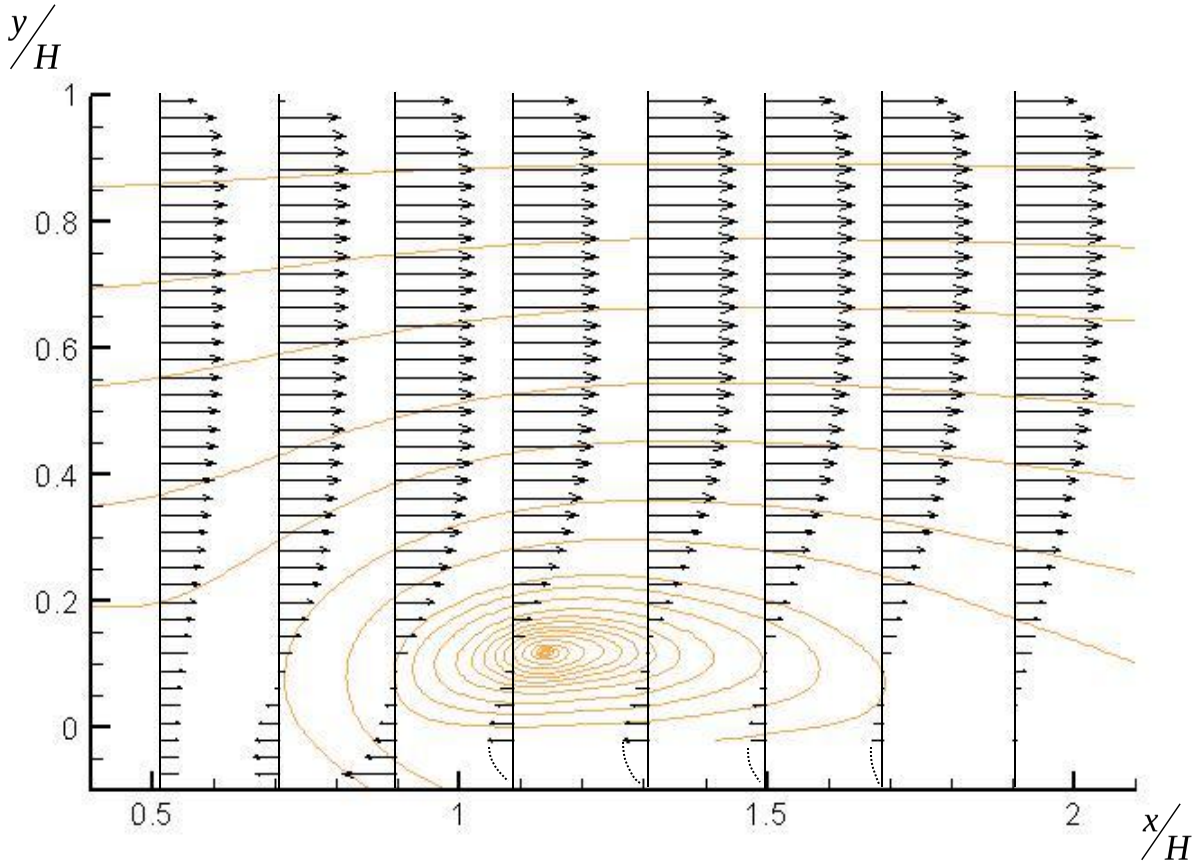

Figure 50: Streamwise velocity profiles within a separated recirculation bubble (14% case)

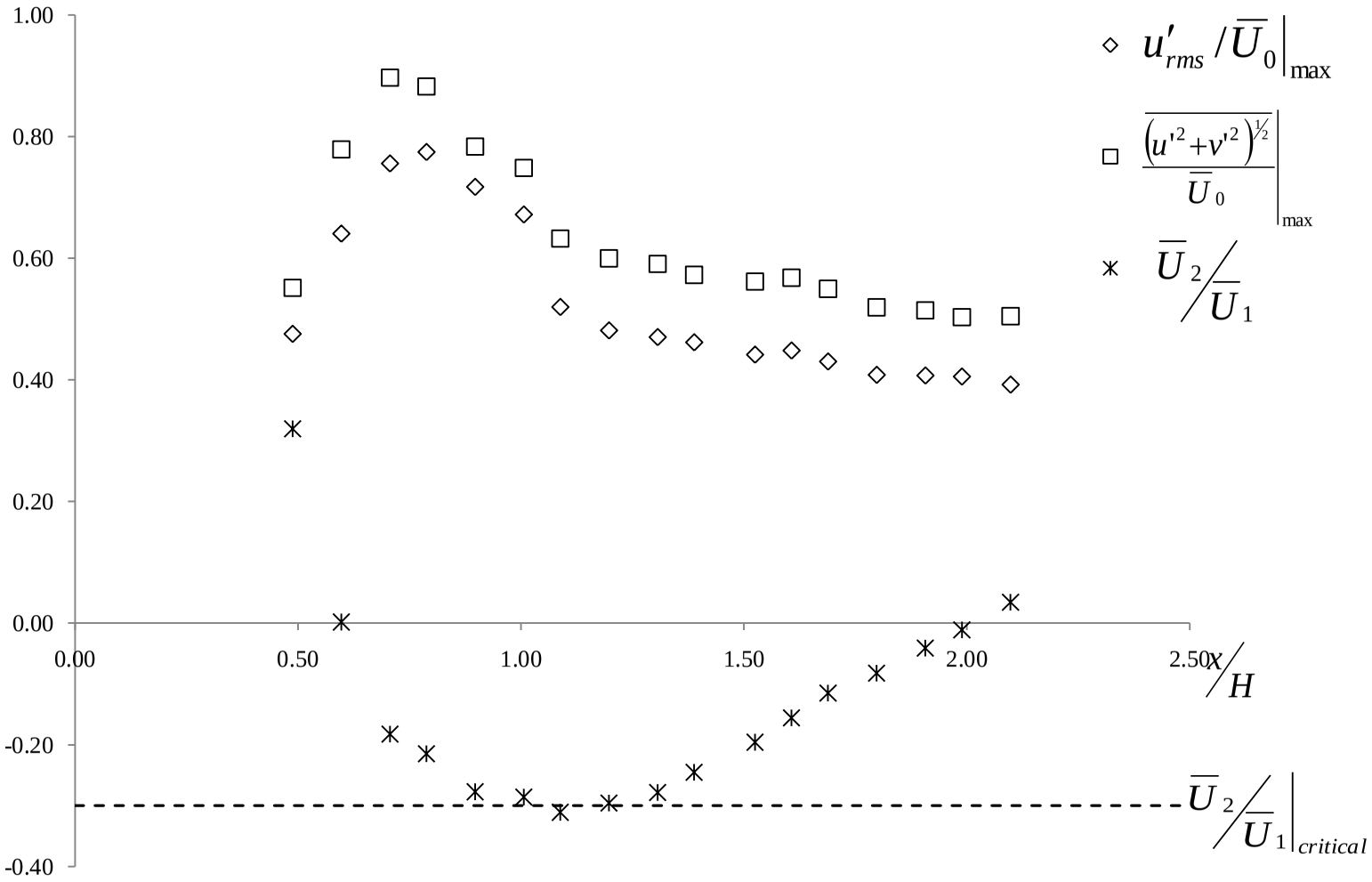

Figure 51: Velocity statistics within separated recirculation bubble (14% case)

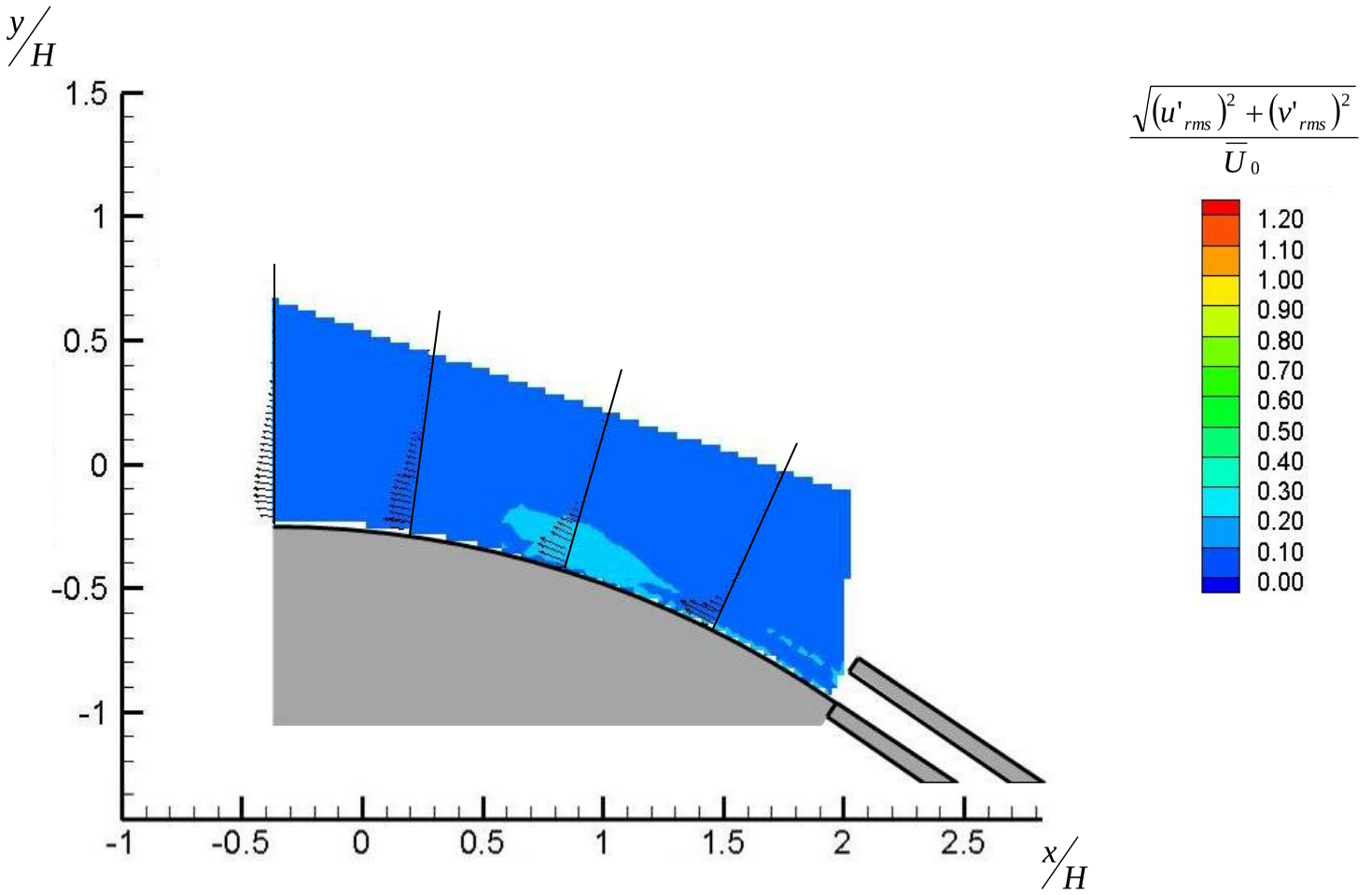

Figure 52: Coanda jet at all secondary flow rates
a.) 5%

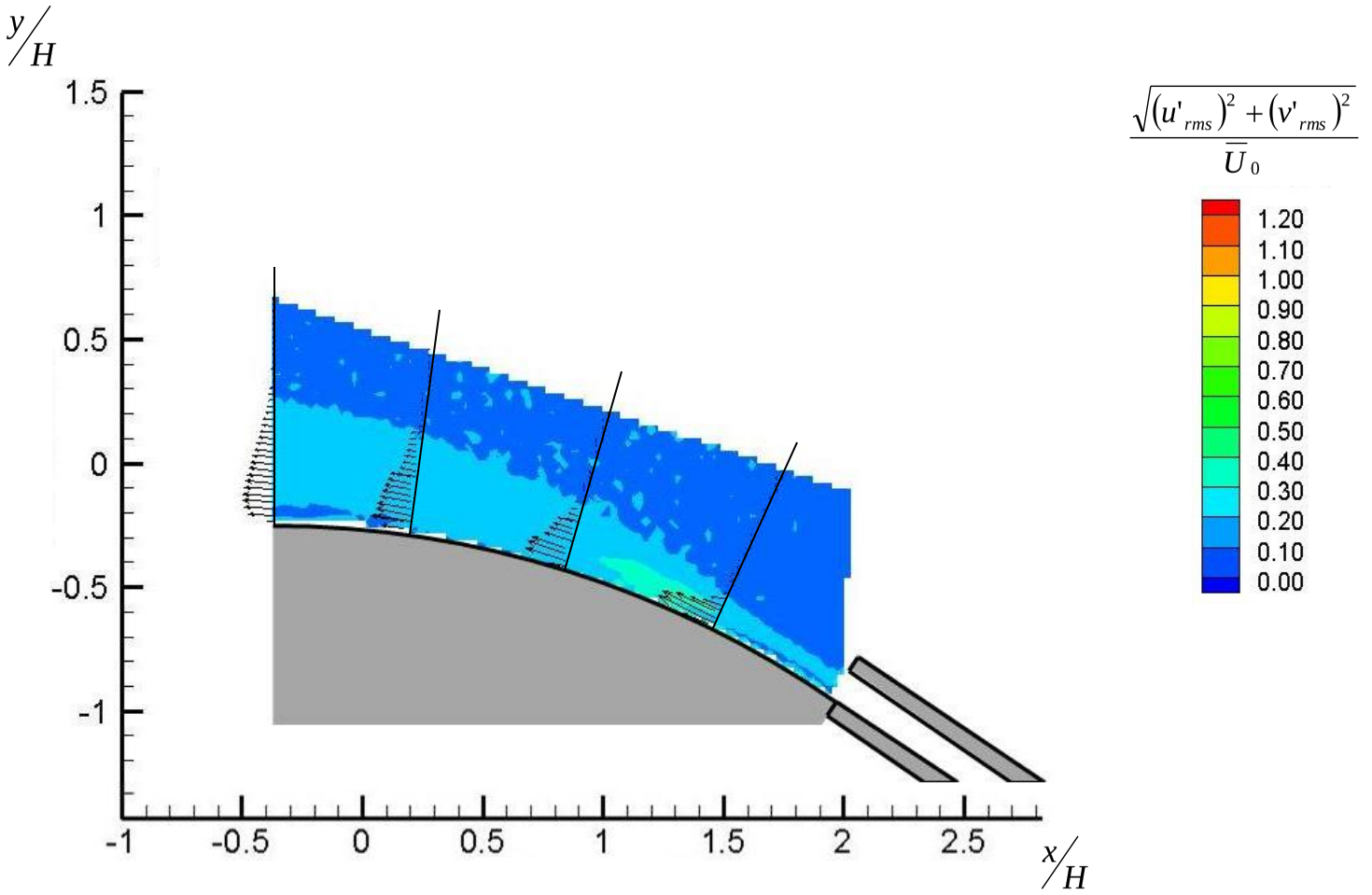

Figure 52: Coanda jet at all secondary flow rates
b.) 9%

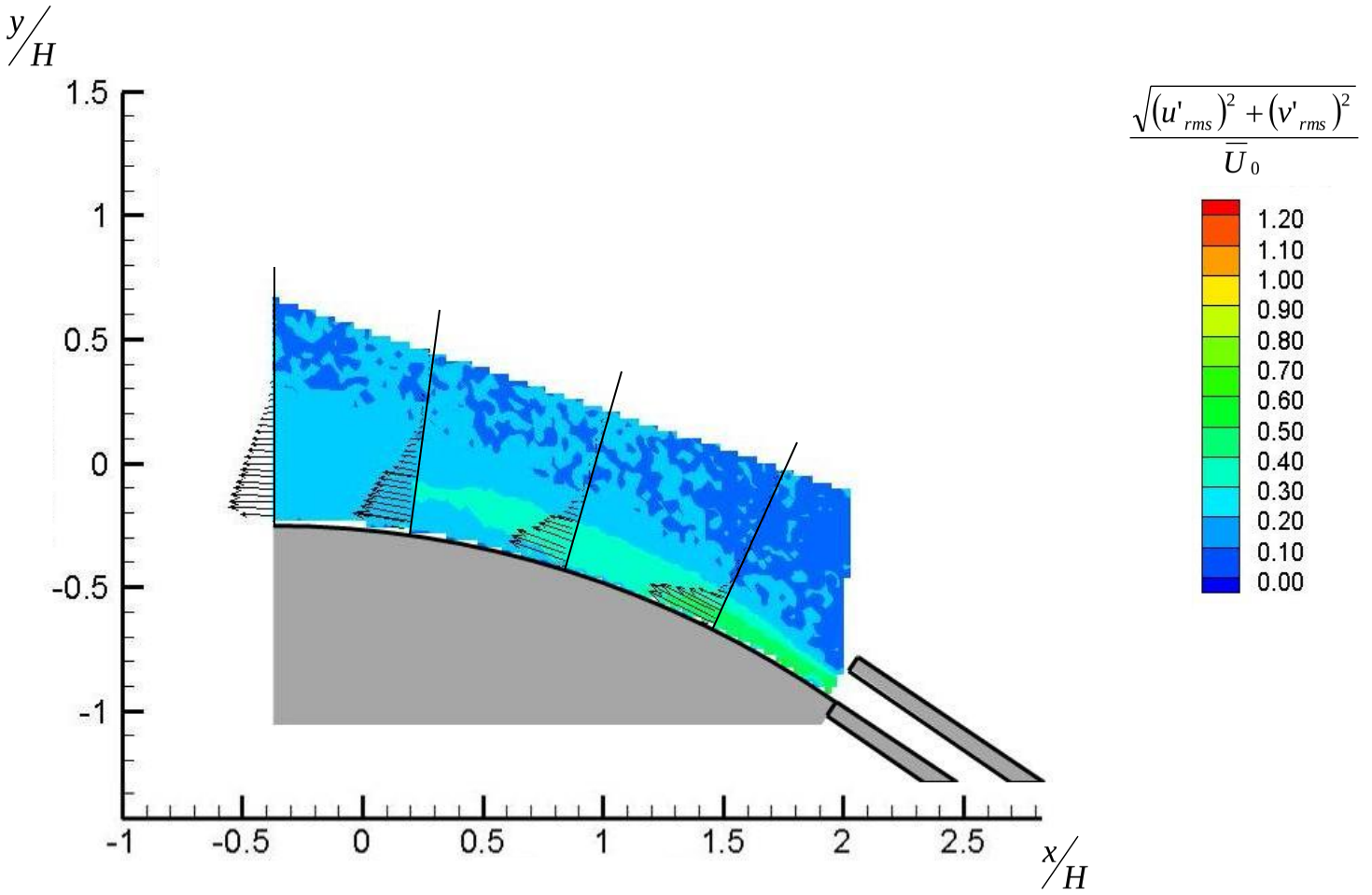

Figure 52: Coanda jet at all secondary flow rates
c.) 14%

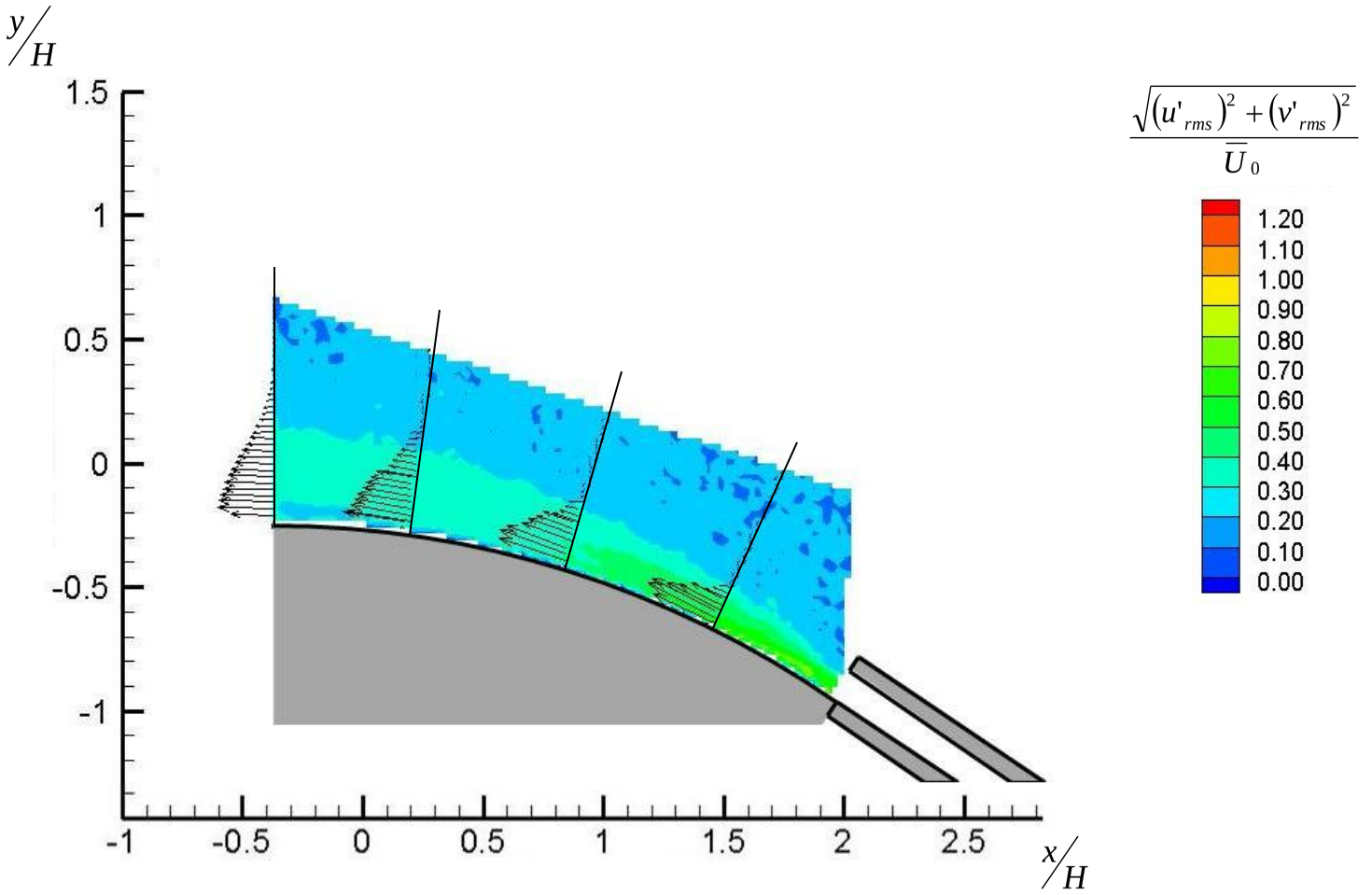

Figure 52: Coanda jet at all secondary flow rates
d.) 18%

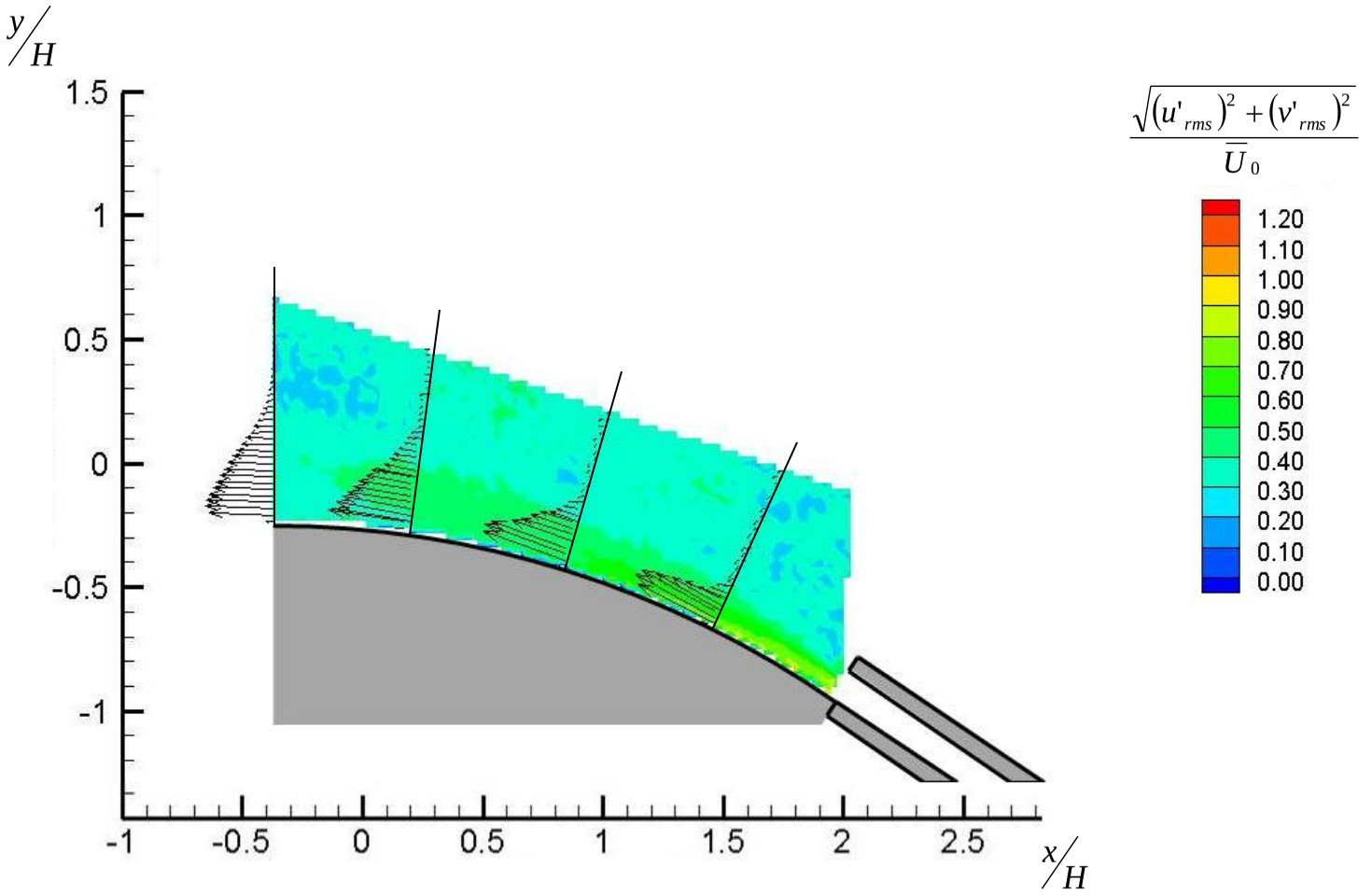

Figure 52: Coanda jet at all secondary flow rates
e.) 23%

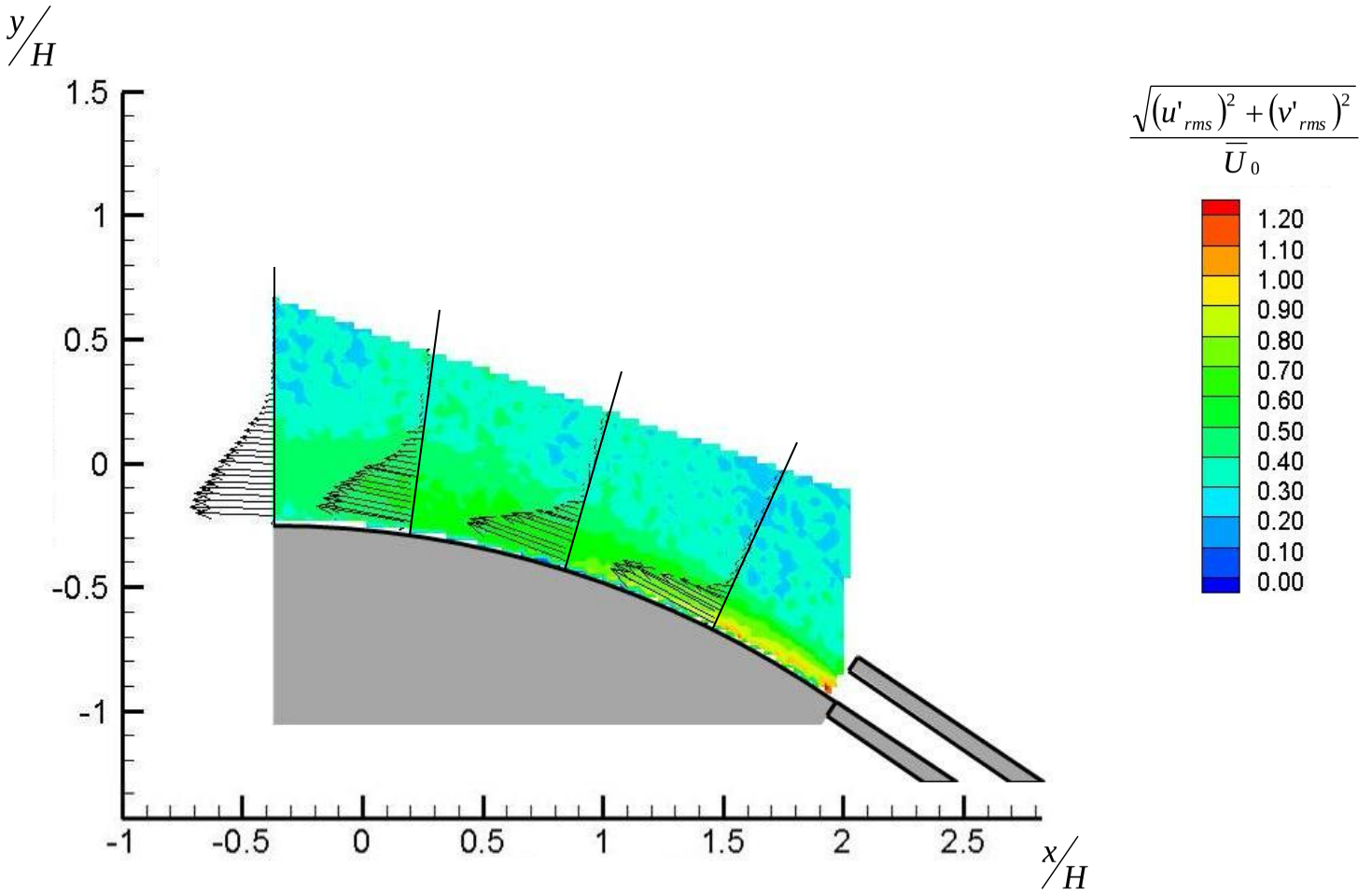

Figure 52: Coanda jet at all secondary flow rates
f.) 27%

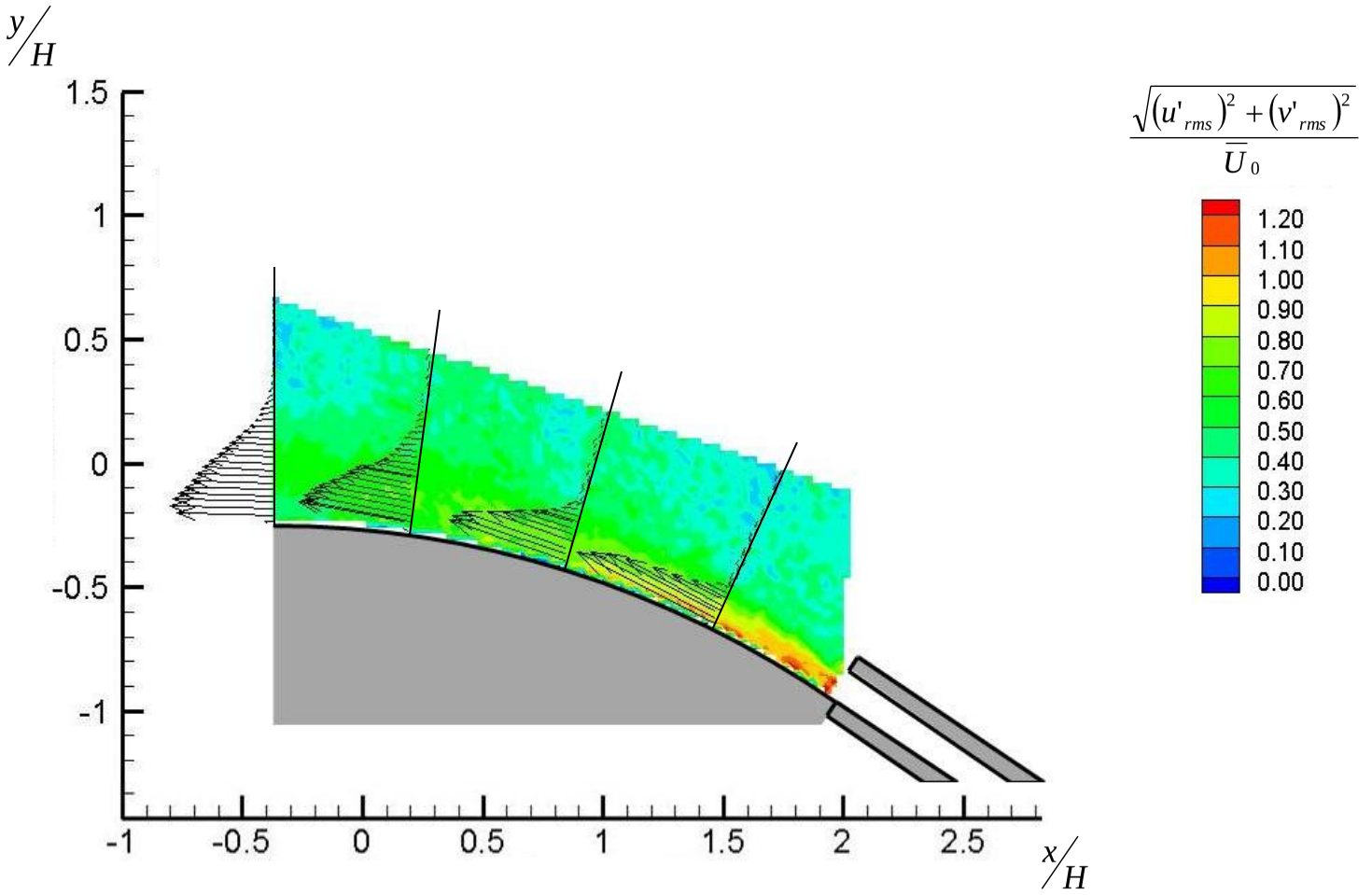

Figure 52: Coanda jet at all secondary flow rates
g.) 32%

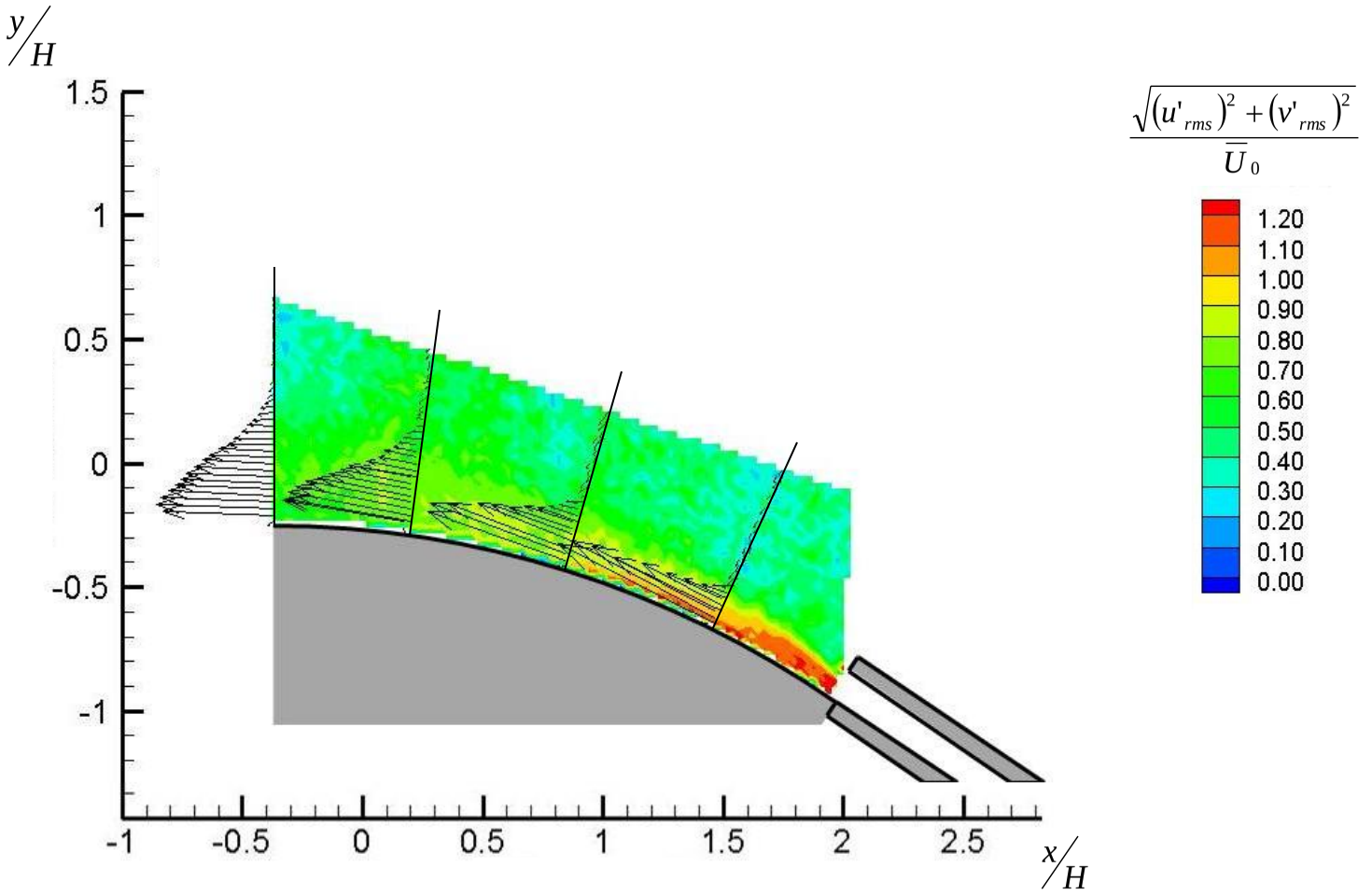

Figure 52: Coanda jet at all secondary flow rates
h.) 36%

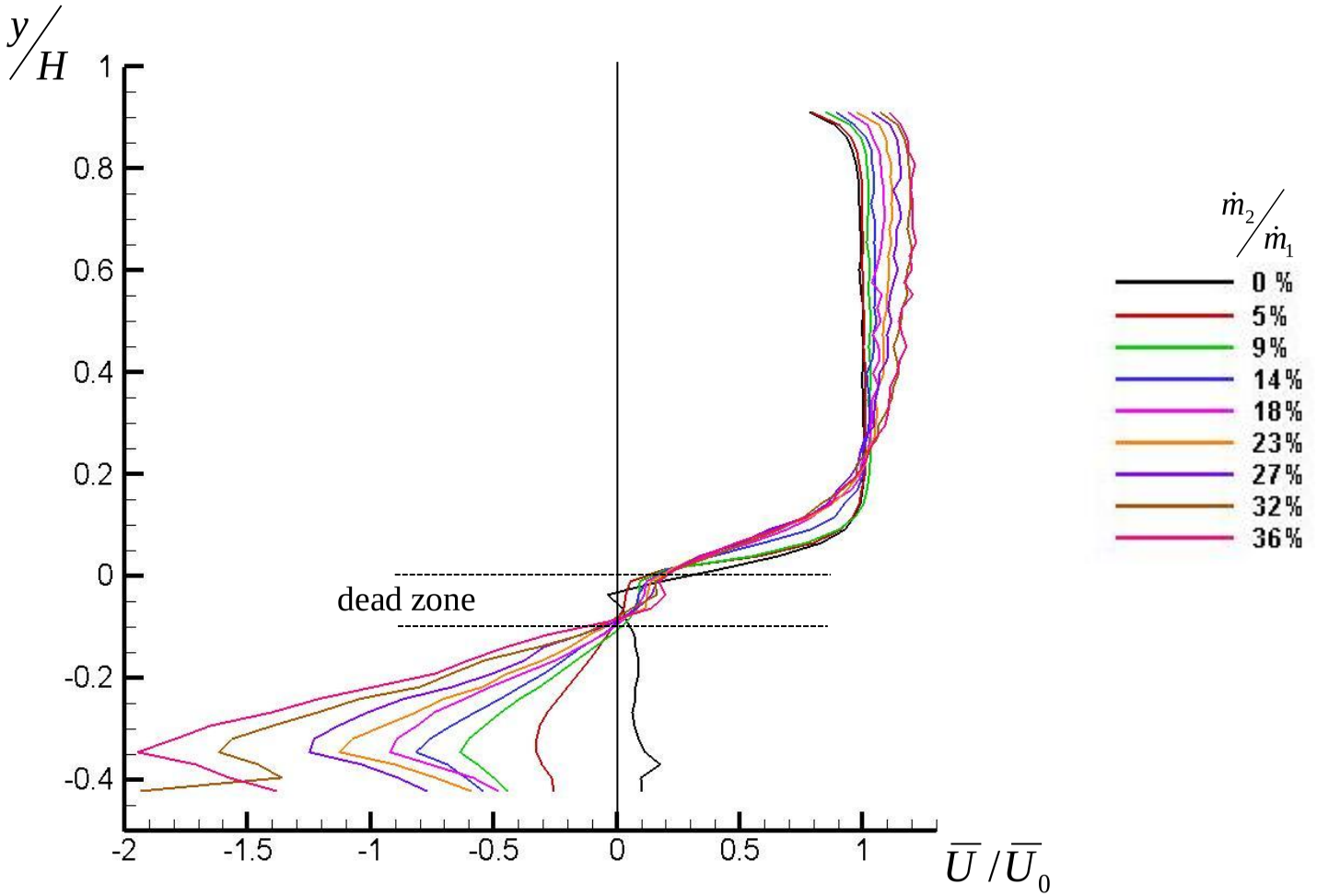

Figure 53: Cross-stream velocity profiles at x/H = 0 for all secondary flow rates for gap heights of a.) g=8mm

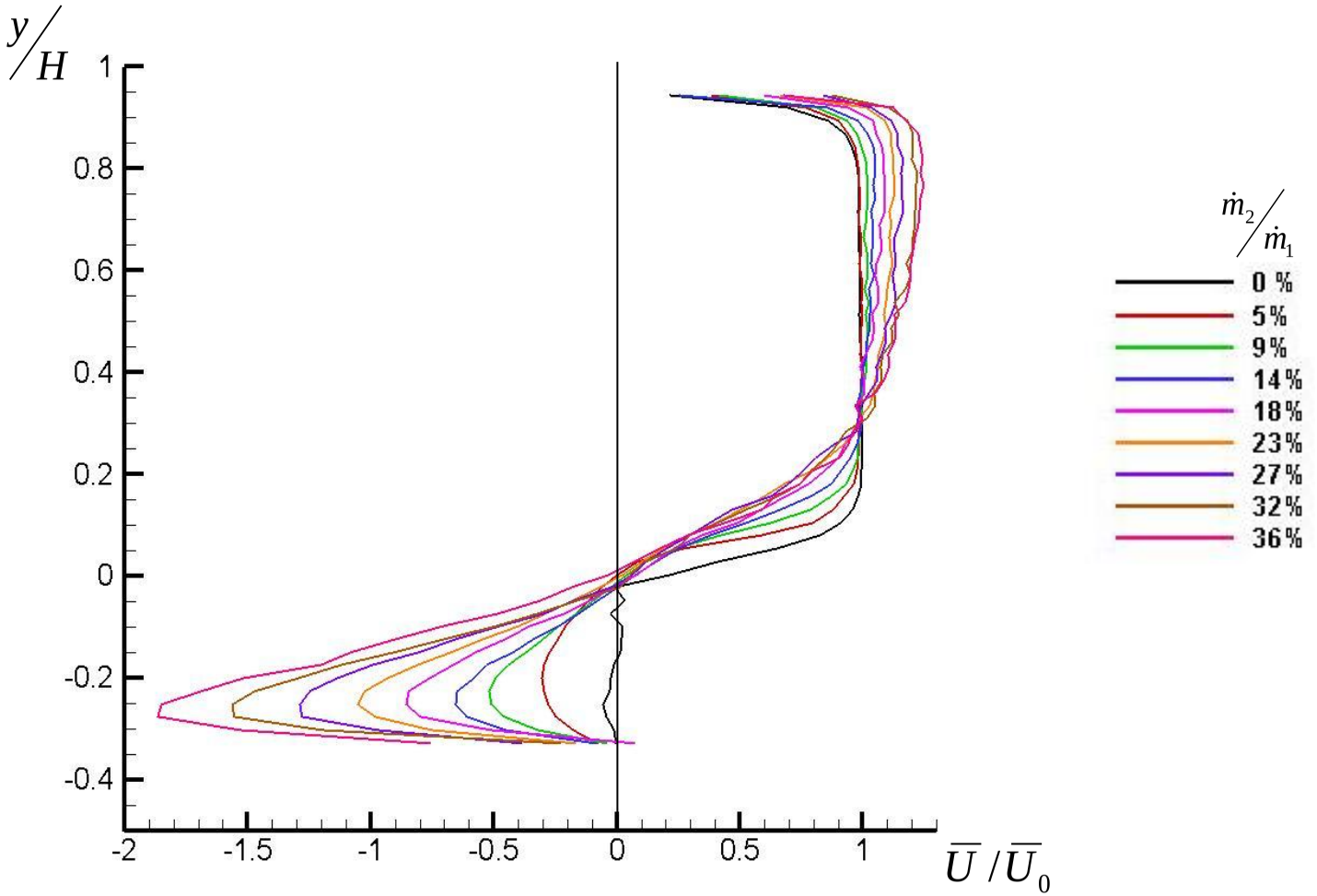

Figure 53: Cross-stream velocity profiles at x/H = 0 for all secondary flow rates for gap heights of b.) g=6mm

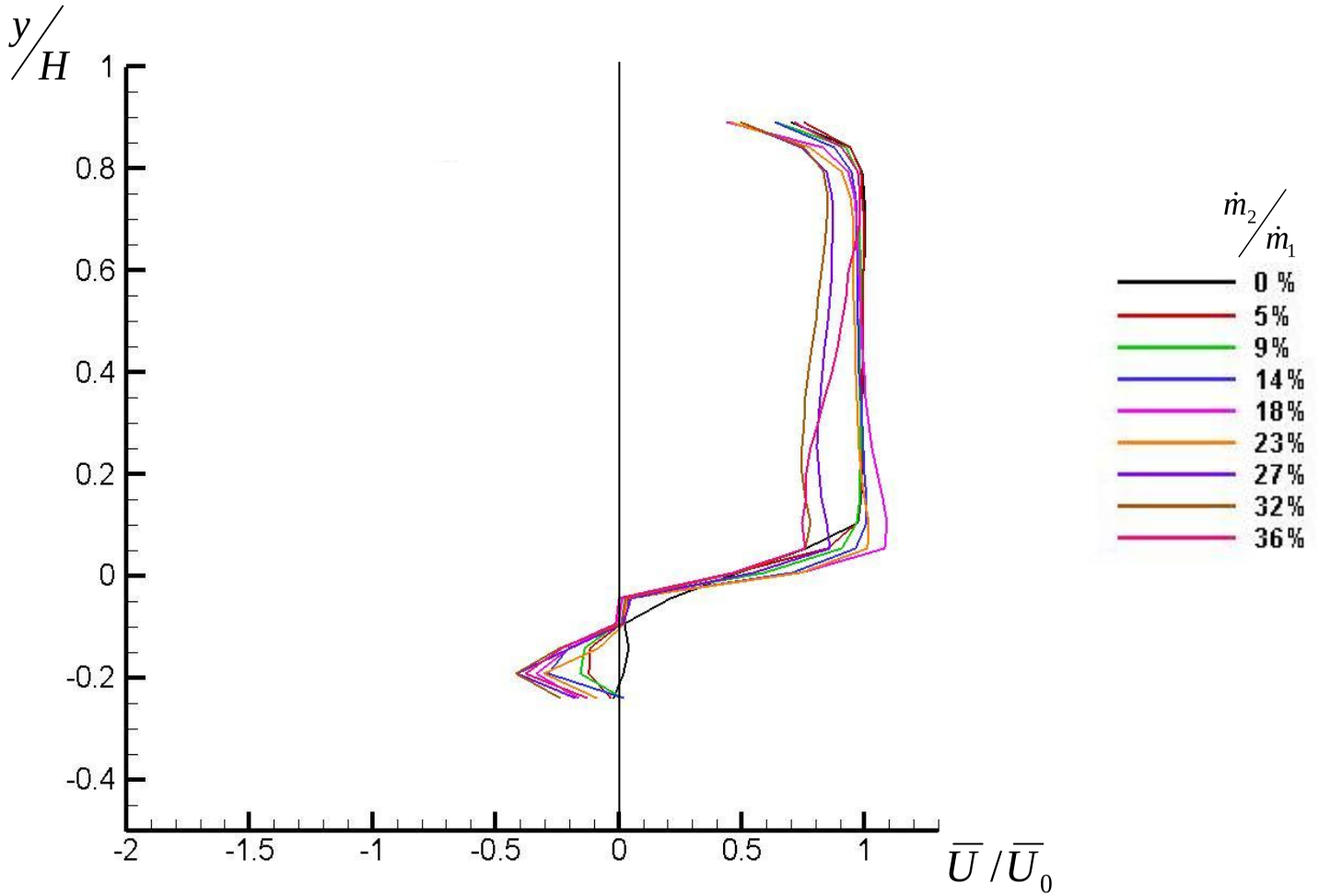

Figure 53: Cross-stream velocity profiles at x/H = 0 for all secondary flow rates for gap heights of c.) g=4mm

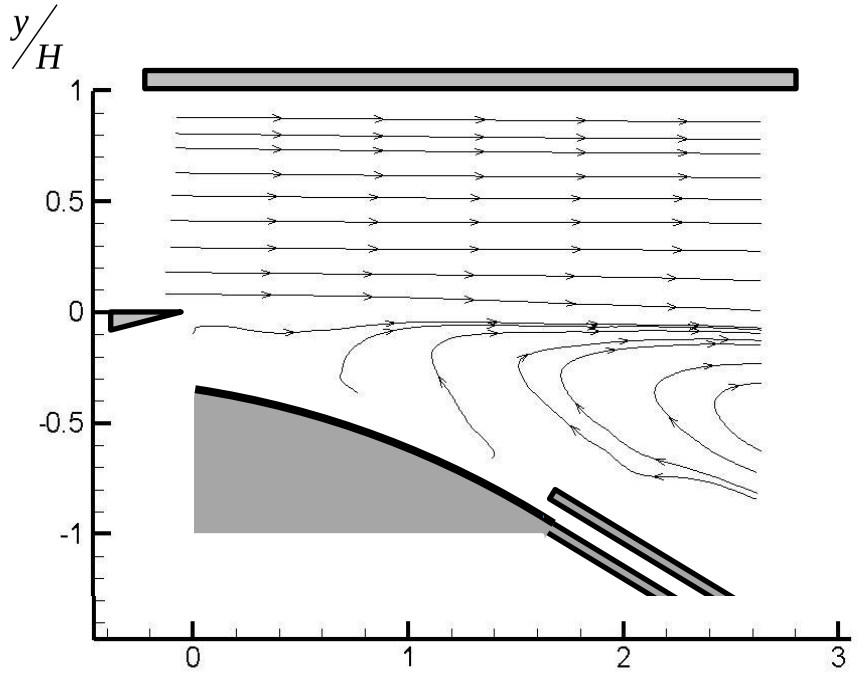

a.) 0%

Figure 54 : Mean streamlines for all secondary flow cases for geometry II

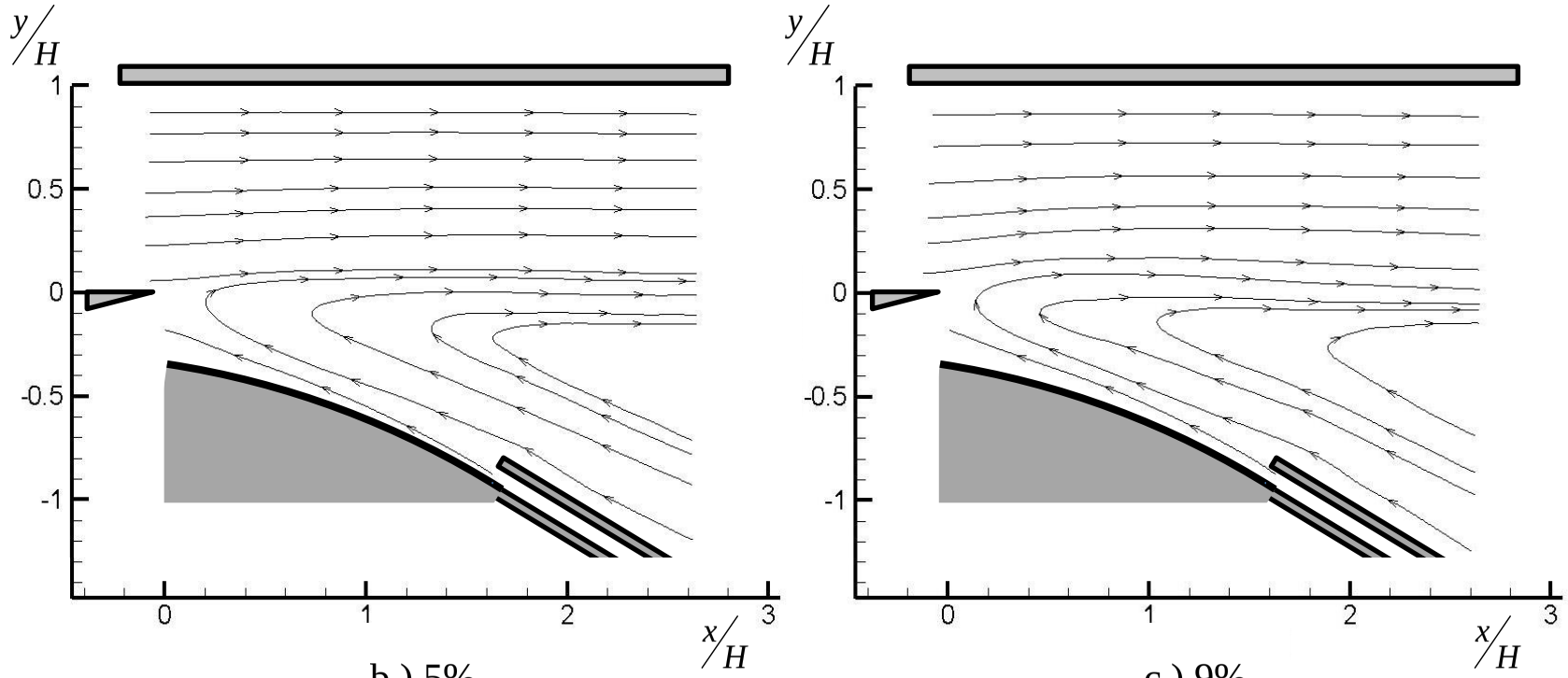

Figure 54 : Mean streamlines for all secondary flow cases for geometry II

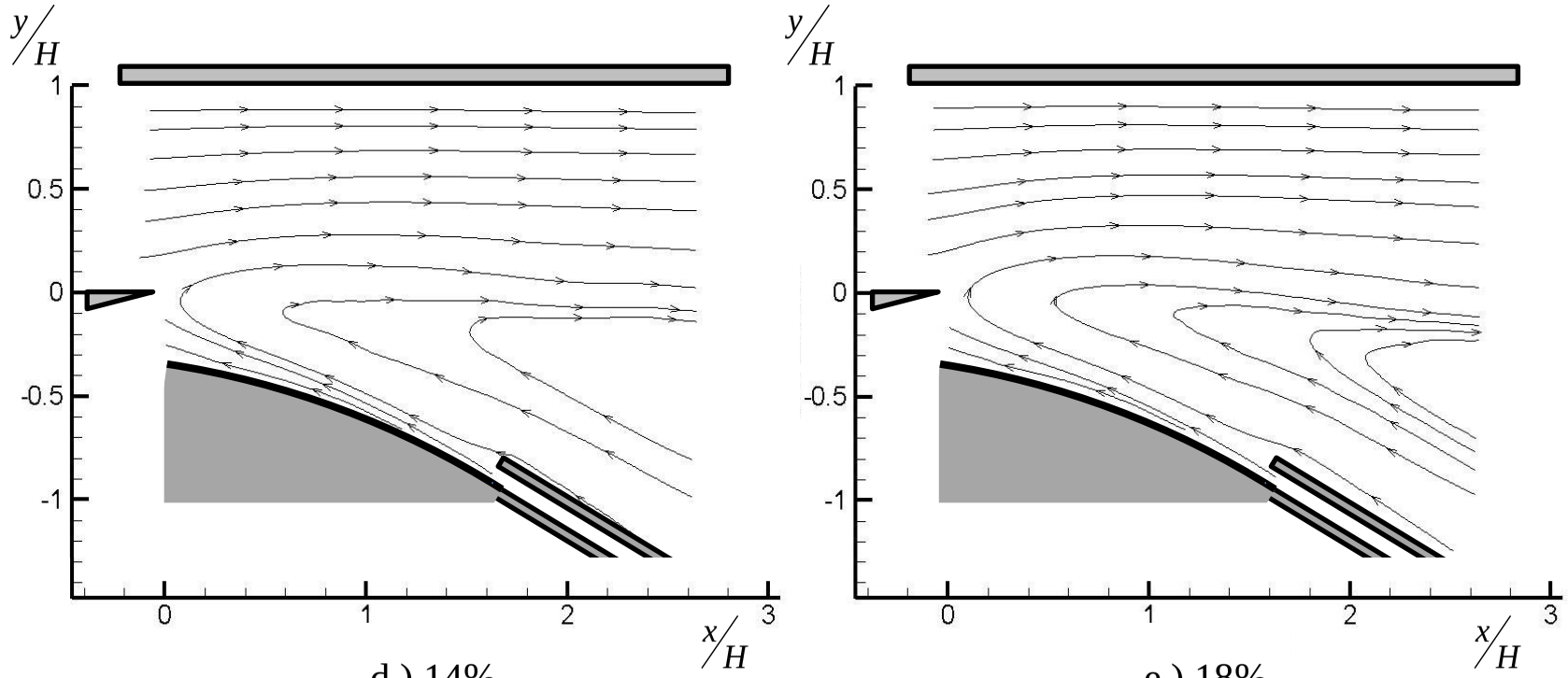

Figure 54 : Mean streamlines for all secondary flow cases for geometry II

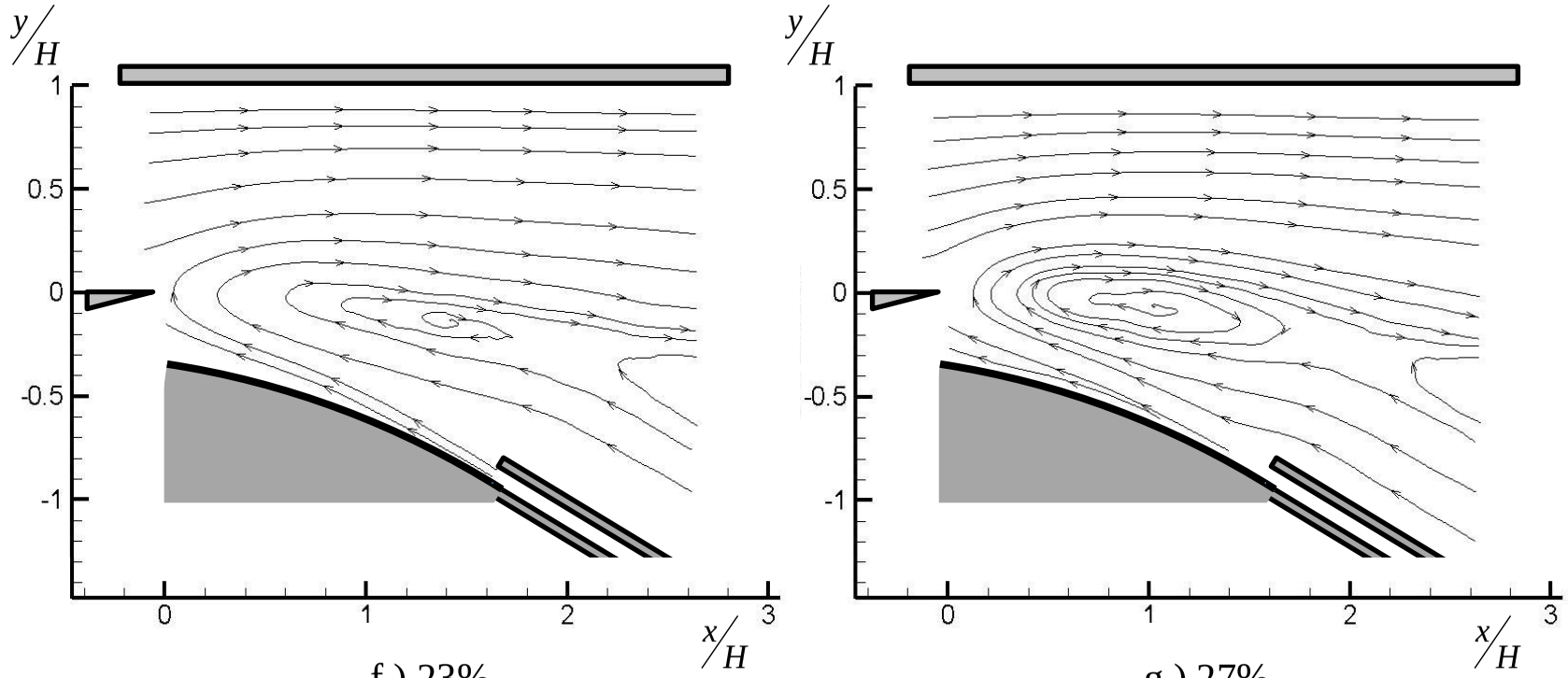

Figure 54 : Mean streamlines for all secondary flow cases for geometry II

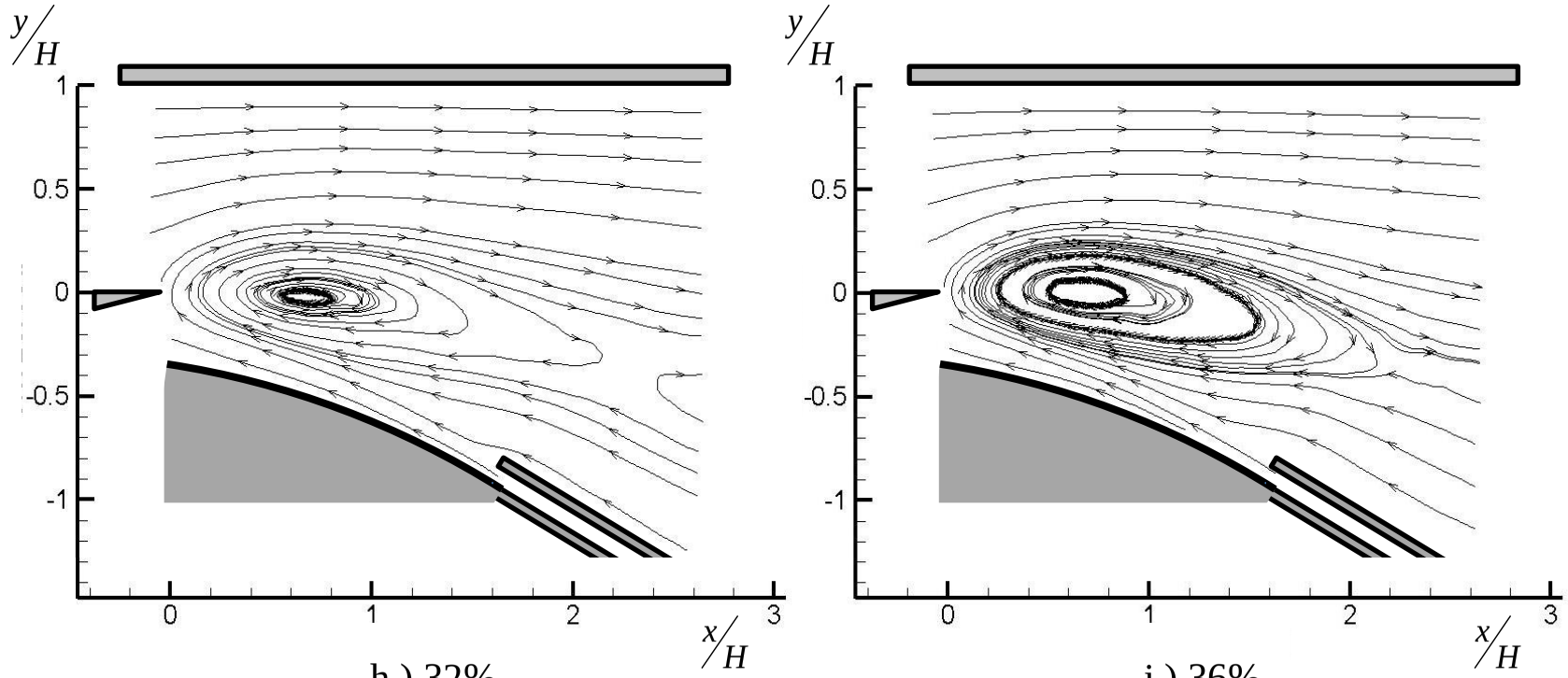

Figure 54 : Mean streamlines for all secondary flow cases for geometry II

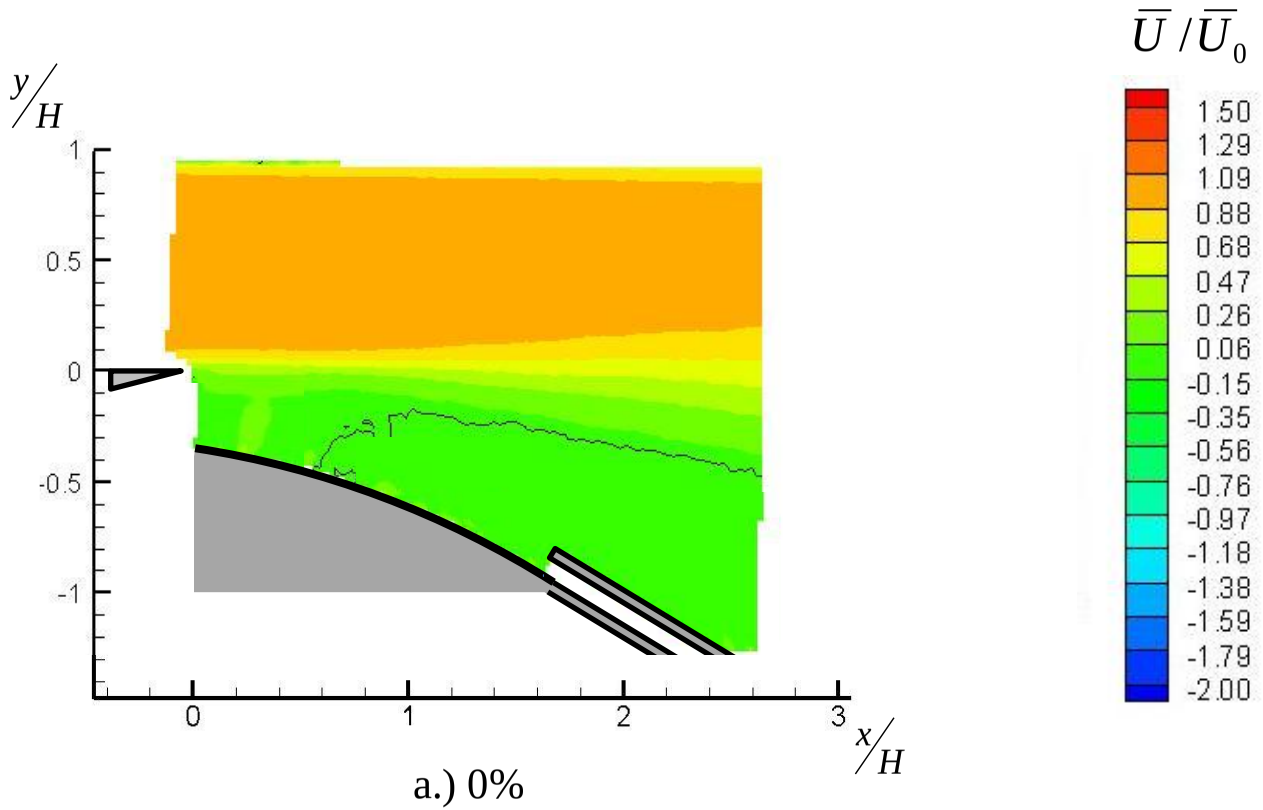

a.) 0%

Figure 55: Mean streamwise velocity contours for Coanda facility for all secondary flow rates

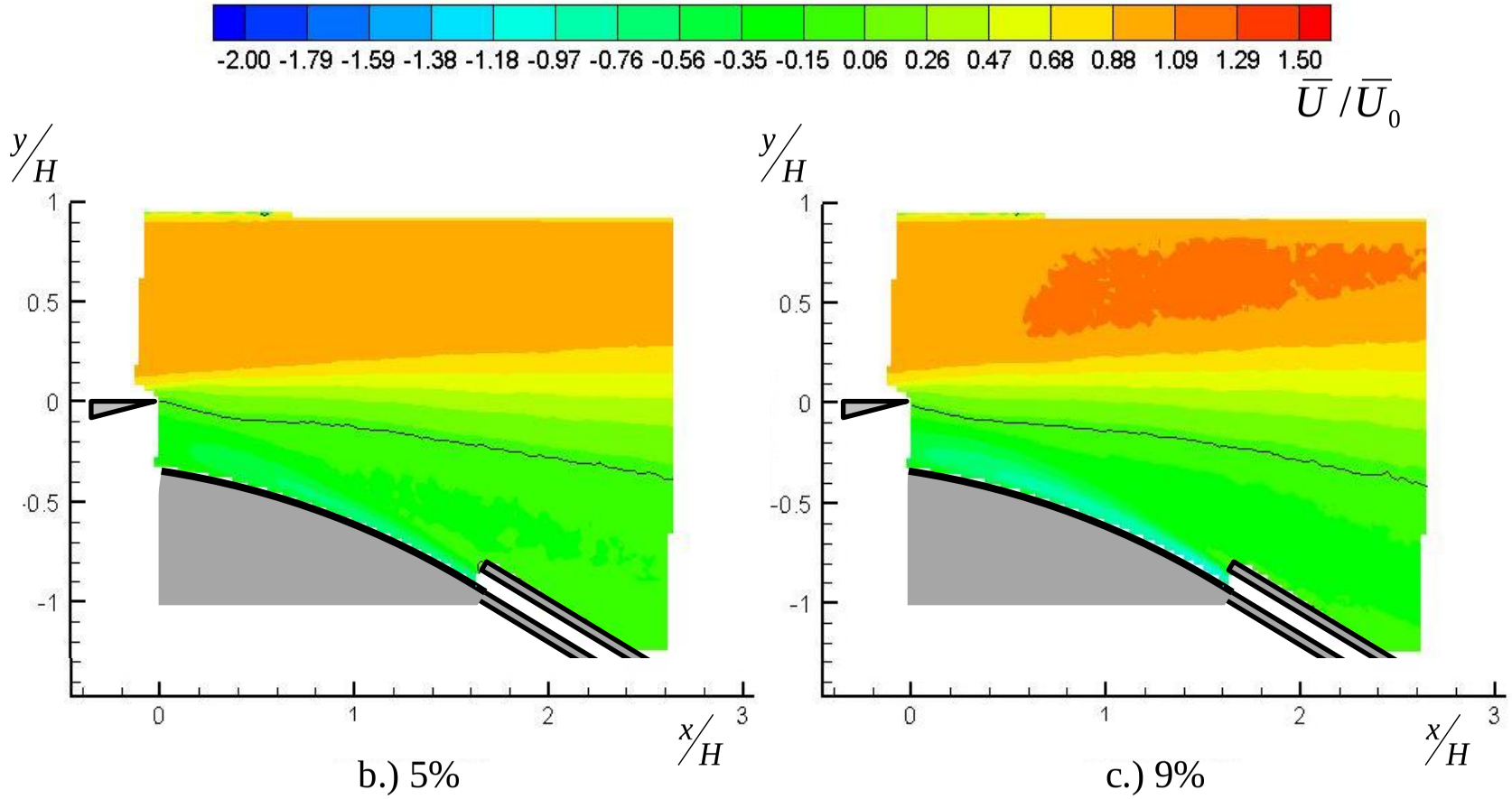

Figure 55: Mean streamwise velocity contours for geometry II at all secondary flow rates

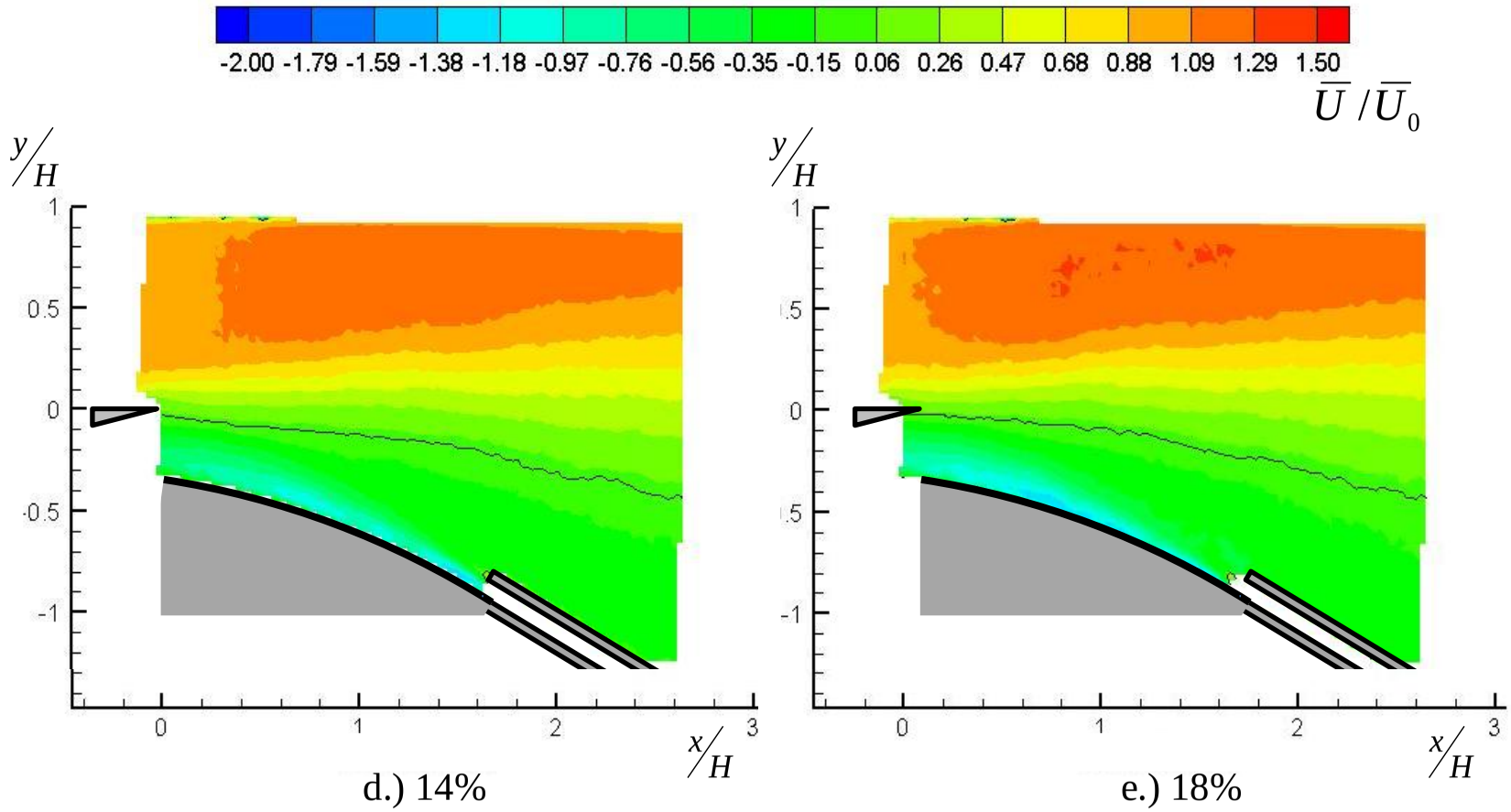

Figure 55: Mean streamwise velocity contours for geometry II at all secondary flow rates

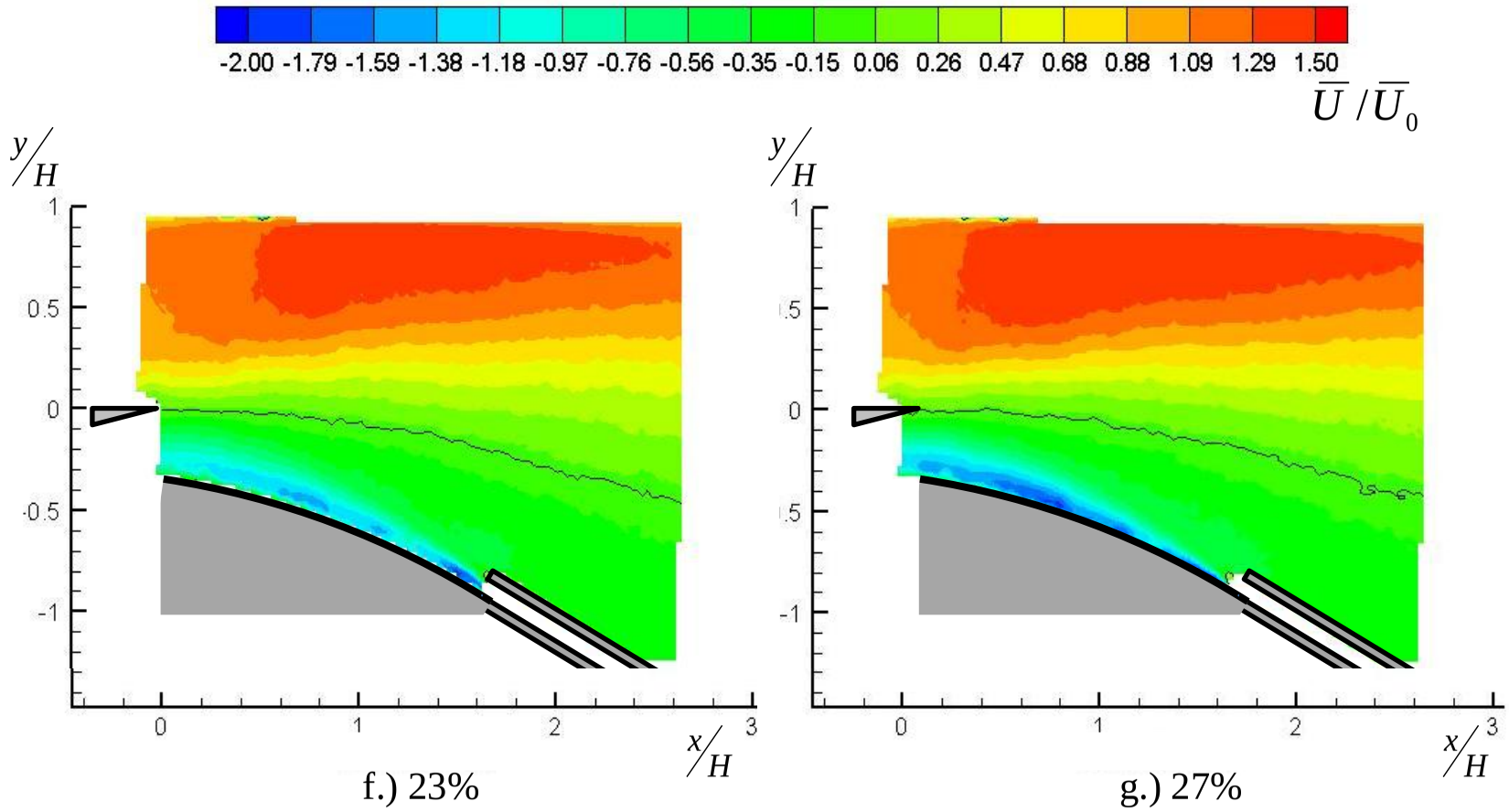

Figure 55: Mean streamwise velocity contours for geometry II at all secondary flow rates

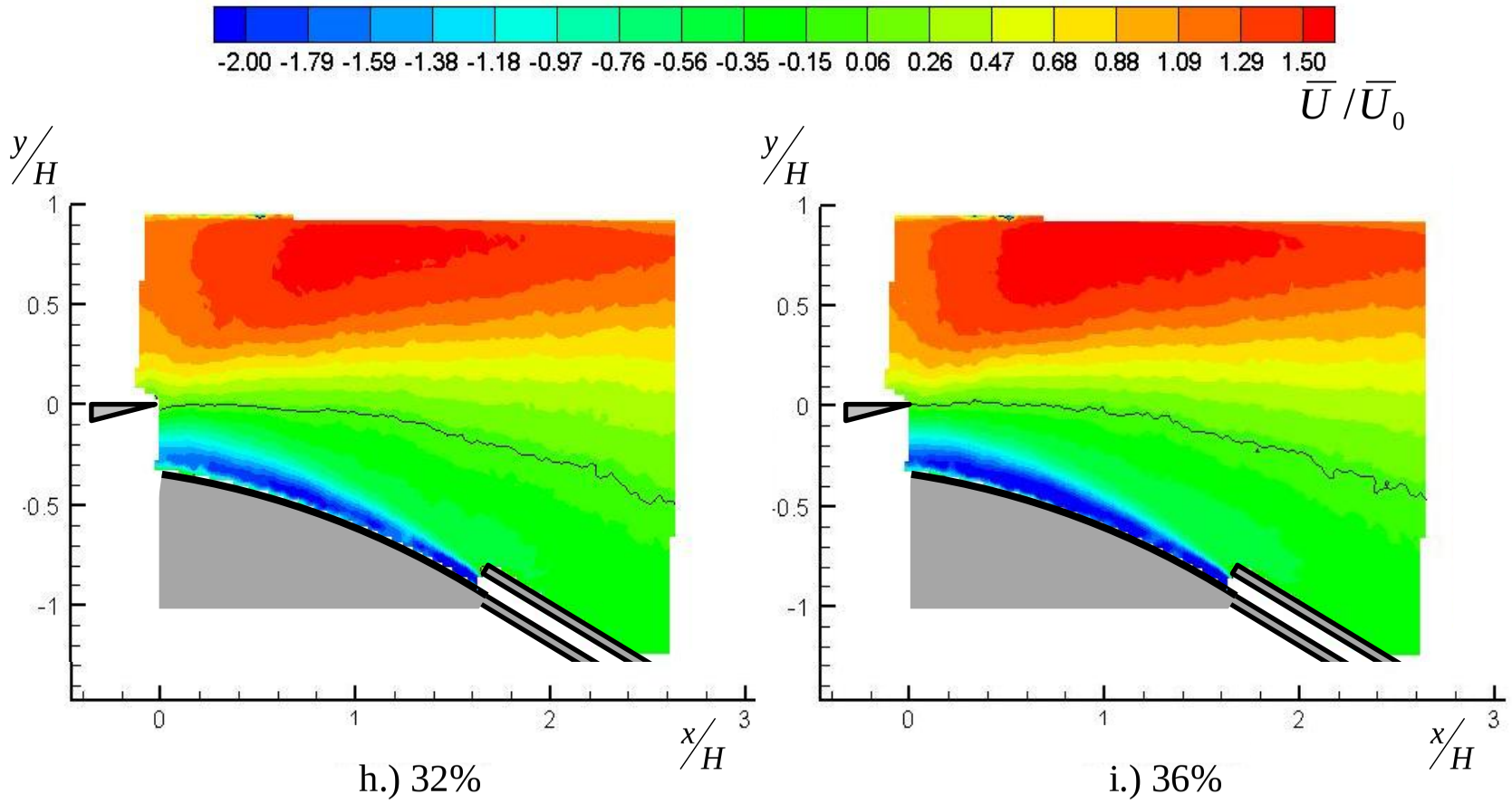

Figure 55: Mean streamwise velocity contours for geometry II at all secondary flow rates

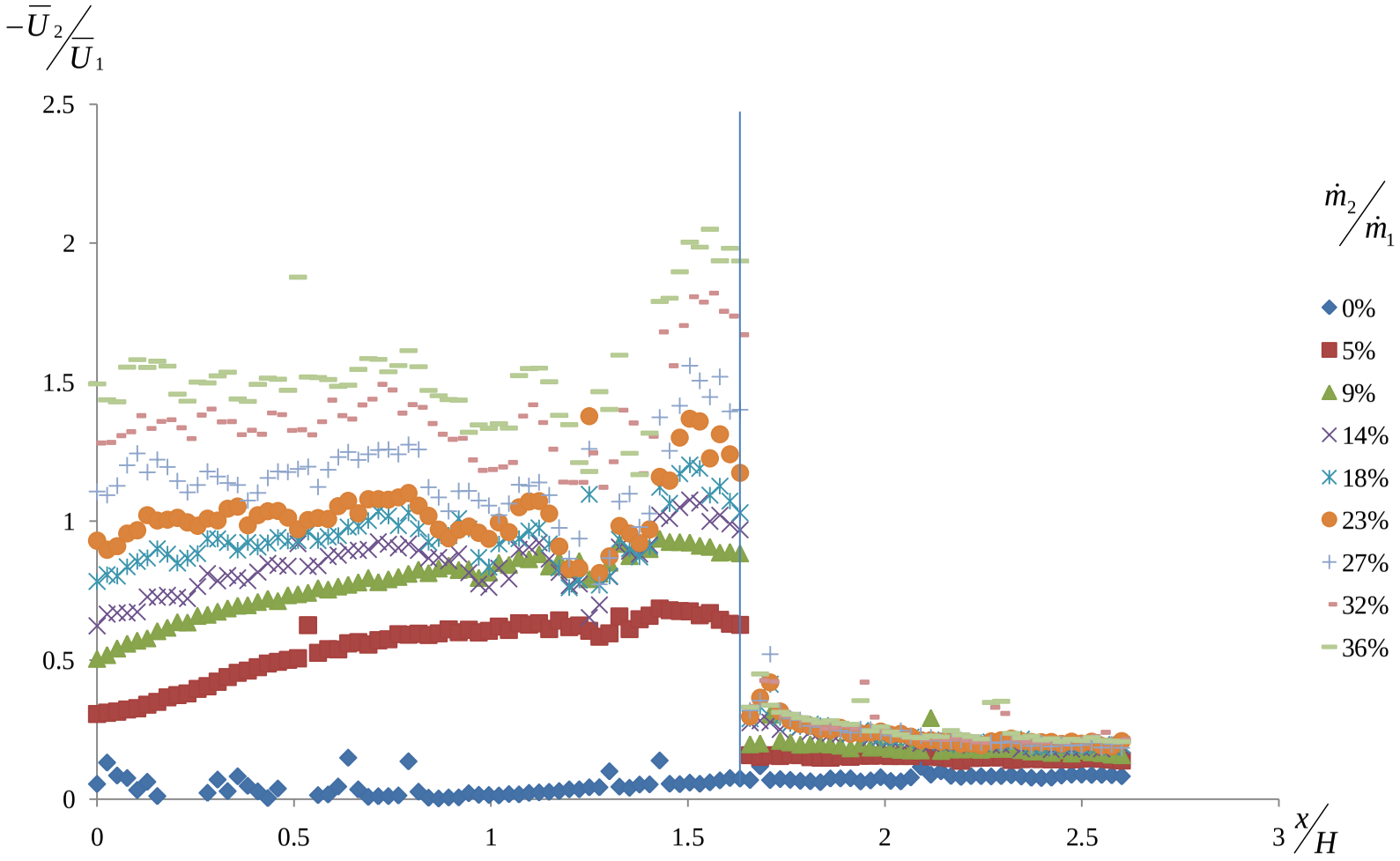

Figure 56: Local streamwise velocity ratios for geometry II at all secondary flow rates

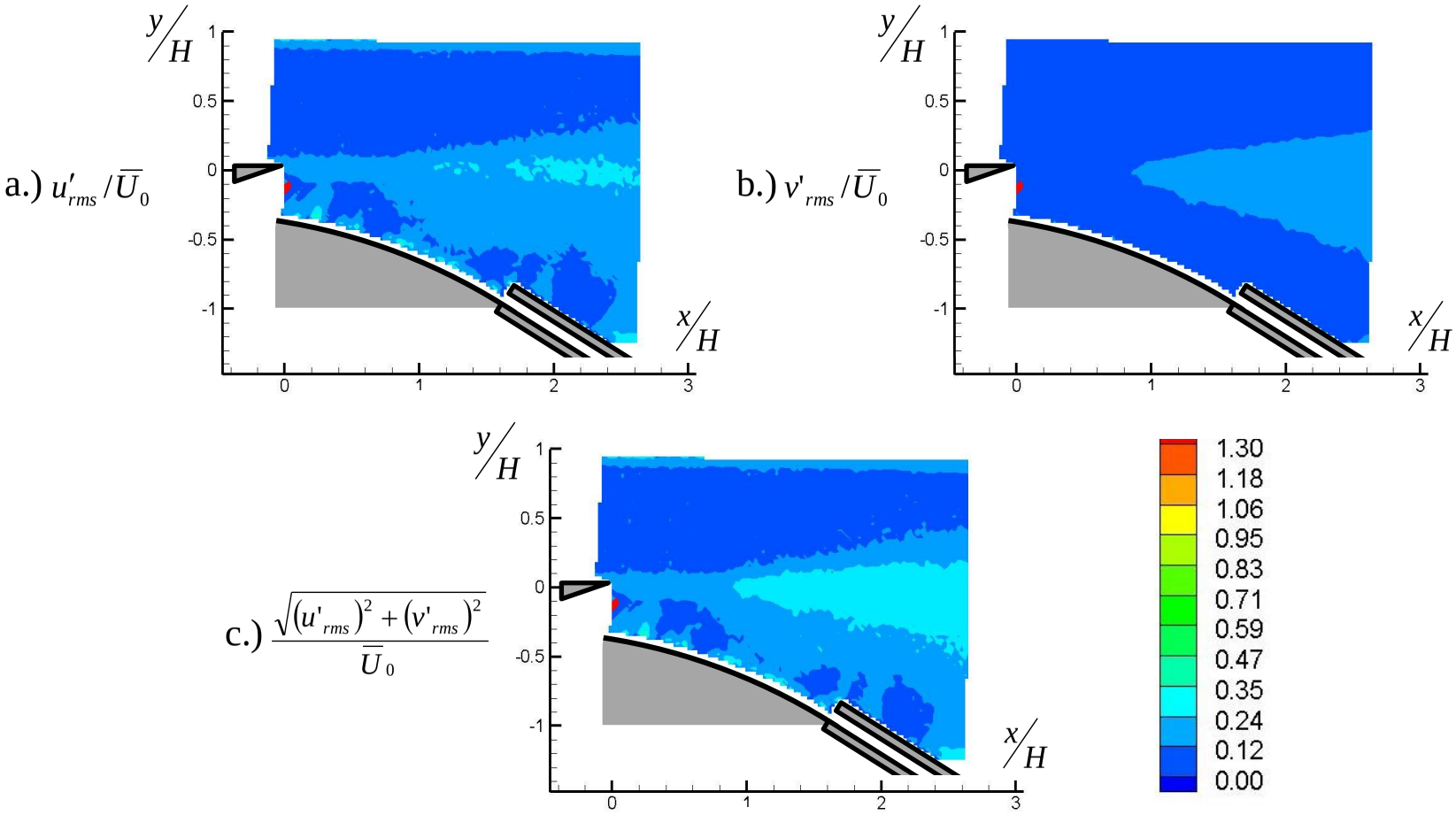

Figure 57: Rms streamwise, cross-stream and total turbulence contours for geometry II at 0% secondary flow rate

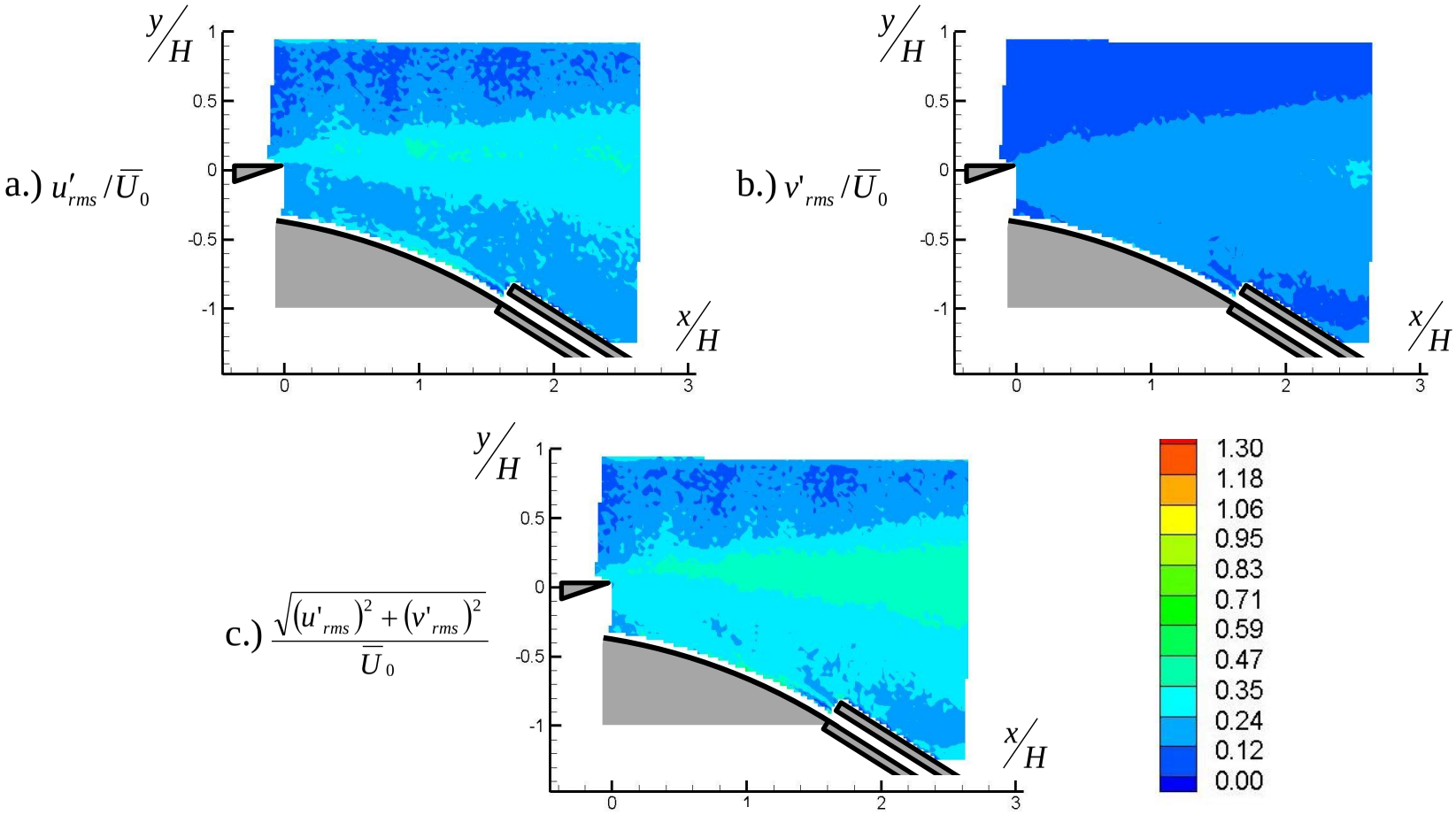

Figure 58: Rms streamwise, cross-stream and total turbulence contours for geometry II at 9% secondary flow rate

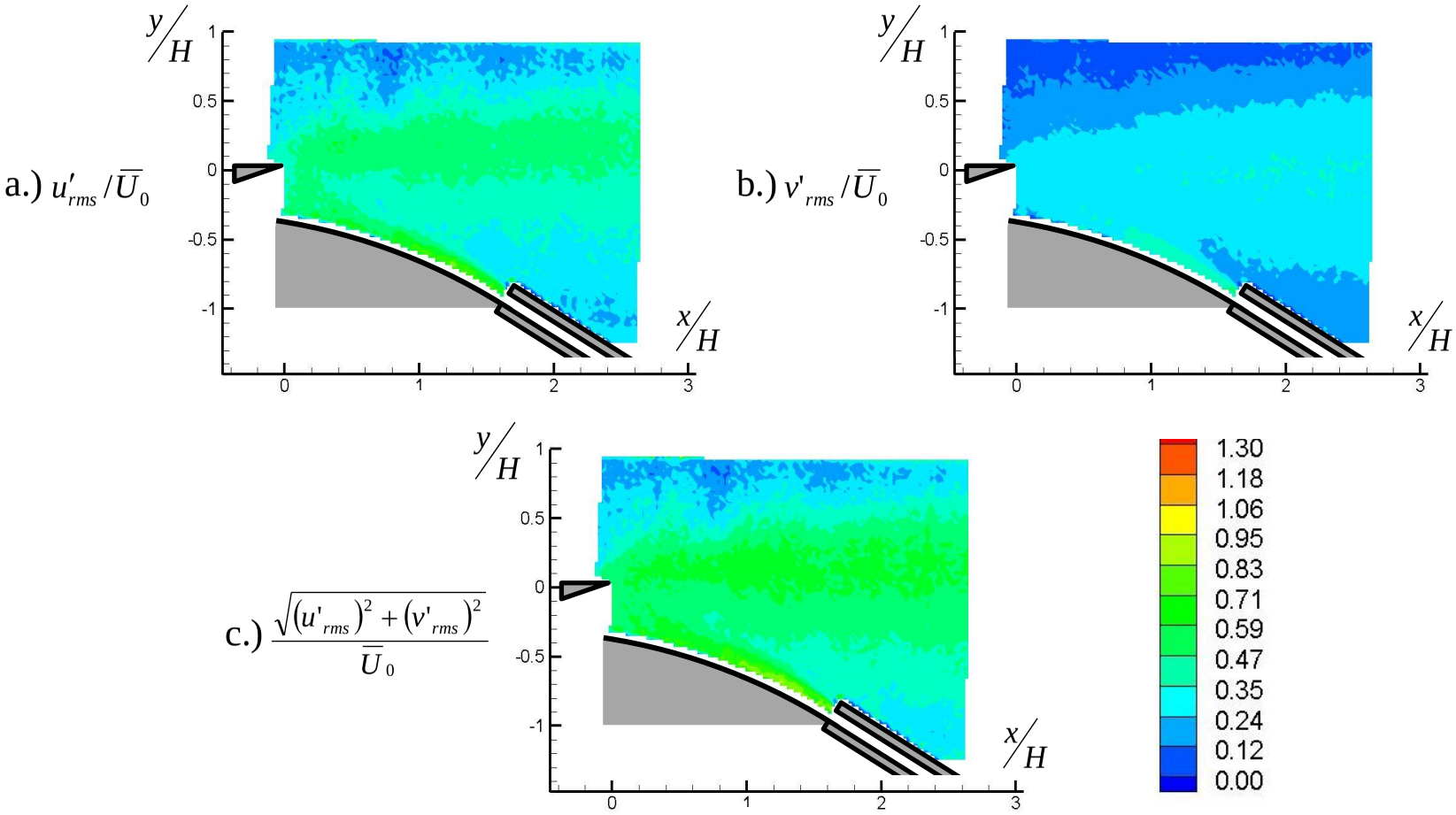

Figure 59: Rms streamwise, cross-stream and total turbulence contours for geometry II at 18% secondary flow rate

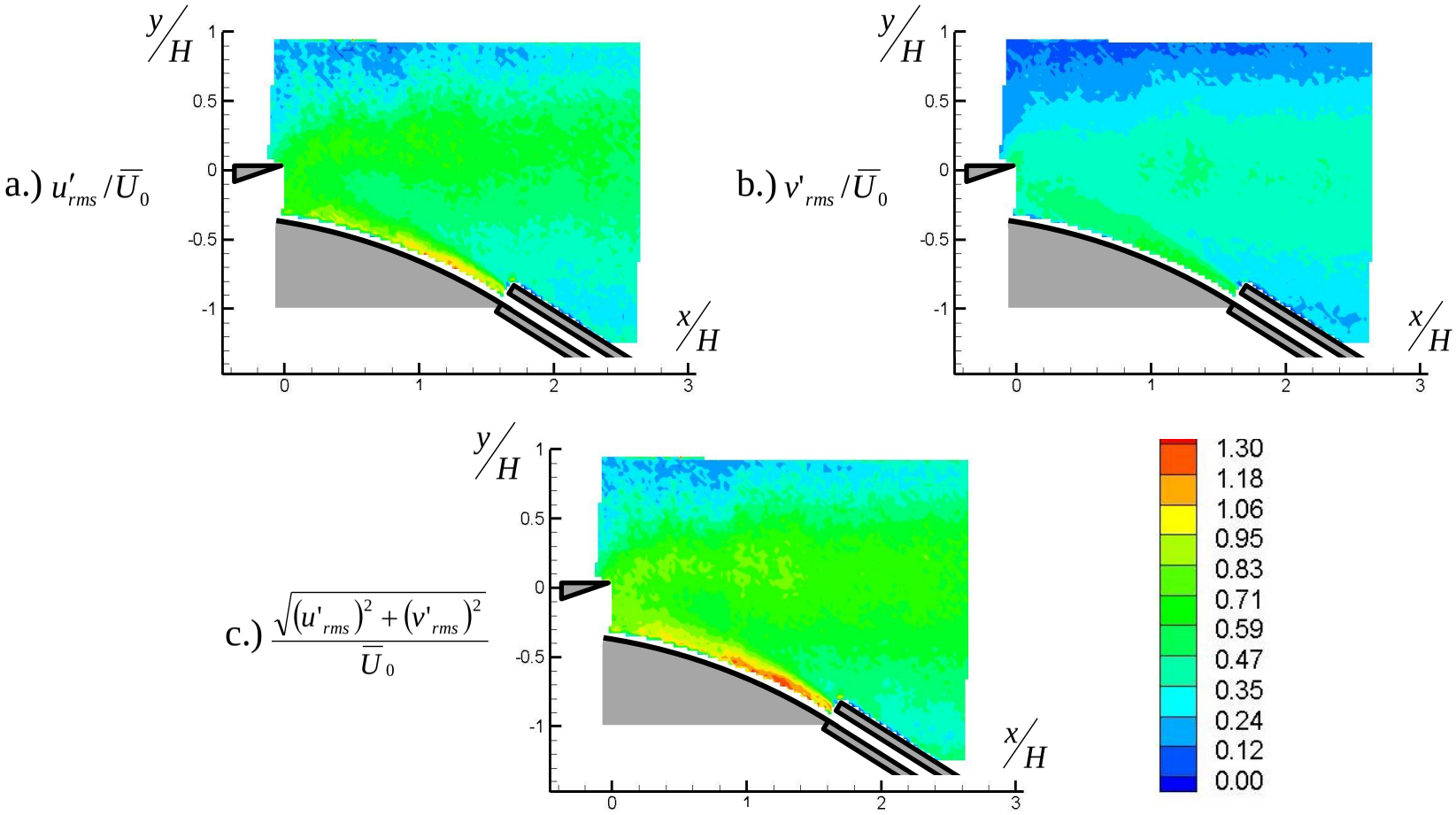

Figure 60: Rms streamwise, cross-stream and total turbulence contours for geometry II at 27% secondary flow rate

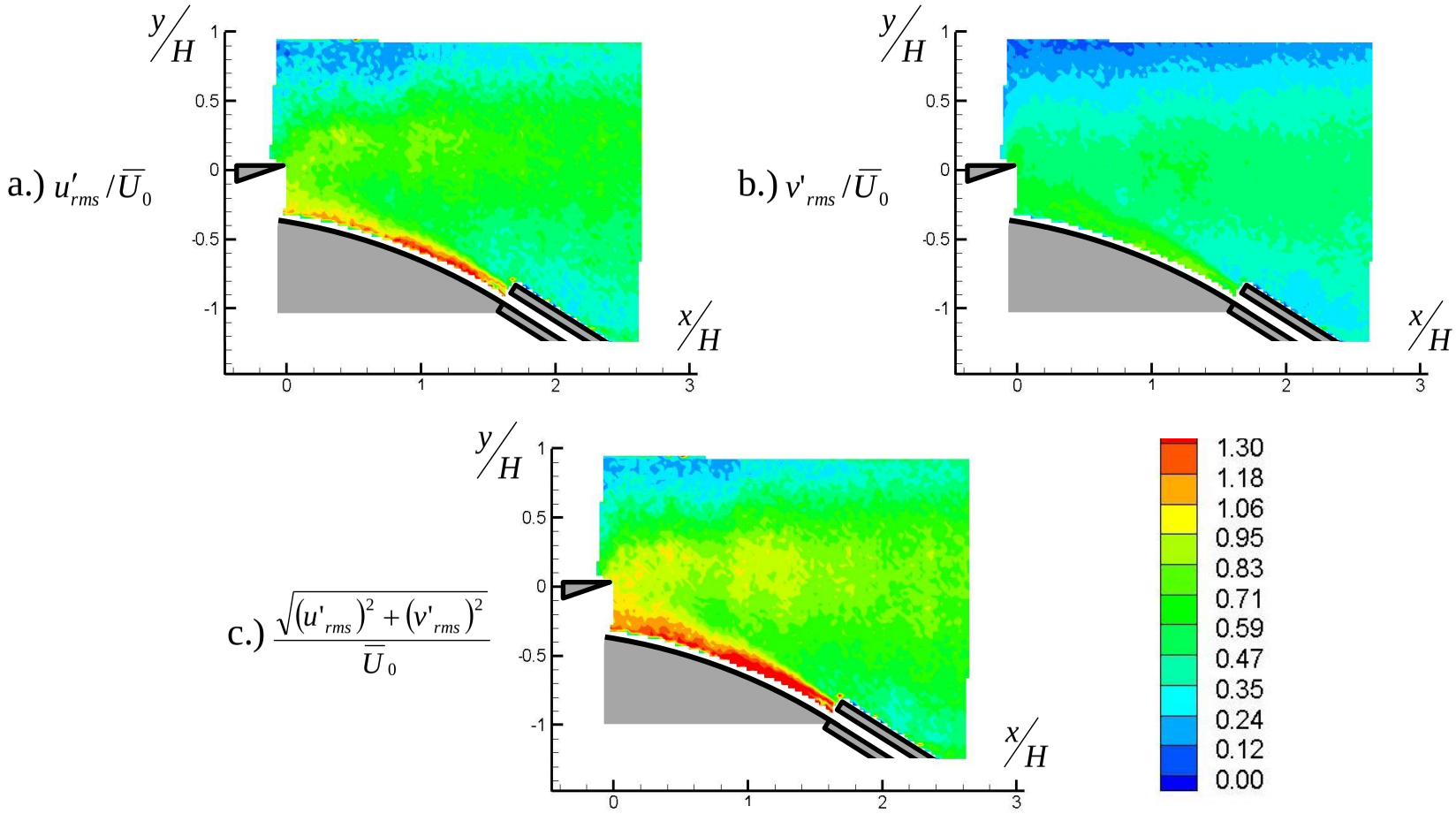

Figure 61: Rms streamwise, cross-stream and total turbulence contours for geometry II at 36% secondary flow rate

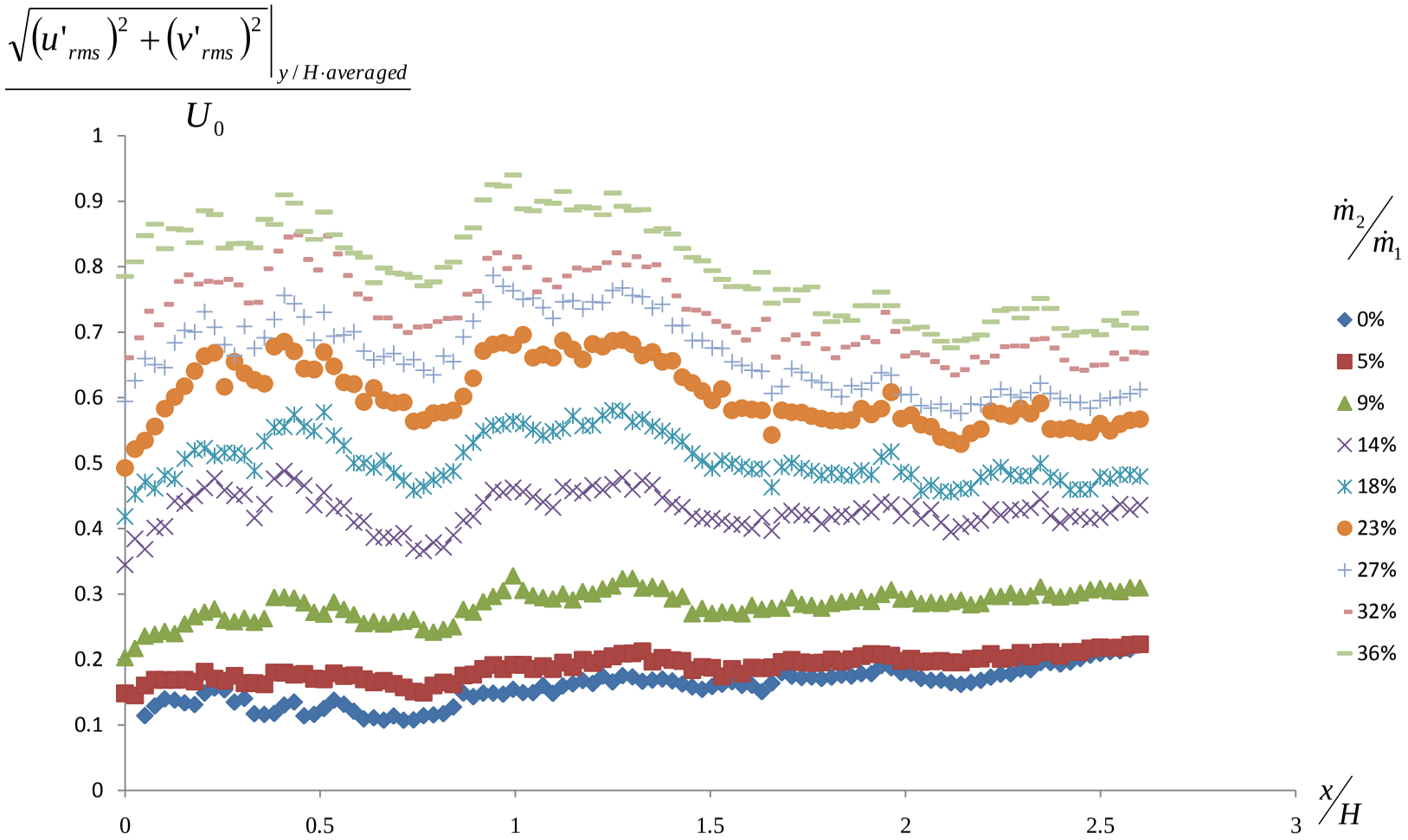

Figure 62: Cross-stream averaged total turbulence distributions for geometry II at all secondary flow rates

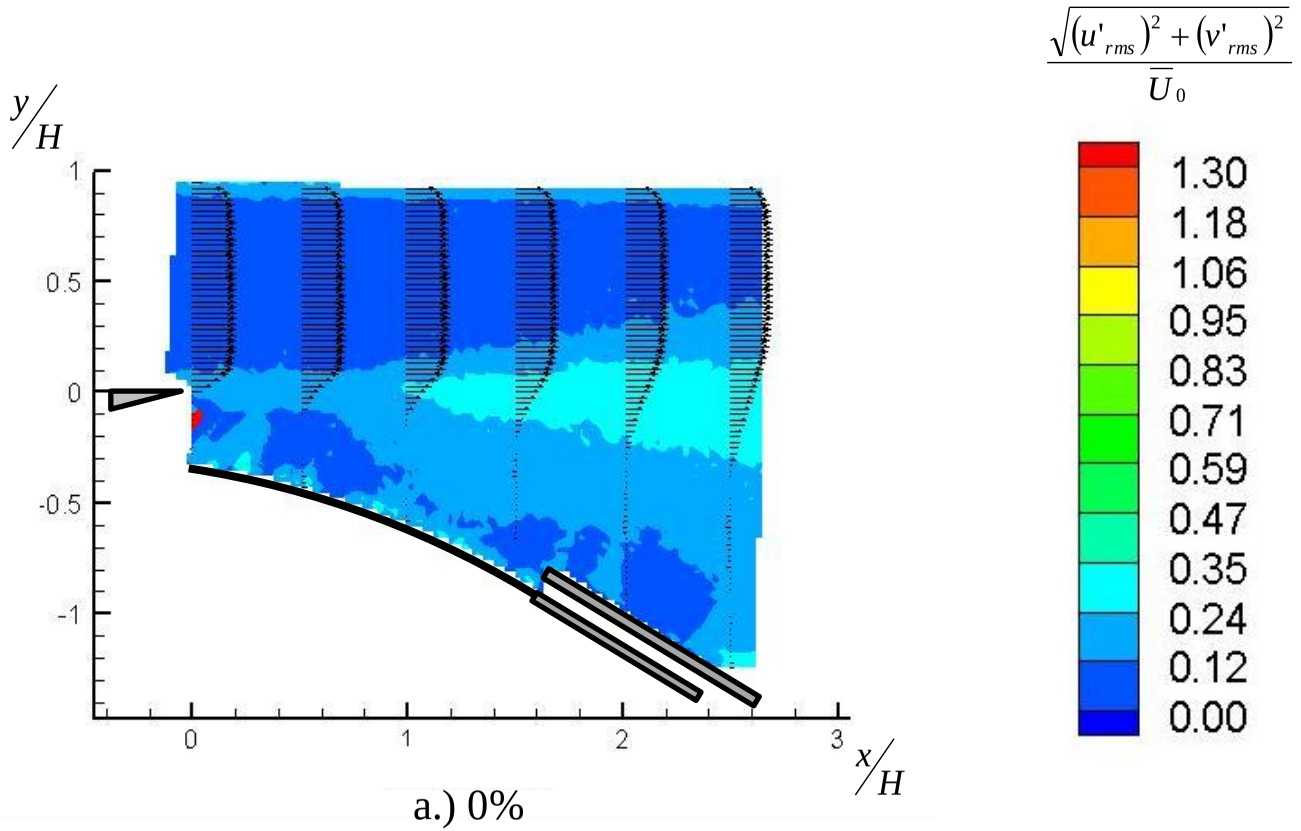

Figure 63: Total turbulence contours with streamwise velocity profiles for geometry II at all secondary flow rates

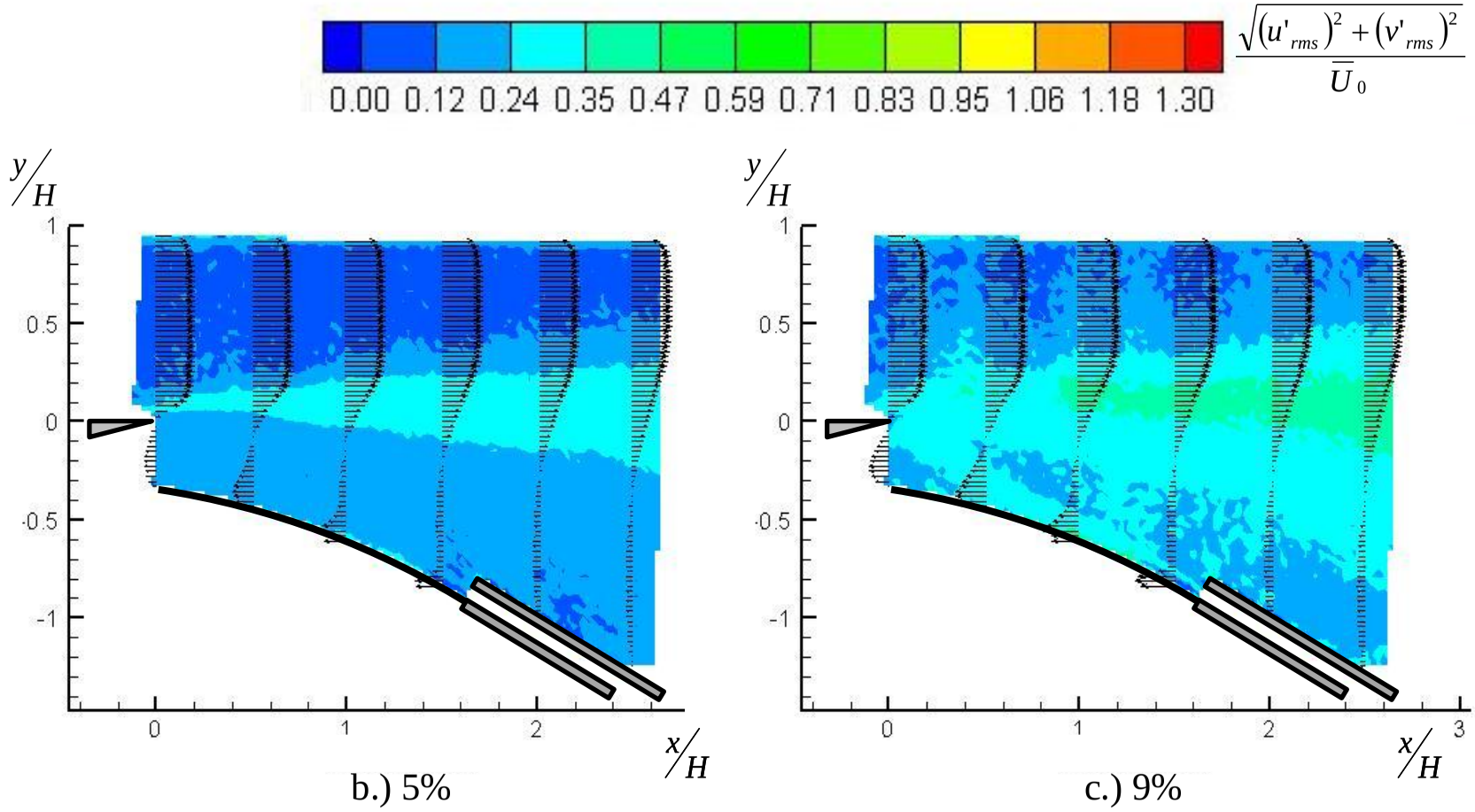

Figure 63: Total turbulence contours with streamwise velocity profiles for geometry II at all secondary flow rates

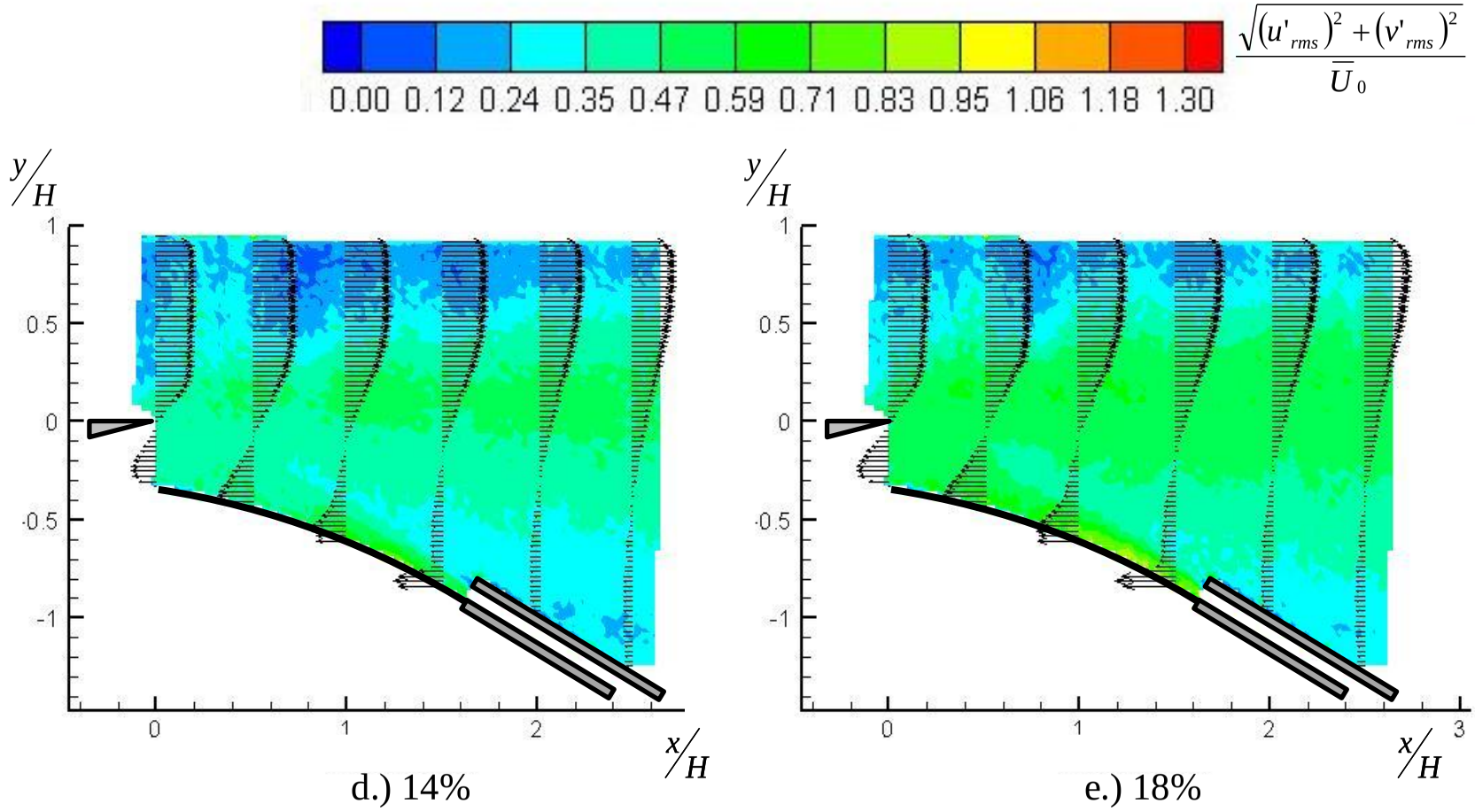

Figure 63: Total turbulence contours with streamwise velocity profiles for geometry II at all secondary flow rates

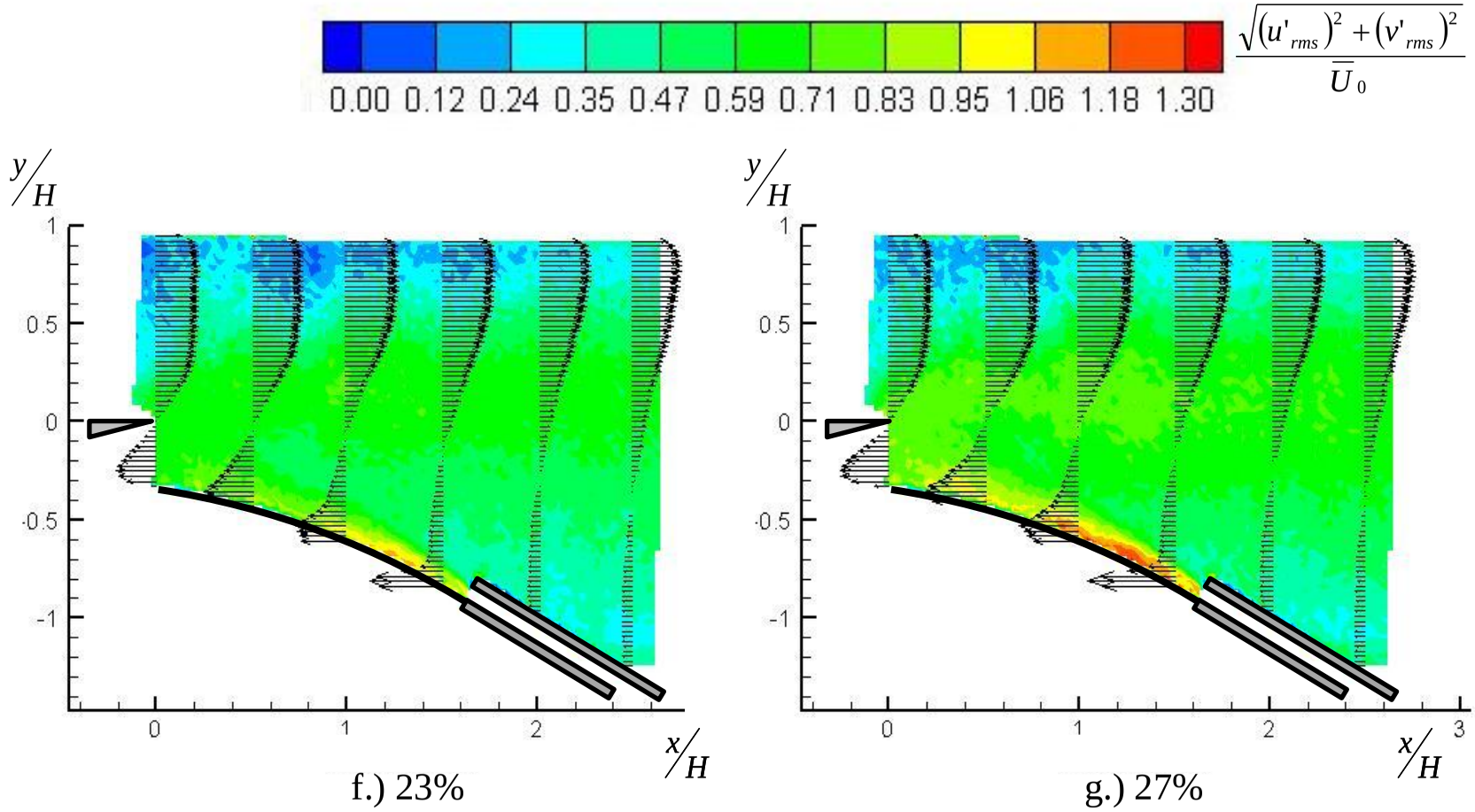

Figure 63: Total turbulence contours with streamwise velocity profiles for geometry II at all secondary flow rates

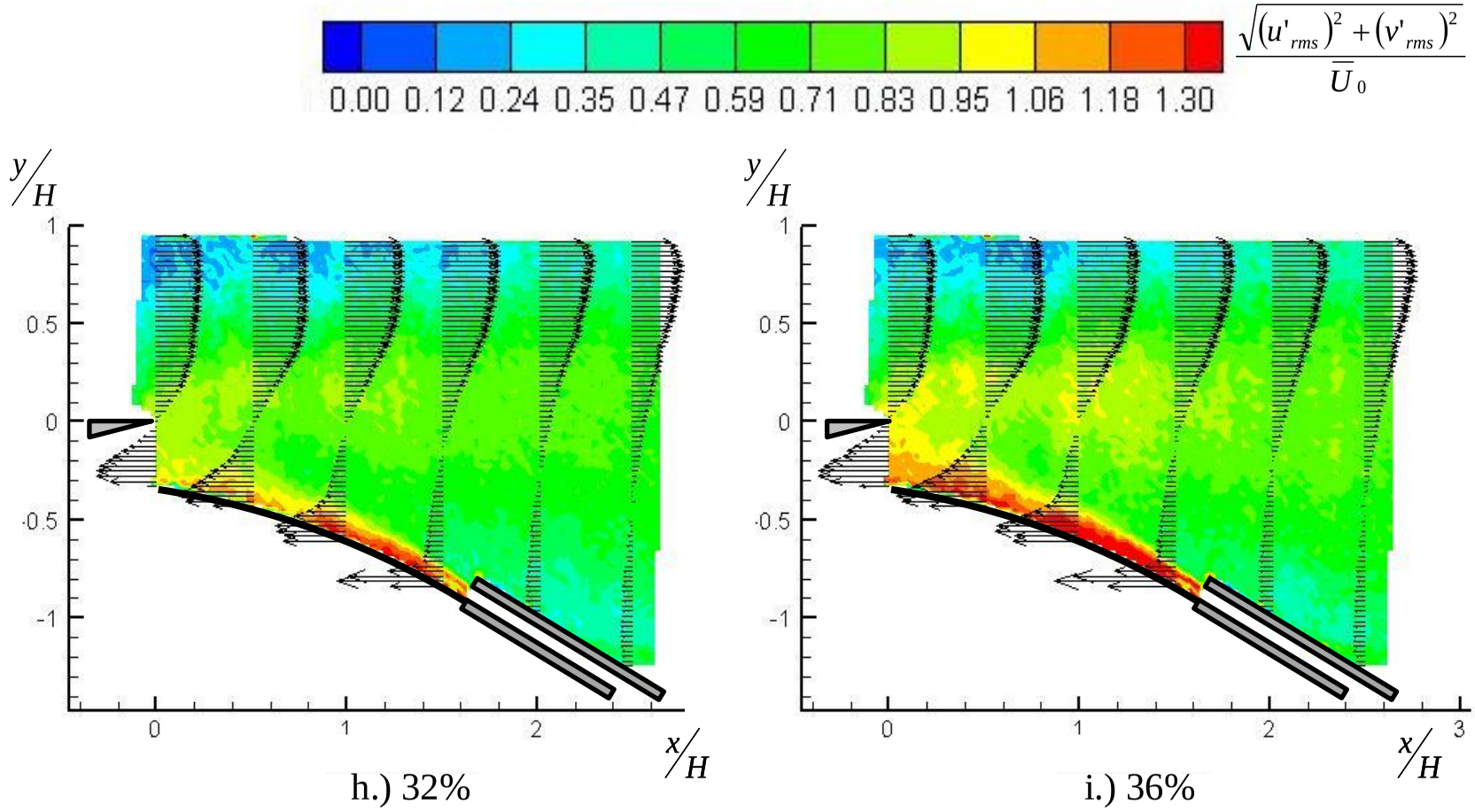

Figure 63: Total turbulence contours with streamwise velocity profiles for geometry II at all secondary flow rates

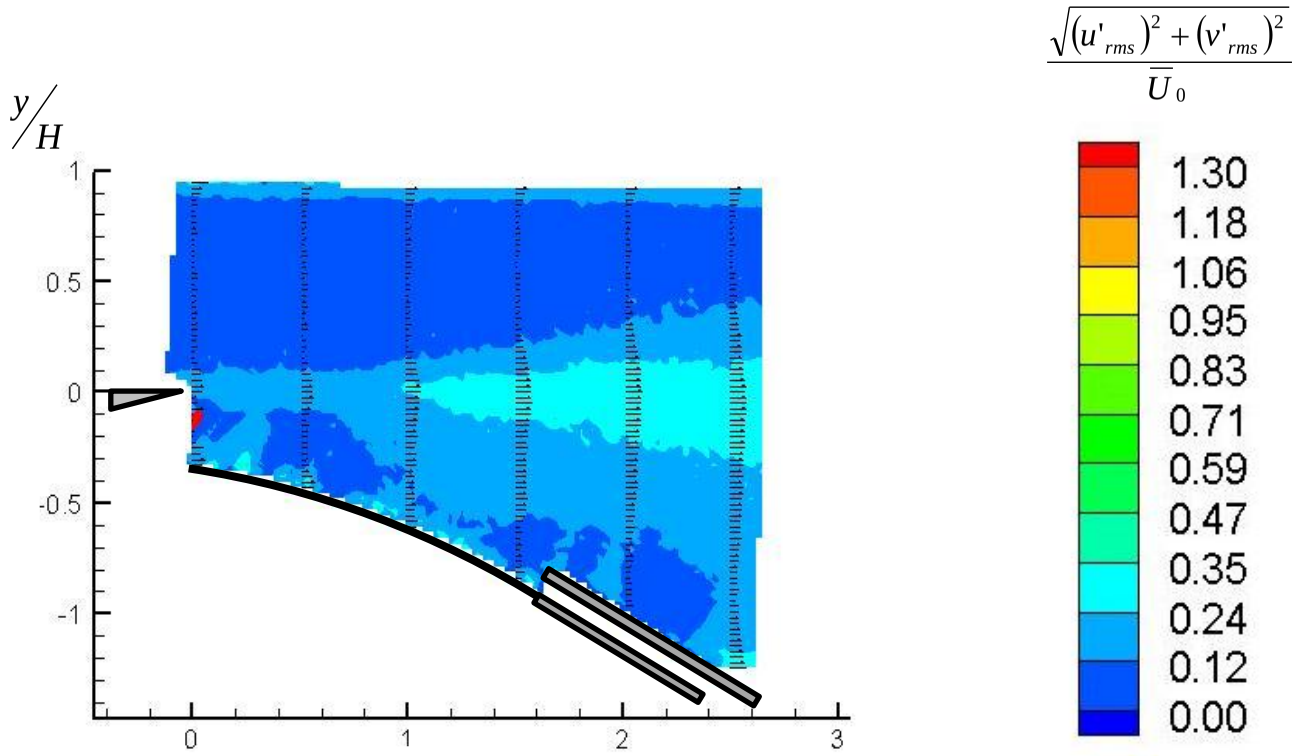

Figure 64: Total turbulence contours with turbulence profiles for geometry II at all secondary flow rates

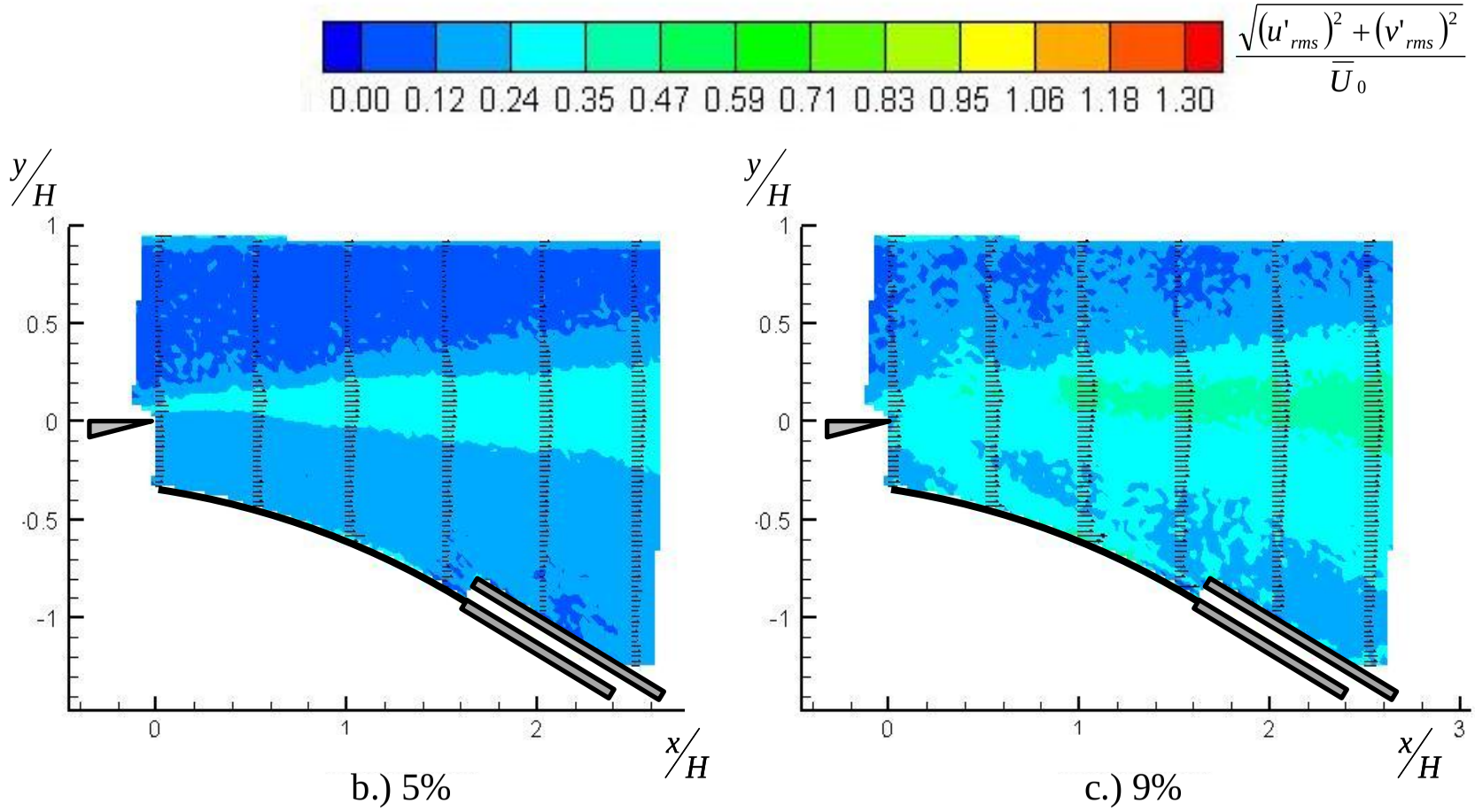

Figure 64: Total turbulence contours with turbulence profiles for geometry II at all secondary flow rates

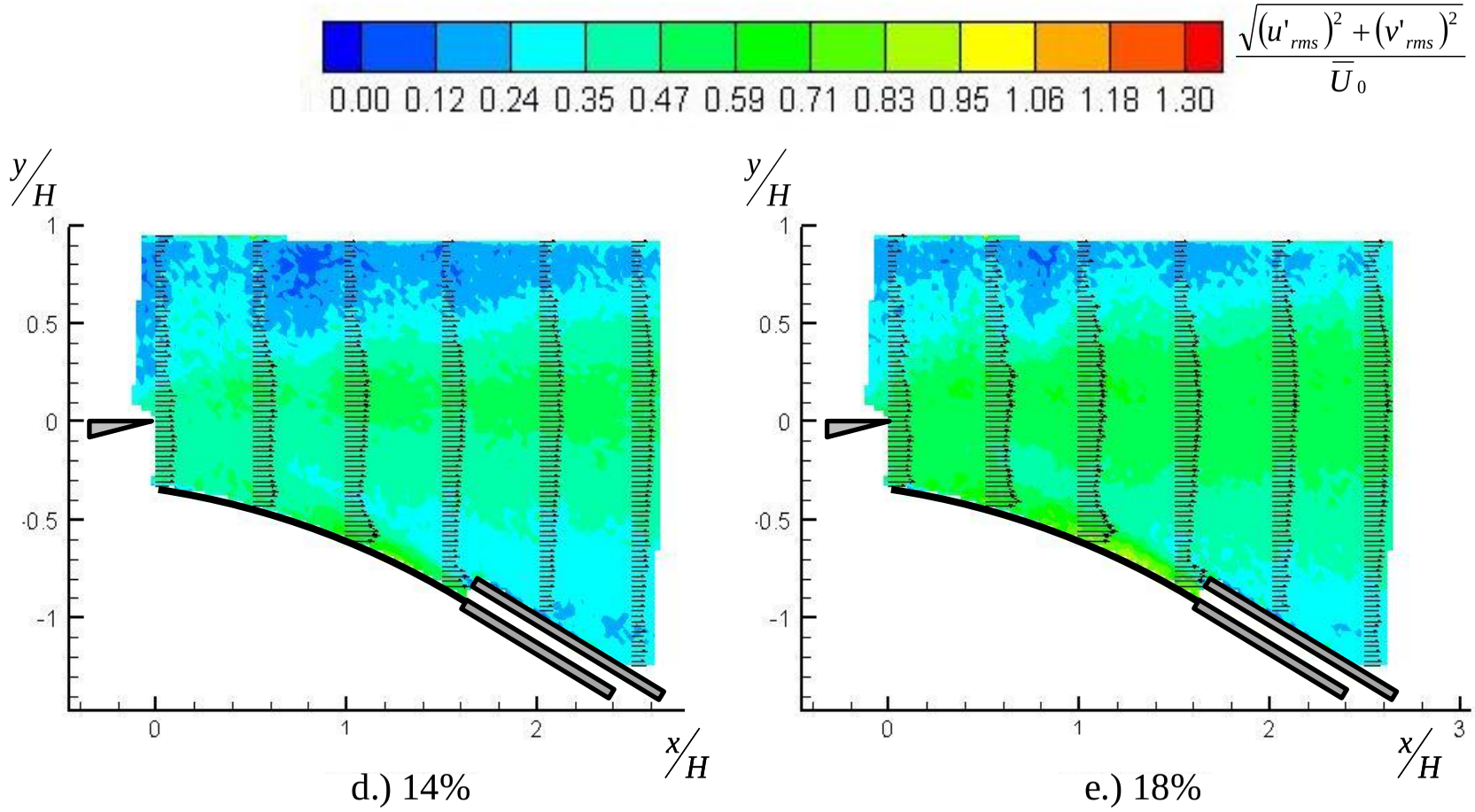

Figure 64: Total turbulence contours with turbulence profiles for geometry II at all secondary flow rates

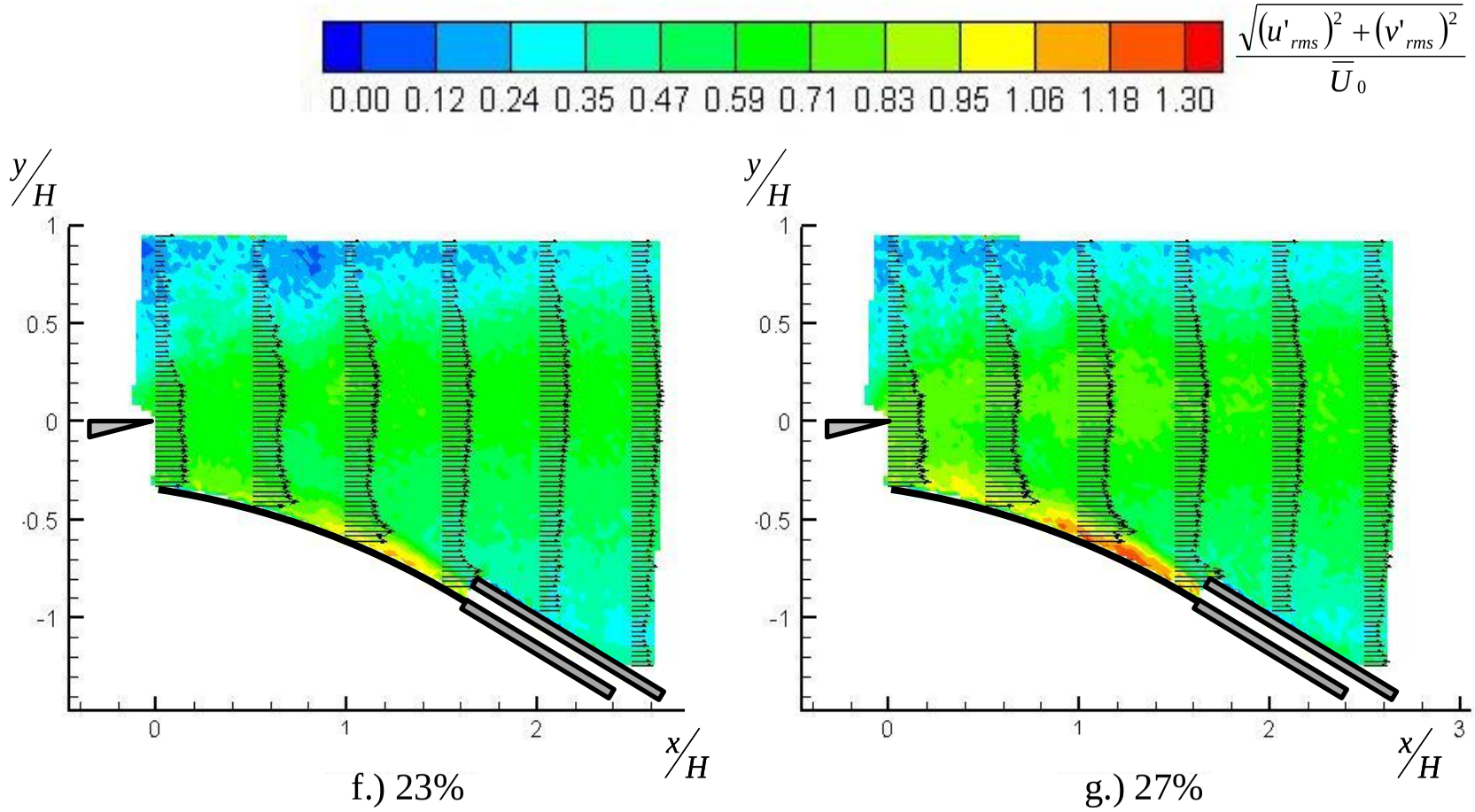

Figure 64: Total turbulence contours with turbulence profiles for geometry II at all secondary flow rates

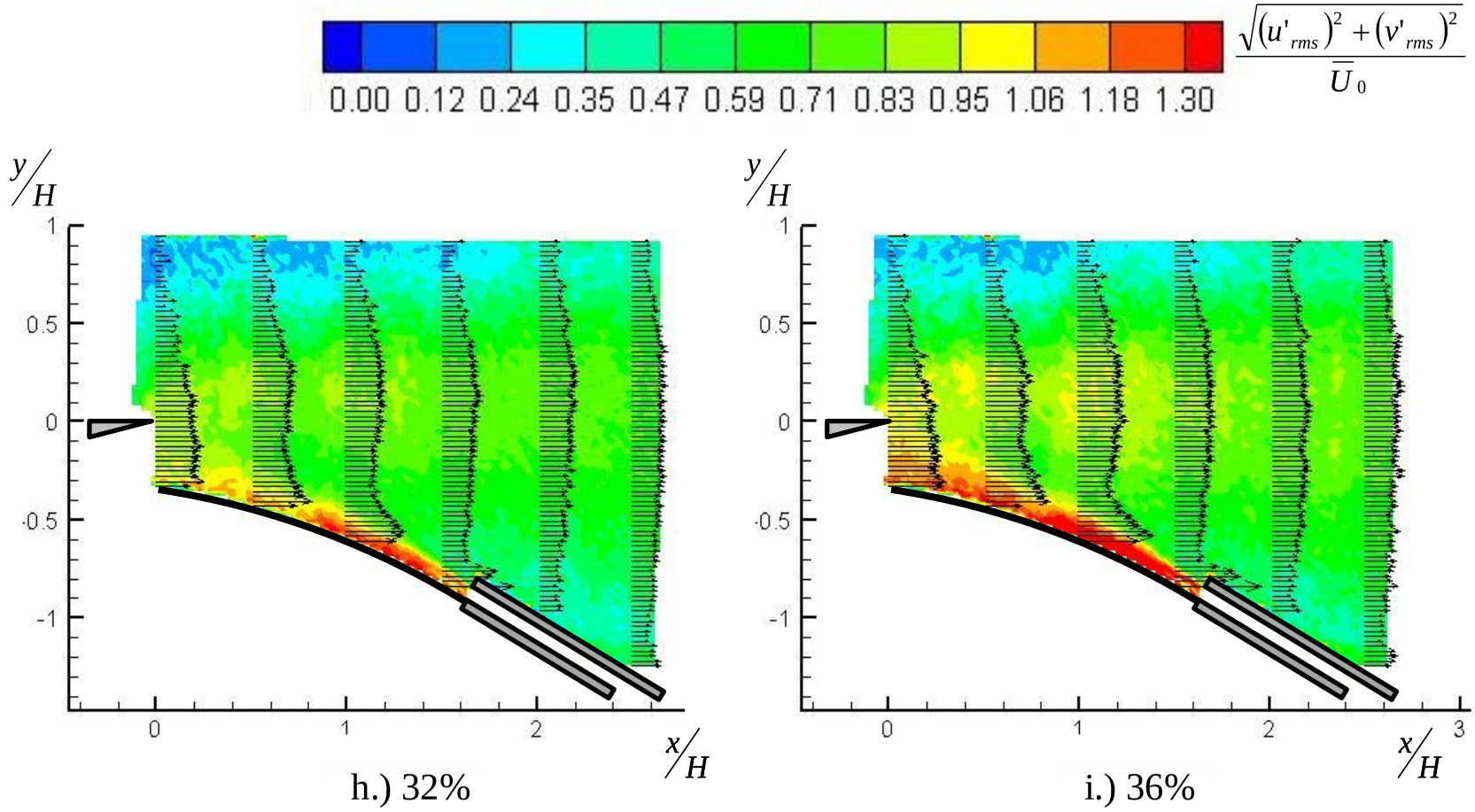

Figure 64: Total turbulence contours with turbulence profiles for geometry II at all secondary flow rates

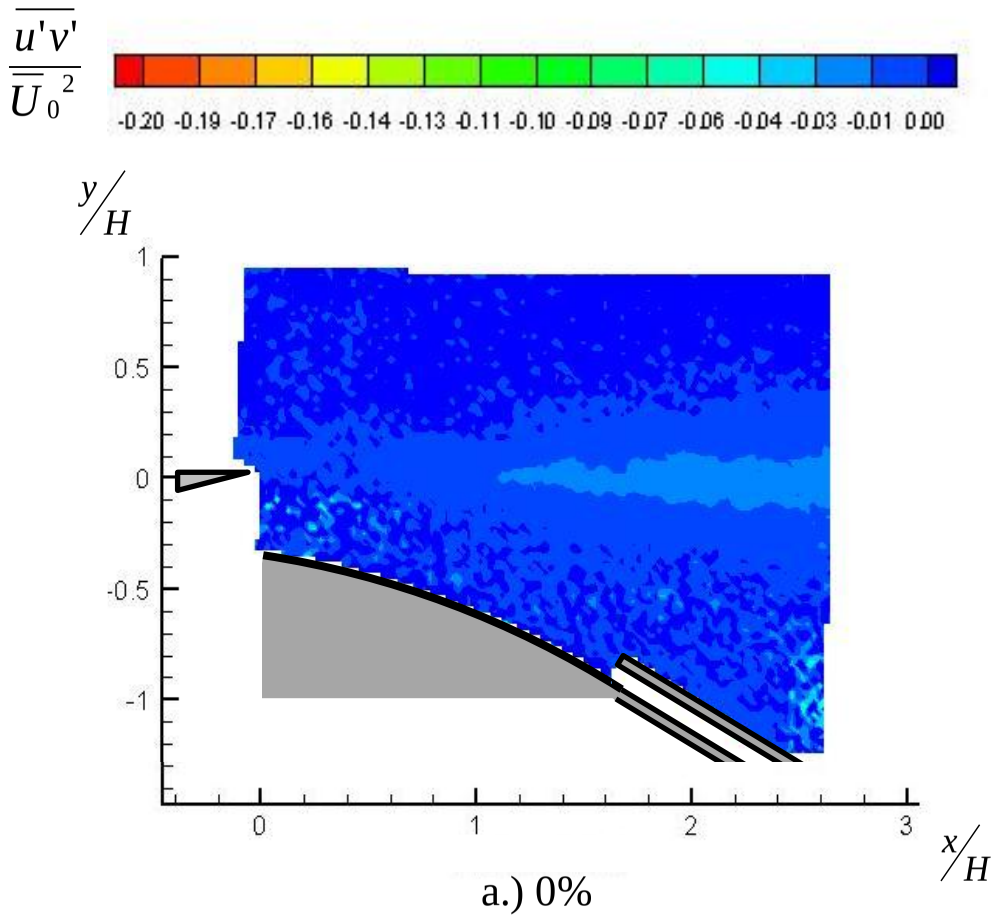

a.) 0%

Figure 65: Reynolds stress contours for geometry II at all secondary flow rates

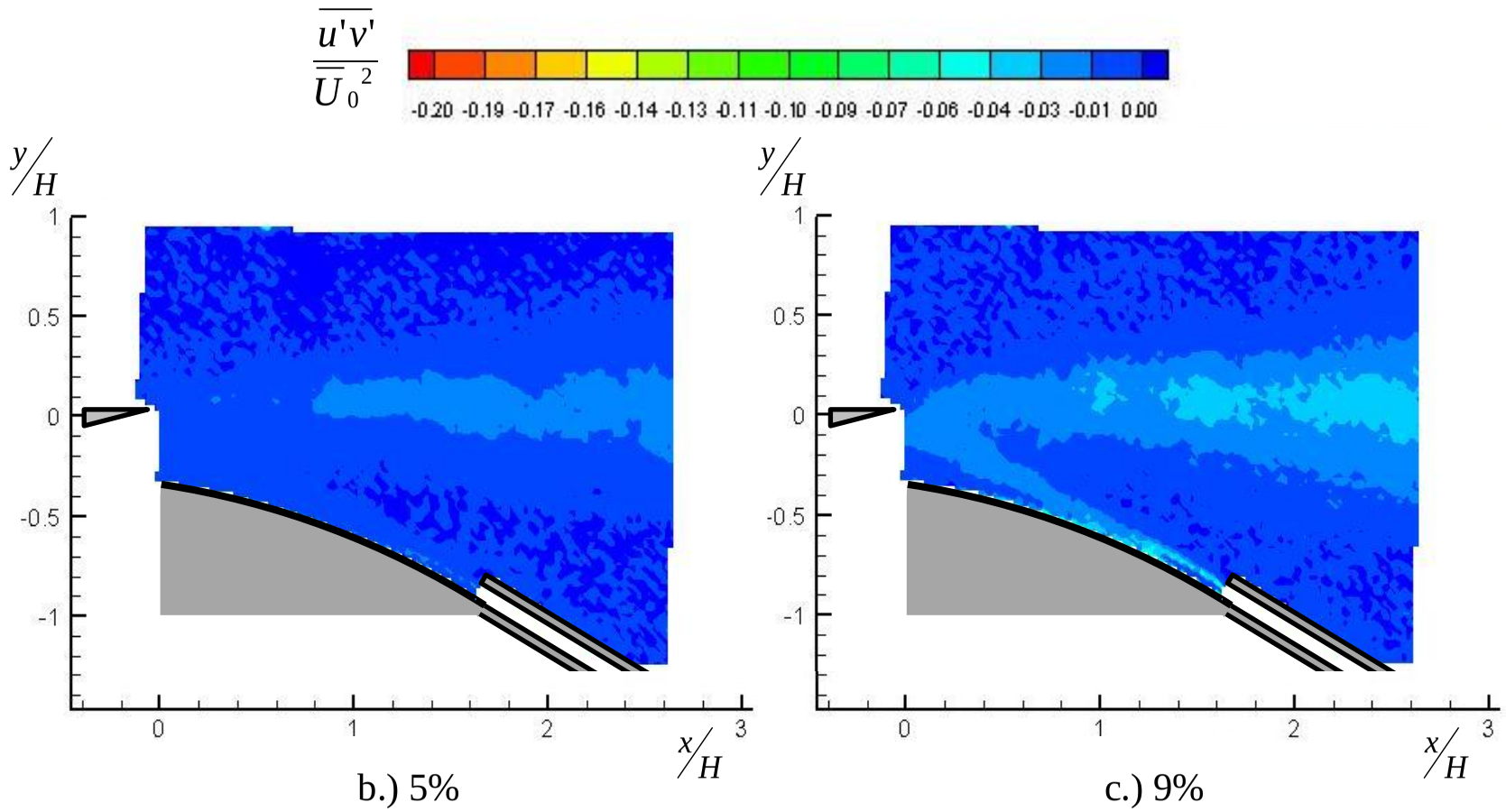

Figure 65: Reynolds stress contours for geometry II at all secondary flow rates

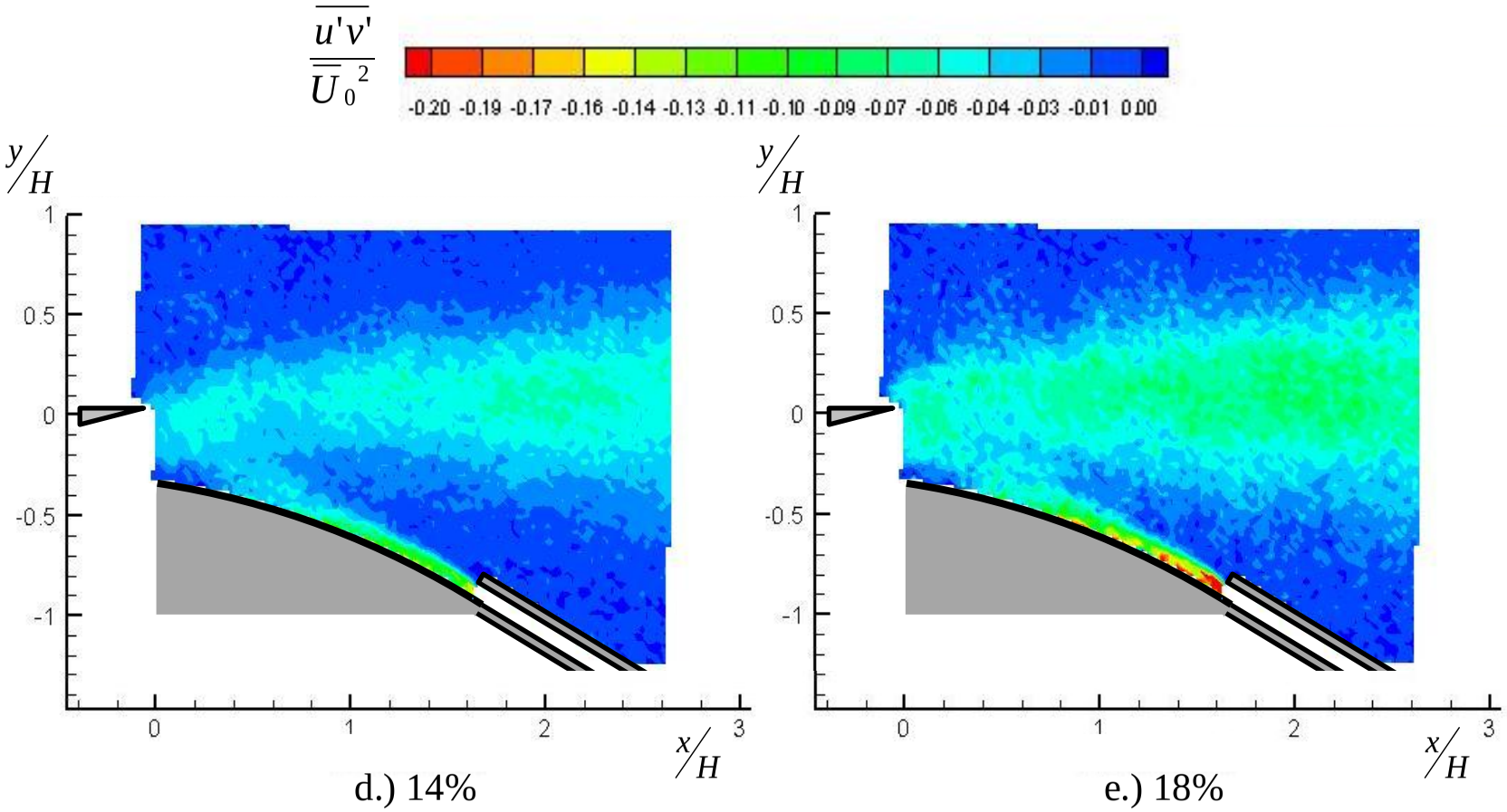

Figure 65: Reynolds stress contours for geometry II at all secondary flow rates

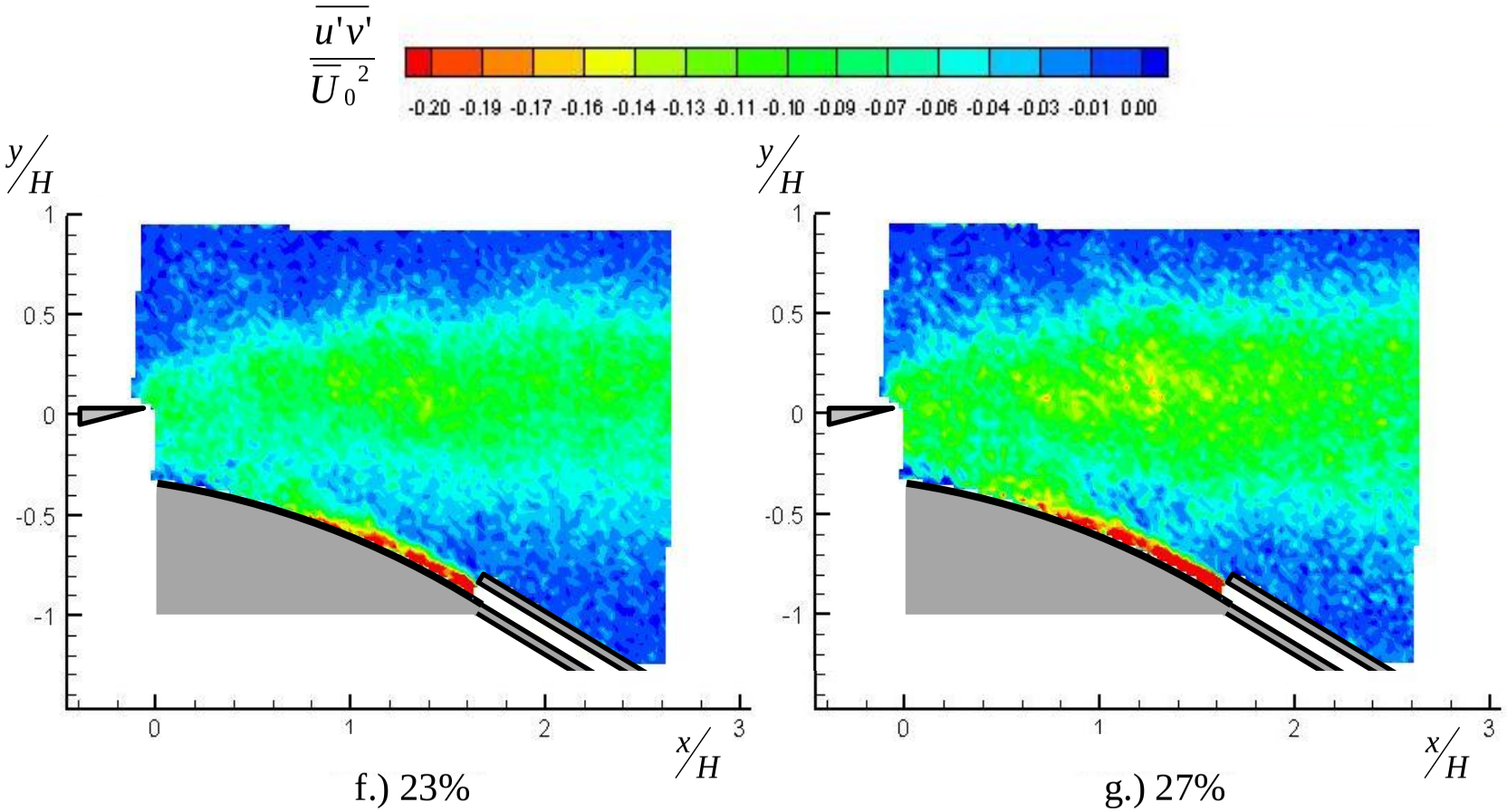

Figure 65: Reynolds stress contours for geometry II at all secondary flow rates

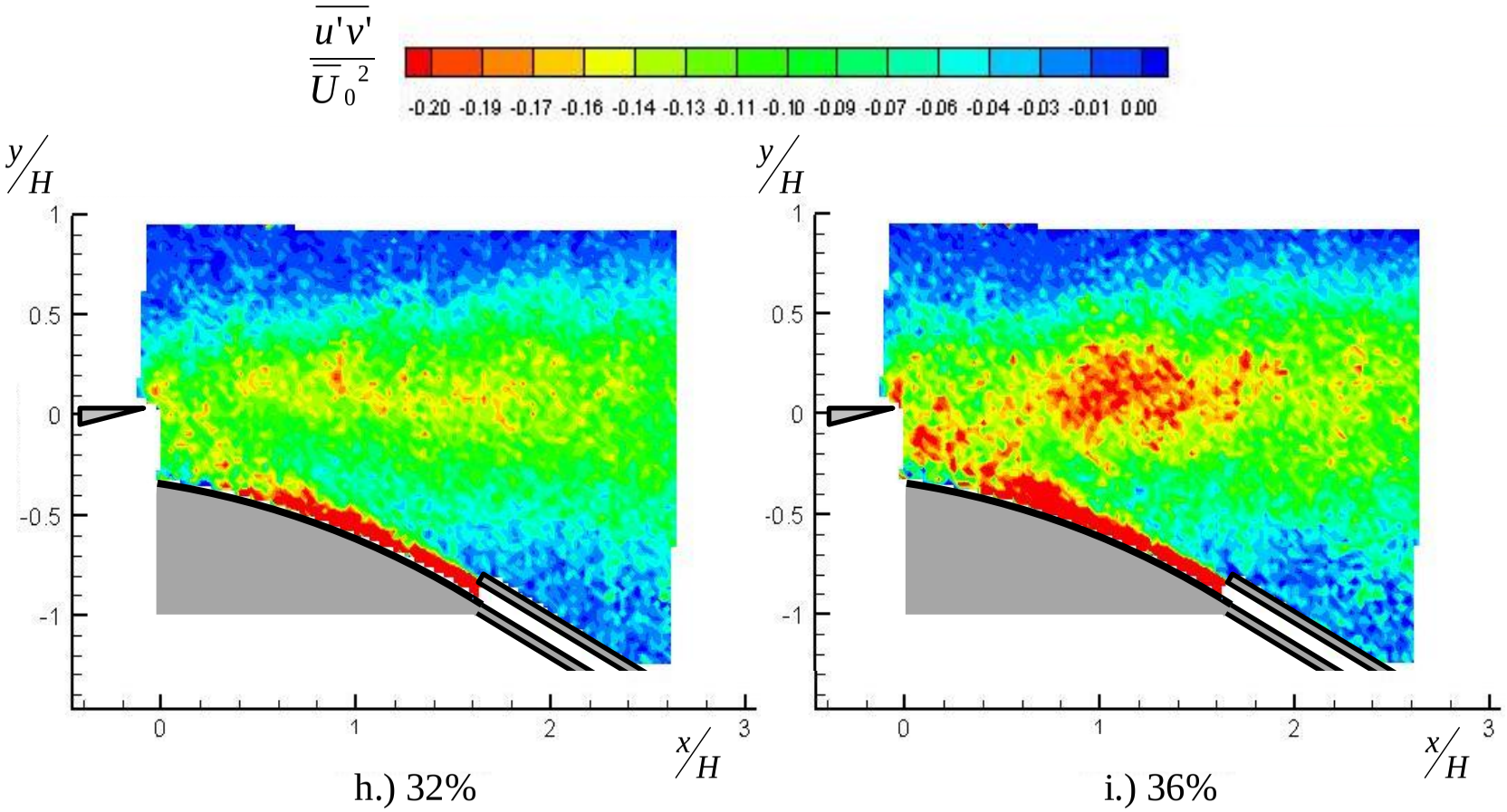

Figure 65: Reynolds stress contours for geometry II at all secondary flow rates

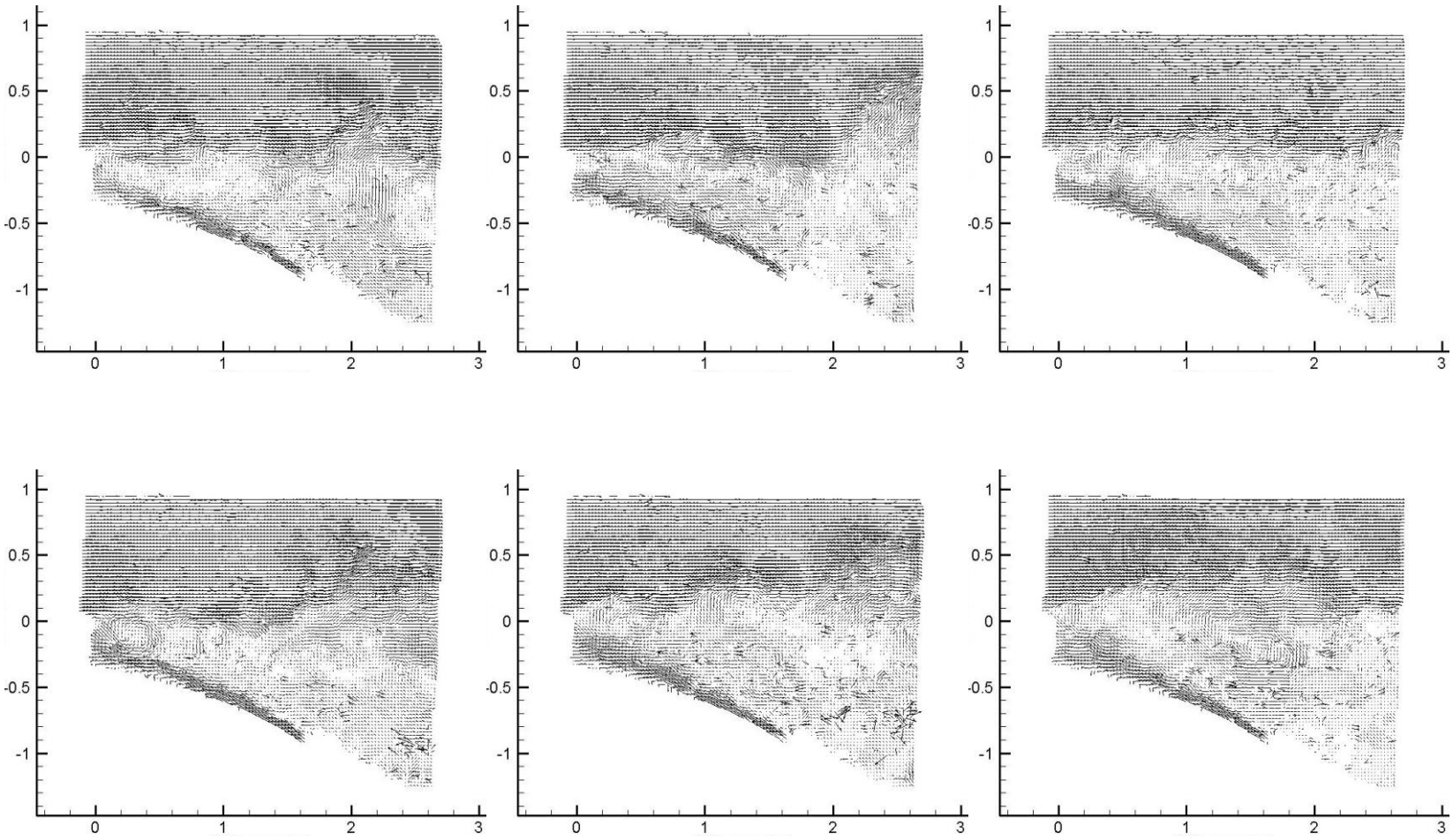

Figure 66: Instantaneous velocity vector fields for geometry II for the 5% secondary flow rate

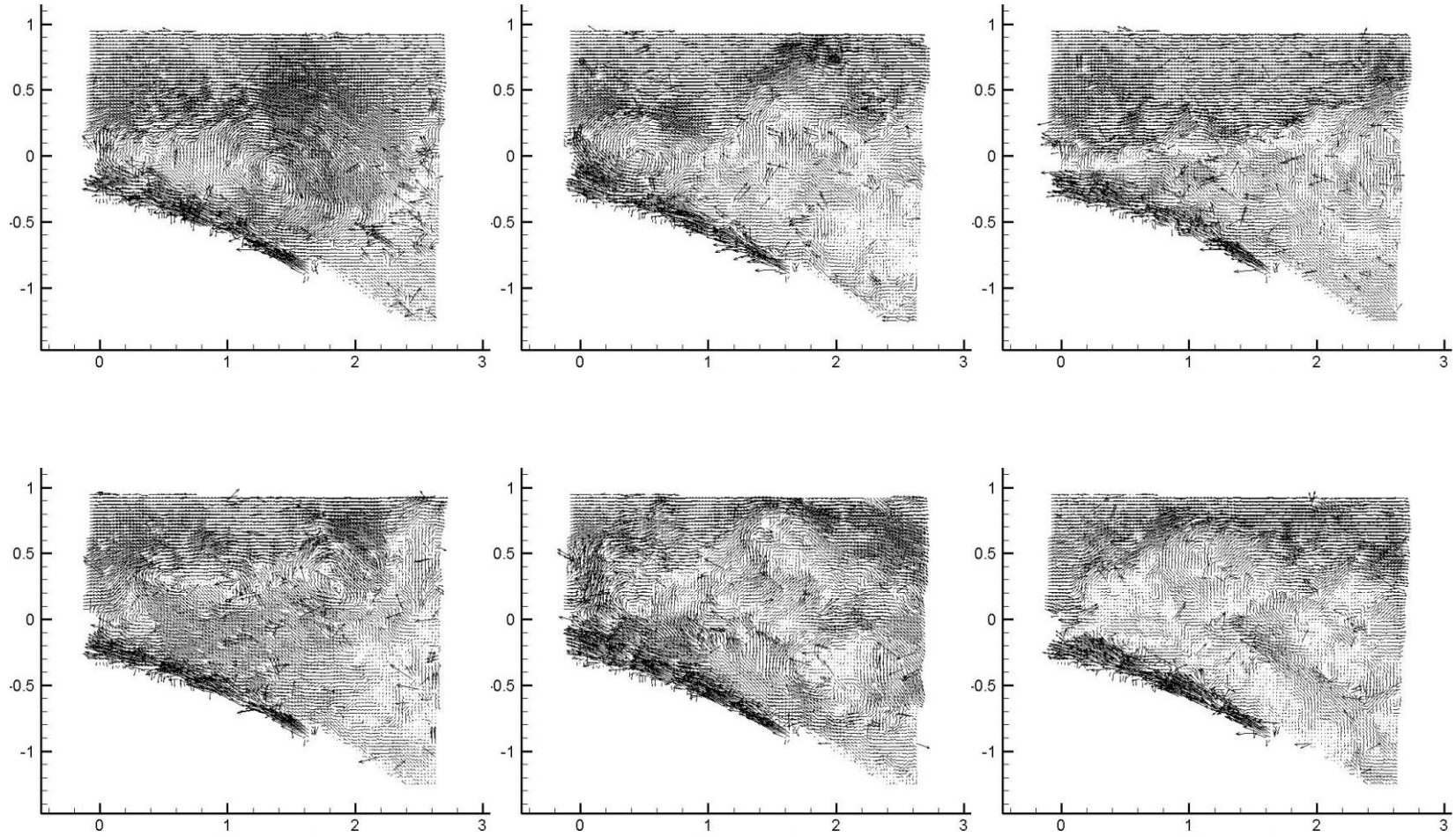

Figure 67: Instantaneous velocity vector fields for geometry II for the 32% secondary flow rate

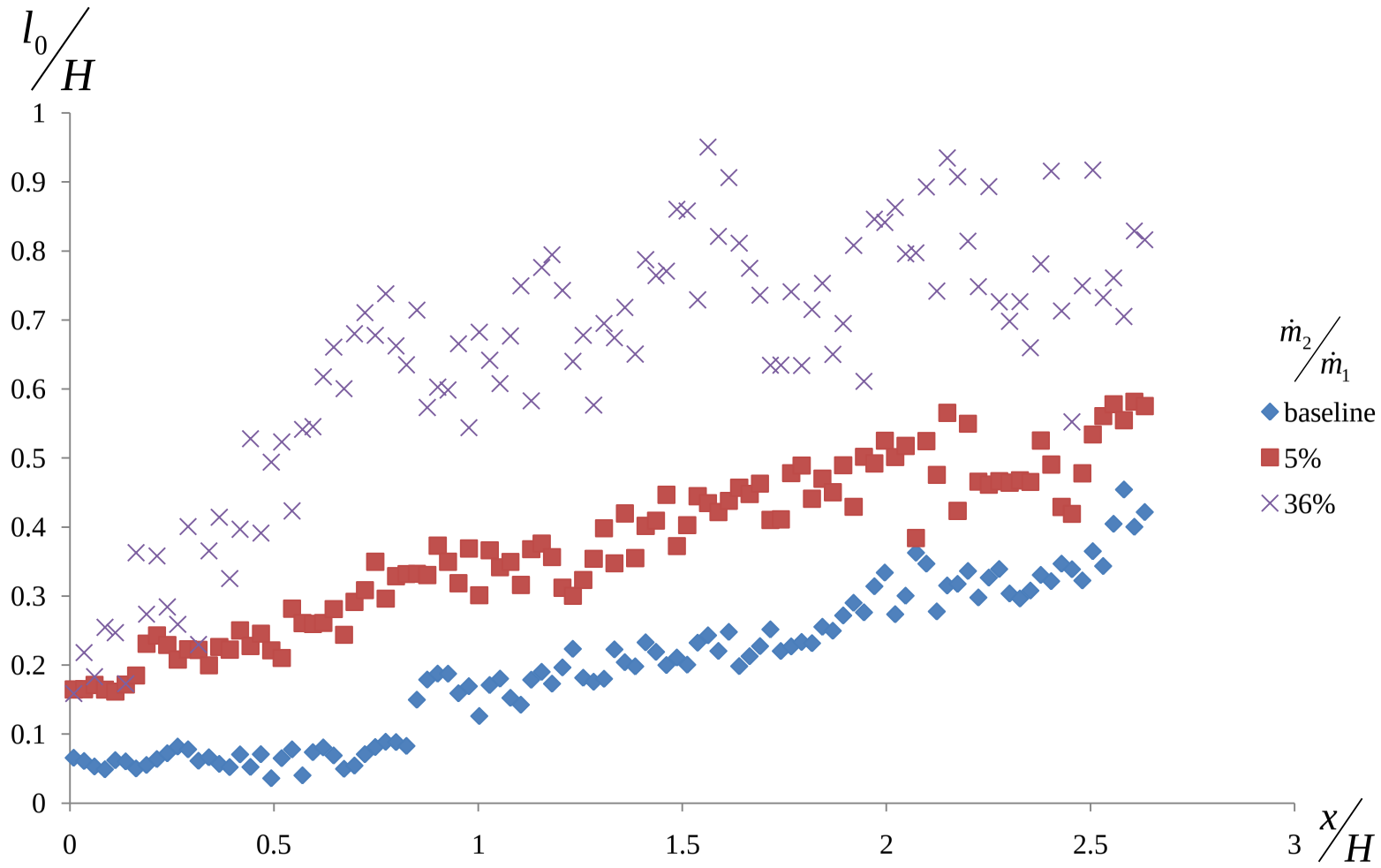

Figure 68: Cross-stream integral length scales in geometry II for the 0%, 5% and 36% secondary flow rates

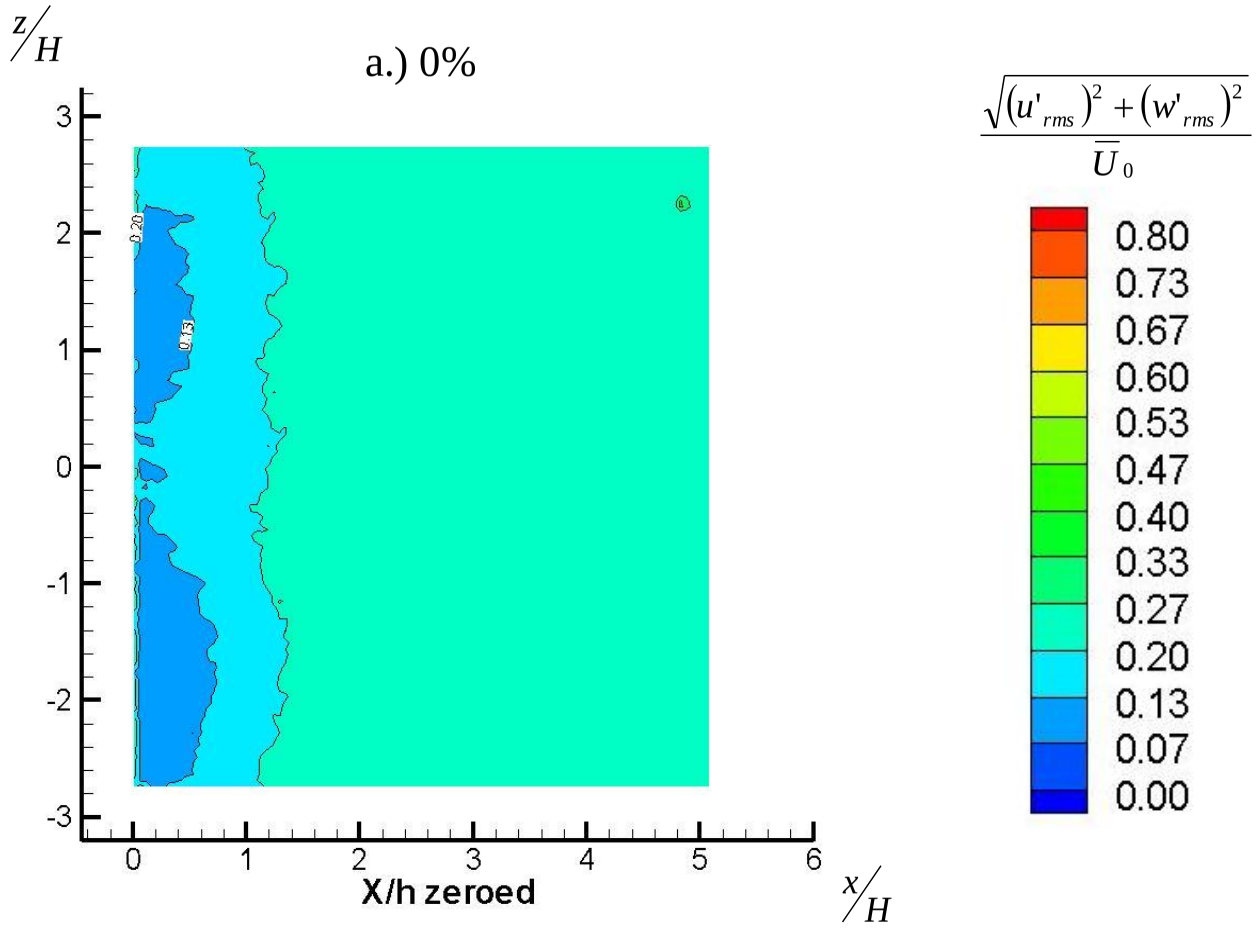

Figure 69 a: Total turbulence contours for spanwise PIV experiments in geometry II for all secondary flow rates

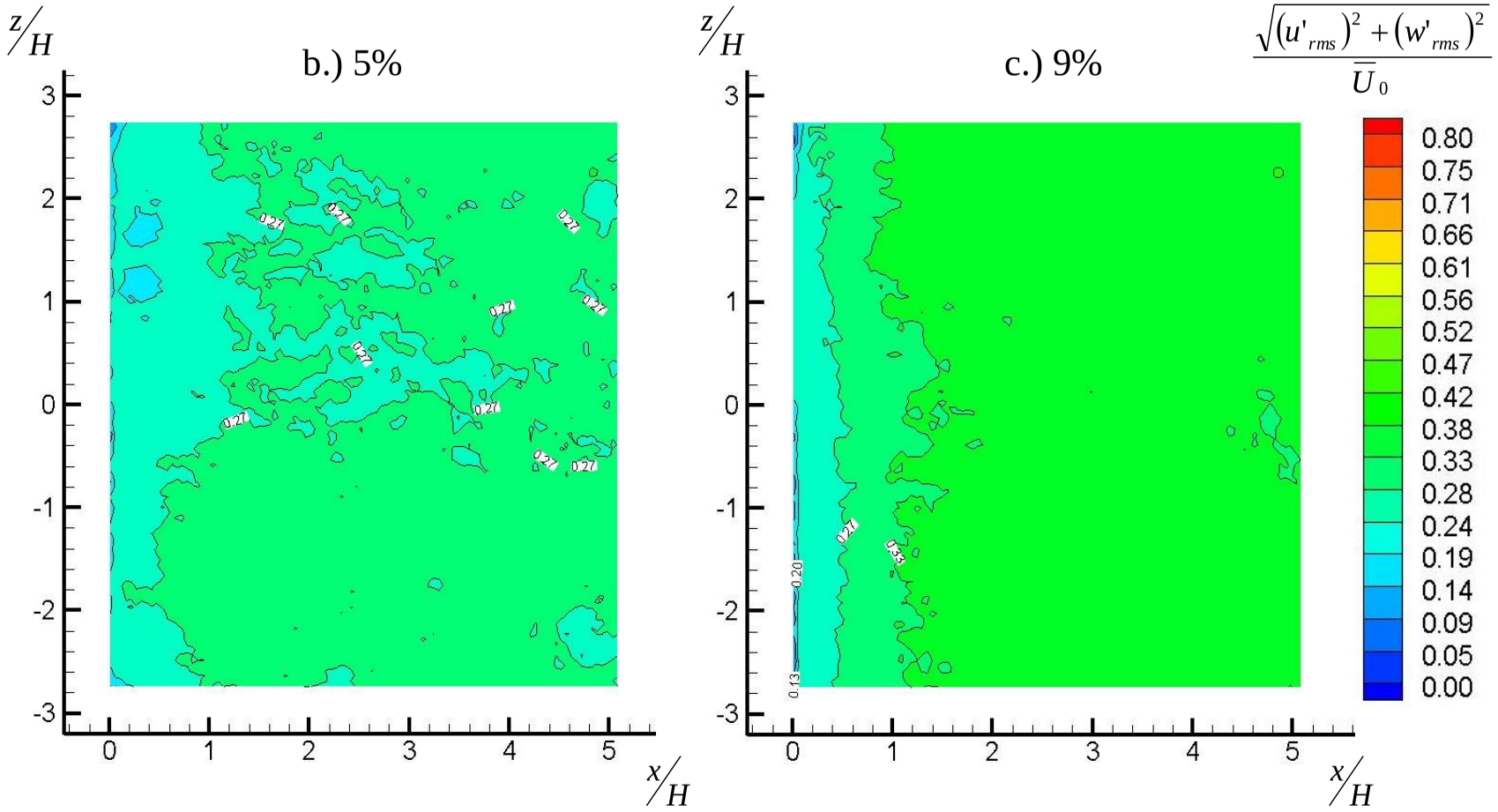

Figure 69 b & c: Total turbulence contours for spanwise PIV experiments in geometry II for all secondary flow rates

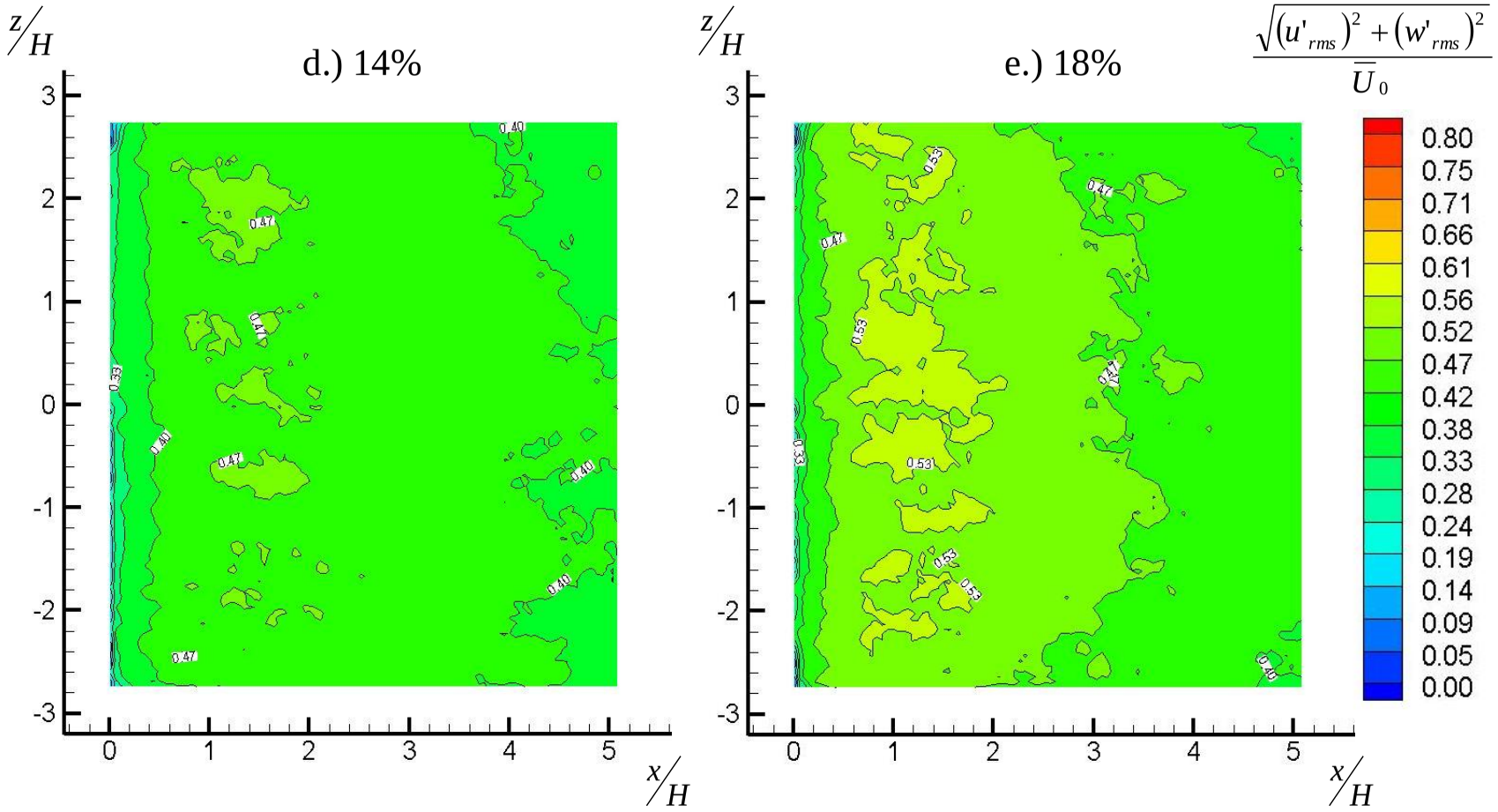

Figure 69 d & e: Total turbulence contours for spanwise PIV experiments in geometry II for all secondary flow rates

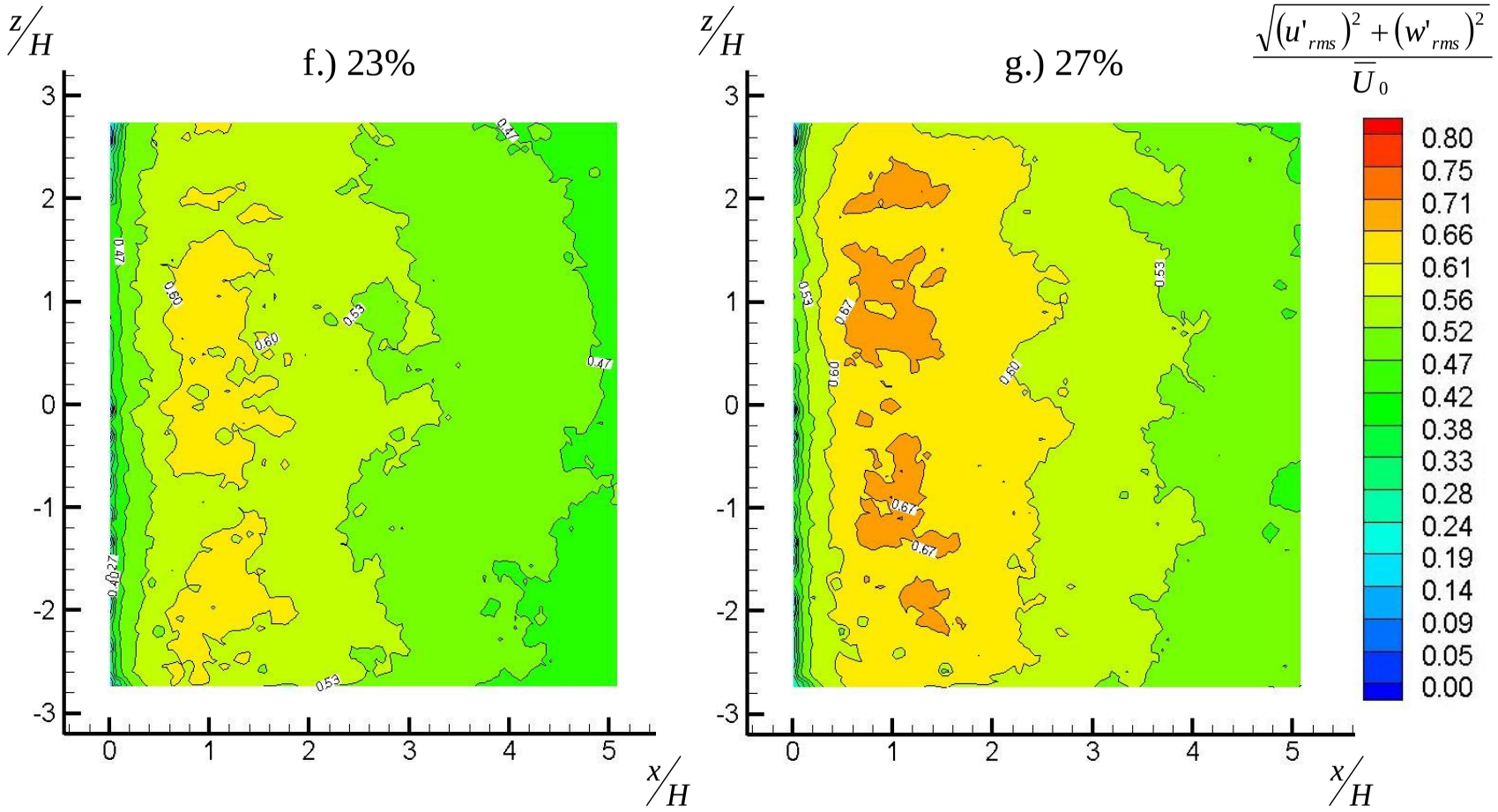

Figure 69 f & g: Total turbulence contours for spanwise PIV experiments in geometry II for all secondary flow rates

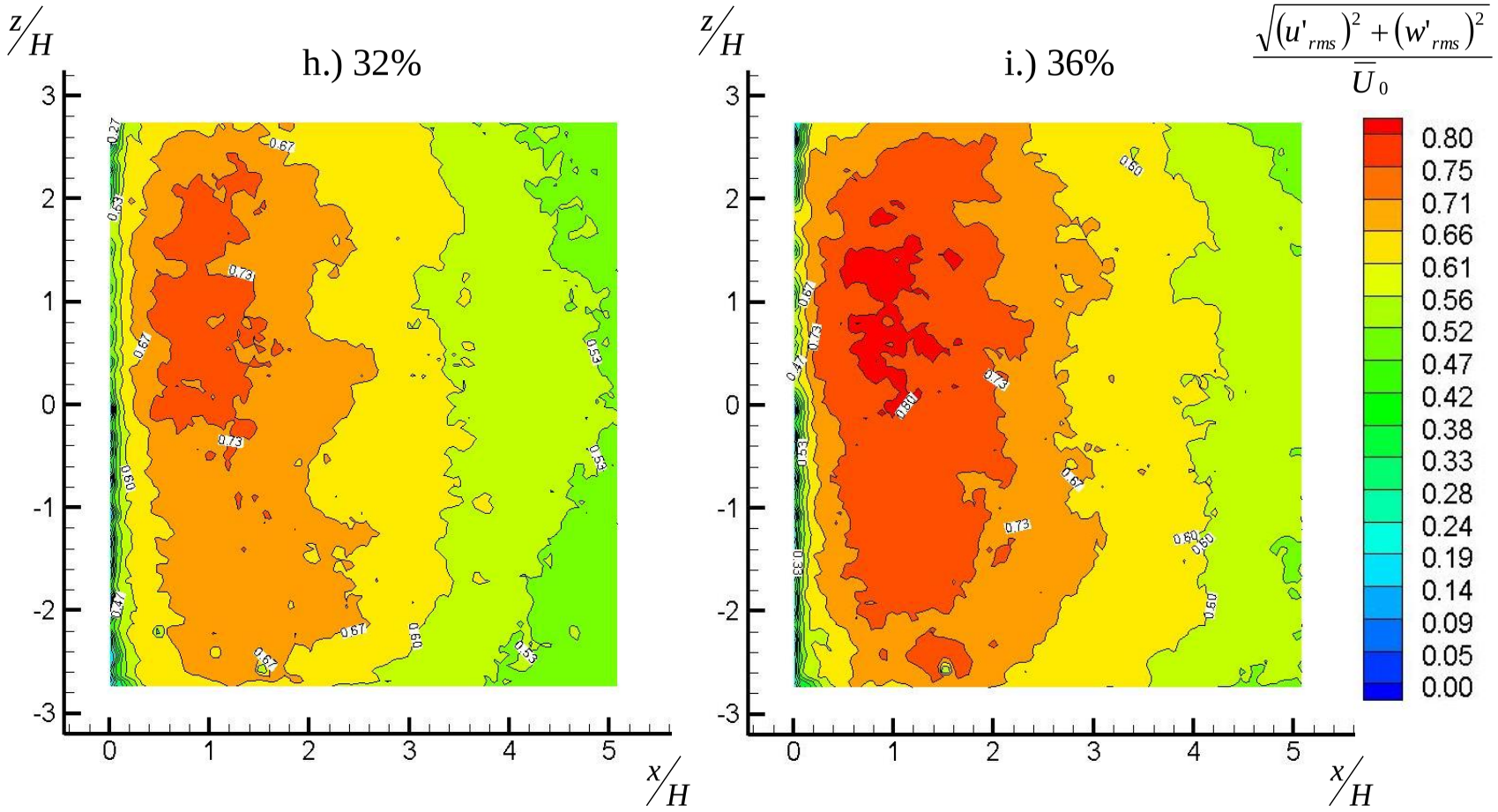

Figure 69 h & i: Total turbulence contours for spanwise PIV experiments in geometry II for all secondary flow rates

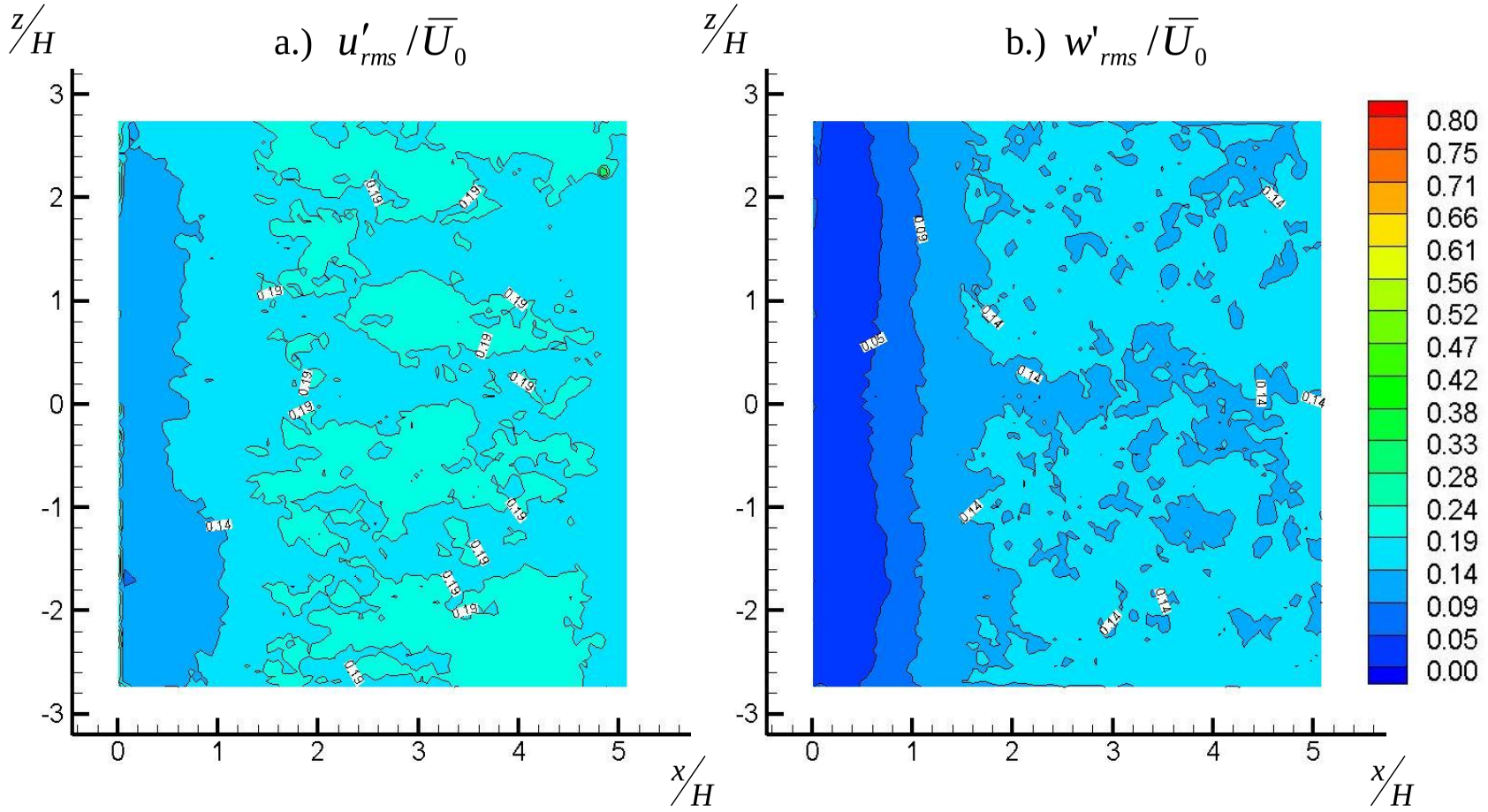

Figure 70: Rms a.) streamwise and b.) spanwise velocity fluctuations for 0% secondary flow rate

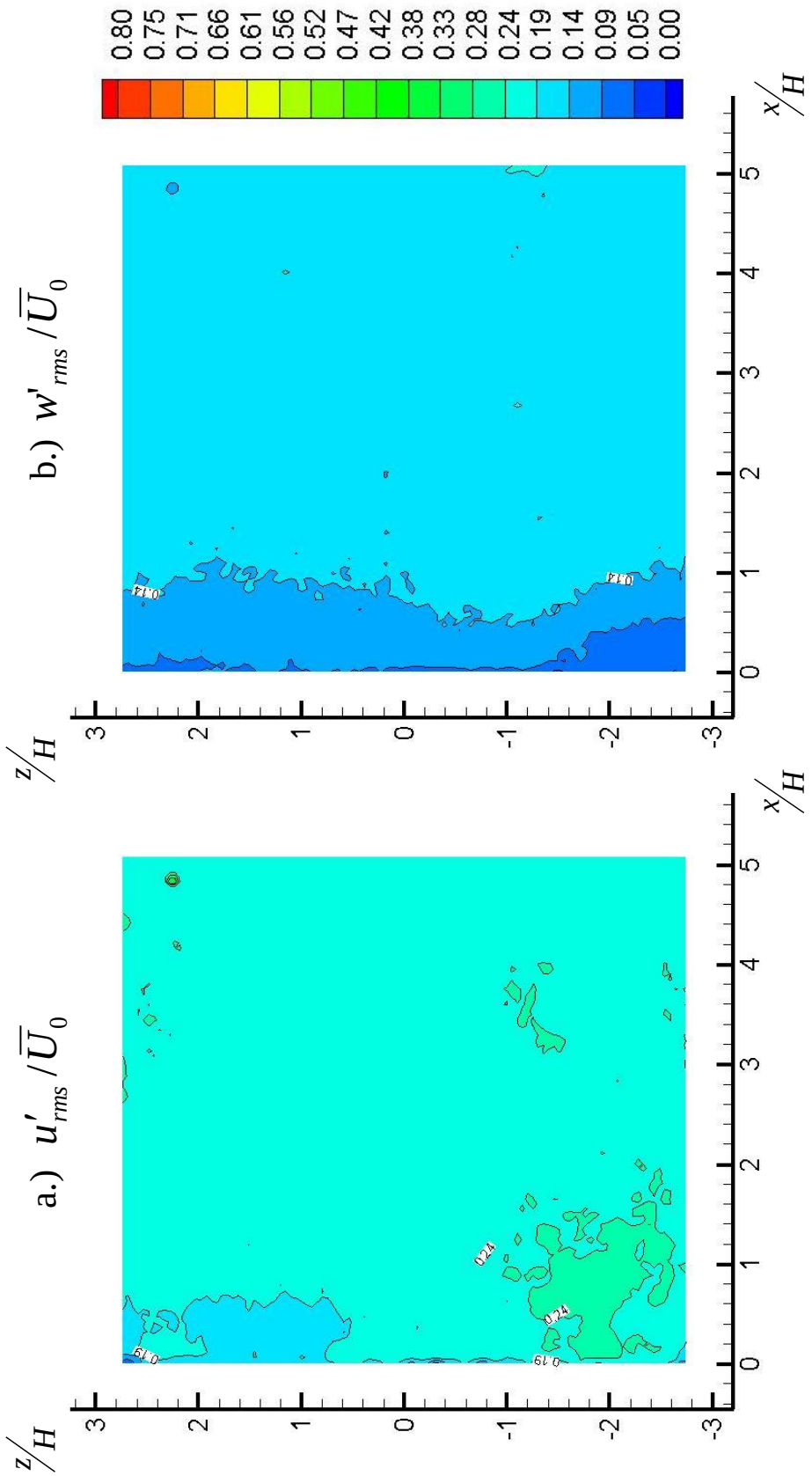

Figure 71: Rms a.) streamwise and b.) spanwise velocity fluctuations for 5% secondary flow rate

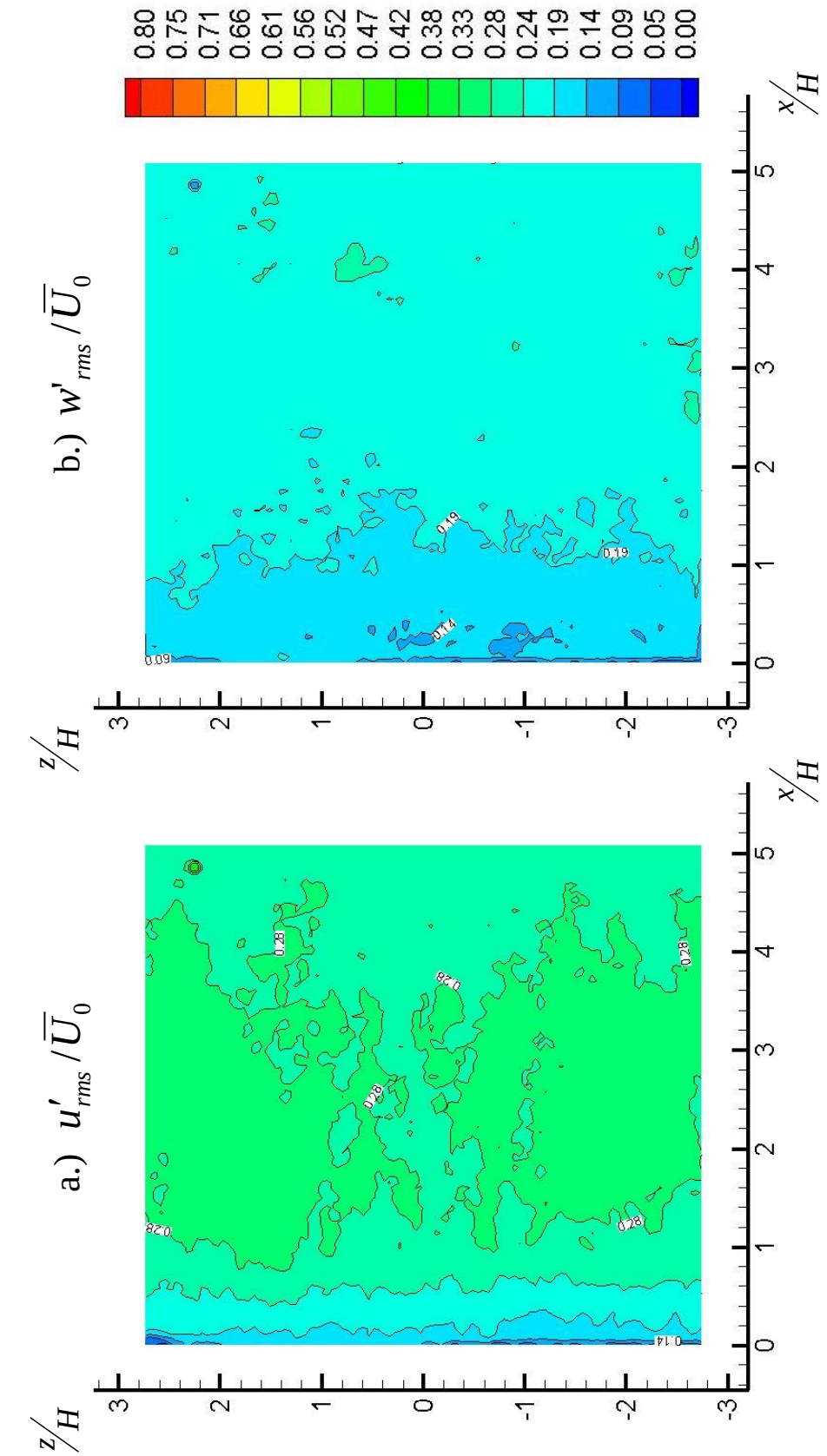

Figure 72: Rms a.) streamwise and b.) spanwise velocity fluctuations for 9% secondary flow rate

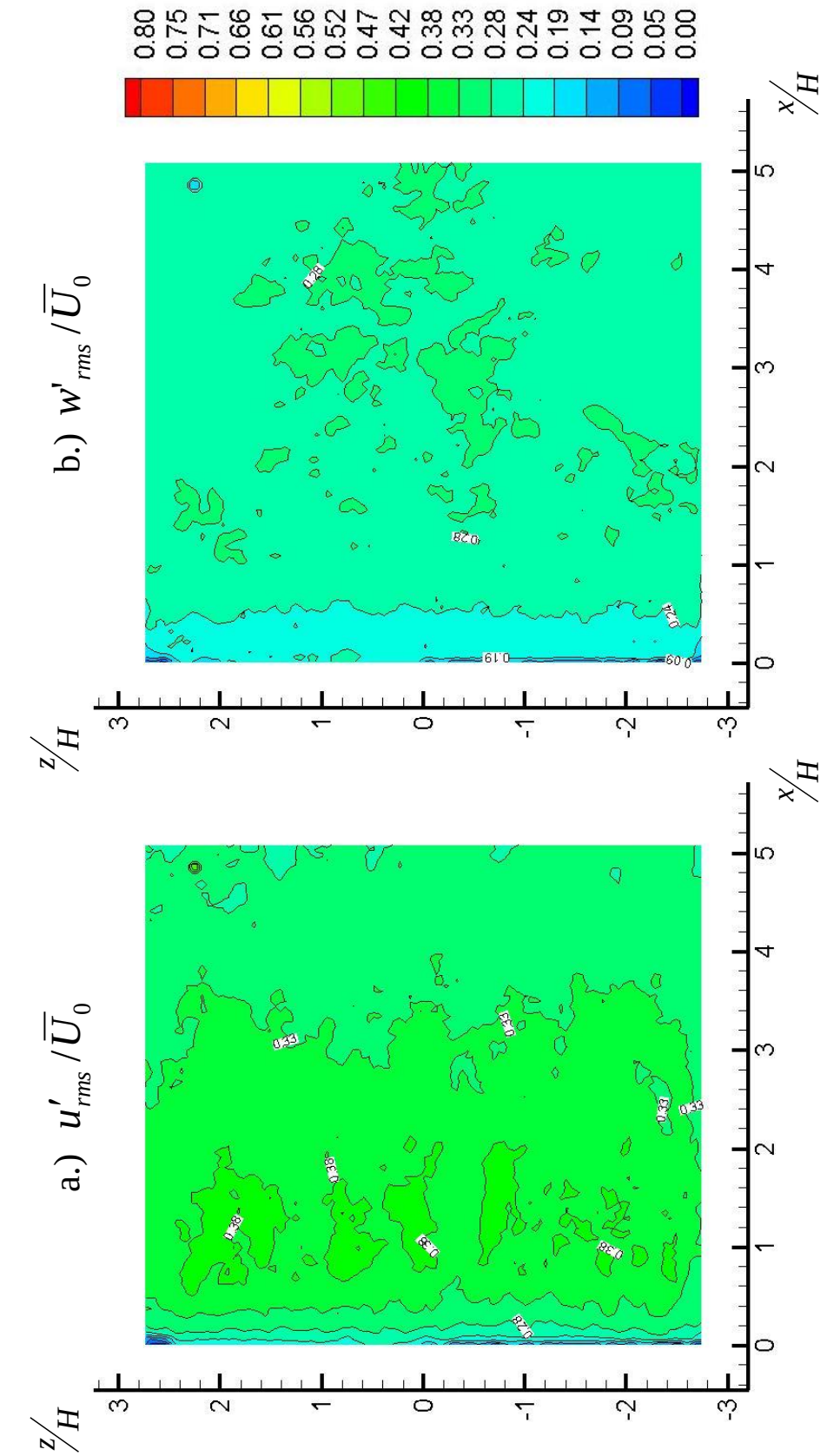

Figure 73: Rms a.) streamwise and b.) spanwise velocity fluctuations for 14% secondary flow rate

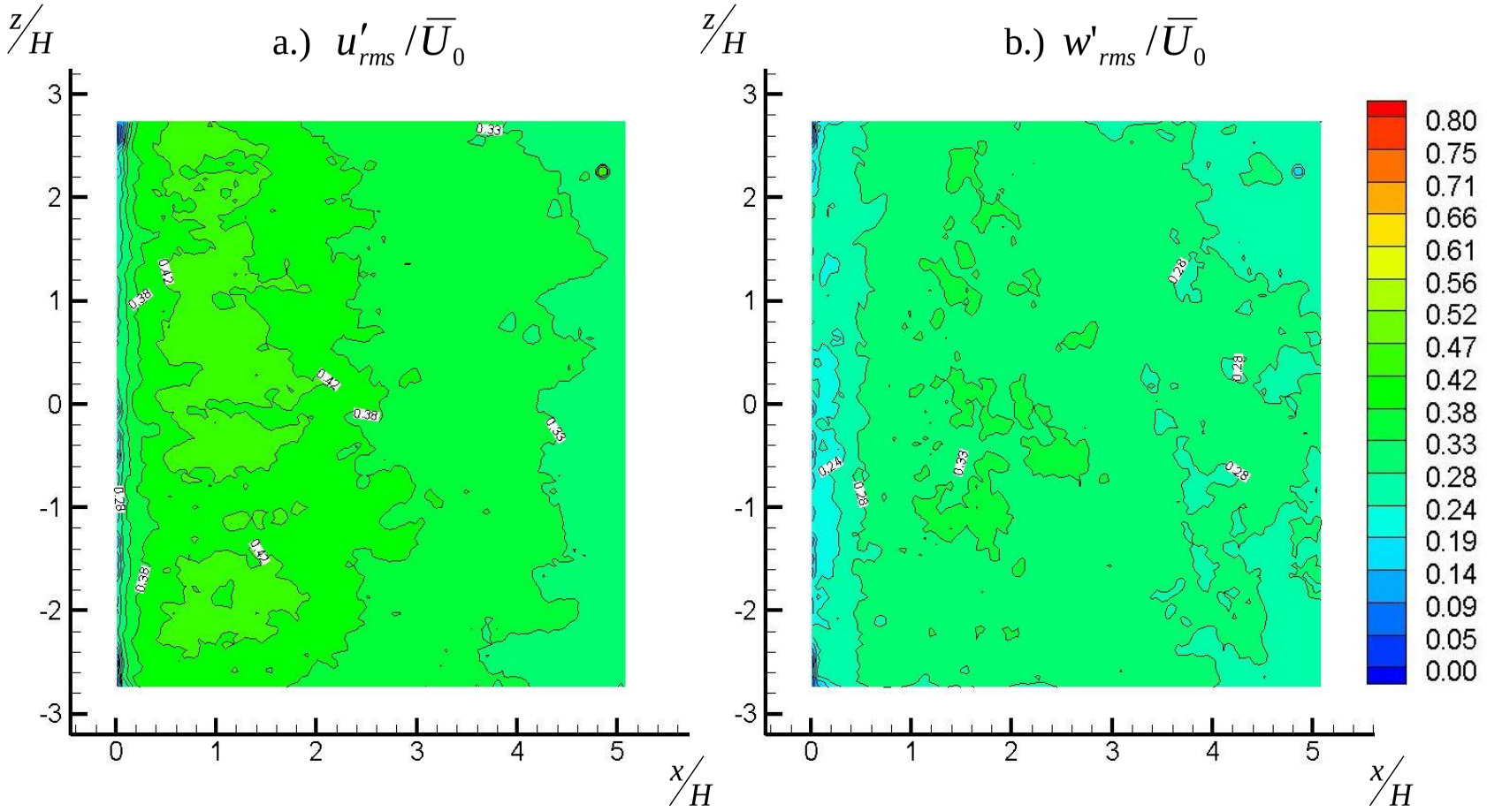

Figure 74: Rms a.) streamwise and b.) spanwise velocity fluctuations for 18% secondary flow rate

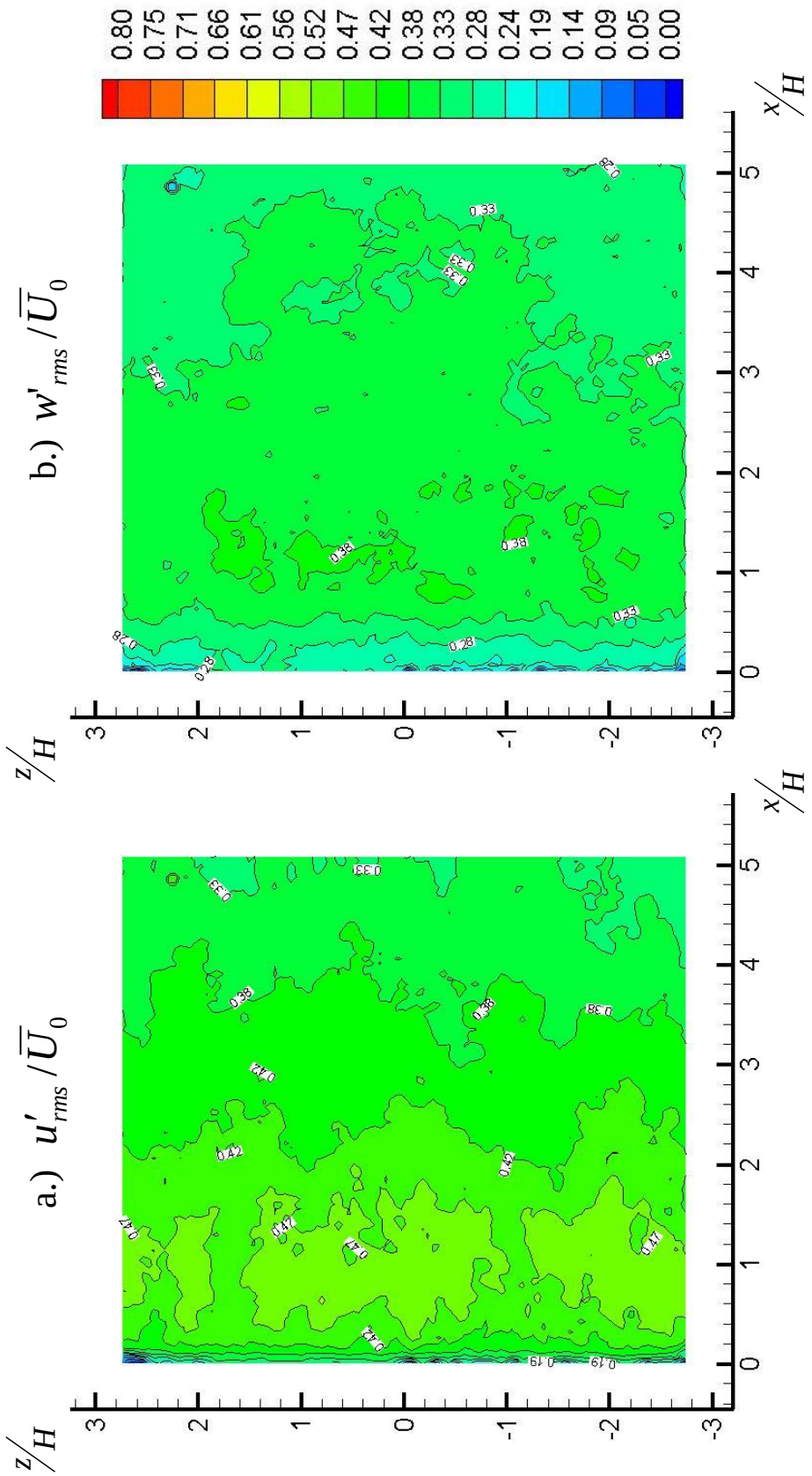

Figure 75: Rms a.) streamwise and b.) spanwise velocity fluctuations for 23% secondary flow rate

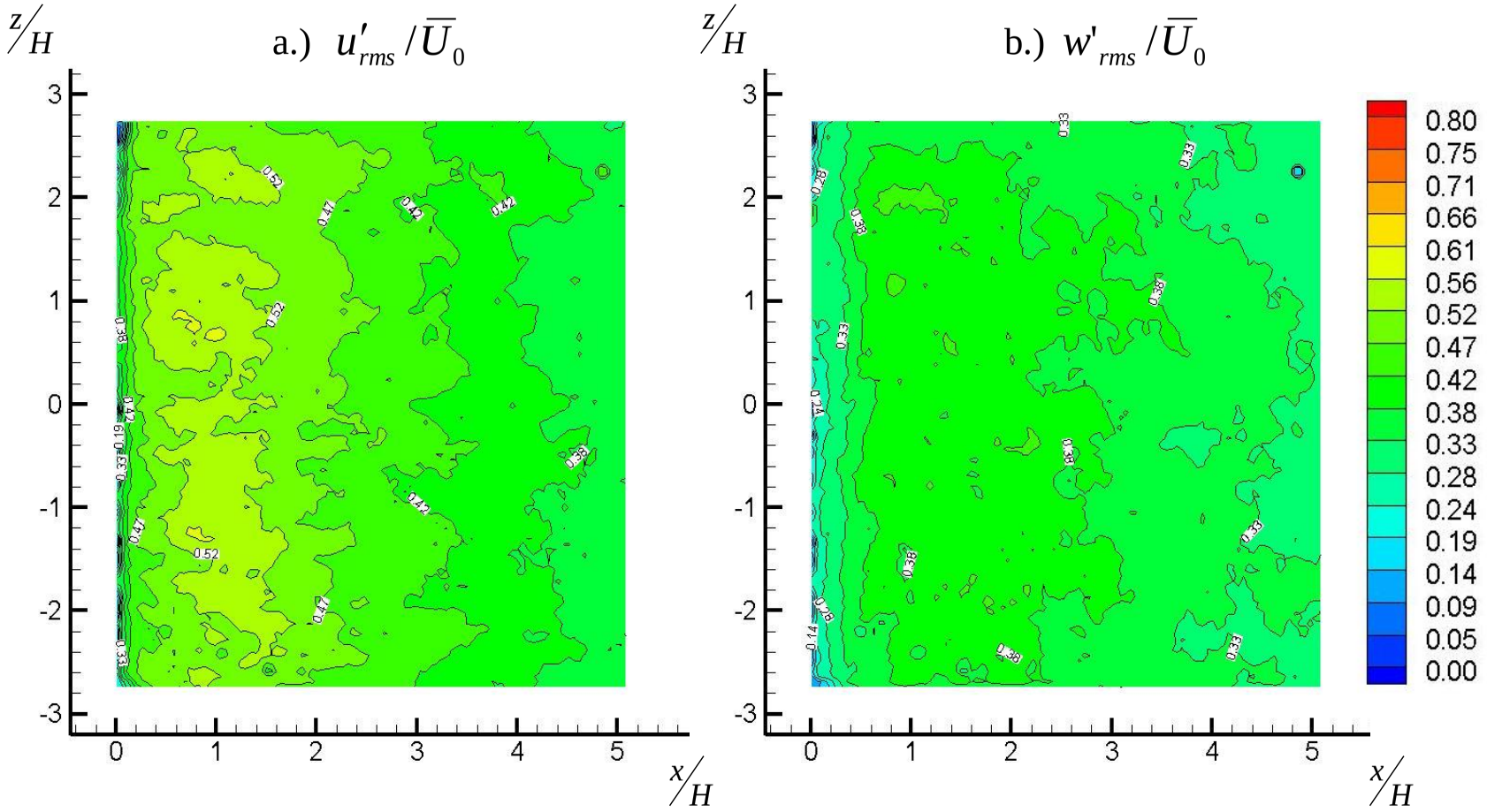

Figure 76: Rms a.) streamwise and b.) spanwise velocity fluctuations for 27% secondary flow rate

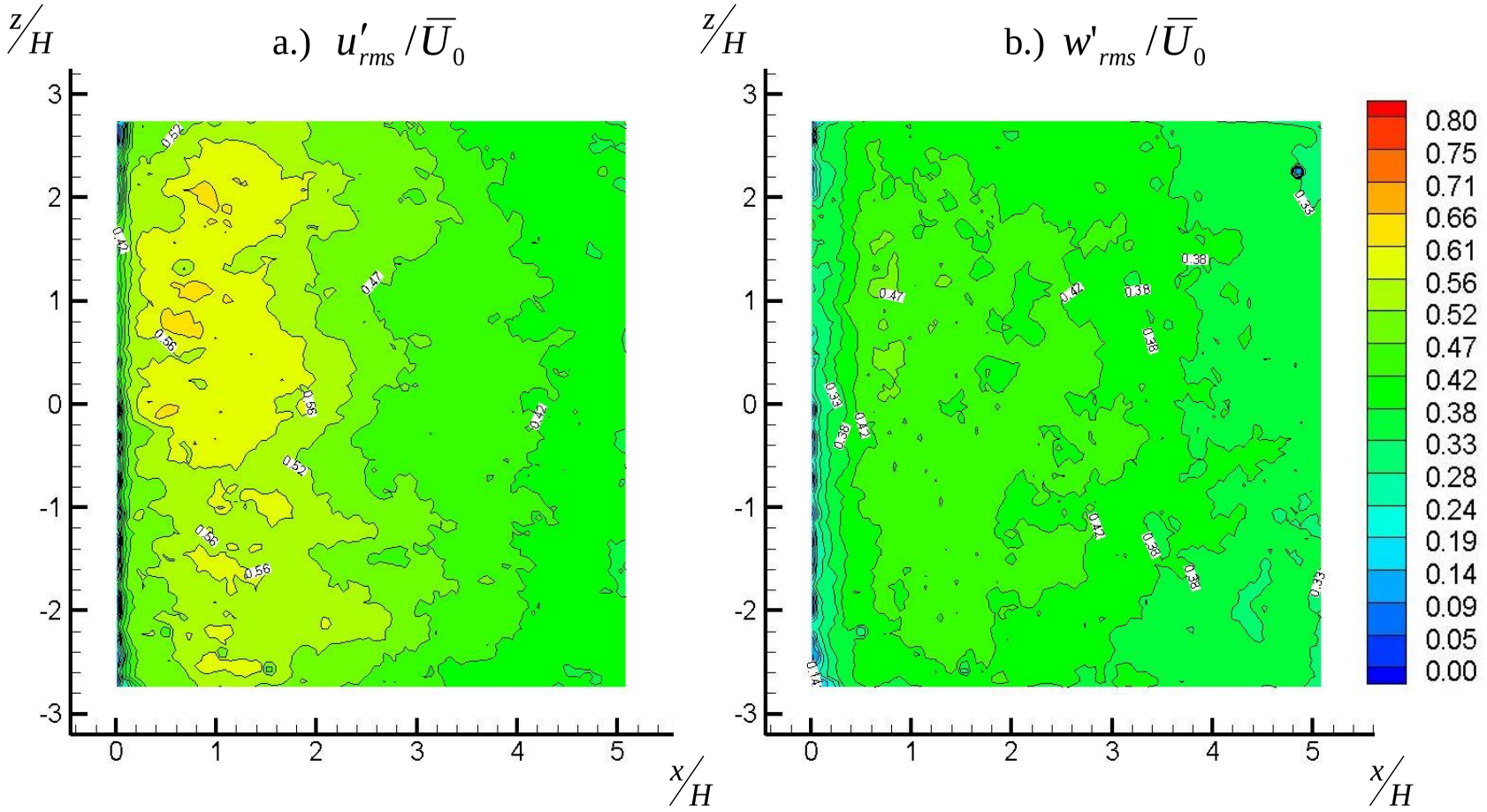

Figure 77: Rms a.) streamwise and b.) spanwise velocity fluctuations for 32% secondary flow rate

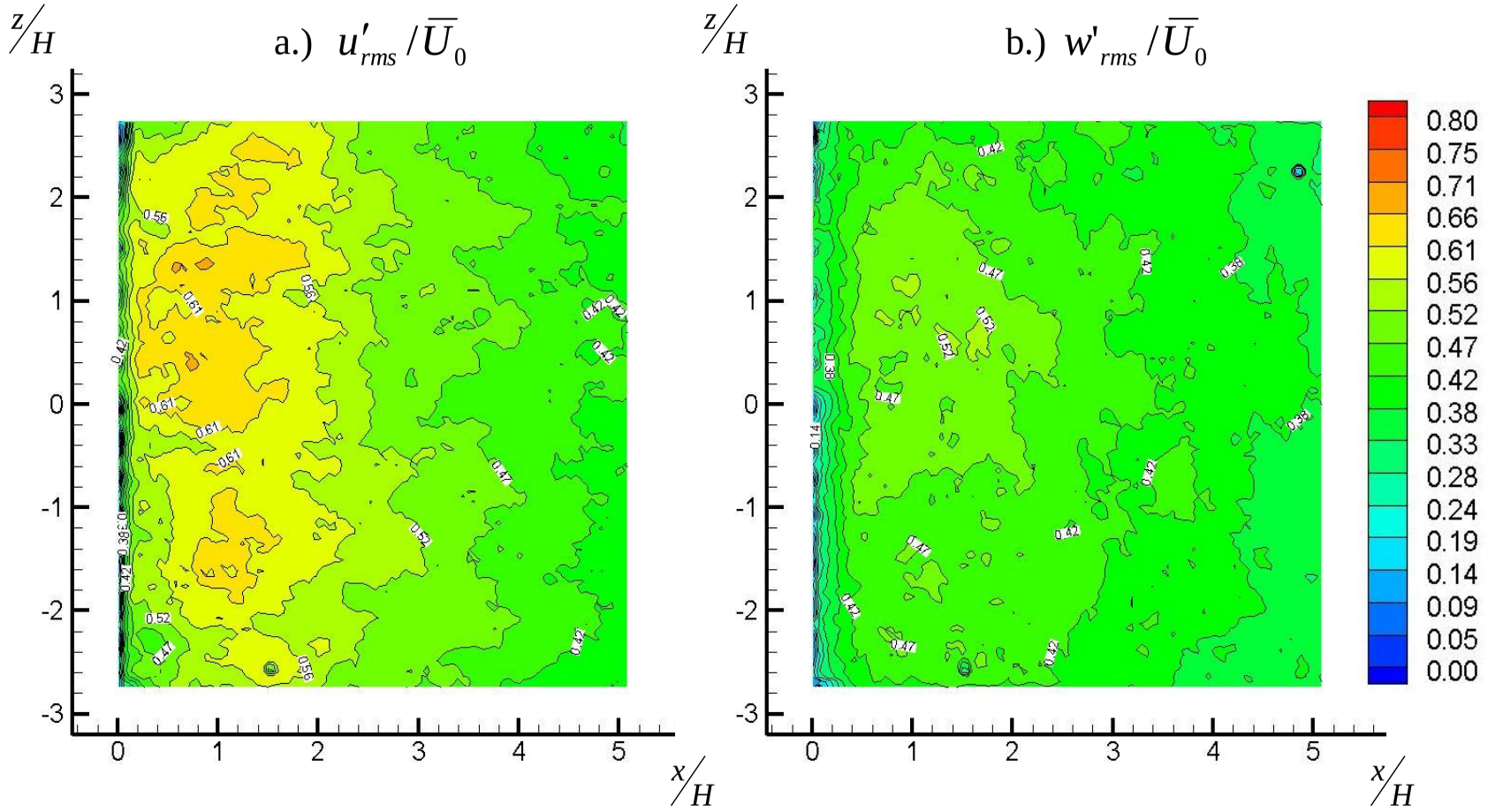

Figure 78: Rms a.) streamwise and b.) spanwise velocity fluctuations for 36% secondary flow rate

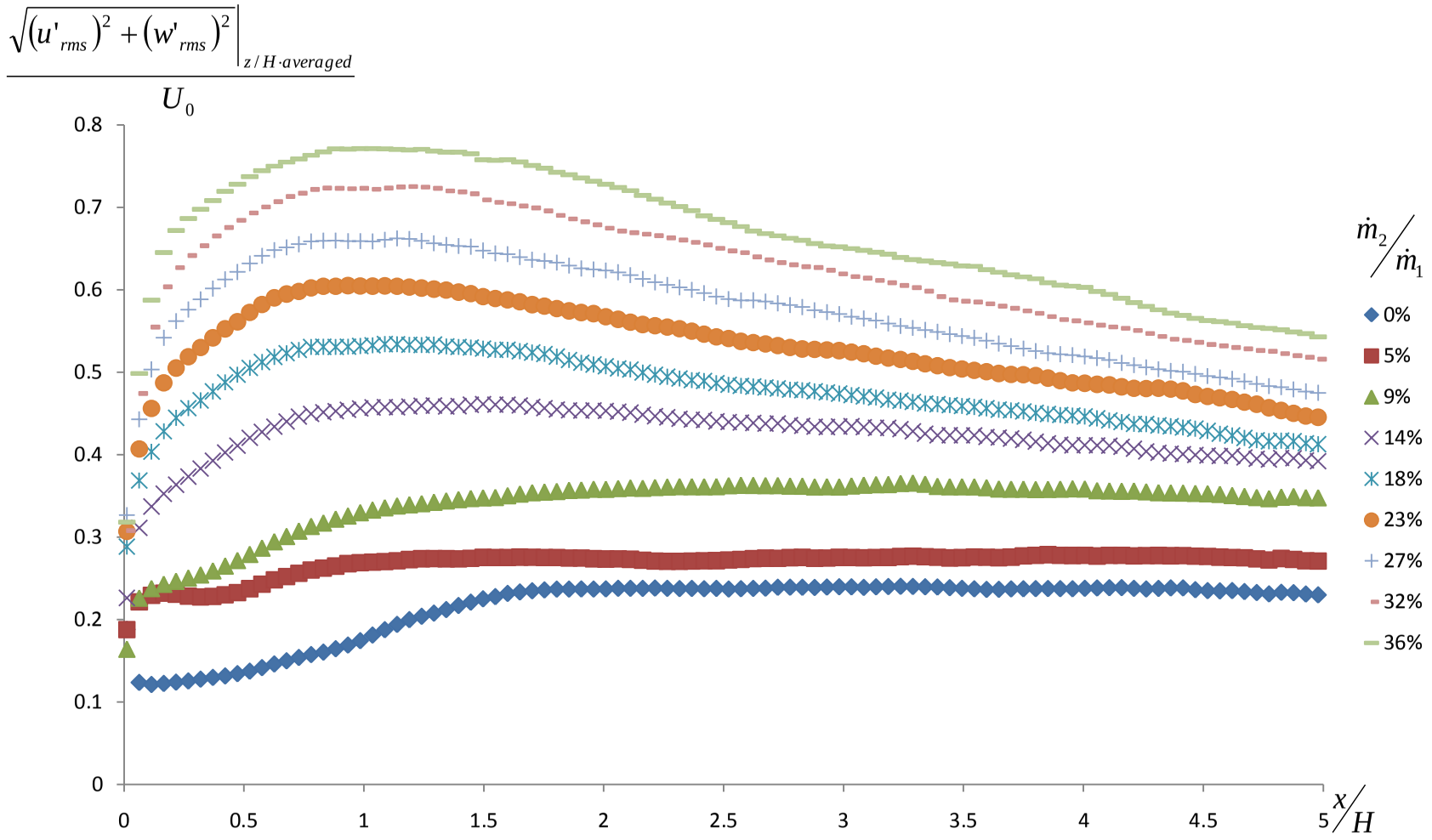

Figure 79a: Spanwise averaged total turbulence levels for all secondary flow rates

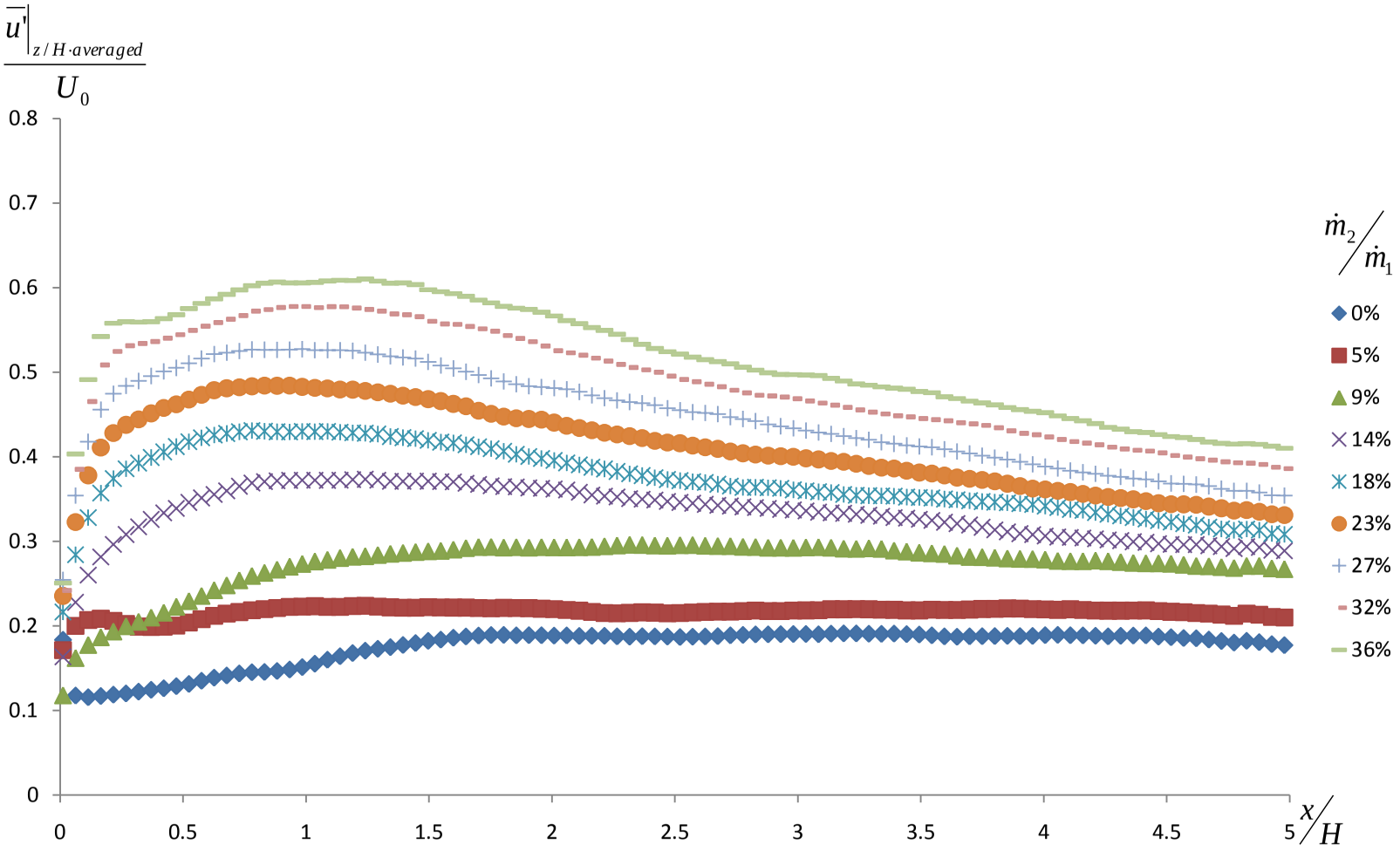

Figure 79b: Spanwise averaged streamwise Rms velocity fluctuation levels for all secondary flow rates

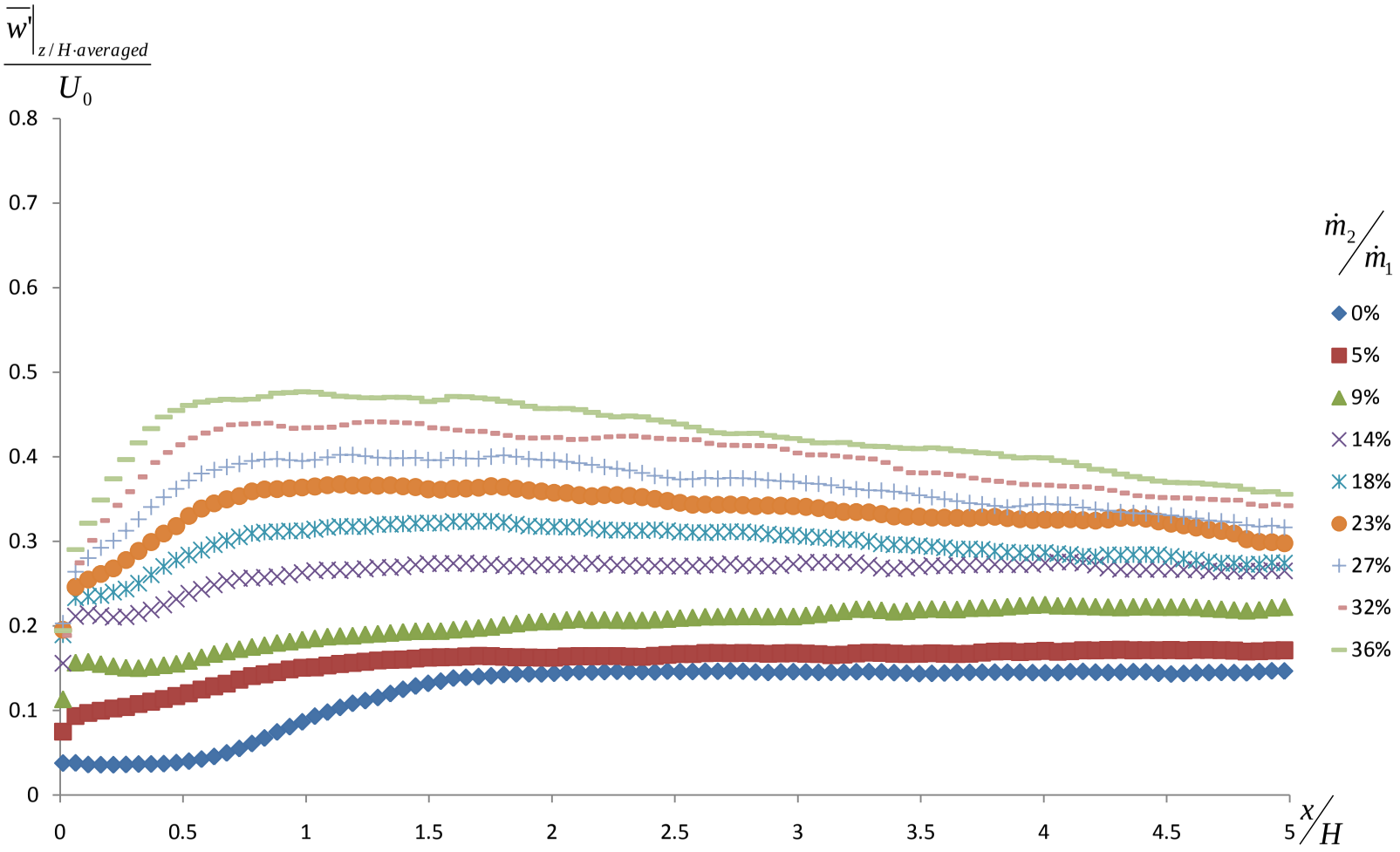

Figure 79c: Spanwise averaged spanwise Rms velocity fluctuation levels for all secondary flow rates

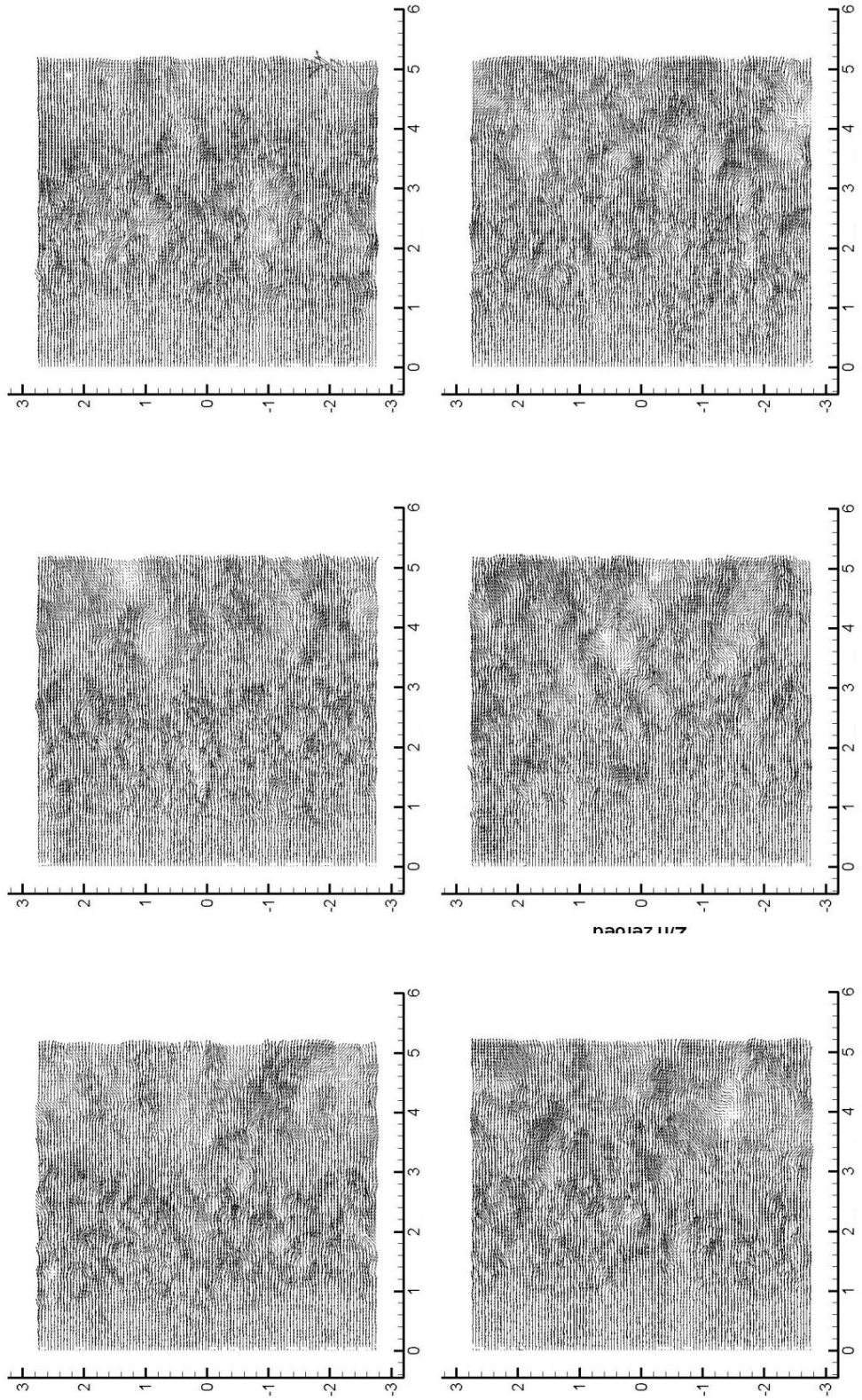

Figure 80: Spanwise instantaneous velocity fields for geometry II with 0% secondary flow rate

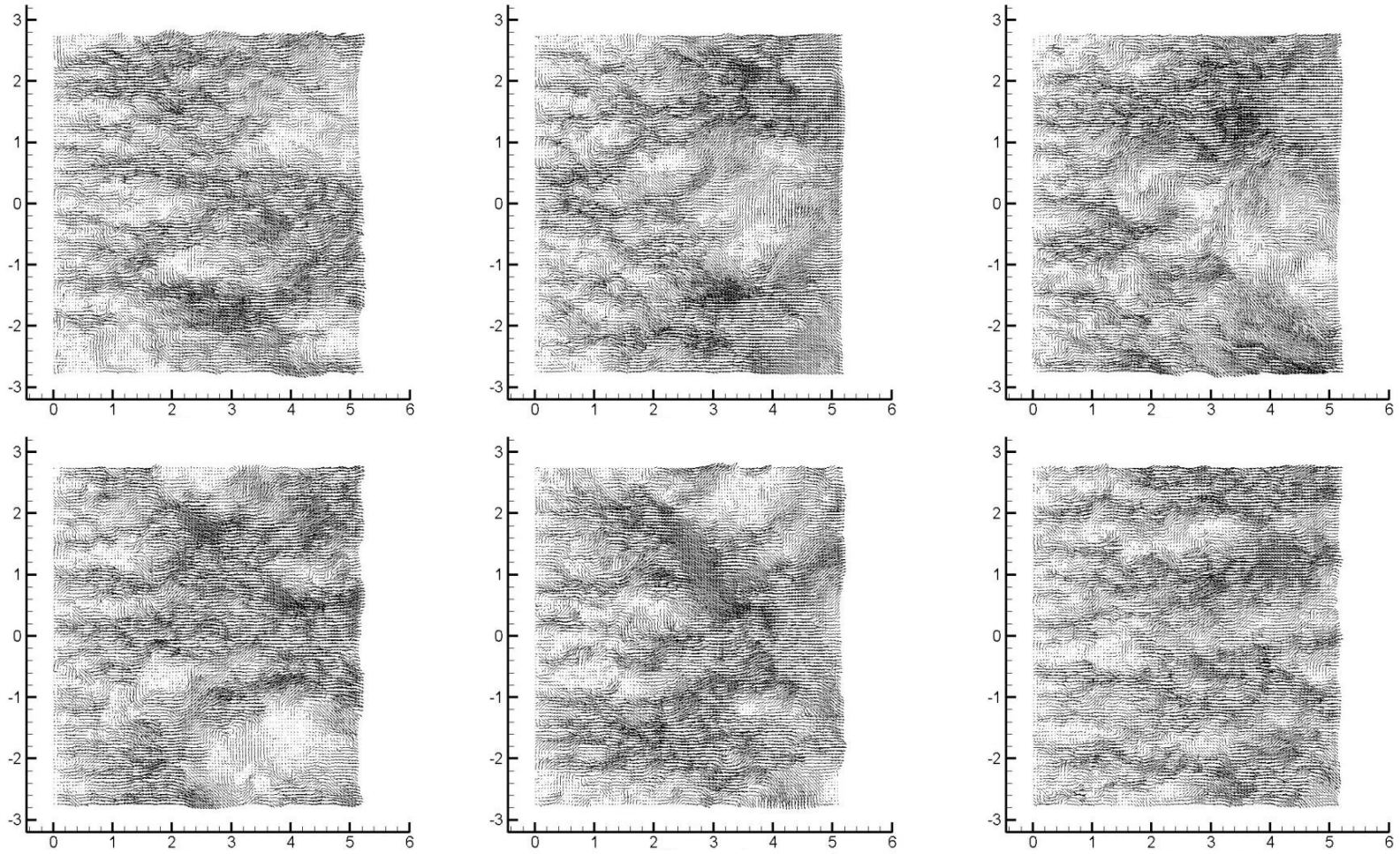

Figure 81: Spanwise instantaneous velocity fields for geometry II with 9% secondary flow rate

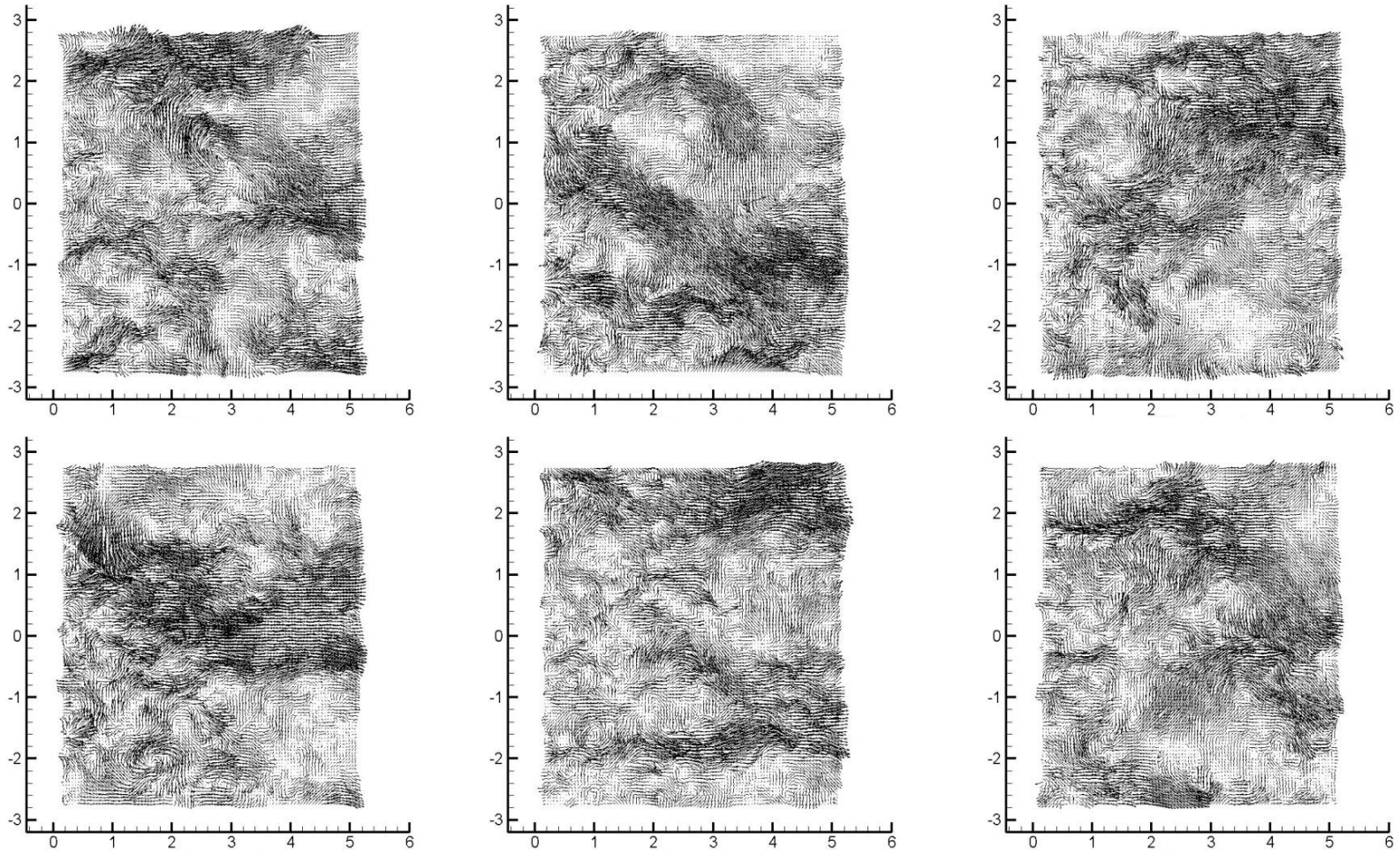

Figure 82: Spanwise instantaneous velocity fields for geometry II with 32% secondary flow rate

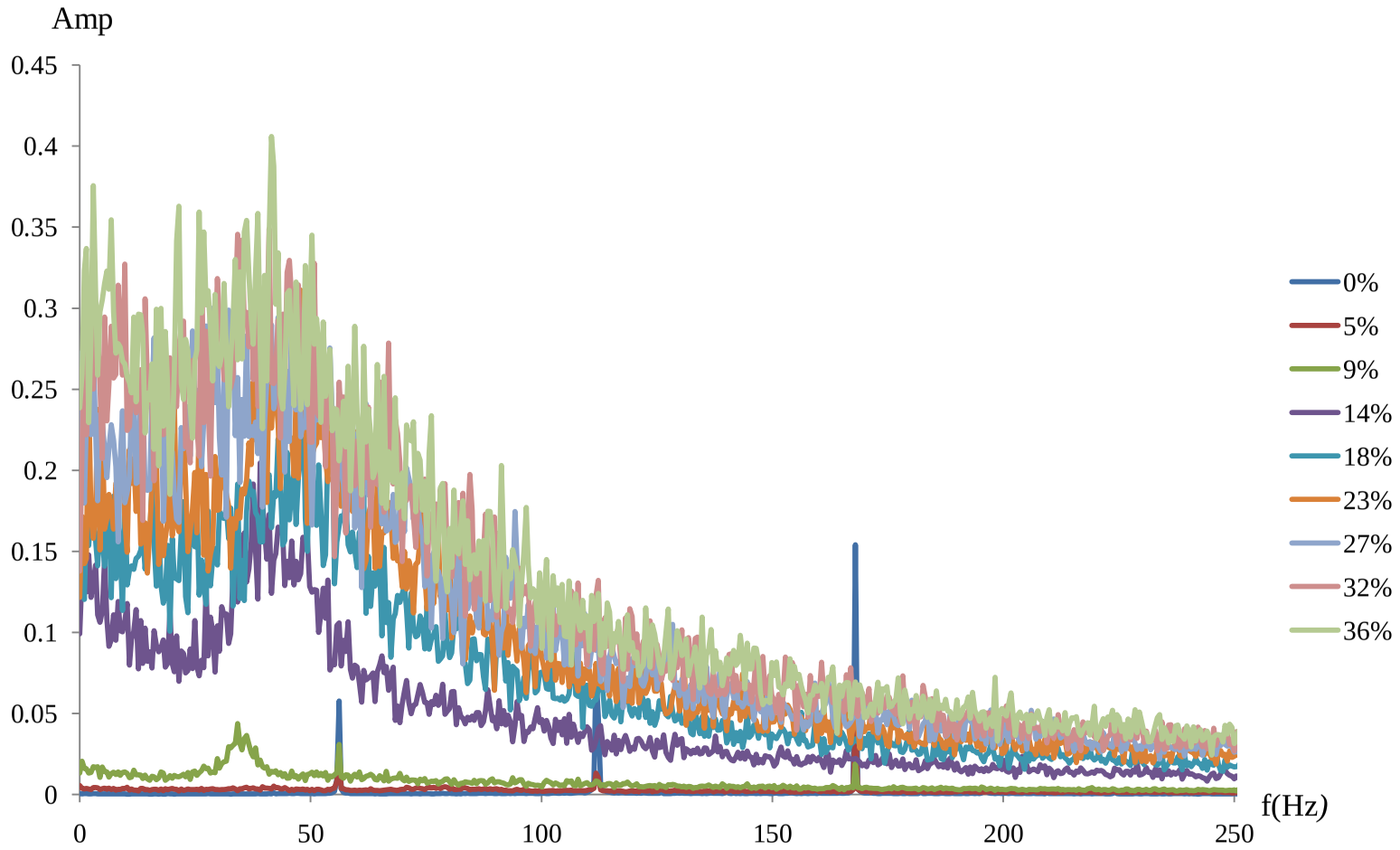

Figure 83: Spectral distributions of geometry II for all secondary flow rates

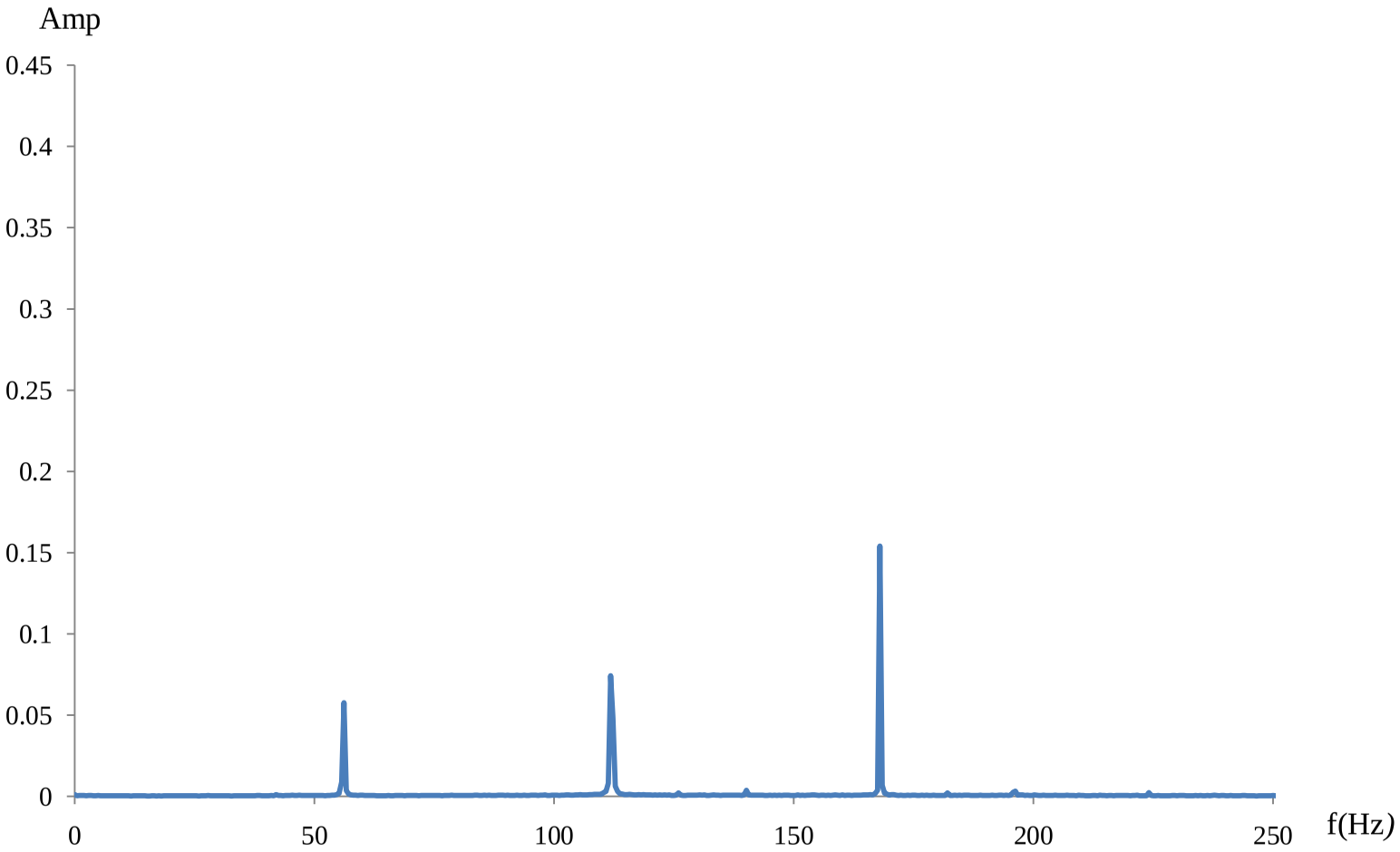

Figure 84: Spectral distributions in geometry II
a.) 0%

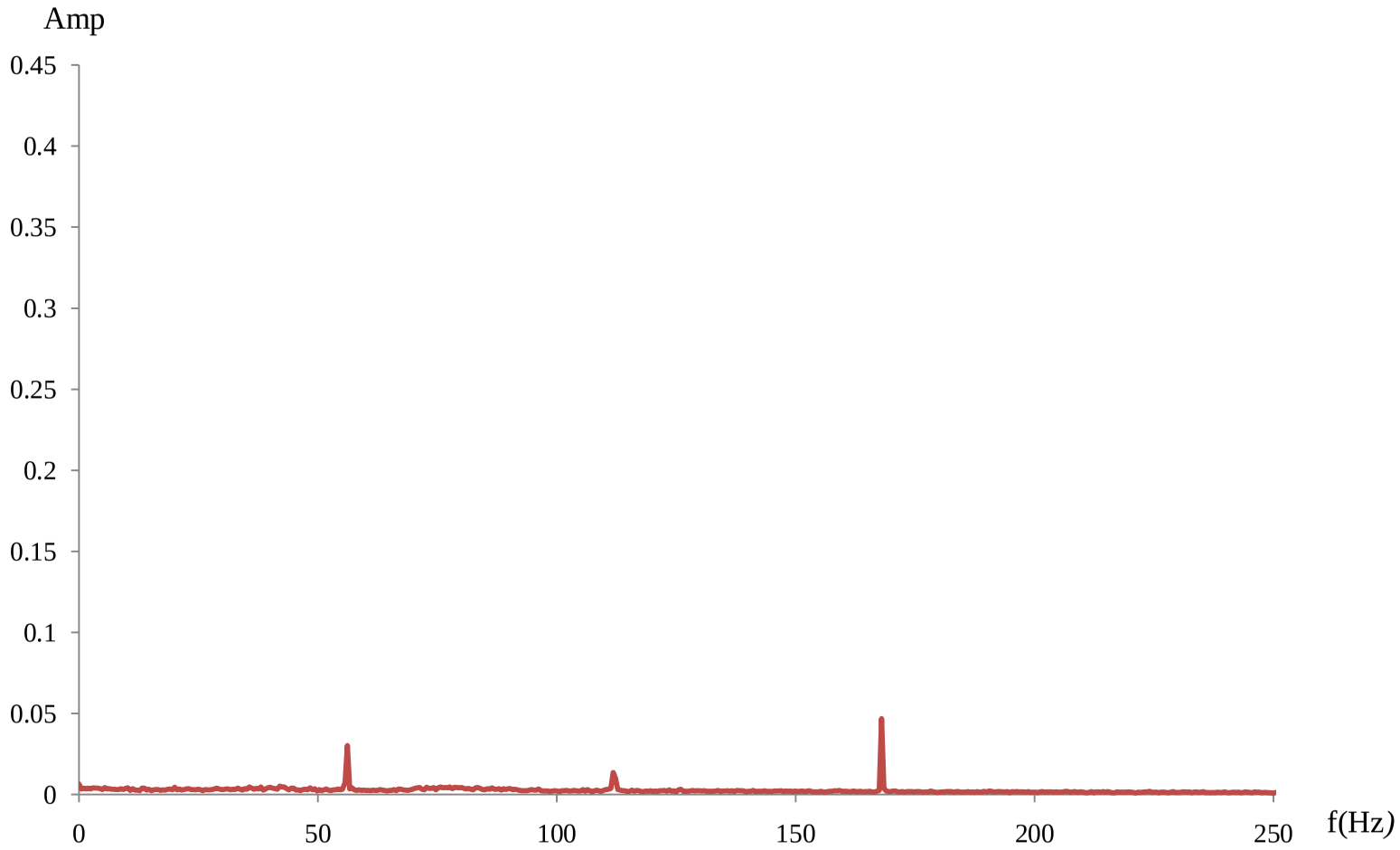

Figure 84: Spectral distributions in geometry II
b.) 5%

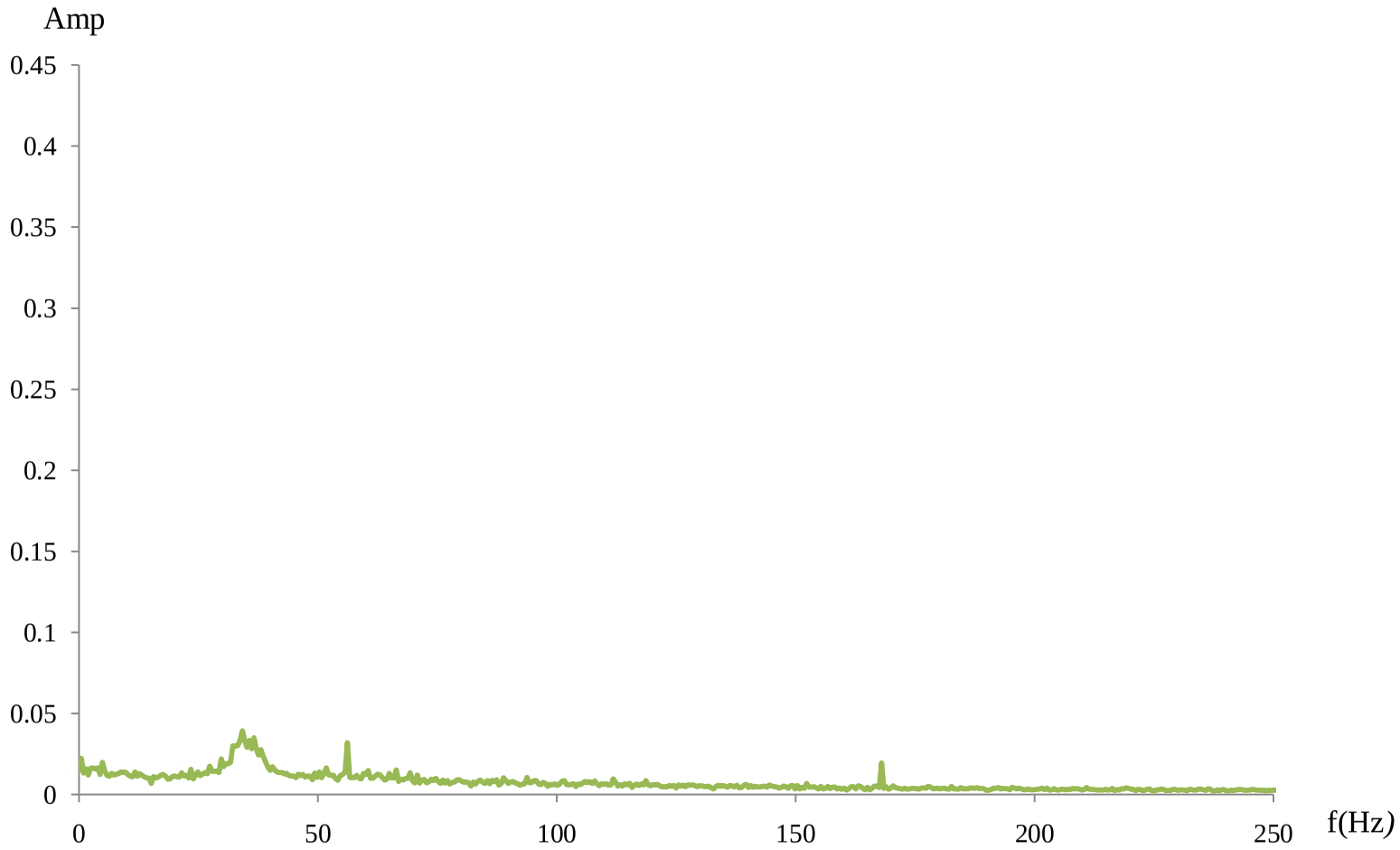

Figure 84: Spectral distributions in geometry II
c.) 9%

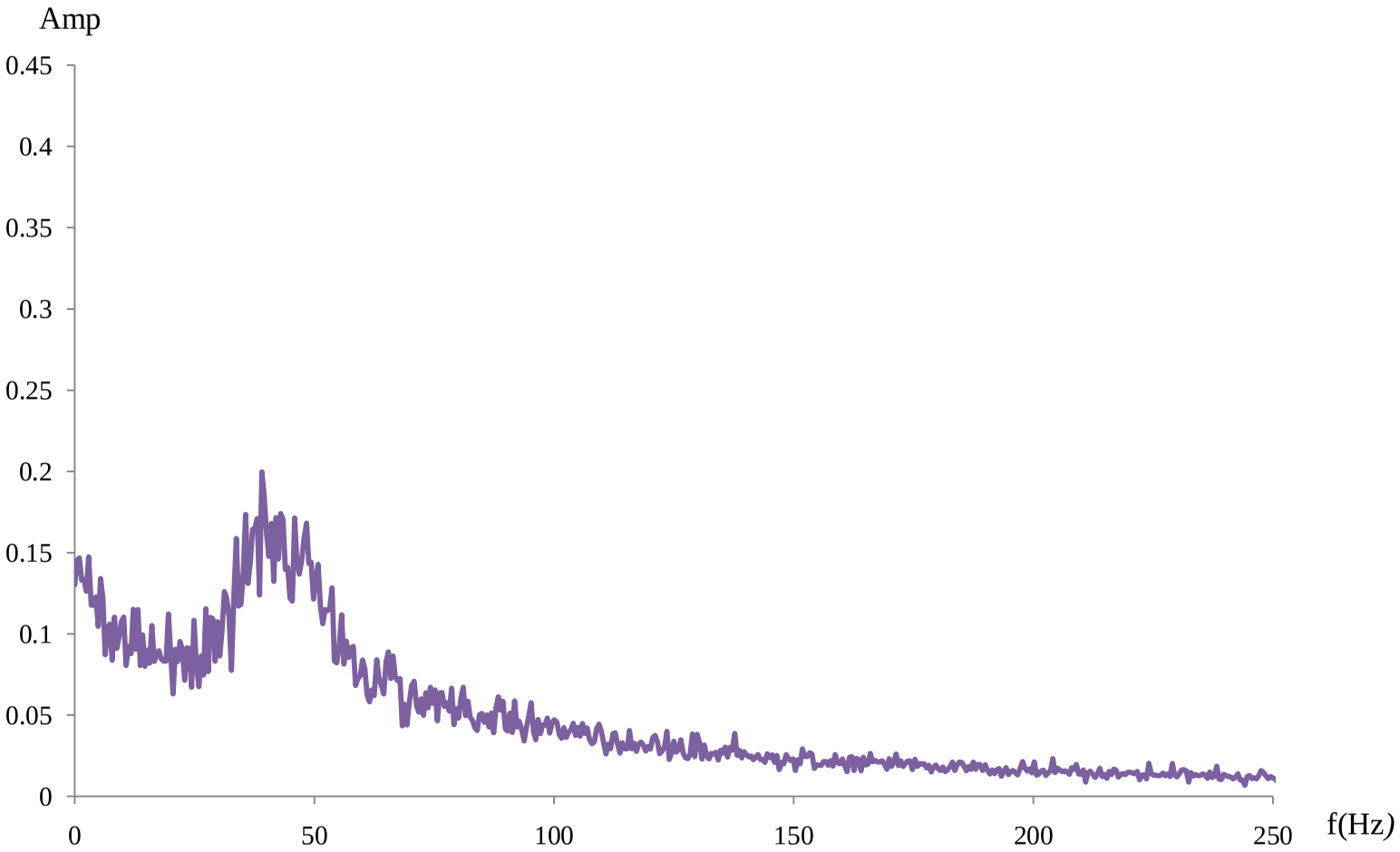

Figure 84: Spectral distributions in geometry II
d.) 14%

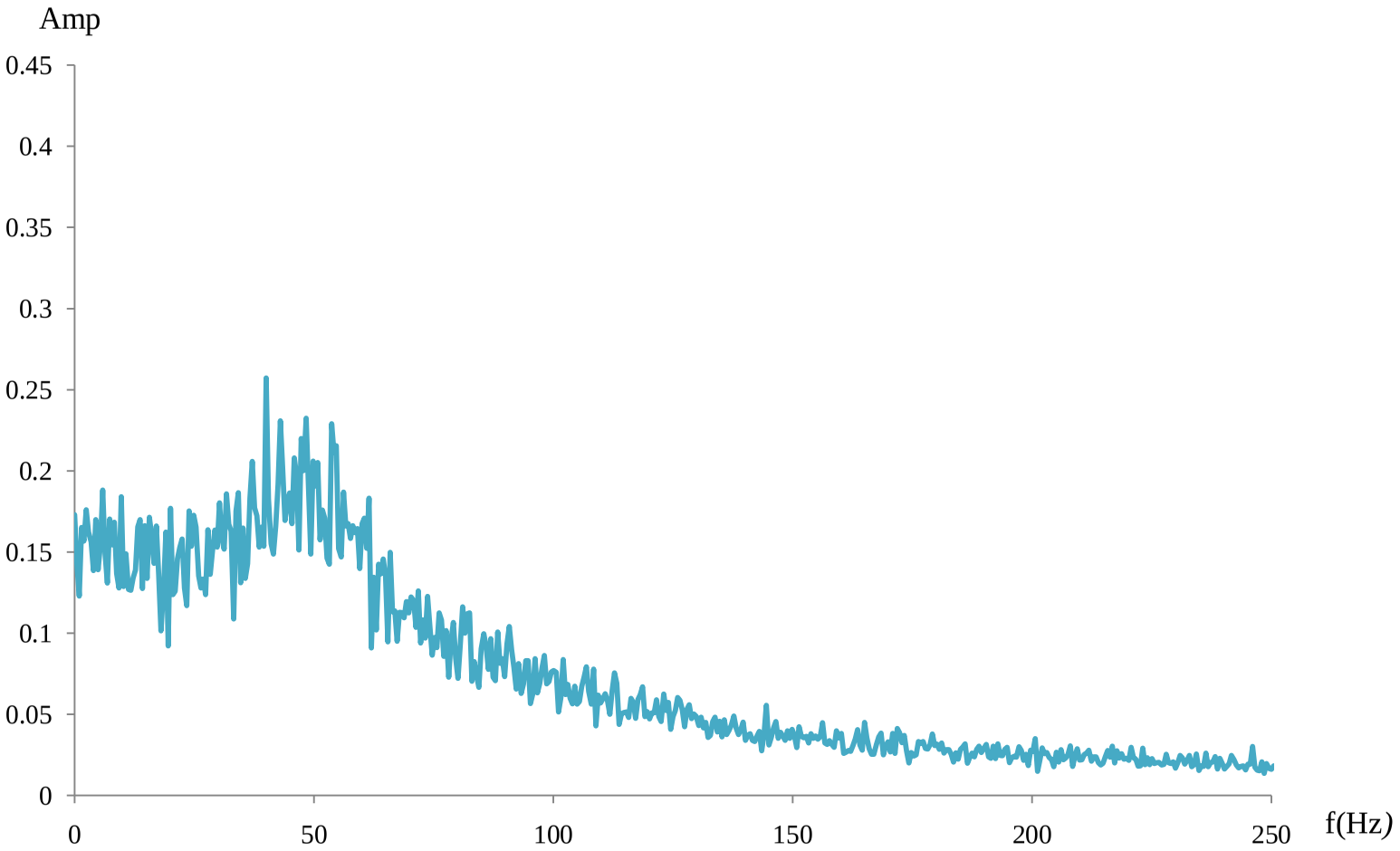

Figure 84: Spectral distributions in geometry II
e.) 18%

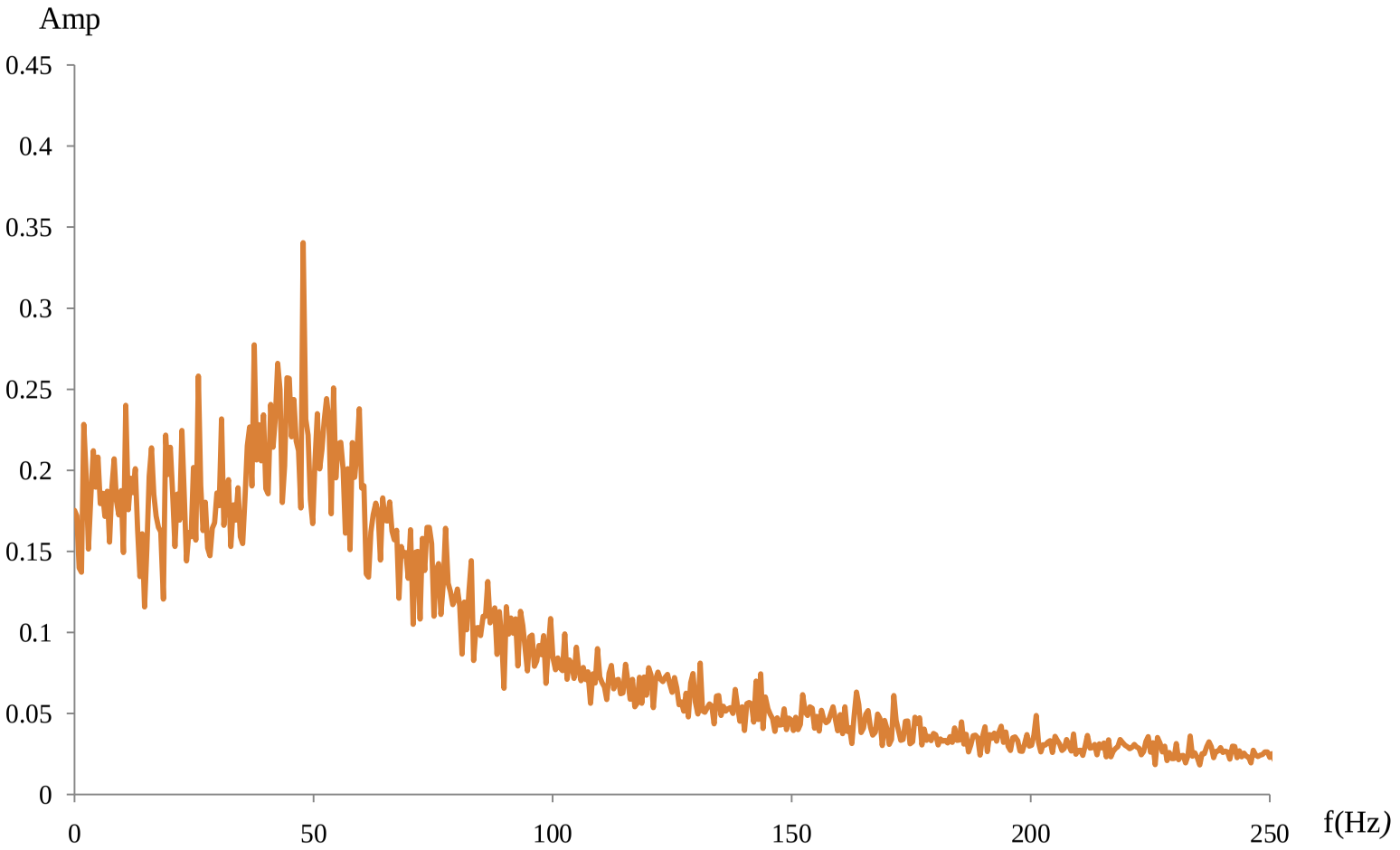

Figure 84: Spectral distributions in geometry II
f.) 23%

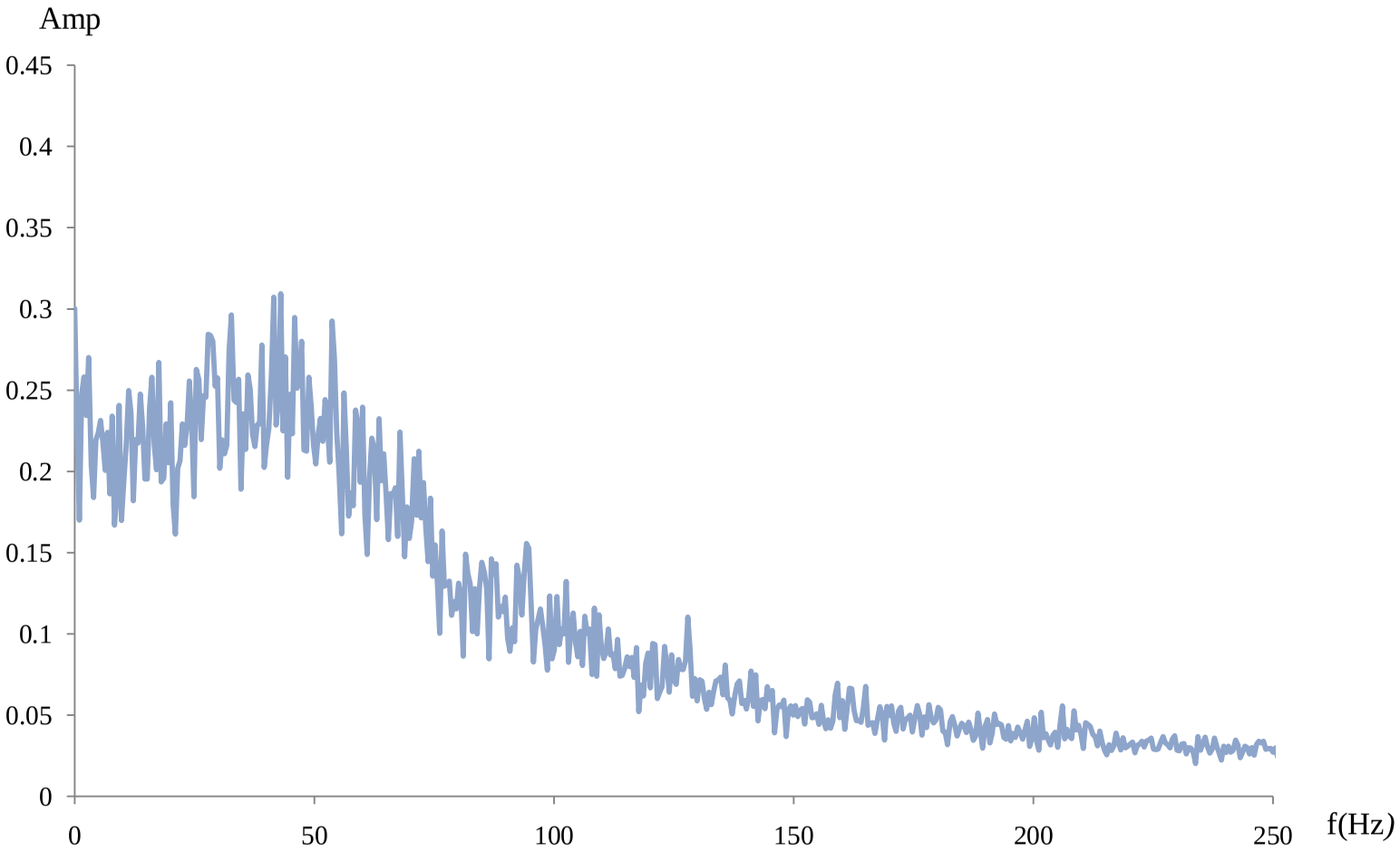

Figure 84: Spectral distributions in geometry II
g.) 27%

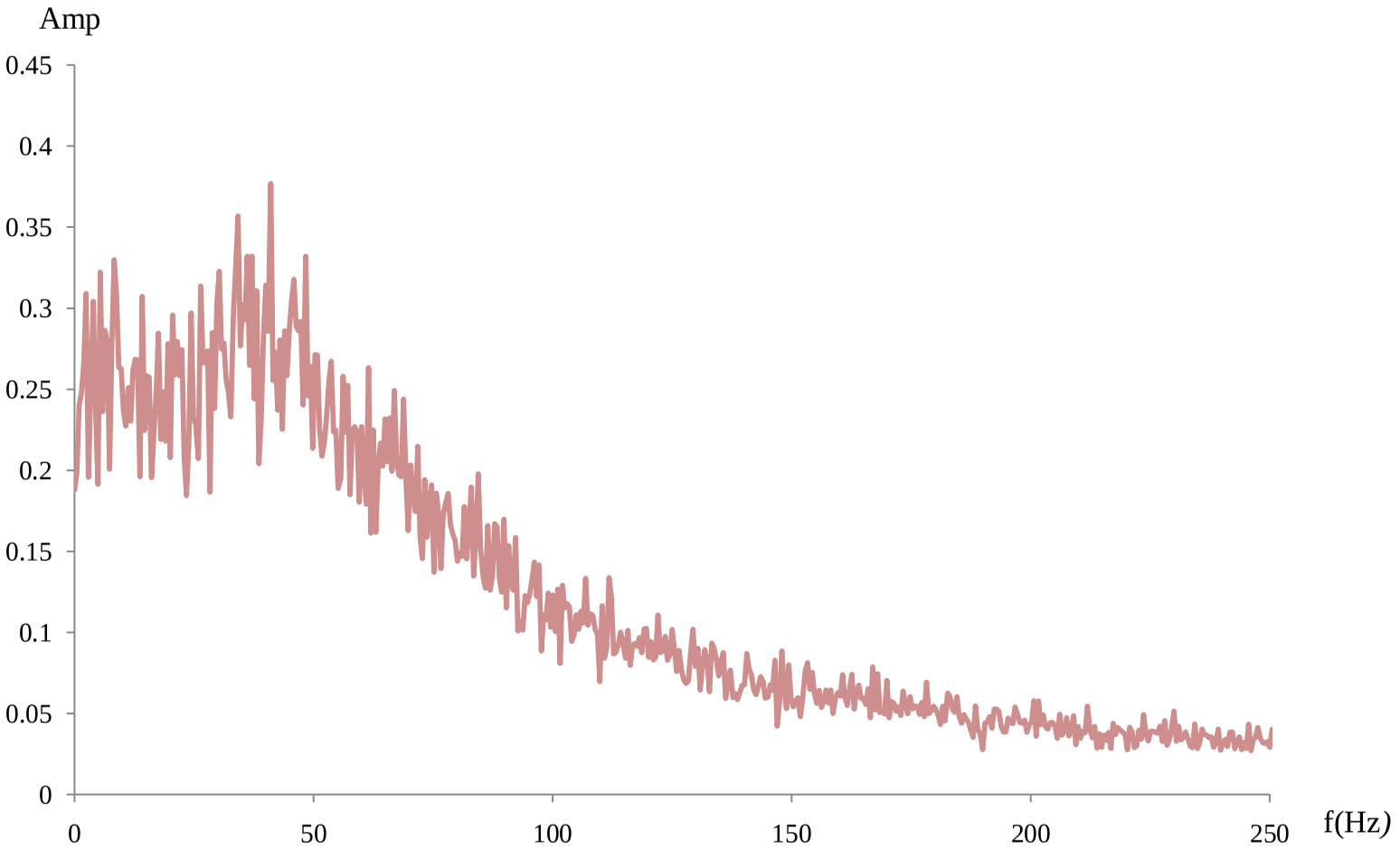

Figure 84: Spectral distributions in geometry II
h.) 32%

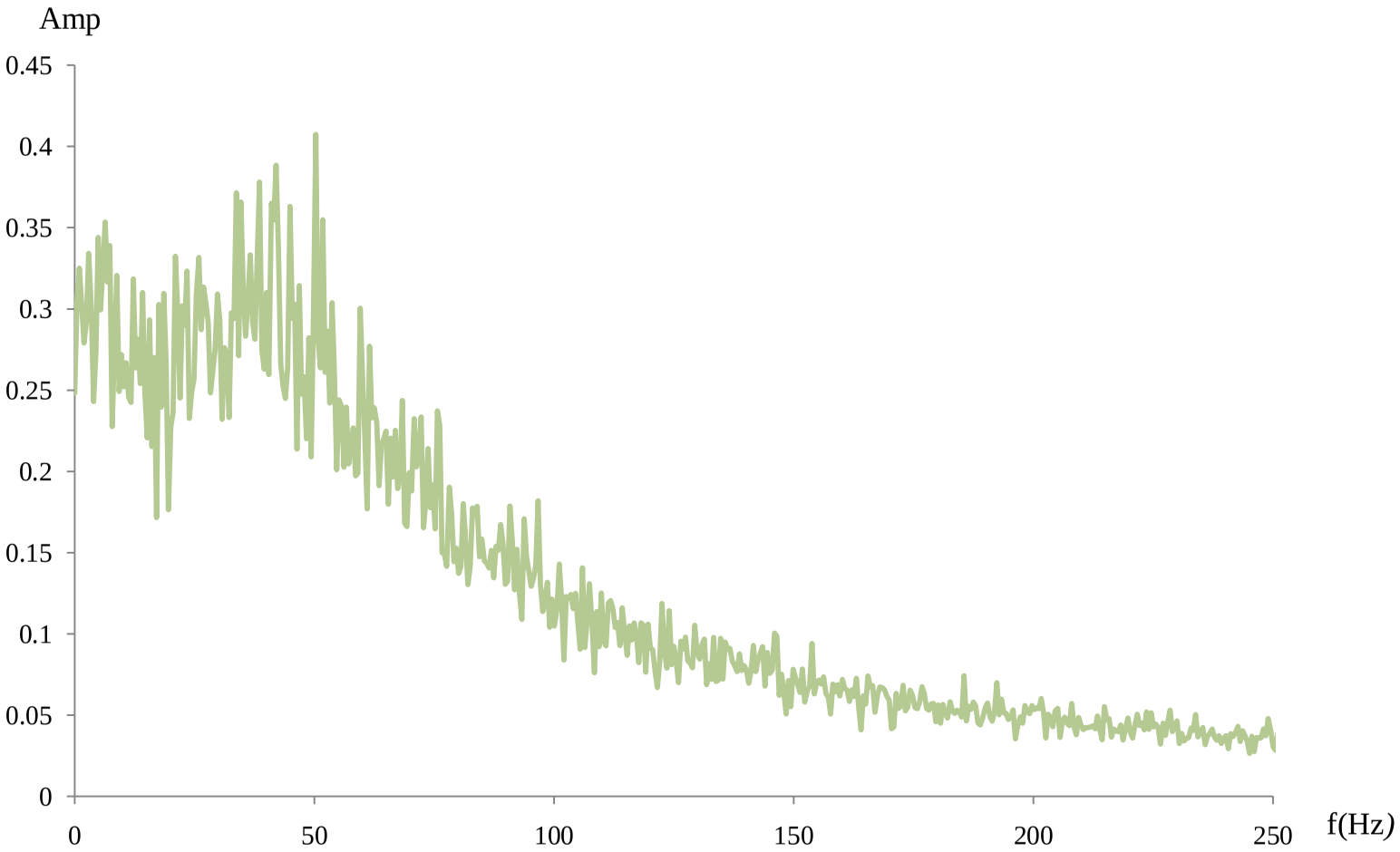

Figure 84: Spectral distributions in geometry II
i.) 36%

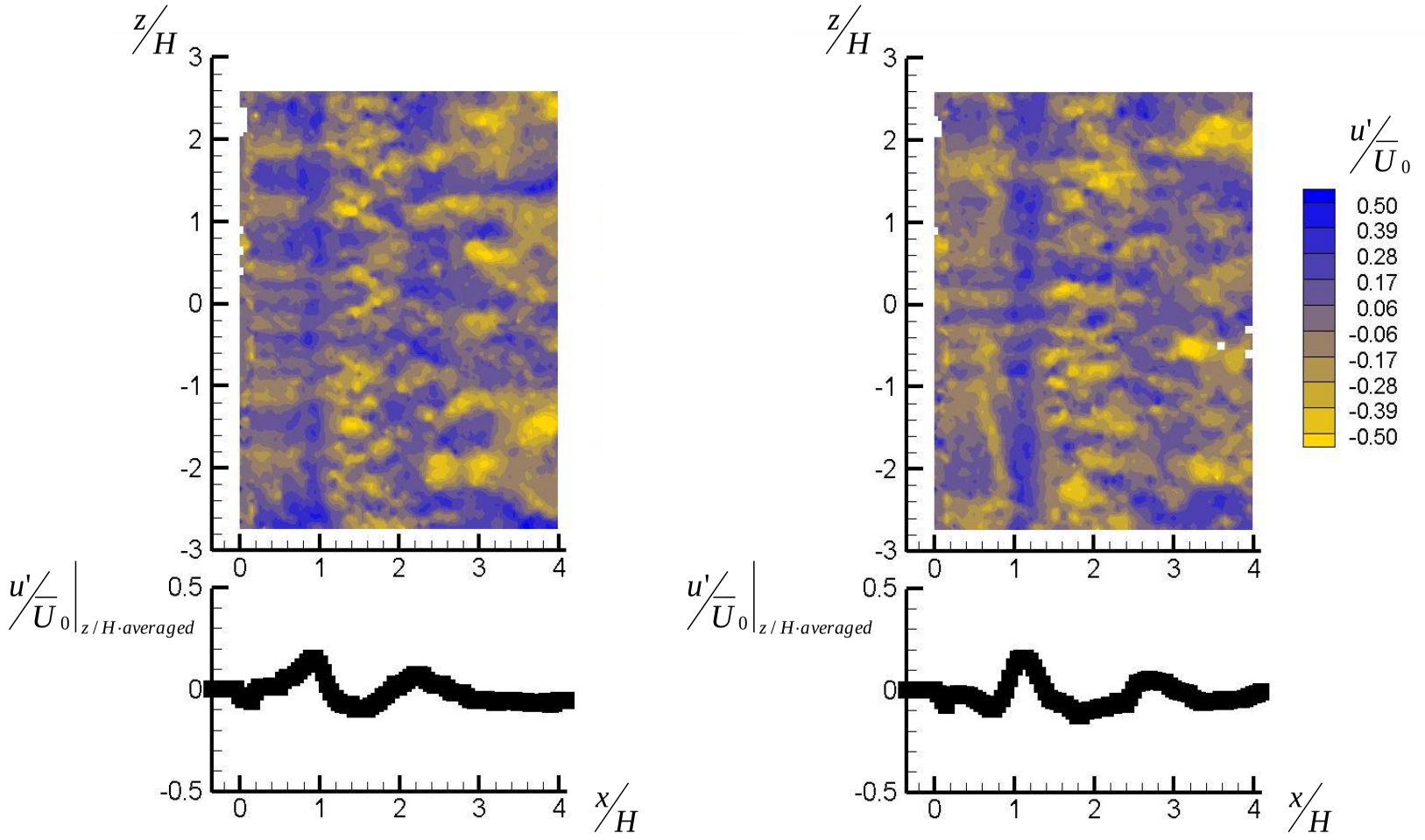

Figure 85: Representative instantaneous contours and spanwise averaged streamwise velocity deviation from the local mean in geometry II for the unforced 0% secondary flow rate case

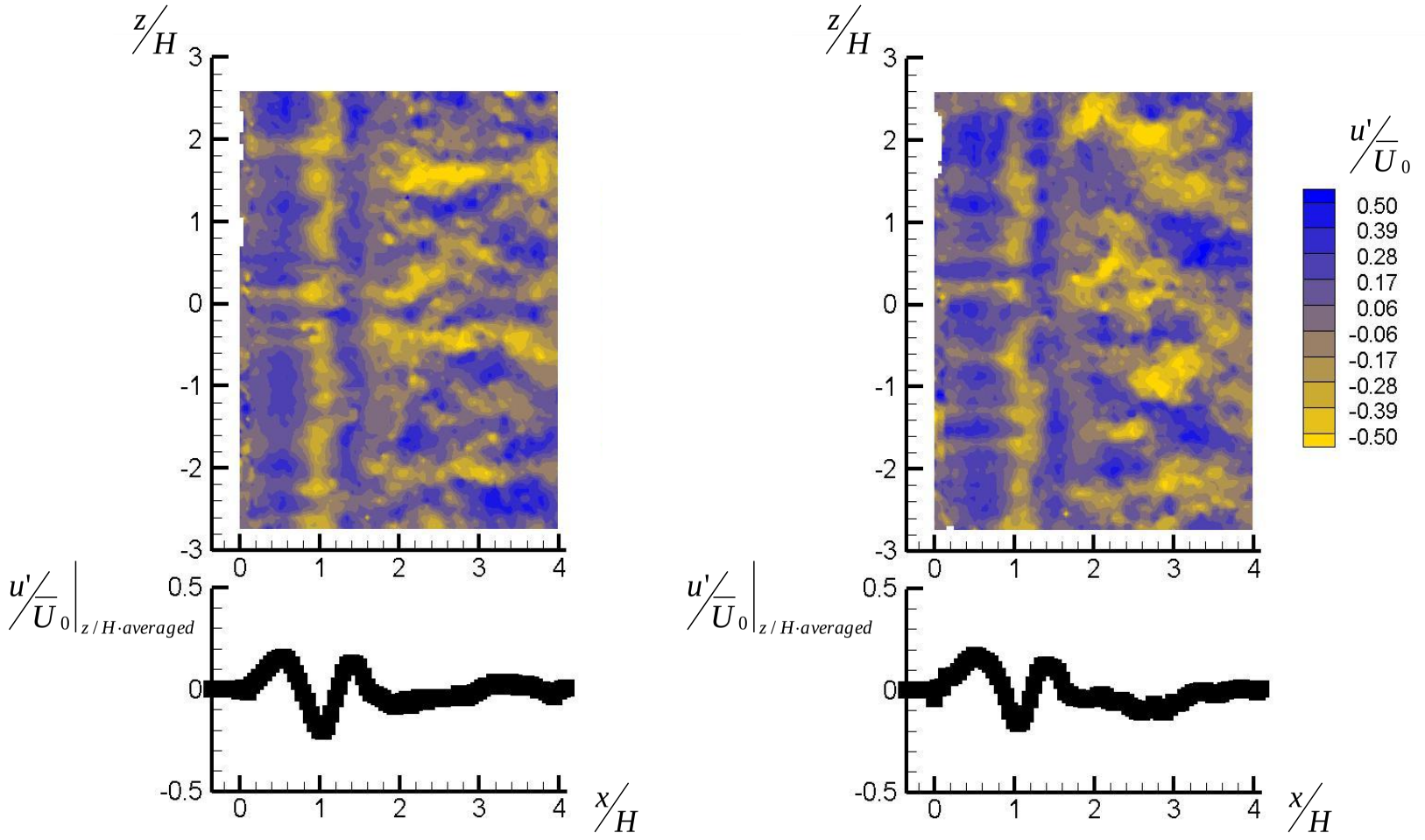

Figure 86: Representative instantaneous contours and spanwise averaged streamwise velocity deviation from the local mean in geometry II for the forced 0% secondary flow rate case

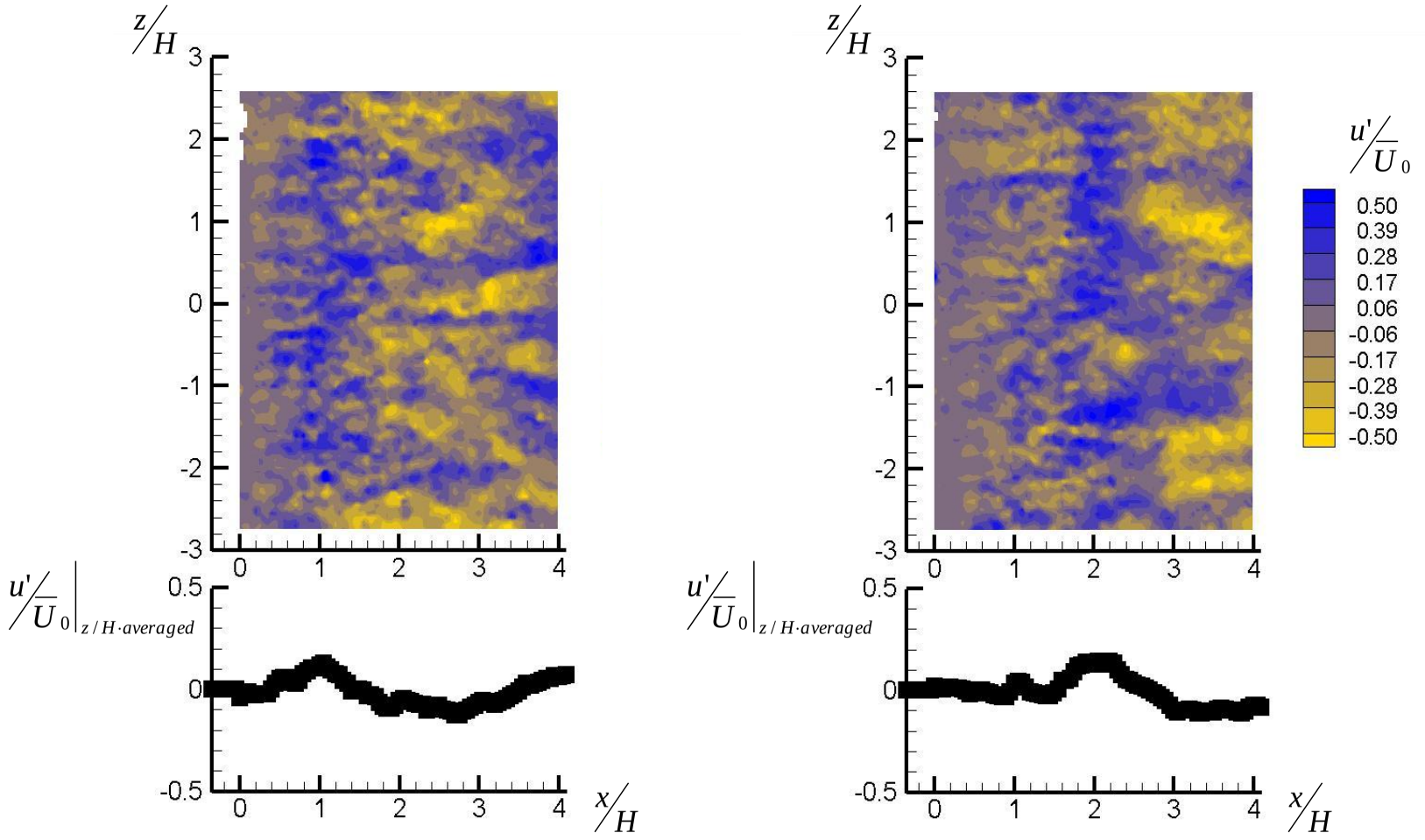

Figure 87: Representative instantaneous contours and spanwise averaged streamwise velocity deviation from the local mean in geometry II for the unforced 3% secondary flow rate case

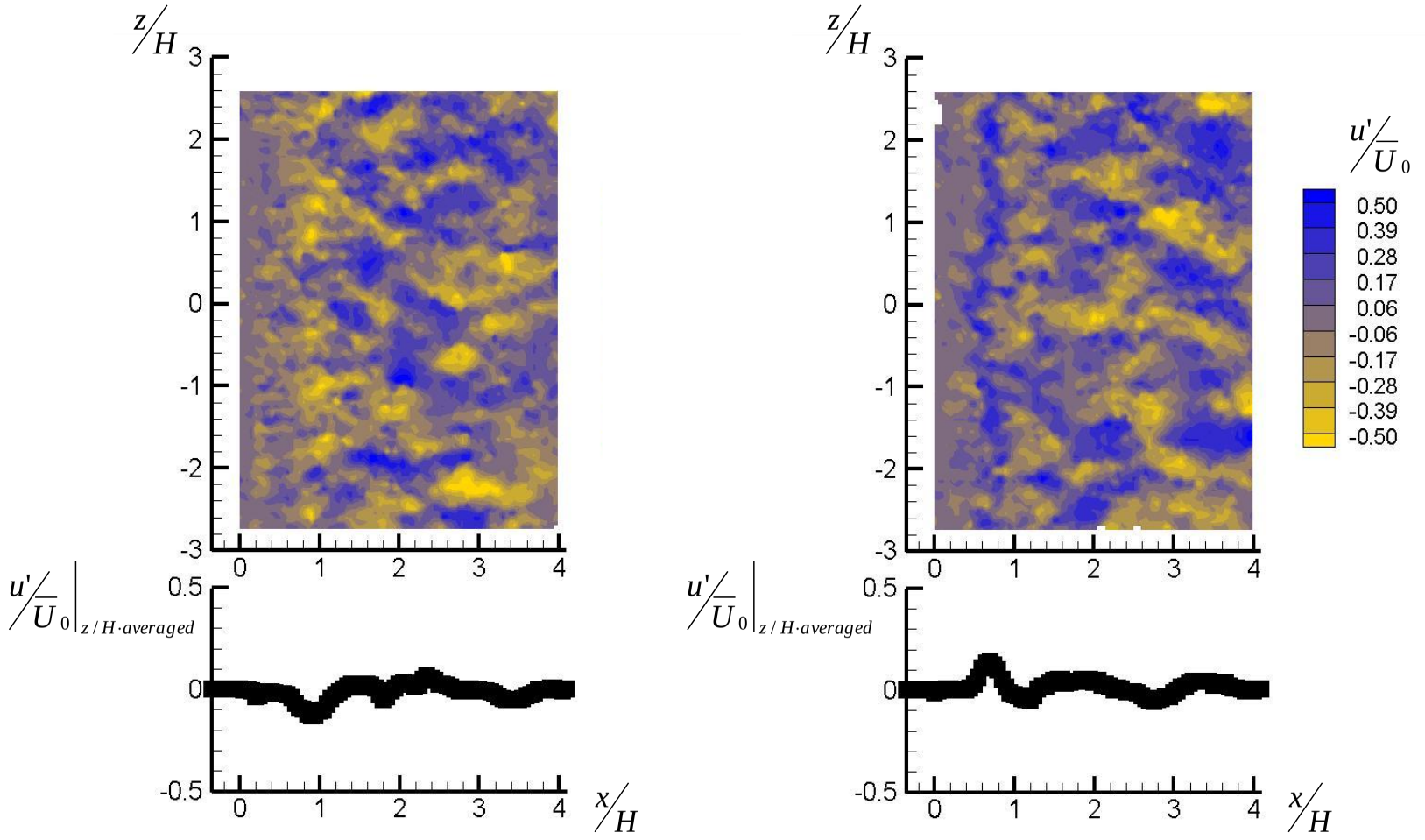

Figure 88: Representative instantaneous contours and spanwise averaged streamwise velocity deviation from the local mean in geometry II for the forced 3% secondary flow rate case

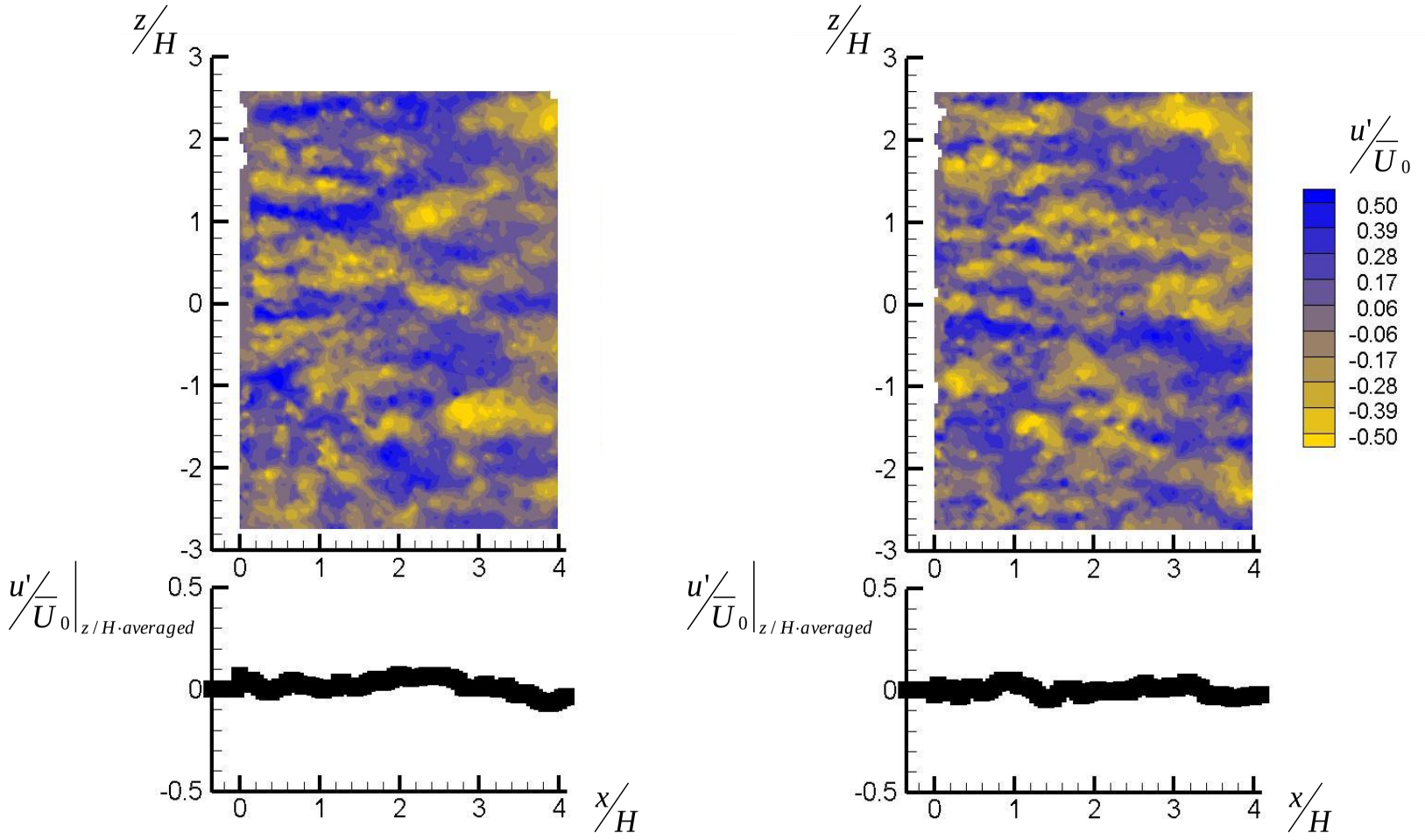

Figure 89: Representative instantaneous contours and spanwise averaged streamwise velocity deviation from the local mean in geometry II for the unforced 5% secondary flow rate case

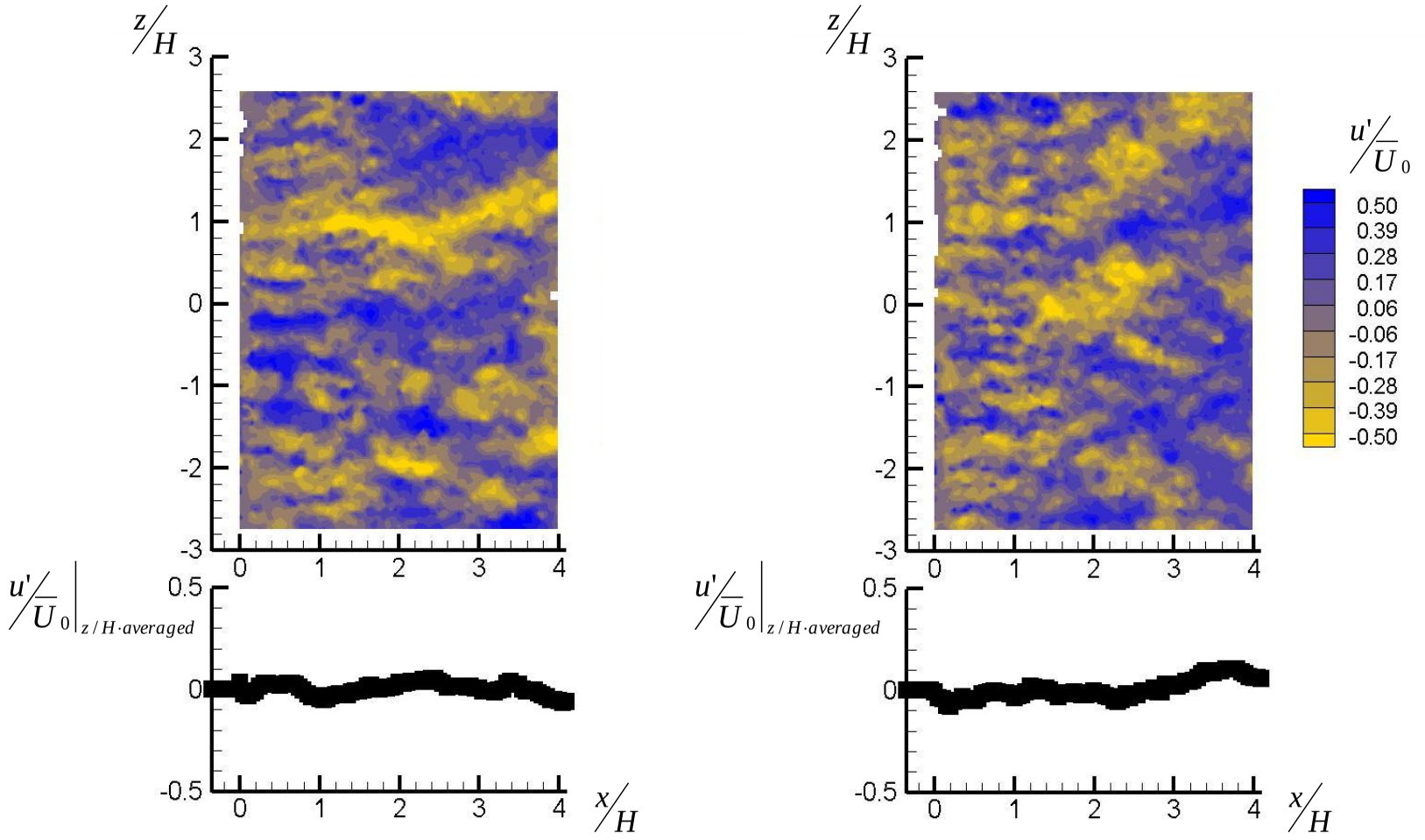

Figure 90: Representative instantaneous contours and spanwise averaged streamwise velocity deviation from the local mean in geometry II for the forced 5% secondary flow rate case

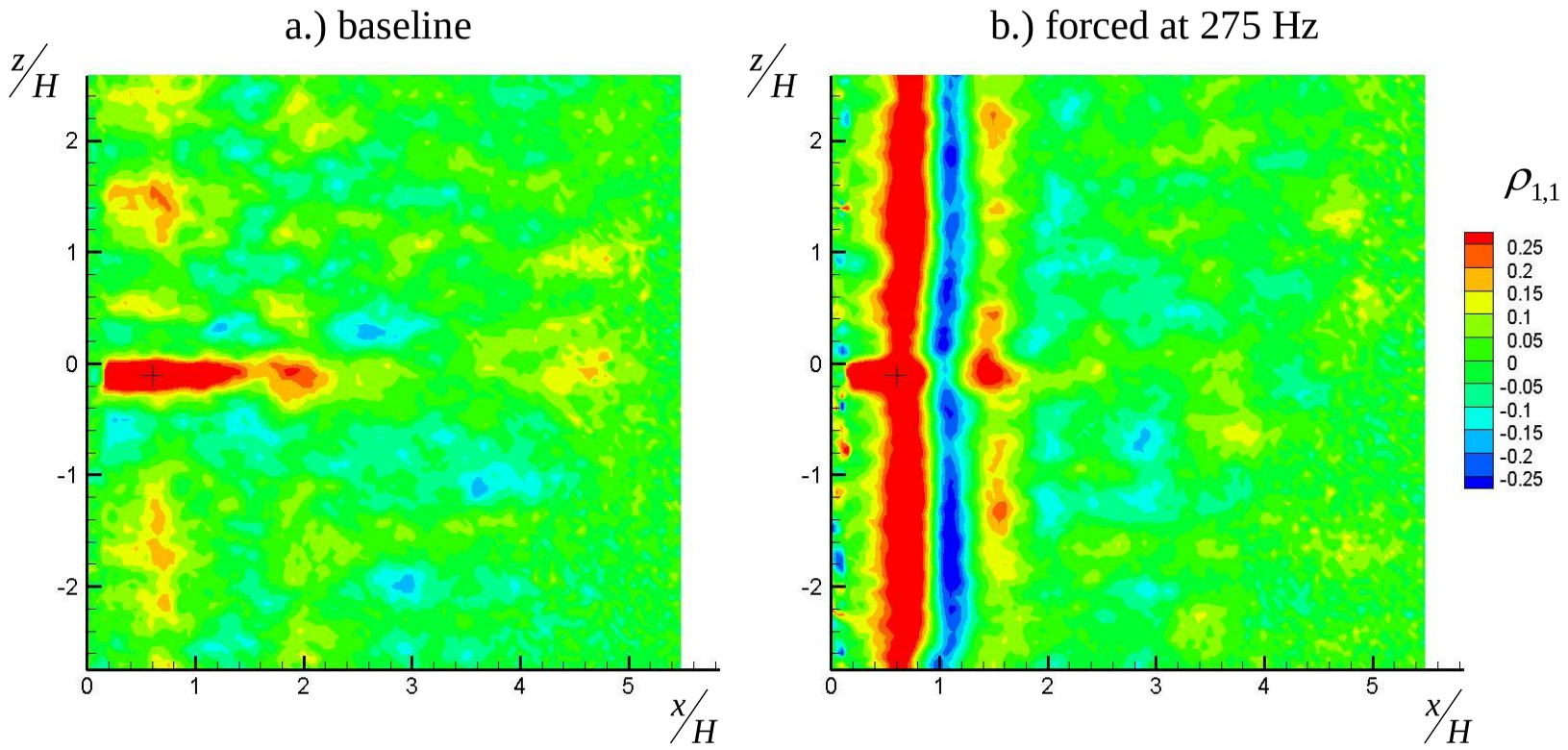

Figure 91: Correlation coefficient distributions for a.) unforced and b.) forced geometry II for the 0% secondary flow rate case

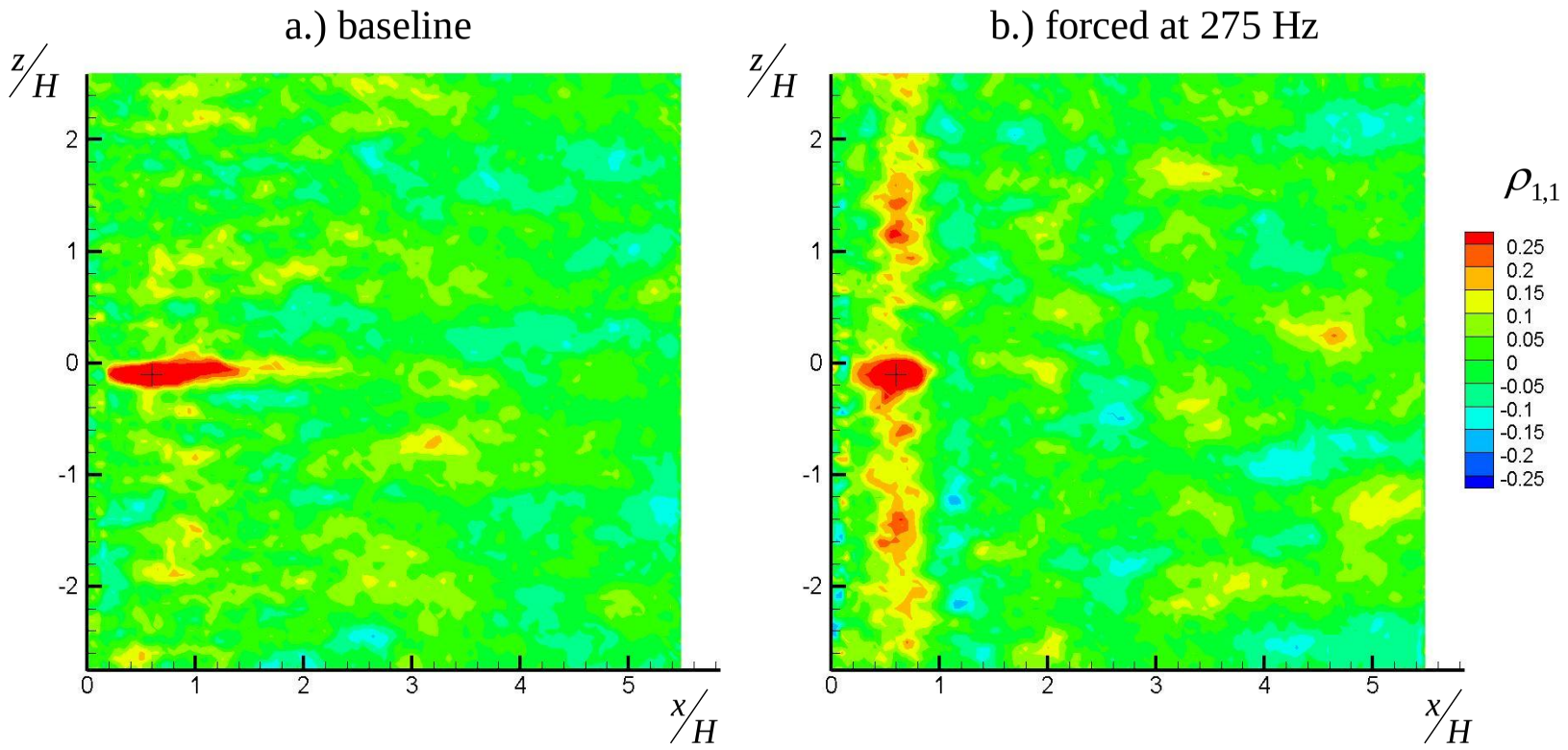

Figure 92: Correlation coefficient distributions for a.) unforced and b.) forced geometry II for the 3% secondary flow rate case

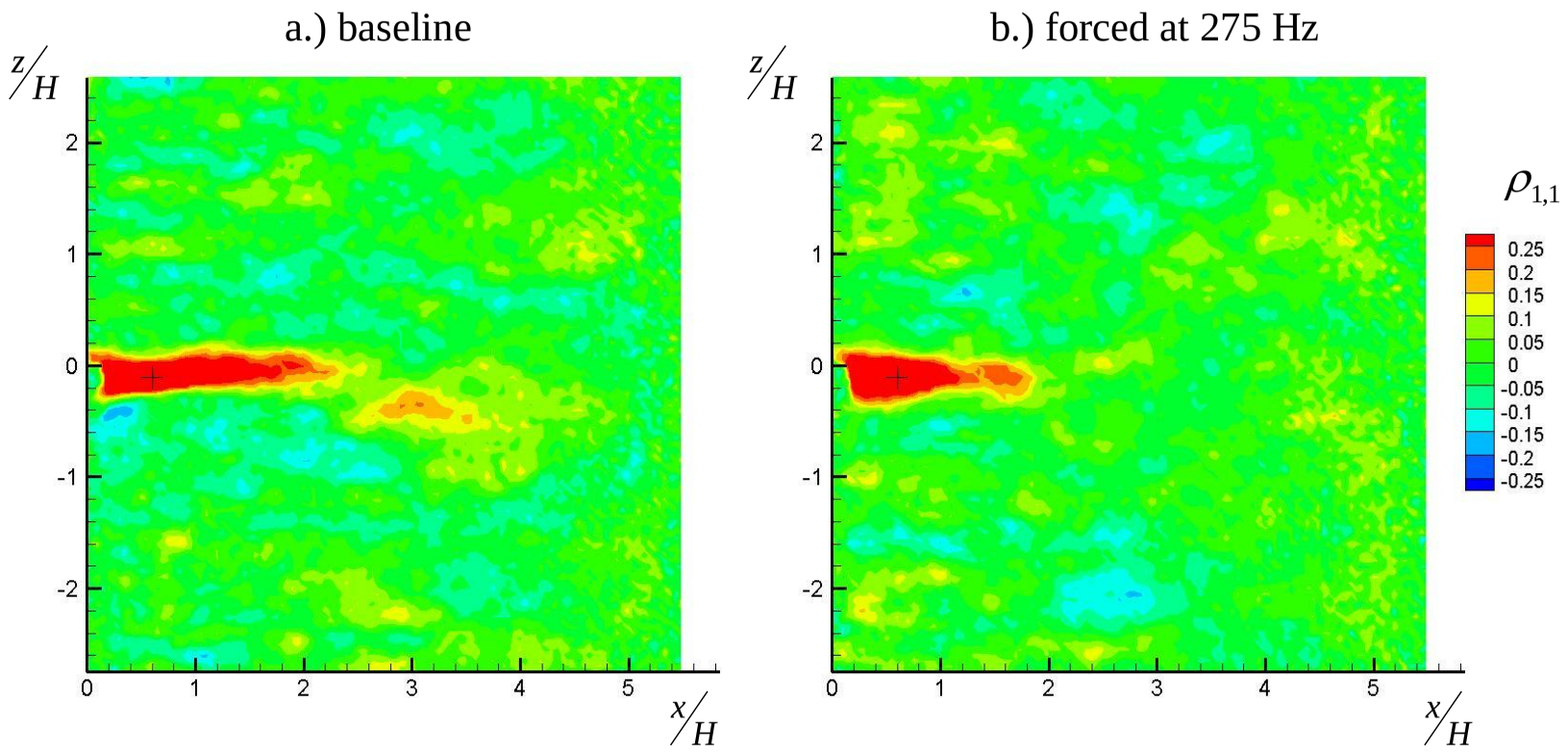

Figure 93: Correlation coefficient distributions for a.) unforced and b.) forced geometry II for the 5% secondary flow rate case

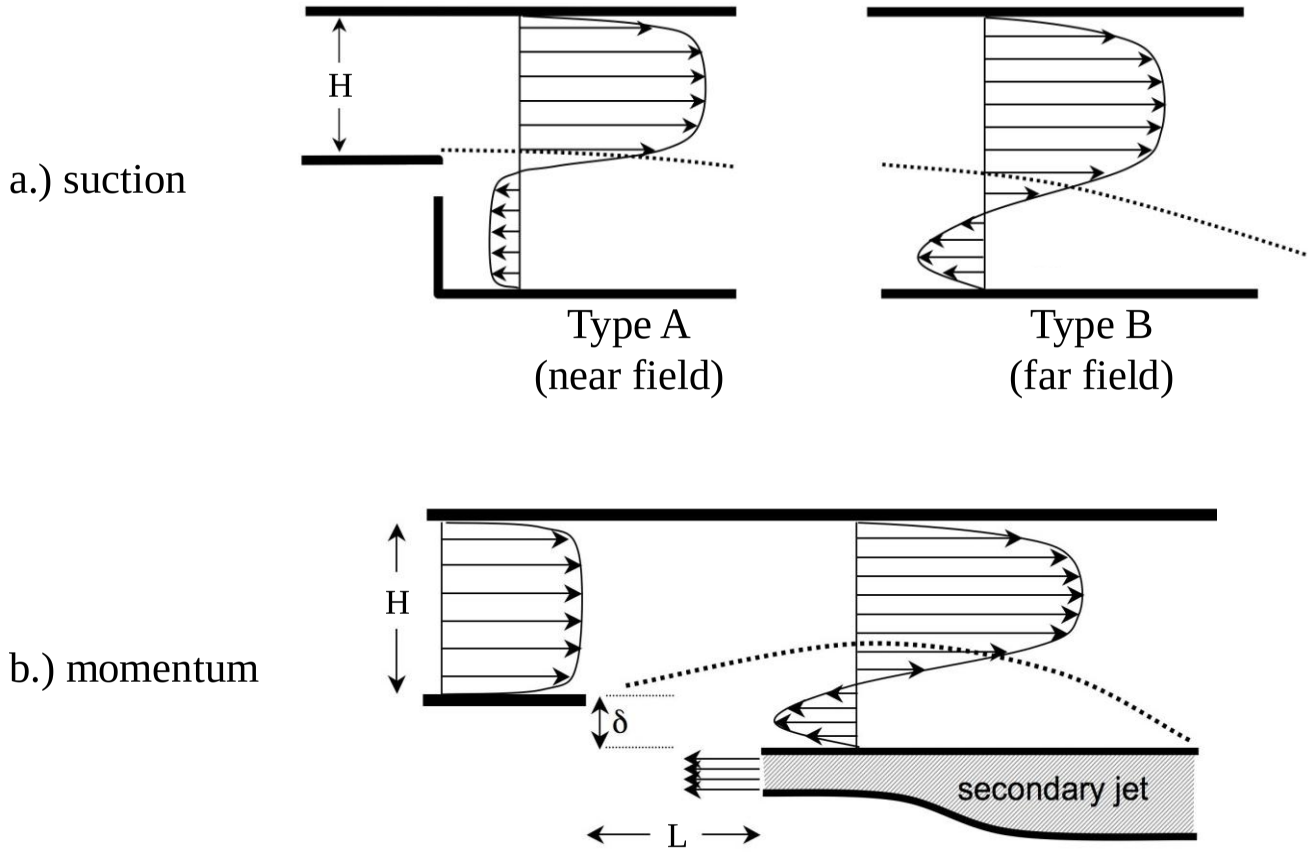

Figure 94: Suction and momentum driven mean streamwise velocity profiles

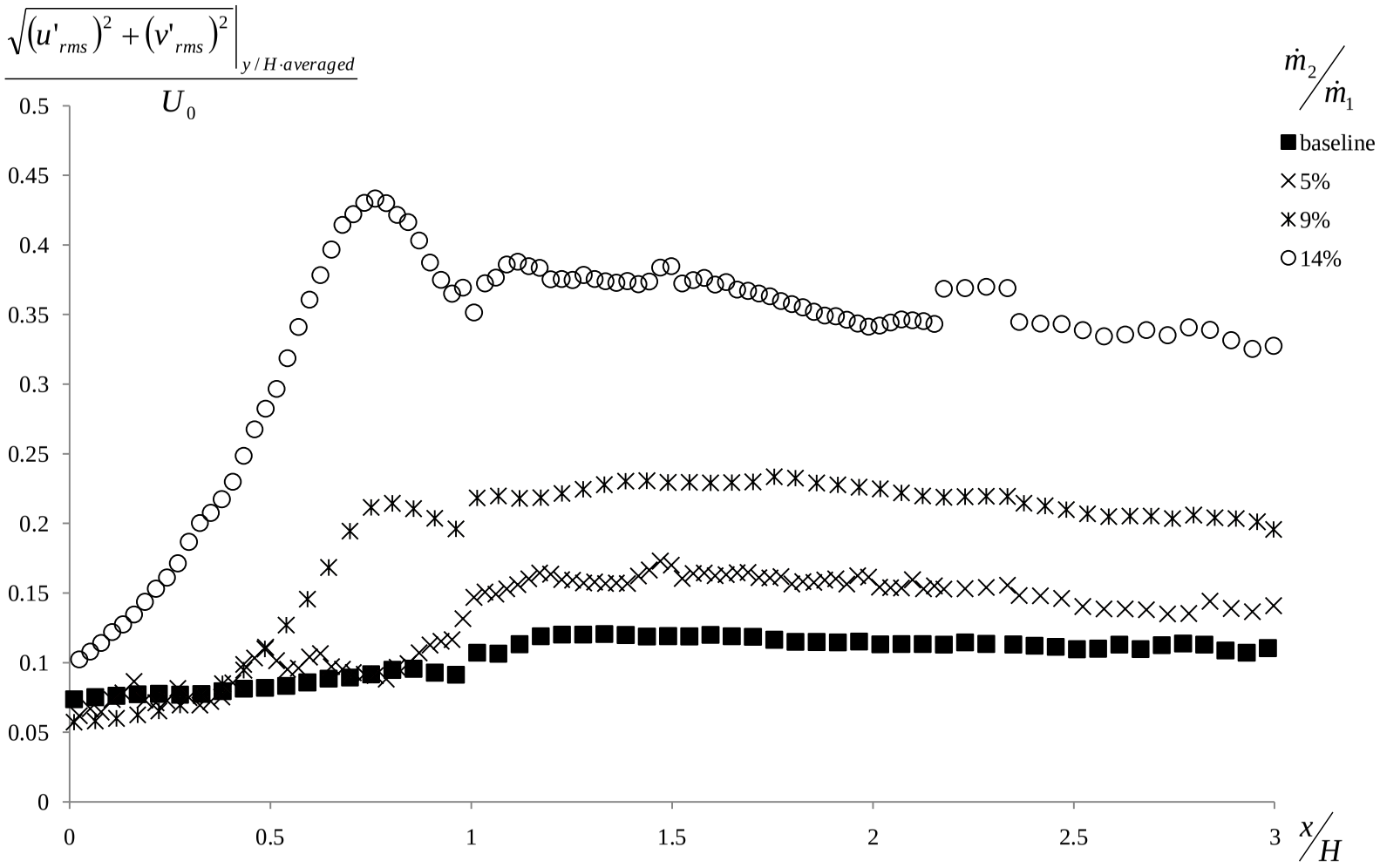

Figure 95: Cross-stream averaged total turbulence for baseline, 5% and 9% for Geometry I

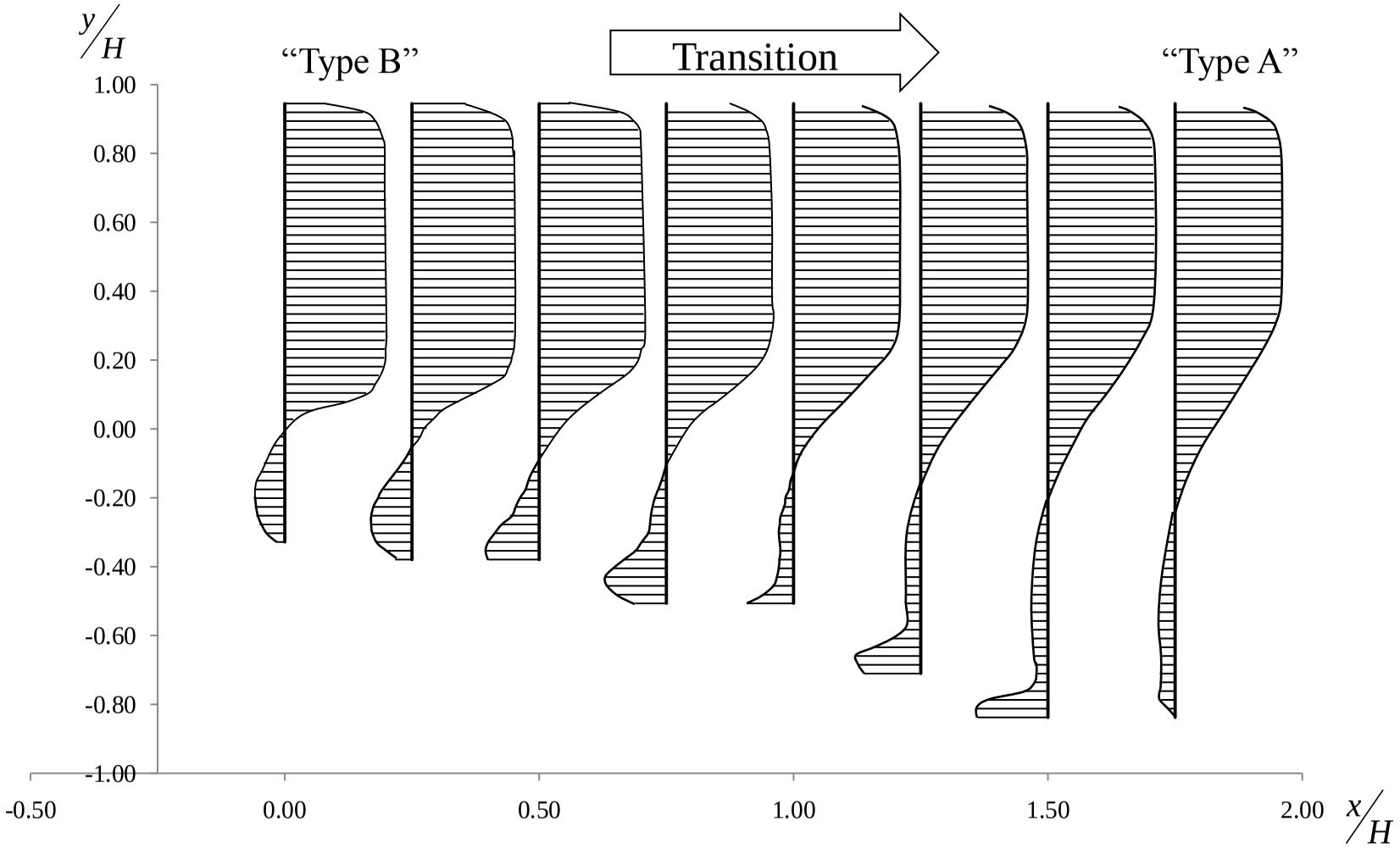

Figure 96: Streamwise velocity profiles within Geometry II for 5% secondary flow rate

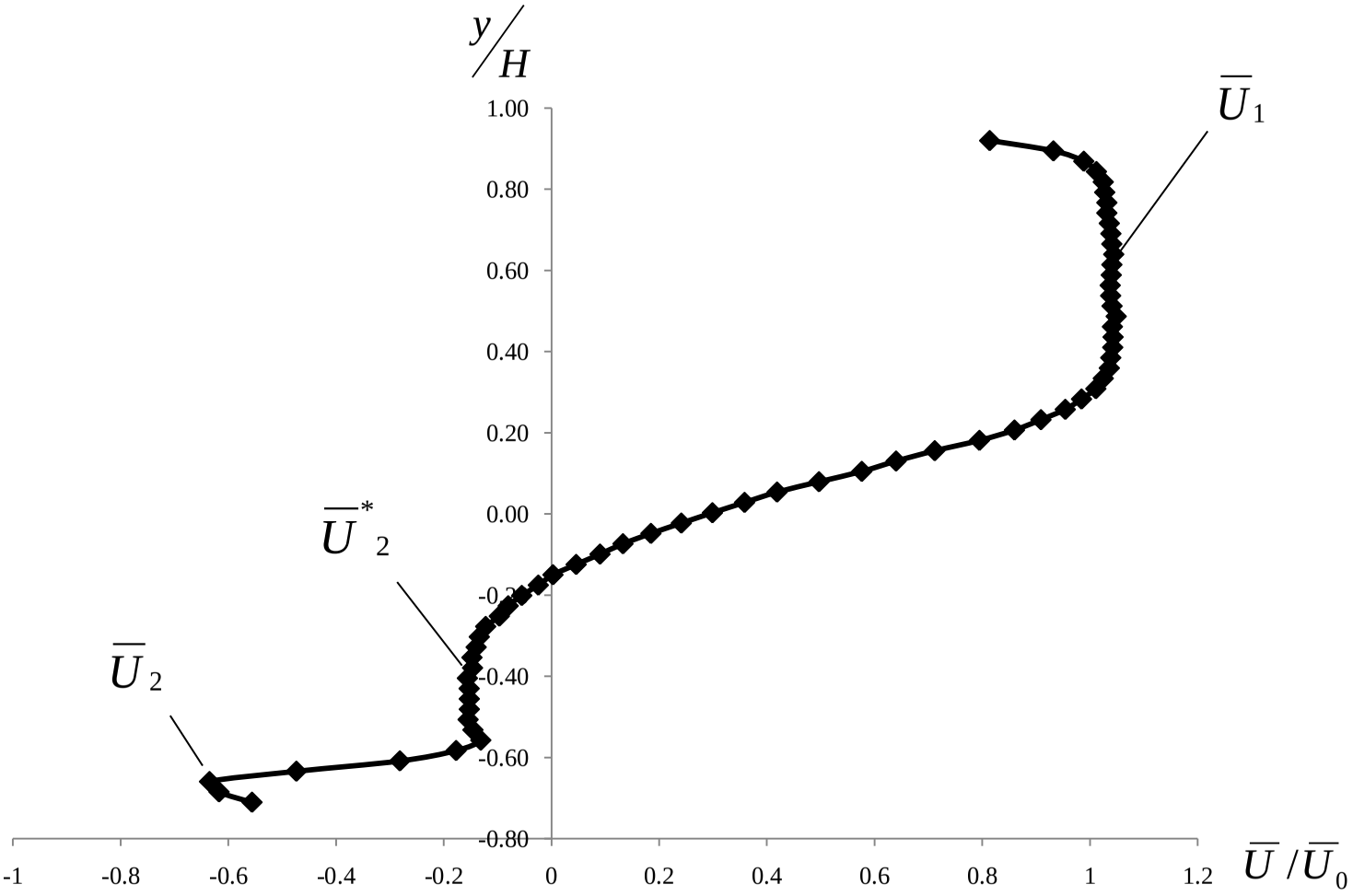

Figure 97: Streamwise velocity profile at x/H = 1.25 for 5% secondary flow rate for Geometry II

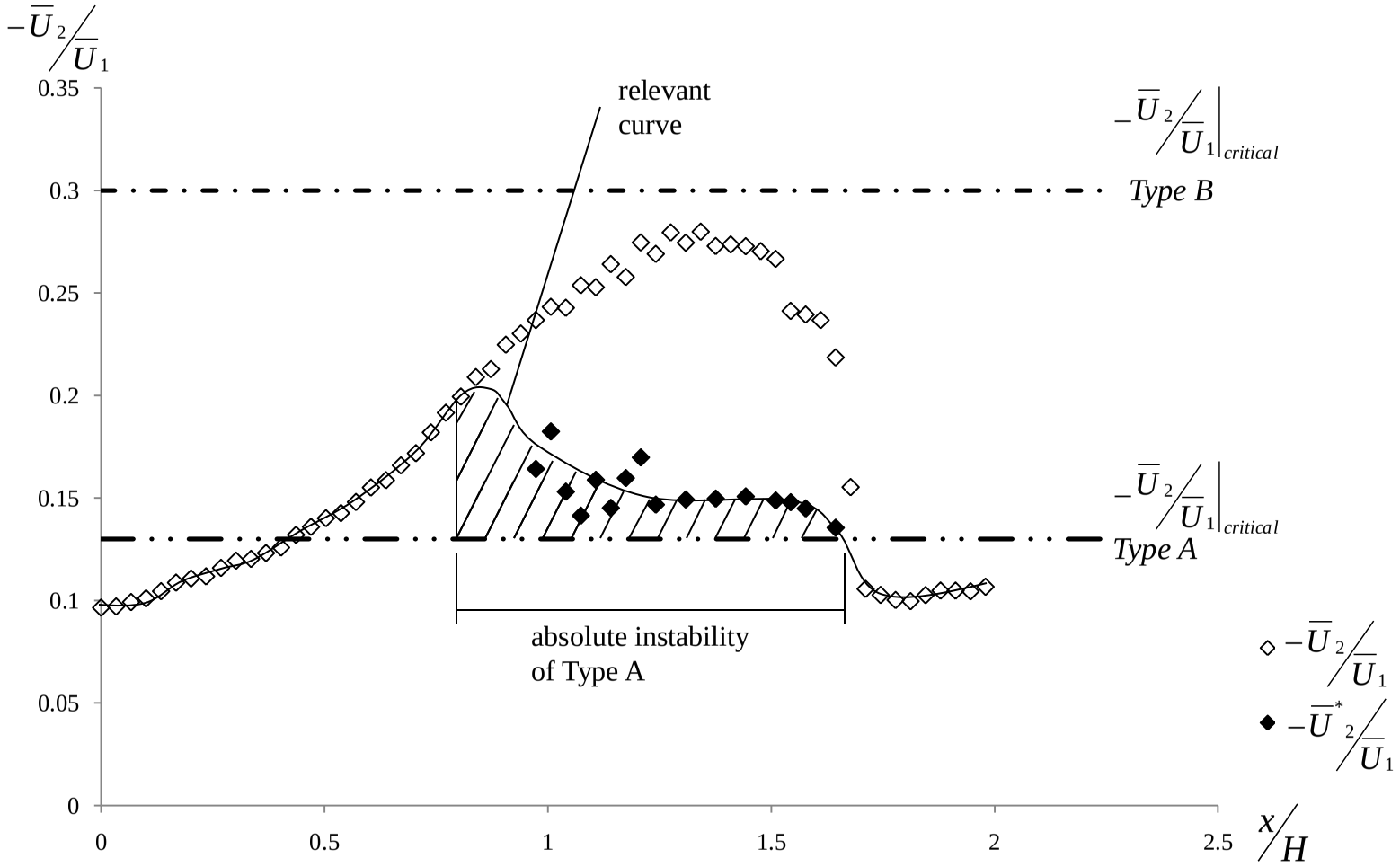

Figure 98: Streamwise velocity ratio distributions for Geometry II at the lowest secondary flow rate (3%)

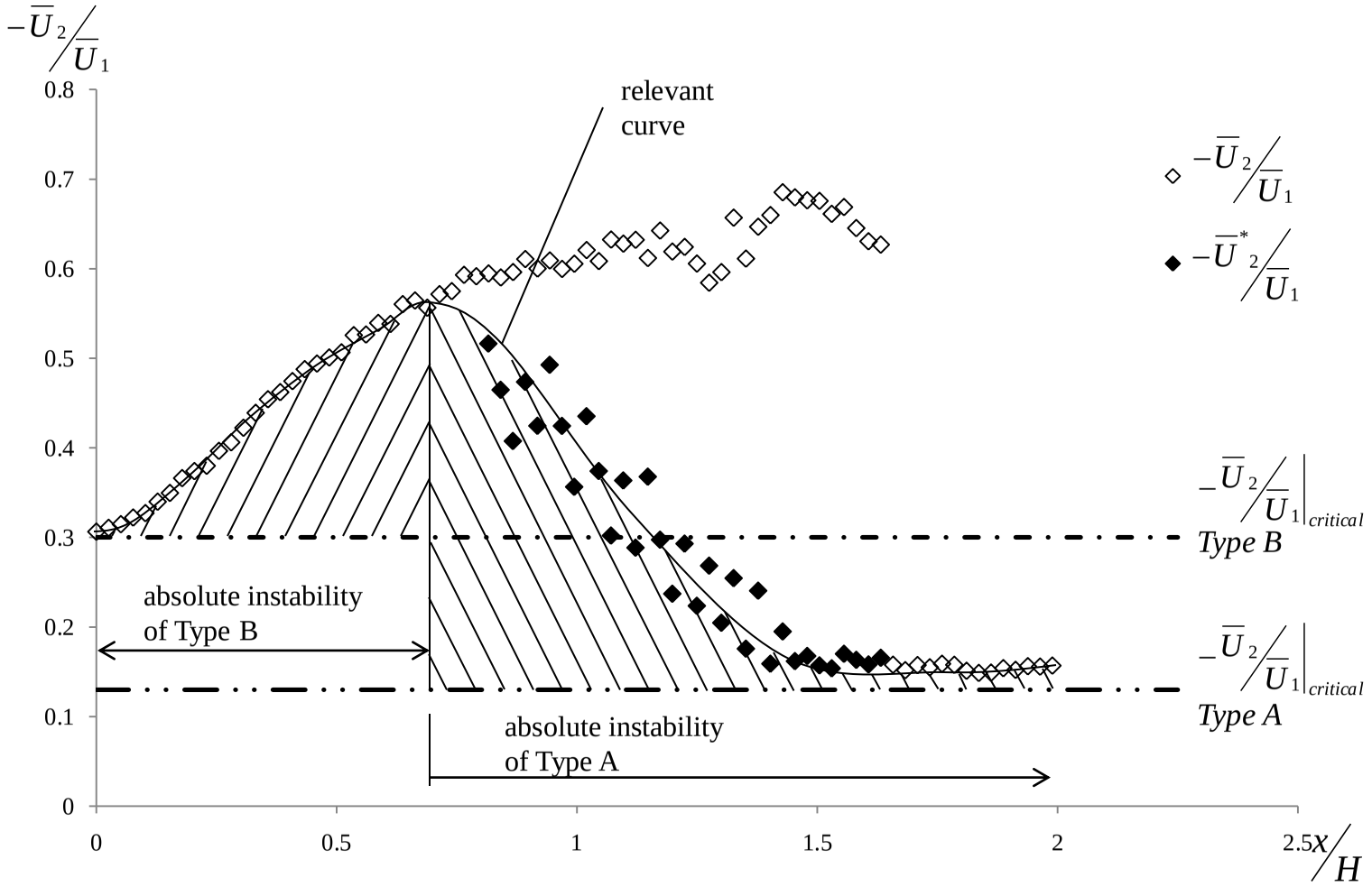

Figure 99: Streamwise velocity ratio distributions for Geometry II at 5% secondary flow rate

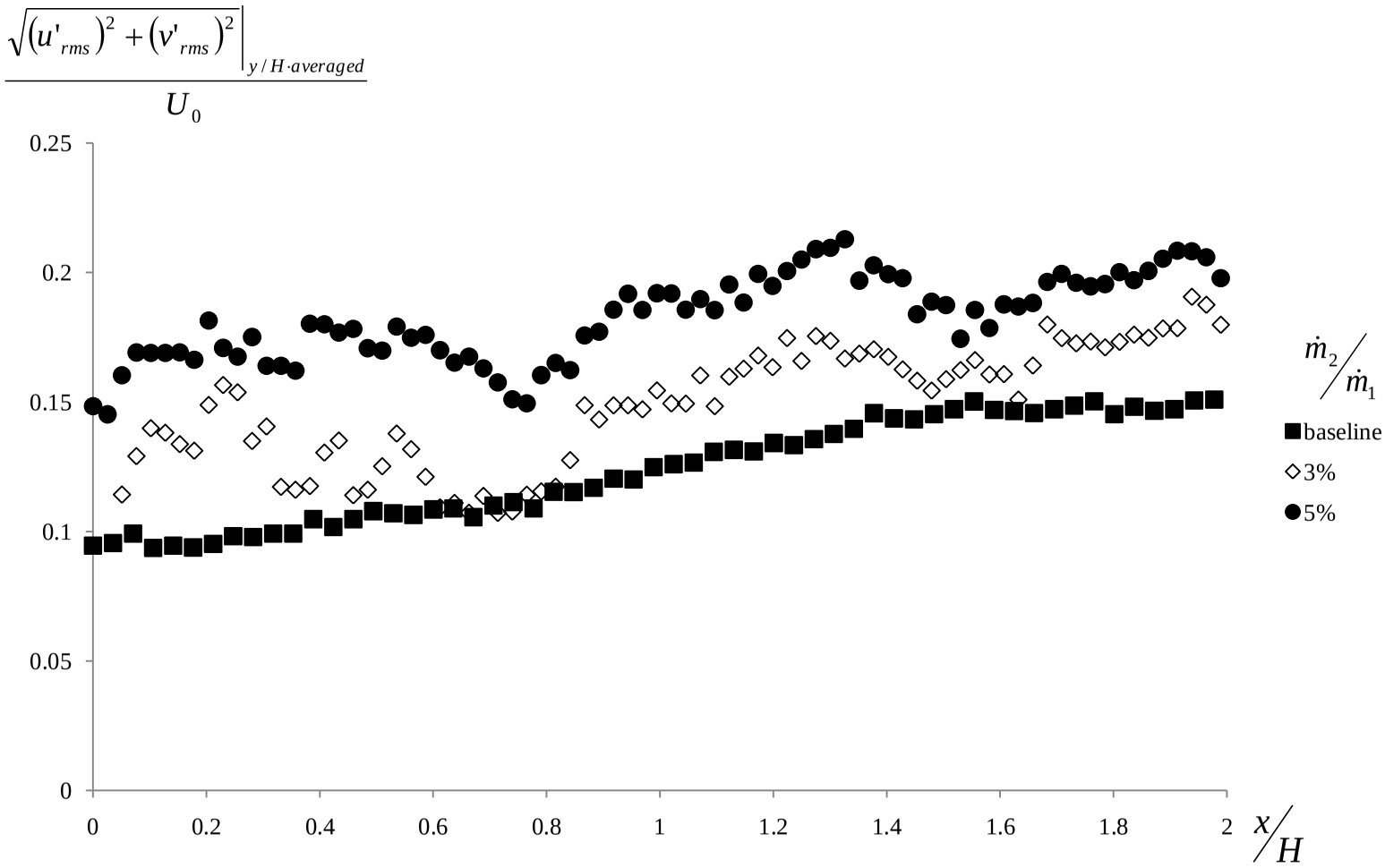

Figure 100: Cross-stream averaged total turbulence for baseline, 3% and 5% for Geometry II

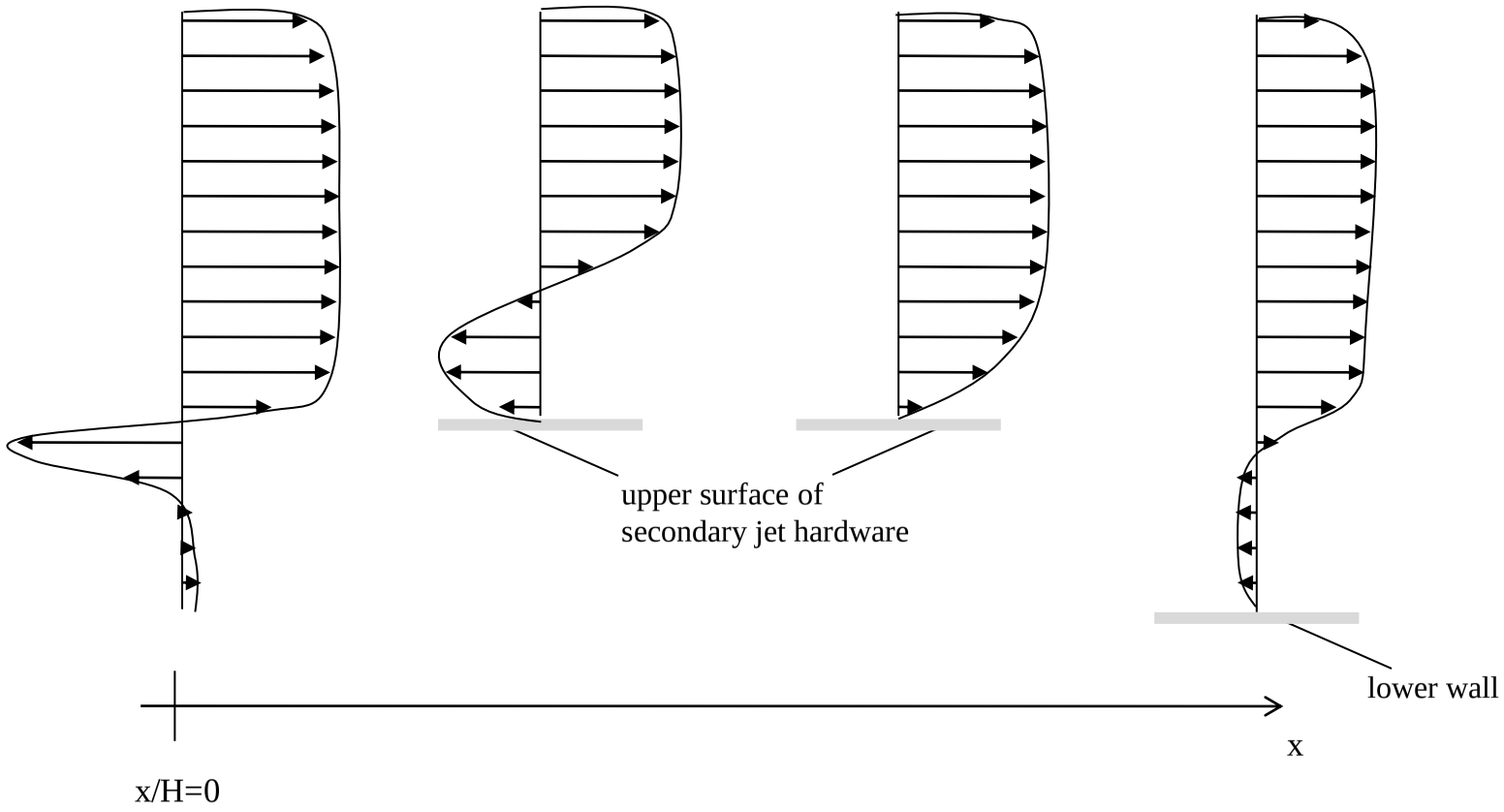

Figure101: Schematics of the mean streamwise velocity profile development within Geometry I facility

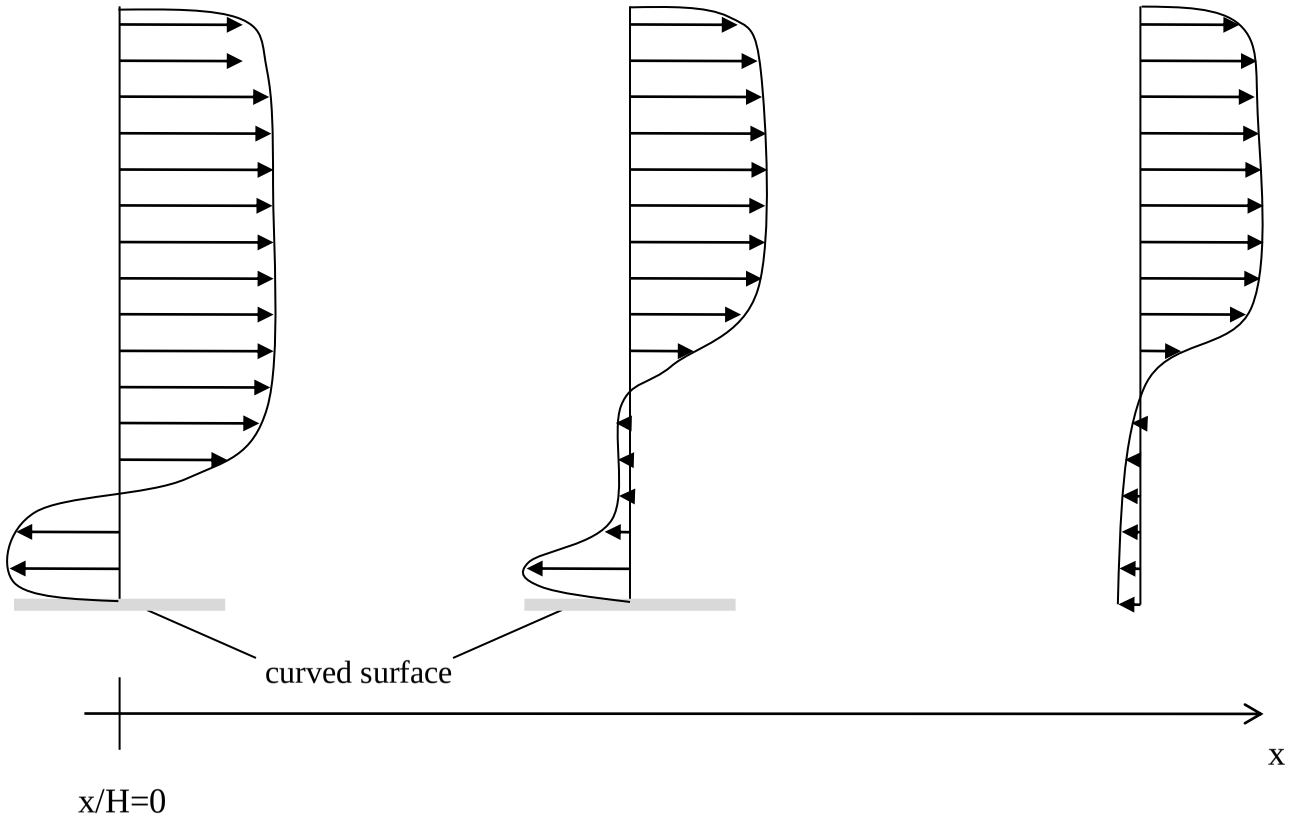

Figure 102: Schematics of the mean streamwise velocity profile development within Geometry II facility